RÉPUBLIQUE FRANÇAISE
Liberté Égalité Fraternité

Université de Toulouse

Doctorat de l'Université de Toulouse

préparé à Toulouse INP

Étude expérimentale de la stabilisation des flammes dans des brûleurs poreux : application des diagnostics optiques dans des géométries imprimées en 3D

Thèse présentée et soutenue, le 2 octobre 2024 par

Enrique FLORES-MONTOYA

École doctorale
MEGEP - Mécanique, Energétique, Génie civil, Procédés

Spécialité
Energétique et transferts

Unité de recherche
IMFT - Institut de Mécanique des Fluides de Toulouse

Thèse dirigée par
Laurent SELLE et Thierry SCHULLER

Composition du jury
M. Ronan VICQUELIN, Président, Université Paris-Saclay
M. Andreas DREIZLER, Rapporteur, Technical University of Darmstad
Mme Terese LØVÅS, Rapporteuse, Norwegian University of Science and Technology
M. Xavier PRADIP, Examinateur, Université de Rouen
M. Laurent SELLE, Directeur de thèse, CNRS Occitanie Ouest
M. Thierry SCHULLER, Co-directeur de thèse, Université Toulouse III - Paul Sabatier

Membres invités
M. Nicolas JEREZ, Bulane

Abstract

Porous Media Burners (PMBs) are a combustion technology based on heat recirculation where a flame is stabilized within the cavities of an inert porous matrix. In PMBs, heat is transferred upstream from the burned to the unburned gas through the solid matrix yielding a preheating of the reactants. This increases their burning rate allowing for more compact combustion devices and the operation beyond conventional flammability limits. As a result, the stabilization of flames at ultra-lean equivalence ratios is possible, with the subsequent reduction of the flame temperature and NO_x emissions. In these burners, a substantial fraction of the power is radiated by the hot solid phase, with radiated power fractions ranging between $20-30\%$. This, together with their elevated efficiency and low pollutant emissions, has motivated their commercial use in various infrared heating applications. In the past years, PMBs have received renewed interest owing to their potential as fuel flexible burners. Their ability to stabilize flames over a wide range of burning rates makes them promising candidates to handle the uneven flame properties of hydrogen and hydrocarbon fuels.

The mechanism of heat recirculation in PMBs is well understood. However, there is still limited knowledge about many pore-scale phenomena that have a critical impact on the macroscopic behavior of the system and its performance. Advanced nonintrusive diagnostics could be used to study local flame stabilization mechanisms and improve current models. However, experimental measurements in PMBs are hindered by the lack of optical access to the interior of the porous matrix. This dissertation presents an experimental study on porous media combustion and is devoted to the application of optical diagnostics. Optically accessible PMBs are produced by combining computer-defined topologies with additive manufacturing techniques. This methodology provides an extensive optical access in a 3D burner configuration without altering the matrix structure. Optical access is leveraged to apply $CH^\star$ chemiluminescence, Mie-scattering imaging and μPIV. Topology tailoring is exploited to analyze the influence of the geometrical parameters of the porous matrix. Direct flame visualization enables the tracking of the reaction region as a function of the operating conditions, which can be used for model validation. The present results bring to light several limitations of current low order models and highlight the influence of the pore size on flame stabilization. Flame-front tracking is also used to investigate the effect of H_2-enrichment on the behavior of the flame. This technique reveals different stabilization trends in H_2-enriched flames that are not well retrieved by current models. Mie-scattering permits the quantification of the re-equilibration distance and the analysis of the flame shape. μPIV measurements show the influence of the topology on the interstitial flow and on the contribution of hydrodynamic effects to flame stabilization.

This PhD seeks to open new paths for the application of non-intrusive diagnostics in PMBs and to improve the current understanding of flame stabilization mechanisms.

Keywords : heat recirculation, porous media combustion, optical diagnostics, fuel flexible burners, flame stabilization, optically accessible burners, topology tailoring.

Acknowledgements

I wish to express my deepest gratitude to all those who have supported me throughout my PhD journey.

First and foremost, I would like to thank my supervisors, Laurent Selle and Thierry Schuller, for their invaluable guidance, support, and encouragement. Their expertise and insights have been crucial in shaping this research. At the lab, you have managed to create a perfect ecosystem where hard work and a good vibes are combined in the exact proportions to obtain both astonishing scientific results and an amazing working environment. Thank you for the invaluable scientific and vital lessons. I am deeply grateful for this incredible opportunity and I feel very fortunate for this experience.

Acknowledgment is also due to the industrial partner of this thesis, Bulane, for their support and funding. Special thanks to Nicolas Jerez and Clément Guyonnet for their guidance and assistance. I really hope that our results help you in spreading hydrogen and decarbonizing combustion.

My sincere thanks are also addressed to Sébastian Cazin for his technical support with the optical diagnostics. His assistance was essential to the success of laser experiments. I am also very grateful to Vincent Baylac from the CIRIMAT laboratory for his technical support with the manufacturing of our burners. This collaboration rendered our parametric analysis affordable and feasible. In the same vein, I extend my gratitude to Stefano and Laurent from the IMFT workshop for their technical assistance, as well as to Moïse Marchal for his help with the lasers and the optics.

Heartfelt thanks go to my fellow PhD students. Their camaraderie, discussions, and moral support have made this journey enjoyable and memorable. A special acknowledgement is due to Pierre-Alexandre Masset, my dear friend and co-author, not only for his invaluable contributions to our papers but also for his moral support and encouragement. I also wish to thank Hugo Pers, Hervé Magnes, Gillien Latour, Andrea Aniello, Sylvain Marragou, Hugo Paniez, and all the others for creating such an amazing environment at the lab.

My time in Toulouse has undoubtedly been one of the most enriching periods of my life. Thanks are due to all my Spanish friends for all the incredible adventures and for making this experience more easygoing.

Finally, I am profoundly thankful to my family and my girlfriend for their unwavering support and encouragement. Their love and understanding have been a constant source of strength and motivation.

Thank you all for making this achievement possible.

Contents

Abstract i

Remerciements iii

Nomenclature viii

1. Introduction 1
- 1.1. Context . . . 2
- 1.2. State of the art . . . 6
  - 1.2.1. Excess-enthalpy combustion and heat recirculation . . . 7
  - 1.2.2. Insights on Porous Media Combustion . . . 8
    - 1.2.2.1. Infinite porous medium . . . 8
    - 1.2.2.2. Finite porous medium . . . 10
    - 1.2.2.3. Real systems . . . 11
    - 1.2.2.4. Burner configuration . . . 13
  - 1.2.3. Applications . . . 15
    - 1.2.3.1. Radiant burners . . . 15
    - 1.2.3.2. Domestic heating . . . 16
    - 1.2.3.3. Steam reforming . . . 17
    - 1.2.3.4. Other applications . . . 17
- 1.3. Research gap . . . 18
- 1.4. Objective of this thesis . . . 22
  - 1.4.1. Publications during the thesis . . . 23
    - 1.4.1.1. Works related to porous media combustion . . . 23
    - 1.4.1.2. Other works . . . 24

2. Experimental setup 25
- 2.1. The POROSITO test rig . . . 26
  - 2.1.1. Burner base . . . 26
  - 2.1.2. Burner head . . . 26
  - 2.1.3. Mixing system . . . 27
- 2.2. Topology-tailored burners . . . 29
  - 2.2.1. Triply-Periodic Minimal Surfaces . . . 29
  - 2.2.2. Pore size and void fraction control . . . 29
  - 2.2.3. From a mathematical function to a printable CAD . . . 31
  - 2.2.4. Graded and swirled topologies . . . 32
  - 2.2.5. Optical access . . . 33
  - 2.2.6. Additive manufacturing technique . . . 35
  - 2.2.7. Inventory of porous burners . . . 38
- 2.3. Diagnostics . . . 39
  - 2.3.1. Imaging . . . 39
  - 2.3.2. Thermometry . . . 39
- 2.4. Experimental procedure . . . 40
- 2.5. Images post-treatment . . . 42

2.6. Conclusions of the chapter . . . 44
2.A. Uncertainties analysis . . . 45
2.A.1. Load and mixture composition . . . 45
2.A.2. Inlet temperature . . . 46

3. Volume Averaged Model **51**
3.1. Modeling approaches in Porous Media Combustion . . . 52
3.1.1. Theoretical models . . . 52
3.1.2. Direct Pore Level Simulations . . . 53
3.1.3. Volume averaged models . . . 55
3.2. Volume Averaged Model . . . 56
3.2.1. Conservation equations . . . 56
3.2.2. Effective diffusive fluxes . . . 57
3.2.3. Interphase heat exchange . . . 57
3.2.4. Heat losses . . . 61
3.2.5. Boundary conditions . . . 61
3.3. Evaluation of model constants . . . 62
3.3.1. Topological parameters . . . 62
3.3.2. Material-dependent parameters . . . 63
3.4. Conclusions of the chapter . . . 65

4. Flame-front tracking in PMBs **67**
4.1. Introduction . . . 68
4.2. Results & Discussion . . . 68
4.2.1. Stability domain . . . 68
4.2.2. Axial profiles of $CH^\star$ and temperature . . . 69
4.2.3. Flame-front tracking . . . 71
4.2.4. Sensitivity to the interphase heat exchange submodel . . . 73
4.3. Conclusions of the chapter . . . 74
4.A. Influence of solid phase properties . . . 75

5. Speed-up drivers for H_2-enriched flames **79**
5.1. Introduction . . . 80
5.2. Controlled flashback . . . 80
5.3. Results & Discussion . . . 82
5.3.1. Influence of porosity . . . 82
5.3.2. Influence of H_2-enrichment . . . 84
5.4. Conclusions of the chapter . . . 88

6. Pore-scale laser diagnostics **89**
6.1. Introduction . . . 90
6.2. Experimental setup . . . 91
6.2.1. Seeding system . . . 92
6.2.2. The POROSITO test rig . . . 92
6.2.3. Laser-suited PMBs . . . 94
6.2.4. Influence of seeding . . . 95
6.3. Mie-Scattering in a PMB . . . 96
6.3.1. Preliminary considerations . . . 96
6.3.2. Results . . . 99
6.4. PIV measurements at the scale of a pore . . . 100
6.4.1. Diagnostics setup . . . 100

6.4.2. Calibration process . . . 101
6.4.3. Experimental procedure . . . 103
6.4.4. Images processing . . . 103
6.4.5. Results . . . 103
6.5. Influence of the burner topology . . . 108
6.6. Conclusions of the chapter . . . 111
6.A. Supplementary material . . . 112

Conclusions of the chapter **115**
Conclusions . . . 115
Future research directions . . . 117

Appendices **119**
A. Predicting flashback limits in H_2-enriched CH_4/air and C_3H_8/air laminar flames 121

List of Figures **139**

List of Tables **145**

Bibliography **147**

Nomenclature

Abbreviations

(P)LIF	(Planar) Laser Induced Fluorescence
AM	Additive Manufacturing
CAD	Computer Aided Design
CARS	Coherent Anti-stokes Raman Scattering
DPLS	Direct Pore-Level Simulations
FFB	Fuel-Flexible Burners
LHV	Lower Heating Value
MFC	Mass Flow Controller
NG	Natural Gas
P2G	Power-to-Gas
PDF	Probability Density Function
PMB	Porous Media Burner
PMC	Porous Media Combustion
RES	Renewable Energy Sources
SLM	Selective Laser Melting
STD	See-Through Direction
STL	Standard Triangle Language
TPMS	Triply Periodic Minimal Surface
TRL	Technology Readiness Level
VAM	Volume-Averaged Model(ling)

Reactive fluid mechanics

$\dot{\omega}_k$	species reaction rate per unit volume
$\dot{\omega}_T$	heat release rate per unit volume in the temperature equation
$\dot{\omega}_T^0$	heat release rate per unit volume in the total energy equation
$\overline{\dot{m}}$	mass flux ($= \rho_g u_g$)
$\dot{m}$	mass flow rate ($[\mathrm{kg\,s^{-1}}]$)

$\dot{n}$	molar flow rate ($[\mathrm{mol\,s^{-1}}]$)
$\dot{q}_{\mathrm{loss}}$	radial heat loss term
λ_g	gas thermal conductivity
$\mathbf{J_k}$	species mass flux
$\mathbf{u}$	velocity vector ($= (u, v, w)$)
$\mathbf{V_c}$	correction velocity
$\mathbf{x}$	position vector ($= (x, y, z)$)
$\mathcal{T}_g^{\mathbf{eff}}$	effective macroscale heat diffusion flux
μ	dynamic viscosity
ν	kinematic viscosity
ρ_g	gas density
$\underline{\underline{\boldsymbol{\tau}}}$	viscous stress tensor
$c_{p_g,k}$	individual species gas heat capacity per mass unit
c_{p_g}	gas heat capacity per mass unit
D^{int}	intrinsic diffusivity
D_k	mixture averaged diffusion coefficient of species k
$J_k^{\mathbf{eff}}$	effective macroscale species diffusion flux
p	pressure
T_g	gas temperature
T_{ad}	adiabatic flame temperature
T_{in}	inlet temperature
W_k, W	species and mean molecular weights
Y_k, X_k	species mass and molar fractions
$Y_{k_{in}}$	inlet mixture composition

Porous matrix characterization

β	radiative extinction coefficient
ϵ	porosity
η	transmissivity
η_{λ_r}	spectral transmissivity
κ	TPMS wavenumber ($= 2\pi/\Lambda$)
Λ	TPMS period
λ_s	solid thermal conductivity
λ_s^{eff}	macroscale effective thermal conductivity
$\mathcal{D}$	Diamond TPMS equation

$\mathcal{G}$	Gyroid TPMS equation
$\mathcal{P}$	Primitive TPMS equation
Ω_g, Ω_s	gas and solid domain
$\partial\Omega$	fluid-solid interface
τ	phase tortuosity
Ξ	solid emissivity
D^{dis}	dispersion diffusion coefficient
D_{ψ}^{eff}	effective macroscale diffusivity of a quantity ψ
d_p	pore size
h	surface heat transfer coefficient
h_V	volume heat transfer coefficient
l_{dis}	dispersion proportionality constant
S_v	surface density
t	TPMS threshold
T_s	solid temperature
V_g, V_s	gas and solid volume

Length scales

δ_R	reaction thickness
δ_T	flame thickness
D	diameter of the burner
D_b	diameter of the thermocouple's bead
d_p	pore diameter
L	length of the porous matrix
l_{g}	gas diffusion length scale
$l_{\text{re-eq}}$	interphase re-equilibriation length scale
l_{r}	reaction length scale
l_{s}	solid diffusion length scale

Other symbols

α	hydrogen molar fraction in the fuel
α_P	hydrogen power fraction
ΔT	preheating temperature in excess of T_{in}
$\delta\psi$	uncertainty in variable ψ
ϵ_b	emissivity of the thermocouple's bead

σ_B	Stefan-Boltzmann constant
A	area of the burner cross-section ($= \pi D^2/4$)
P	thermal power
p_{amb}	ambient pressure = 1 atm
R	universal gas constant
r	radial coordinate
S_{L_0}	burning velocity of a 1D unstretched adiabatic flame
S_{L_P}	preheated flame speed
T_{amb}	ambient temperature (= 300 K)
$T_{\max}$	maximum temperature reached in the domain
T_b	temperature of the thermocouple's bead
u_B	bulk flow velocity ($= \dot{m}/(\rho_{in} A \epsilon)$)
x	longitudinal coordinate
x^*, y^*	local coordinates in μPIV images
x_f	flame front position
x_v	evaporation front position
y, z	transverse coordinates

Reduced parameters

η_{rec}	recirculation efficiency
Ze	Zel'dovich number
ϕ	equivalence ratio
Da	Damkholer number
Le_k	species Lewis number
Sc_k	species Schmidt number
θ	dimensionless temperature ($= (T - T_{in})/(T_{ad} - T_{in})$)
ξ	dimensionless axial coordinate ($= x/L$)
Pe	pore-based thermal Péclet number
Pr	Prandtl number
Re	pore-based Reynolds number

Sub/superscripts

^{eff}	effective property at the macroscopic scale
$_0$	reference 1D adiabatic laminar flame
$_f$	related to fuel f

$_g$	gas related
$_{i,\ j}$	indices
$_k$	related to species k
$_s$	solid related
$_{in}$	inlet quantity

Chapter 1

Introduction

In this chapter, an analysis of the societal context that motivates this research is presented. The focus is on two specific issues related to the energy transition: the storage of the excess energy from renewables and the decarbonization of combustion processes. In this context, Porous Media Burners (PMBs) are considered for their potential role as high-efficient, low-NO_x and fuel-flexible radiant burners.
This is followed by a comprehensive introduction to porous burners that covers the seminal works, the driving mechanisms, and the current and potential applications.
Next, we delve into the research gap that this thesis aims to address: the scarcity of nonintrusive diagnostics in porous media combustion. The latest works in this area are reviewed to offer an in-depth picture of the current state-of-the-art. Finally, the objective of this dissertation is identified and the structure of the manuscript is outlined.

Overview

1.1. Context **2**
1.2. State of the art **6**
1.2.1. Excess-enthalpy combustion and heat recirculation 7
1.2.2. Insights on Porous Media Combustion 8
1.2.3. Applications 15
1.3. Research gap **18**
1.4. Objective of this thesis **22**
1.4.1. Publications during the thesis 23

"*Will to win, collective action, and surprise.*"

Francisco Flores

1.1. Context

Storage of RES excess energy

Meeting the net-zero goal imposed by the Paris Agreements of 2015 enforces us to undertake massive reductions in CO_2 emissions [1]. To tackle this challenge, fossil fuels must be replaced by Renewable Energy Sources (RES). In the past decades, their role in the electricity production has largely increased and they already represented 44% of the total electricity production in Europe in 2023 [2]. In the foreseeable future, their share in the global electricity mix is expected to continue increasing. However, RES such as windmills and solar energy are characterized by a non-dispatchable nature: their variability and unpredictability make it challenging for energy supply to consistently meet demand. This problem is already manifesting under the form of negative electricity prices in certain countries of Europe such as Spain, France and Belgium (cf. Fig. 1.1). At present, one of the most common solutions for large-scale energy storage is Pumped Hydro Storage (PHS) [3]. However, this technology is limited by the geographical conditions. In Europe, the Alps concentrate the largest PHS potential and a significant portion is already utilized to balance the energy generation from RES at the European level [4, 5]. In the coming decades, grid-balancing may become a primary challenge owing to the growing share of variable RES and the progressive saturation of PHS capacities. Therefore, it is necessary to develop alternative storage methods at large scale [3, 6].



Figure 1.1. – Headlines announcing negative electricity prices in the European pool.

Decarbonization of combustion processes

As illustrated in Fig. 1.2, combustion accounts for nearly 90% of the total energy supply in the world [7]. Combustion devices are characterized by a high power density and flexibility, which partly explains why they are hard to replace by other technologies. Moreover, combustion systems cover a broad range of the power spectrum: from microcombustors featuring a few watts of power to gas turbines whose nominal power can reach hundreds of megawatts [8, 9]. Decarbonizing combustion processes is therefore a key step in the transition to a zero-emissions economy. While electrification is often the most straightforward path for decarbonization, several technologies and industrial processes, known as hard-to-electrify, cannot drop combustion. In some applications such as the heavy industry, this is because of the elevated temperatures required. In others, such as in air transportation, electrification is hindered by the elevated power density requirements.

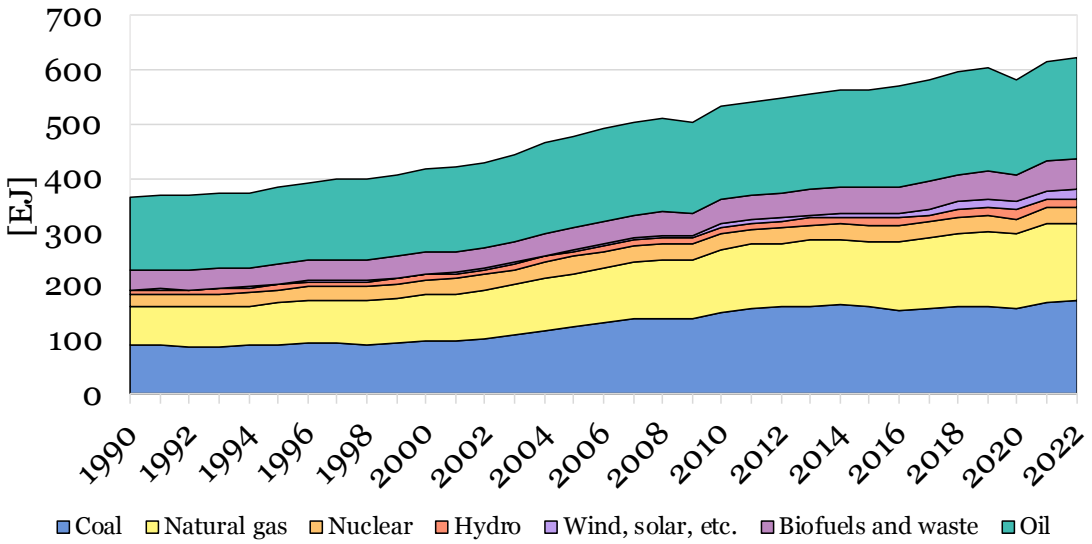

Figure 1.2. – Evolution of the global total energy supply in EJ by source. Reproduced from IEA [7].

Hydrogen as an energy carrier

Owing to its high specific energy density and null direct CO_2 emissions, hydrogen is a promising substitute for fossil fuels in hard-to-electrify sectors, such as long-distance transport and heavy industry [10]. Moreover, hydrogen is an energy carrier and can be used to store the energy surplus from RES via the Power-to-Gas (P2G) strategy. P2G leverages excess electricity to produce hydrogen from water electrolysis [11, 12]. Energy stored in the form of hydrogen can be either consumed in fuel cells to produce electricity or used in burning systems. It is important to stress that this strategy makes both economical and energetic sense only when applied to the surplus energy that would otherwise be wasted. This is because of the significant energetic toll incurred in each transformation: from electricity to chemical energy (electrolysis) and from chemical storage to mechanical energy (thermal engine). In many cases, blending hydrogen into the current NG pipeline is deemed as a viable path for a partial and progressive decarbonization of combustion applications [13, 14]. This scenario is somewhat more realistic since it permits a smooth transition from fossil fuels to hydrogen-based combustion. In addition, this option takes advantage of the existing NG pipeline infrastructure to convey the fuel to the end-users.

Technological and scientific hurdles

H_2-usage is yet to be mastered and requires overcoming various challenges associated to this fuel. Some of them such as diffusion leaking [15] and hydrogen embrittlement [16] are related to its handling rather than to combustion. Nonetheless, hydrogen combustion is faced with fundamental questions related to flame stabilization, combustion instabilities, NO_x mitigation and transition to detonation [17]. Several practical aspects related to safety such as the dim visibility of H_2 flames are also major hurdles [18]. When it comes to flame stabilization, several properties of hydrogen are responsible for a qualitative change in the flame behavior with respect to conventional hydrocarbon fuels. On the one hand, hydrogen flames feature larger burning velocities and a broader flammability range [17]. On the other hand, the disparity between its thermal and mass diffusivity produces preferential diffusion effects. Thermo-diffusive effects alter

the stabilization properties of lean hydrogen flames and can result in combustion instabilities [19, 20].

Nonetheless, in the P2G scenario, hydrogen will not be burned alone but blended with other hydrocarbon fuels such as NG. When it comes to domestic applications, it is generally accepted that hydrogen contents of up to 20% in volume can be accommodated by the existing end-use systems with little or minor adjustments [21–25]. However, a hydrogen substitution of $\sim 20\%$ in volume barely results in a 7% reduction of the CO_2 mass emissions per energy unit [21]. The current blending limits imposed by end-use systems prevent a substantial substitution and therefore a significant decarbonization.

Furthermore, because of the intermittent nature of RES, the content of H_2 in the NG network may experience important fluctuations. Therefore, when integrating hydrogen into the current system, it is crucial to keep flexibility in mind. The gradual transition to a hydrogen economy requires the development of Flexible Fuel Burners (FFB) which can operate safely and efficiently with varying hydrogen contents in the fuel [26, 27]. Because of the disparity between the flame properties of hydrogen and hydrocarbon fuels, fuel-flexible combustion technologies are deemed even more challenging than monofuel hydrogen burners.

In the past years, the combustion of hydrogen and hydrogen/hydrocarbon blends has been the object of a large number of R&D projects involving important investments [28, 29]. The industry and the scientific community are teaming up to develop H_2-suited combustion technologies for different applications and to adapt existing devices to this fuel [30–38].

Combustion technologies

The development of fuel flexible burners across different sectors is closely tied to the specificities of each application. The requirements imposed by the end-use system shape each combustion technology. Because burning systems are ubiquitous, there are almost as many combustion technologies as combustion applications. Coaxial injectors are used in liquid-fuel rockets, piston engines in automobiles and partially premixed self-aspirating burners in household applications. For instance, condensing boilers used for domestic heating are equipped with multiperforated premixed laminar burners such as the one shown in Fig. 1.3. This technology is used for its broad power range, high efficiency and low NO_x emissions [31, 35].

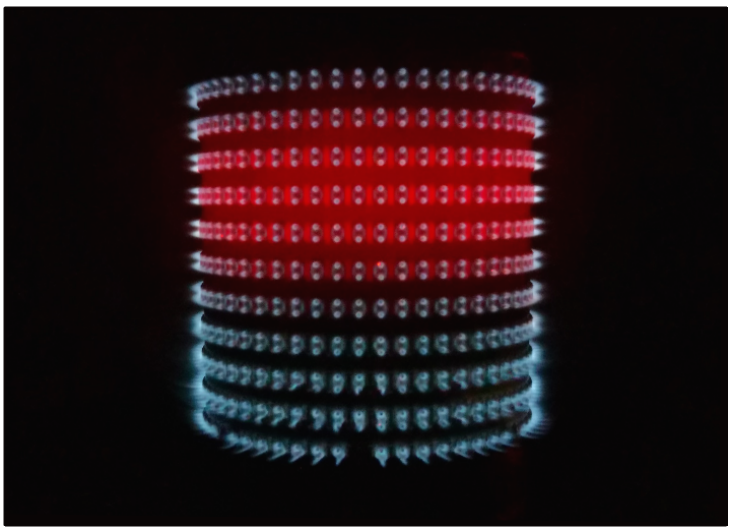

Figure 1.3. – Multiperforated premixed laminar burner used in condensing boilers. Credits to Hugo Pers.

Porous Media Burners

Porous Media Burners (PMBs) are another combustion technology where a flame is stabilized within the cavities of an inert porous matrix [39, 40]. The solid phase recirculates heat from the burned to the unburned gas yielding a preheating of the reactants. This increases the flame burning rate and may result in super-adiabatic temperatures, which is why this combustion technology is often termed excess-enthalpy combustion [41, 42]. Increasing the burning rate per flame unit surface translates into combustion systems with higher power density and hence in more compact burners [43].

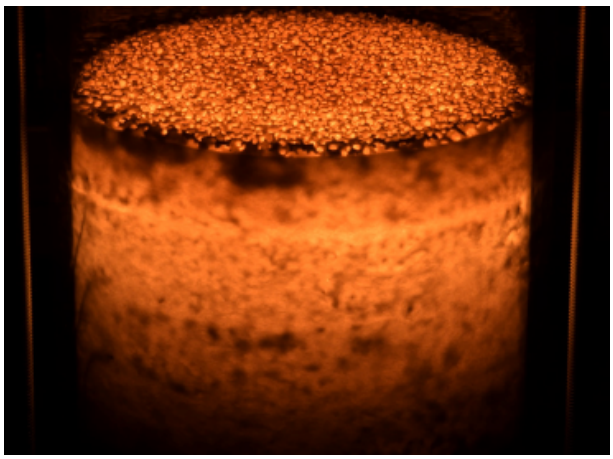

Figure 1.4. – Porous Media Burner in laboratory conditions. Credits to François Muller.

Heat recirculation increases the reactivity of the fresh gasses, extending the flammability limits of the mixture [44]. The ability to operate beyond conventional flammability limits is an interesting feature from the point of view of safety. This is because, in the event of a leakage or flame extinction, the risk of undesired deflagrations reduces if the unburned mixture is not flammable in standard conditions. Owing to the low attainable equivalence ratios, relatively low flame temperatures are obtained and hence NO_x emissions can be arbitrarily low. In porous media burners, the solid phase reaches elevated temperatures and glows, producing a strong radiative flux that can be used for heating. Finally, because of the low Reynolds number, the flow regime is laminar and these burners are usually quiet. This is a notable practical advantage since noisy burners may be incompatible with some domestic applications. The most remarkable features of porous media burners are summarized down below:

1. Elevated radiant yields: infrared heating
2. Enhanced burning rates: high power density
3. Low flame temperatures: reduced NO_x emissions:
4. Ultra-lean operation: non-flammable leaking
5. Laminar regime: quiet operation

Applications of PMBs

So far, radiant burners such as PMBs have found their commercial application in industrial heating processes where high temperatures are required but convective heat exchange is not desired [45]. For example, some applications like annealing treatments or food processing require protective atmospheres. This prevents the exposure of the heating target to the corrosive combustion products. Moreover, this combustion technology has also been considered for steam reforming and domestic heating applications [46, 47].

Fuel flexibility

PMBs have proven to work efficiently with different gaseous fuels such as methane and propane [48–50], liquid fuels [51, 52] and unconventional fuels such as syngas [53] and biogas [54]. This is because in PMBs the enhancement of the burning rate is achieved via heat recirculation. This represents a major advantage over other technologies such as catalytic reactors, that often have restrictions on operating conditions, fuel chemistry and fuel quality [43]. Different studies have considered the effects of hydrogen enrichment on canonical fuels such as methane and natural gas [55–57] and on alternative energy vectors such as ammonia [58, 59]. These works suggest that PMBs could be used to accommodate significant levels of hydrogen enrichment. Because of their unique combination of properties, PMBs are promising candidates to address the challenges associated with hydrogen blending in various applications.

Fundamental studies are required

The mechanism of heat recirculation in PMBs is well understood [60–64] and the macroscopic behavior of flames within porous matrices has been extensively documented [39, 59, 65, 66]. However, there is still limited knowledge about many pore-scale phenomena such as the thermal quenching, preferential diffusion effects and flame wrinkling [67–69]. Because combustion and heat transfer are highly nonlinear, these local phenomena have a critical impact on the macroscopic behavior of the system and its performance. Current low order models used in porous media combustion do not incorporate the modeling of all these local phenomena, which results in a poor accuracy [67, 68, 70]. Improving the predicting power of low order models could help designing more efficient and fuel-flexible combustion devices. For that, it is crucial to gain understanding into the complex flame-wall interactions at the pore level so that the appropriate upscaling parameters and emerging properties are incorporated into current models. A deeper understanding of these processes can be achieved via advanced diagnostic techniques [71, 72].

In this work, a fundamental experimental study of flame stabilization in porous burners is presented. A deeper understanding of flame stabilization mechanisms in PMBs may permit the development of fuel flexible burners for both industrial and domestic heating applications. This can in turn contribute to the broader goal of decarbonizing combustion processes across multiple sectors.

1.2. State of the art

The objective of this section is to introduce the reader to the fundamental concepts of Porous Media Combustion (PCM). The origins, driving mechanisms, governing parameters, burner designs and existing applications are explored. For a deeper understanding, readers are encouraged to refer to the extensive reviews available in the literature, which cover various aspects of porous media combustion [43–45, 73–75]. Also, the PhD thesis of Pierre-Alexandre Masset [76] provides a pedagogic introduction to the topic.

Before delving into the details, a few clarifications are necessary. This thesis considers exclusively premixed flames where the fuel and oxidizer are perfectly mixed before entering the combustion chamber. Diffusion flames are out of the scope of the present work. PMC is often categorized into two divisions: unsteady and steady combustion. The former is often referred to as filtration combustion and involves a combustion wave slowly translating across a porous medium [77–79]. Steady combustion, where the process is stationary, is the focus of this work. In steady porous media combustion, two modes are possible: surface combustion and submerged combustion. This thesis focuses on submerged combustion, where flames are stabilized *inside* the porous matrix. Finally, the combustion within inert porous matrices is addressed, excluding

catalytic combustion processes with surface reactions [80] and heterogeneous combustion involving the burning of the porous material itself. This narrowed scope allows for a concentrated discussion on the stationary, submerged combustion in inert porous media burners (PMBs), providing a clear framework for the subsequent dissertations.

1.2.1. Excess-enthalpy combustion and heat recirculation

The concept of excess enthalpy combustion was introduced by Weinberg in 1971 [41]. In this pioneering work, Weinberg proposed that super-adiabatic temperatures could be reached if part of the energy from the burned gasses was transferred to the fresh reactants whilst avoiding the dilution of reactants with the products. Generally, this is achieved by exposing the combustion gasses to solid walls, that provide a conductive and/or radiative pathway for heat to be transferred from the hot combustion products to the fresh reactants. This process, known as heat recirculation, results in super-adiabatic flame temperatures and enhanced burning rates [42, 81, 82]. Note that the terms superadiabatic and excess enthalpy refer to local quantities since the overall energy balance is given by the conservation of energy and cannot be altered.

A few years later, Takeno and Sato [83] suggested that heat recirculation could also be achieved *internally* by introducing a flame inside an inert porous matrix. Because of the larger thermal conductivity of the solid matrix, heat is recirculated upstream via the solid phase leading to an excess enthalpy flame. The theoretical analysis was soon followed by experimental demonstration, with the first porous media burners being tested by Takeno and coworkers [39, 40]. In these early works on heat recirculating reactors, different burner configurations were proposed [84]. However, ever since, most of the research has focused on a few burner designs. For simplicity, two major categories are distinguished: counterflow and unidirectional flow reactors. An extensive review on these two kinds of heat recirculating burners can be found in [43].

A schematic of a counterflow reactor is shown in Fig. 1.5a. In this burner design, there are two or more channels with a reactive mixture flowing in opposite directions. A flame is stabilized inside each channel and the combustion products from one channel preheat the reactants in the adjacent ones. Generally, highly conductive thin walls are used to enhance the transverse heat transfer by convection and the upstream heat transfer by conduction. The counterflowing reactor of Fig. 1.5a is an illustrative example, but there are other burner designs such as folded channels, dual-folded channels and spiral burners [42, 85].

Numerous theoretical works have analyzed the stabilization of flames in counterflowing reactors, including the multiplicity of solutions, their stability properties, the importance of conductive and convective heat transfer and the impact of external heat losses on the operating range [86–89]. Numerical models with different degrees of complexity have also been used to predict the extension of the flammability limits [90, 91]. Experimental realizations of counterflowing channel burners have been implemented in [92–95] for both ultra-lean and ultra-rich combustion of methane, propane and heptane. These examples confirmed the key characteristics of counterflow heat recirculating reactors and showed that stable operating points could be achieved beyond both the lean and the rich flammability limits [43].

PMBs belong to the second category of heat recirculating burners: unidirectional reactors. In this configuration, the gas flows in one direction and heat is transferred upstream by conduction and/or radiation by solid walls (cf. Fig. 1.5b and c). The simplest unidirectional flow reactor consists of an array of parallel tubes or channels with a small diameter and is represented in Fig. 1.5b. A pilot test of this design is found in the work of Min and Shin [65] where premixed laminar flames were stabilized inside a ceramic honeycomb structure. If this design is replaced by a reticulated porous matrix or a packed bed structure (cf. Fig. 1.5c), axial and transverse dispersion are generated in the open-cell structure and this promotes the effective diffusion of mass and heat across the gas phase.

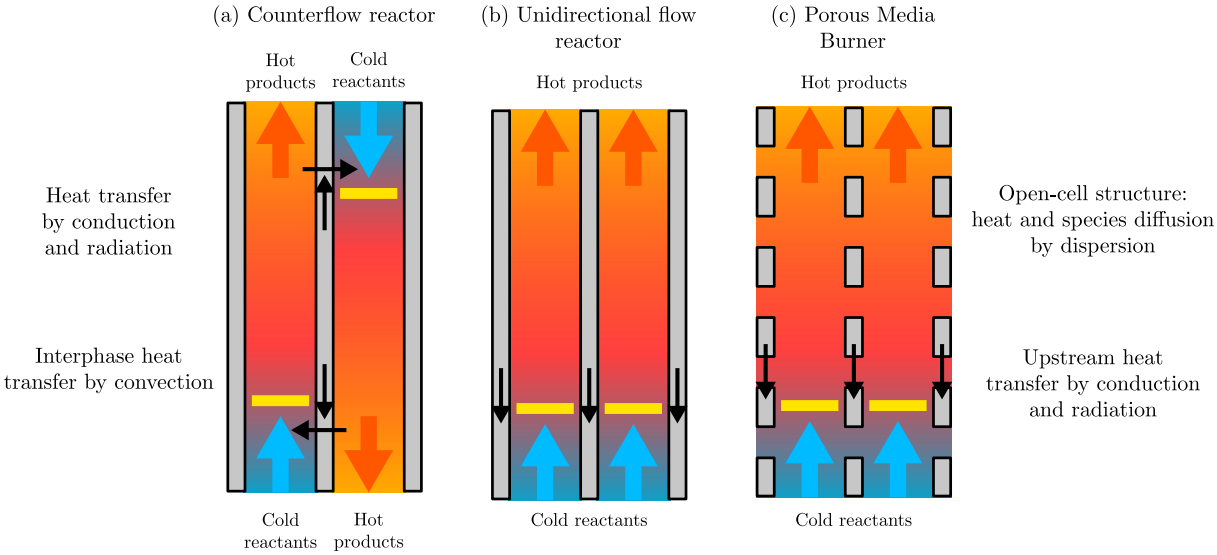

Figure 1.5. – Unidirectional and counterflow heat recirculating reactors.

After the first experimental demonstrations, porous burners have increasingly sparked the interest of the combustion community. In PMBs, the radiant efficiency, defined as the fraction of the power emitted under the form of thermal radiation, is around $20 - 30\%$ [45]. This distinctive feature together with their relative low price and their low pollutant emissions have motivated their use as radiant burners for infrared heating applications in the industry [44, 45]. In the past years, their broad turndown ratios and their ability to extend the flammability limits have drawn the attention of researchers focused on low-carbon combustion. PMBs are considered promising candidates for dealing with the uneven combustion properties of hydrogen and hydrocarbon flames in flexible fuel applications. Their ability to handle a wide range of fuel compositions and operating conditions makes them particularly suitable for applications where fuel flexibility is crucial. As such, PMBs are positioned as a viable technology for advancing towards a more sustainable and adaptable energy future.

1.2.2. Insights on Porous Media Combustion

To provide further insight into the combustion process inside a porous matrix, a simplified one-dimensional scenario is considered and compared to the corresponding adiabatic free flame. This simple analysis will reveal the main features and governing parameters in PMC. From now on, the focus is on isobaric combustion processes at atmospheric pressure. This is a good hypothesis for deflagrations where a minimal pressure variation takes place across the flame [96], and in porous media burners where the pressure drop across the porous matrix is generally small [45].

1.2.2.1. Infinite porous medium

Figure 1.6 outlines the temperature and heat release rate profiles in a premixed adiabatic free flame (a) and in a flame stabilized inside an infinite porous medium (b). In an adiabatic free flame, reactants are injected at an inlet temperature of T_{in} with a composition defined by $Y_{k_{in}}$. For single-fuel mixtures with air, the description of the fuel composition can be reduced to a single parameter: the equivalence ratio, ϕ. T_{ad} is the adiabatic flame temperature and corresponds to the temperature that is obtained if all the chemical energy stored in the fuel is employed to increase the enthalpy of the inlet mixture. For lean flames, the temperature increase across the flame can be approximated by $T_{ad} - T_{in} = Q_f Y_{f_{in}}/c_p$, where $Y_{f_{in}}$ is the fuel mass

fraction at the inlet, c_p is the specific heat at constant pressure and Q_f is the energy released by combustion per fuel mass unit. The freestream flow velocity $u_{x\to-\infty}$ is known as laminar burning velocity S_{L_0} and is a priori unknown. Conceptually speaking, it is the velocity at which a steadily propagating flame translates with respect to the fresh gasses. Mathematically, in the system of equations that describe the propagation of laminar 1D flames, S_{L_0} is the inlet velocity that ensures the steadiness of the system. The computation of the laminar flame speed is generally done numerically – yet some analytical solutions exist [96, 97] – and involves the resolution of an eigenvalue problem [96]. In a laminar free flame, reactants are preheated over a distance known as flame thickness and denoted by δ_T. This lengthscale can be estimated from the equilibrium between convective and diffusive terms in the energy conservation equation and scales as: $\delta_T \propto D_T/S_{L_0}$, where D_T is the thermal diffusivity of the reactants.

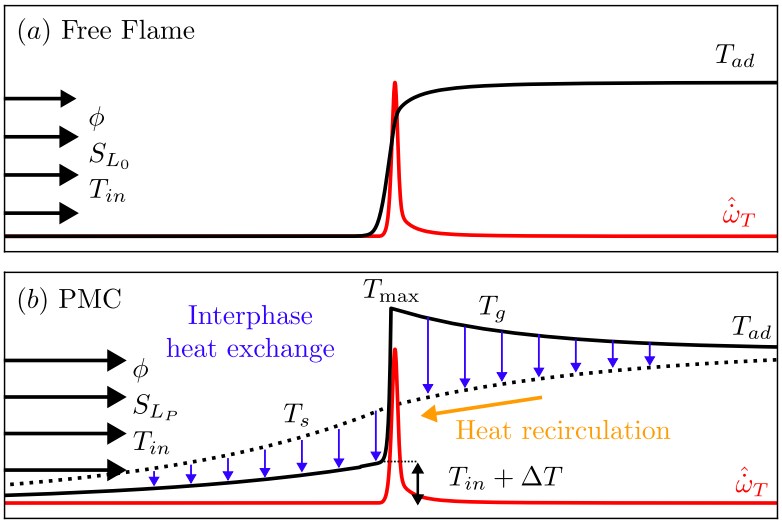

Figure 1.6. – Free flame versus Porous Media Combustion (PMC).

When an adiabatic laminar flame is submerged inside an infinite porous medium, the local energy balance is altered by the interphase heat exchange with the solid matrix. The interphase heat transfer by convection between the two phases is usually assumed to be proportional to the local temperature difference. Far upstream of the flame $x \to -\infty$ the gas and the solid phase are in equilibrium and their temperature is T_{in}. Downstream of the flame, the temperature of both phases must converge towards the adiabatic flame temperature of the mixture $T_{g,s}|_{x\to+\infty} \to T_{ad}$. In the solid, there is an equilibrium between the interphase heat exchange and thermal diffusion. Usually, the thermal conductivity of the solid is much higher than the gas conductivity $\lambda_s \gg \lambda_g$. Because of that, the diffusion lengthscale in the solid is also larger than in the gas. As a result, the solid temperature profile is more spread out, leading to local temperature imbalances between the two phases (cf. Fig. 1.6b). Upstream of the flame, the solid temperature is greater than the temperature of the gas and the porous matrix transfers energy to the reactants by convection. This preheats the reactants, raising their temperature to $T_{in} + \Delta T$ right before the flame. Assuming that the temperature jump across the flame remains constant, the maximum temperature reached by the gas after combustion becomes $T_{\max} = T_{ad} + \Delta T$. Downstream of the flame, the solid phase is colder than the gas and energy is transferred from the burned products to the porous matrix. The gas and the solid phase reach thermal equilibrium after a distance called re-equilibration distance. Note that the presence of the solid matrix gives rise to a new characteristic lengthscale in the system, the solid diffusion lengthscale, l_s. This distance can be estimated from the equilibrium between the interphase heat exchange term and the diffusion term in the solid.

Because the reaction rate varies as the exponential of the temperature, combustion processes are very sensitive to the temperature of the reactants. The preheating of the unburned gas increases its reactivity and promotes the burning rate. As a result, the incoming reactants velocity that ensures the equilibrium of the system, S_{L_P}, is higher than that of the adiabatic free flame. Despite its simplicity, the above-presented idealized case has brought to light the two parameters that are used to quantify the performance of a PMB and, more generally, of a heat recirculating reactor [43]:

1. Nondimensional temperature: $T_{\max}/T_{ad}$
2. Velocity ratio or *speed-up*: S_{L_P}/S_{L_0}

These two parameters describe the enhancement of the combustion process with respect to that of an adiabatic premixed laminar flame. $T_{\max}/T_{ad}$ refers to the ratio between the maximal local temperature attained in the system and the adiabatic flame temperature of the inlet mixture. In many theoretical analyses, an equivalent parameter named recirculation efficiency is used [60, 64]. This parameter is denoted by η_{rec} and defined as $\eta_{\text{rec}} = (T_{\max} - T_{ad})/(T_{ad} - T_{in})$. The second parameter, S_{L_P}/S_{L_0}, is the ratio between the burning velocity in the PMB and the burning velocity of an adiabatic free flame. This velocity ratio quantifies the increase in the burning rate due to the enhanced combustion conditions in the porous medium. As reported in different experimental studies [39, 40, 65], for hydrocarbon flames, the enhancement of the burning rate is typically in the range $2 - 5$. Although this value is significantly lower than what can be achieved in turbulent flames – where the turbulent flame speed can exceed the laminar flame speed by more than 20 times [96] – it still represents a significant gain in specific power and burner compactness.

1.2.2.2. Finite porous medium

The analysis of an infinite porous medium is useful to illustrate the mechanism of heat recirculation in porous reactors. However, real systems are characterized by a finite length. Thus, the case of a flame stabilized inside a finite porous matrix of length L is now considered. While the infinite case is invariant to the flame position, x_f, the finite case is governed by this parameter and hence the performance of the burner is always represented as a function of x_f. Figure 1.7 represents the velocities ratio or speed-up as a function of the position of the flame in the burner together with the gas and solid temperature profiles for three different flame locations.

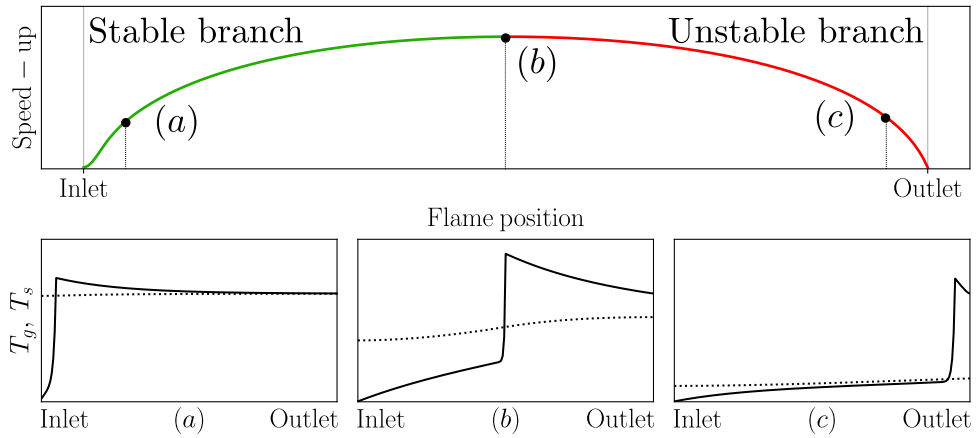

Figure 1.7. – Stabilization curve – Speed-up versus flame position – in a finite length porous medium. (a-c) Gas and solid phase temperature profiles at different flame locations.

When the flame is close to the burner inlet as in Fig. 1.7a, the preheating distance is small and so is the rise in the reactants temperature before the reaction front. Consequently, the level of superadiabaticity and the enhancement of the burning rate are limited. As the flame is displaced downstream, the distance for preheating grows and the recirculation efficiency and the burning rate increase. The maximum flame speed enhancement is reached when the flame is located in the middle of the porous matrix as shown in Fig. 1.7b. At this point, if the flame is pushed further downstream the recirculation efficiency and the speed-up start to decrease. This is due to the reduction in the re-equilibration distance and in the enthalpy excess harvested by the solid matrix and transferred to the fresh reactants.

As illustrated in Fig. 1.7, in the case of a finite porous burner, there may not be thermal equilibrium between the gas and the solid at the boundaries. This results in lower values of the speed-up and recirculation efficiency. When the porous matrix length is sufficiently increased, thermal equilibrium between the phases can be reached at both burner ends when the flame is located in the middle of the porous matrix. As a result, the maximum burning rate tends to that of an infinite porous medium and the stabilization curve of Fig. 1.7 flattens in the center. In combustion devices, the formation of certain pollutants and the completion of the oxidation process can depend on the residence time at high temperatures. In a PMB, these phenomena can also be strongly influenced by the length of the porous matrix. Therefore, the axial dimension of the porous matrix, L, is an important design parameter.

Note that the stabilization curve of Fig. 1.7 has two branches. For a given mass flow rate, there are two equilibrium positions for the flame inside the burner: one upstream and another downstream. This behavior is not exclusive to porous burners and can also be observed in other heat recirculating reactors such as counterflow reactors [90]. These two branches have different stability properties. In the upstream branch, a perturbation in the flame position, x_f, generates a variation of the flame speed that counterbalances the initial perturbation. This is, if the front is displaced downstream, the flame speed increases and this tends to push the flame back to its initial state. Therefore, this branch is stable. In contrast, in the downstream branch, perturbations in the flame front position tend to amplify the velocity imbalance resulting in an unstable equilibrium.

1.2.2.3. Real systems

In real systems, the solid matrix is not a continuum but a cell structure characterized by a porosity ϵ and a pore size d_p. A schematic of a flame stabilized inside the cavities of a porous medium is shown in Fig. 1.8. Porosity, ϵ, represents the ratio of gas to total volume whereas the pore size corresponds to the characteristic size of the cells inside the matrix. It must be borne in mind that these two parameters are independent. The porosity has a direct influence in the burner head loss. In practical applications, limiting the pressure drop through the burner is critical because it affects the dimensioning of the entire feeding system. Hence, porous matrices often feature large void fractions between $70 - 80\%$.

The pore size, d_p, has a strong influence on the flame stabilization since it affects local quenching phenomena. In experimental studies, the typical pore sizes of PMBs vary between $0.5-4$ mm. At small pore sizes, the cell diameter becomes comparable to the flame thickness, δ_T, which has a direct impact on local heat losses. The overlapping between the two characteristic length-scales represents a major modeling difficulty because it is still unclear how nonadiabaticity and flame quenching can be incorporated to reduced order models. The pore size also affects the interstitial flow via frictional losses and the dispersion phenomena [98]. Dispersion refers to the increase in the macroscopic diffusivity of mass and heat owing to the enhanced mixing driven by the meandering nature of the flow inside a porous matrix.

In porous burners, the solid matrix reaches elevated temperatures so that heat transfer by

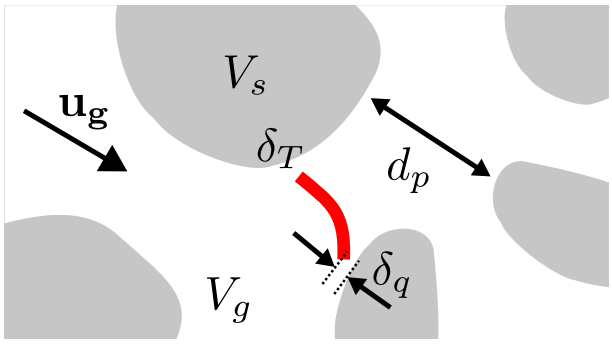

Figure 1.8. – Schematic of a flame inside a porous medium

radiation becomes relevant. An important fraction of the heat recirculated upstream is transferred via solid-to-solid radiation. Here, the pore size and the geometrical details of the structure play a key role on the optical thickness. This influences the radiation extinction coefficient and therefore the heat transfer by radiation through the solid matrix.

Solid surfaces provide an effective path for heat recirculation but also for external heat losses. So far, only adiabatic systems have been considered. However, PMBs are generally used as radiant burners for infrared heating. Therefore, in practical applications there is a remarkable level of heat losses by radiation from the solid matrix. From the point of view of the burner, this is a heat loss, but depending on the application this is generally a yield for the user. As in many combustion devices, global heat losses directly affect the operating domain of the burner. Broadly speaking, heat losses reduce the performance of the burner in terms of attainable recirculating efficiencies, speed-ups and extension of the flammability limits. However, since global heat losses by radiation are also the yield in many applications, a trade-off between combustion enhancement and radiation yields must be accepted. The level of external heat losses is driven by the surface-to-volume ratio of the burner. In a cylindrical axial burner this is inversely proportional to the diameter of the burner, D.

(a) aluminium oxide (alumina) Al_2O_3 (b) silicon carbide SiC

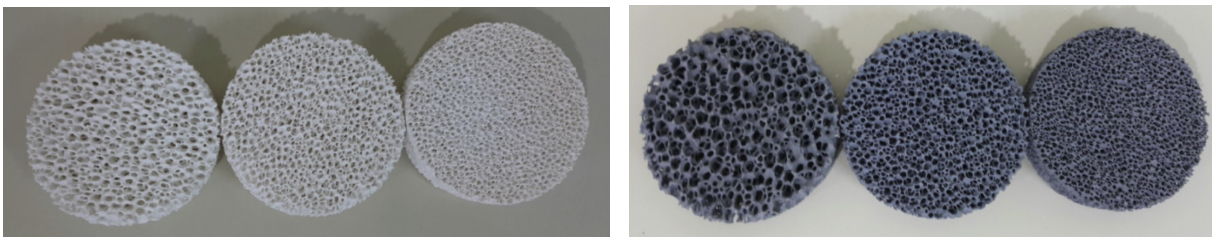

Figure 1.9. – From [99]: (a) alumina and (b) silicon carbide ceramic foams with different pore size used in experimental studies.

The solid matrix material is also a crucial aspect in a porous media burner. The solid thermal conductivity and radiative properties affect the recirculation of heat. For example, [100] showed that the burning rate of the burner increases by 50% when the solid phase conductivity is increased from 5 $Wm^{-1}K^{-1}$ to 15 $Wm^{-1}K^{-1}$. In PMBs, the characteristic time of the system is governed by the thermal diffusion time in the solid phase. Hence, the heat capacity of the porous matrix, c_s, has a direct impact on the time response of the burner. The porous matrix is submitted to extreme operating conditions including: elevated temperatures 1000 – 2000 K, a corrosive environment and thermal cycling. Therefore, materials with elevated fusion temperature and with high corrosion and thermal shock resistance are sought. The mechanical strength and the thermal expansion coefficient must also be taken into account in the material

selection process, especially when integrating the burner into another system.

Generally, ceramic foam such as those shown in Fig. 1.9 are the most popular choice owing to their elevated fusion temperature and inertness. In ceramic materials such as Alumina, Al_2O_3, Silicon Carbide, SiC, and Zirconium Dioxide, ZrO_2, the fusion temperatures are in the range $3000 - 4000$ K. Their main drawback is the low thermal shock resistance, which limits their durability, specially under short-period thermal cycling. Indeed, material durability is a major practical concern in porous media burners and cracking is often reported in experimental studies using ceramic porous foams [101, 102]. Metallic materials have also been considered in certain studies [103, 104] but their low melting point limits their use to lean-burn applications. A major advantage of metallic foams is their enhanced thermal shock resistance when compared to ceramic ones.

1.2.2.4. Burner configuration

After the first theoretical analyses and experimental demonstrations [39, 83] various burner configurations have been studied. In this section, the focus is on axial configurations which are generally used in academic studies. This is partly because axial burners simplify the analysis and are easy to build. Nonetheless, as for multiperforated burners, cylindrical radial burners have also been proposed [105–109].

The simplest burner configuration is a porous media burner where the properties of the porous matrix are homogeneous. This burner design is represented in Fig. 1.10a. In this case, the position of the flame inside the burner depends on the operating conditions. The flame is located at the point where its burning rate equals the velocity of the incoming gas. The burning rate is influenced by the level of preheating of the reactants, which in turn depends on the location of the flame in the burner. Therefore, here there is a two-way coupling between the flame position and the temperature field. In this kind of burners, the turndown ratio or power dynamic range is within the range $2 - 5$ [43, 65, 110, 111].

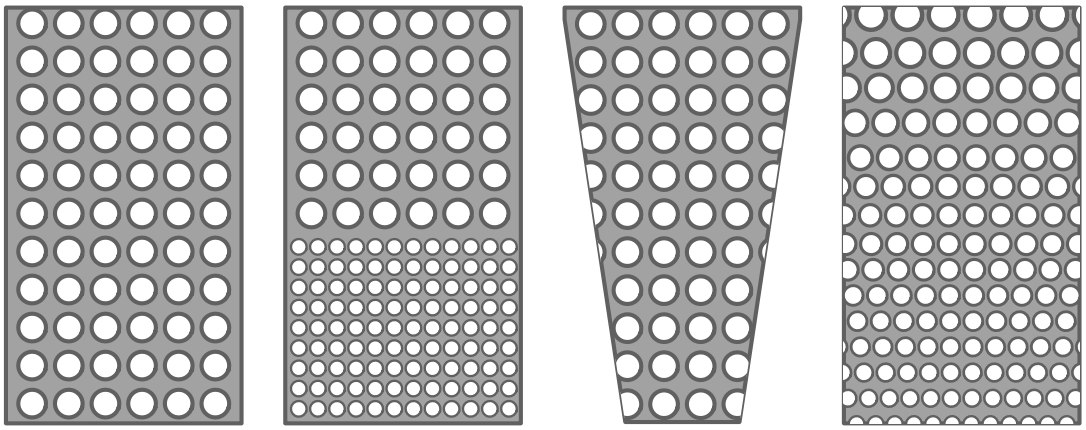

(a) Homogeneous burner (b) Multi-layer burner (c) Diverging burner (d) Graded topology

Figure 1.10. – Different burner designs

The multi layer configuration with two or more porous foams represented in Fig. 1.10b is likely the most popular burner design. It was introduced by Trimis and Durst in [75] and has been used in multiple works ever since [101, 112, 113]. Typically, two porous matrices with different pore sizes are arranged in a stacked configuration. The foam with smaller pores is placed upstream and acts as a flame arrestor, quenching the flame and limiting its upstream propagation. The one with larger pores is located downstream and the flame is generally stabilized at the interface

between the two. In this configuration, based on the critical Péclet number theory [114], the position of the flame inside the burner is fixed. Trimis and Durst reported a power dynamic range of 20:1 for this design [75]. In the step-burner configuration, there is a trade-off between performance and flashback prevention. This is because flashback resistance is increased by limiting the preheating of the reactants, which reduces the enhancement of the burning rate and the global performance. The combination of porous layers with different thermal conductivities can also be used to adjust the response of the system, introducing another degree of freedom in the burner design.

An alternative to step burners are diverging geometries, proposed by Voss et al. in [115] and shown in Fig. 1.10c. In this design, the section of the burner increases in the axial direction producing a decreasing velocity profile from the inlet to the outlet. As in the homogeneous burner, here the flame is located at the point where its speed balances the local velocity. The axial variation of velocity produces a hydrodynamic stabilization and extends the operating domain of the system. This burner design was demonstrated experimentally by [115, 116] who reported dynamic ranges of roughly 6:1. The main drawback of this configuration is that large divergence angles are required to achieve an adequate deceleration of the flow. This results in restrictively large cones and transverse flow inhomogeneities. Alternatively, the streamwise decelerating velocity profile can be achieved using a radial burner. This option has been investigated numerically by Bedoya et al. [68] and experimentally by [108, 109].

Recently, it has been proposed that a graded topology such as the one displayed in Fig. 1.10 could be used to optimize the performance of porous media burners [110, 117]. By introducing a spatial gradation of the topological parameters, one can tune the operating domain of the burner. For example, a streamwise variation of porosity can be used to decelerate the flow in the axial direction, generating hydrodynamic stabilization. Conversely, a continuous reduction of the pore size towards the inlet can be used to quench the flame as the burner approaches the flashback limit. This modulation strategy could be used to extend the flashback limit.

Graded axial burners offer a few advantages with respect to diverging porous geometries. First, the external geometry of the reactor remains unaltered. This simplifies the construction and the integration of the burner. Second, they permit the modulation of both the velocity profile and the pore size distribution, offering an additional path for the enhancement of flame stabilization via quenching. Sobhani et al. [110] used a 1D numerical model to analyze the influence of topological gradations of pore size and void fraction on the burner operating range. They reported that a gradation in the pore size of the matrix could result in an improvement of the flame stability range of nearly 50%.

Later on, Contini and Pereira [117] used numerical simulations to compare a graded topology and a diverging porous burner. In [117], both burners feature the same variation of cross-sectional area and thus the same level of hydrodynamic stabilization. In the conical burner, this is achieved via a variation of the burner section and in the graded topology via an imposed porosity profile. Contini and Pereira reported that the cylindrical burner with a graded topology provides a wider stability range than the diverging geometry. They attributed this difference to the variations in the recirculation efficiency via radiation.

These studies indicate that graded topologies are an effective way to enhance the operating range of the burner. Besides, they offer both practical and operational advantages with respect to diverging burners. From the point of view of fuel-flexibility, graded topologies are a promising option to accommodate varying hydrogen contents in the fuel. This is because they can stabilize flames with very different burning rates. Their main drawback is the manufacturing process. To the author's best knowledge, this kind of geometries cannot be easily produced with conventional manufacturing processes employed for ceramic foams. In a first approximation, one can achieve a topological gradation by stacking multiple thin homogeneous ceramic foams with varying

geometrical properties. This is the approach that was followed in the novel work of Sobhani et al. [110]. However, the discontinuity of the solid matrix raises questions regarding the additional thermal resistance at the junction and the preferential stabilization of the flame at interface between the different porous layers.

In the past decades, there has been outstanding progress in Additive Manufacturing (AM) techniques [118]. Nowadays, it is possible to produce metallic and ceramic components via AM using different techniques. Selective Laser Melting (SLM) [119] can be used to produce metallic samples and lithography-based ceramic manufacturing [120] enables the fabrication of ceramic components. One of the first examples of the application of AM to porous media combustion is found in [104]. In this work, 3D-printed metallic burners made of CoCr alloy were manufactured and tested. They were compared to their reticulated ceramic counterparts in terms of flame stabilization, durability and performance. The lattice 3D printed structures were found to provide a better control of the porosity and higher structural stiffness. Thanks to AM techniques, the first demonstration of a graded topology was accomplished by Sobhani et al. in [121]. In this pioneering work, Sobhani et al. compared various 3D printed ceramic burners with a gradation of the topological properties. The porous matrix with varying pore size was found to extend the stability map when compared to its step-burner equivalent. However, the study points out that matrix durability is the major drawback of this approach. 3D printed ceramic structures exhibit even lower thermal shock resistance than their reticulated counterparts owing to the residual internal stresses stemming from the manufacturing process.

1.2.3. Applications

In this section, a few existing and potential applications of PMBs are examined. Different levels of Technology Readiness Level (TRL) can be found in the various examples listed down below. In some applications such as radiant heating, the technology is mature and commercial examples already exist. Others, like domestic heating, have been demonstrated by prototypes but never commercialized [46]. An in-depth review of the applications of porous media reactors can be found in [74].

1.2.3.1. Radiant burners

Nowadays, a number of industrial processes such as metal heat-treating, coating and paint drying, chemical processing, paper and wood drying and food processing make use of radiant burners. Infrared heating is imperative when two factors are combined: high temperatures and a controlled atmosphere. A good example is the application of annealing heat treatments in the steel industry. This thermal treatment is used to adjust the mechanical properties of semi-finished products after the cold rolling process of the steel strip. The strip is subjected to temperatures between 670°C and 900°C to trigger a recrystallization process that improves the ductility of the product. The process must take place inside a protective gas atmosphere to prevent the oxidation of the strip surface and thus avoid an additional pickling step. Hence, it is essential to ensure a separation between the protective gas atmosphere and the combustion flue gasses and this can only be achieved by means of radiant burners. Other industrial applications such as food processing or paper drying may also be incompatible with convective heating and require radiant burners. Furthermore, radiant heating can simply be a reinforcement for convective heating. Combining both, faster heating times are obtained and this can be used to reduce oven lengths or increase conveyor speeds in industrial applications. At present, there are commercially available porous media burners such as those shown in Fig. 1.11. For example, the RADIMAX Porous Burner of GoGas features a maximal radiation temperature of 1450°C and a maximum thermal surface load of 1000 kW m^{-2} according to the manufacturer website. Another example is the Flameless gas burner technology from Promeos Intelligent Heat.

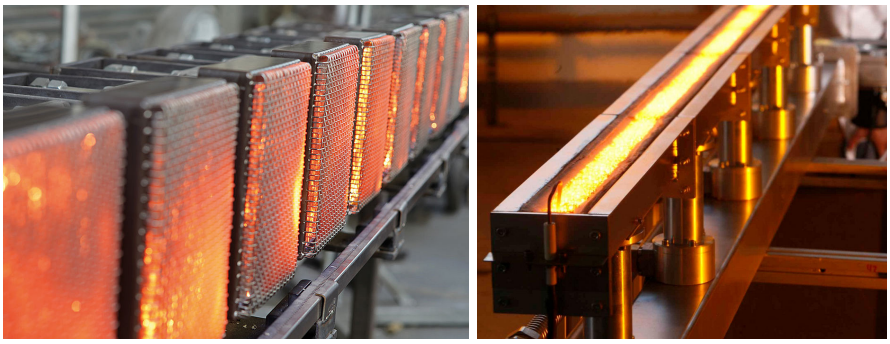

Figure 1.11. – Commercial examples of porous burners. Credits to GoGas and Promeos Intelligent Heat.

1.2.3.2. Domestic heating

The combination of a heat exchanger and a porous media burner could be used to deliver a warm stream of water for space heating and domestic use in household applications. This concept was the subject of an extensive study in the mid 90s by Durst et al. [46]. PMBs were successfully integrated with heat exchangers and various prototypes of up to 30 kW were built and tested. A picture, the blueprints and a schematic of one of these devices are shown in Fig. 1.12. Several industrial partners co-participated in the project and the outcoming prototypes were found to exhibit significant advantages compared to current heating systems. They achieved power turndown ratios of 20:1, with operating equivalence ratios ranging between $0.6 < \phi < 0.9$ and very low NO_x and CO emissions. Those prototypes included a control unit to monitor the operation of the burner, which indicates that a significant level of TRL was achieved by this consortium of universities and industrial partners. Despite the optimistic tone of this technical report, we have not witnessed the arrival of porous burners technology to our domestic appliances in the past 30 years. The reasons might be economic, but the author is uncertain. At present, the current need for fuel-flexible technologies to cope with the potential fluctuations in the H_2-content of the NG network in the context of P2G may give the PMBs technology a second chance.

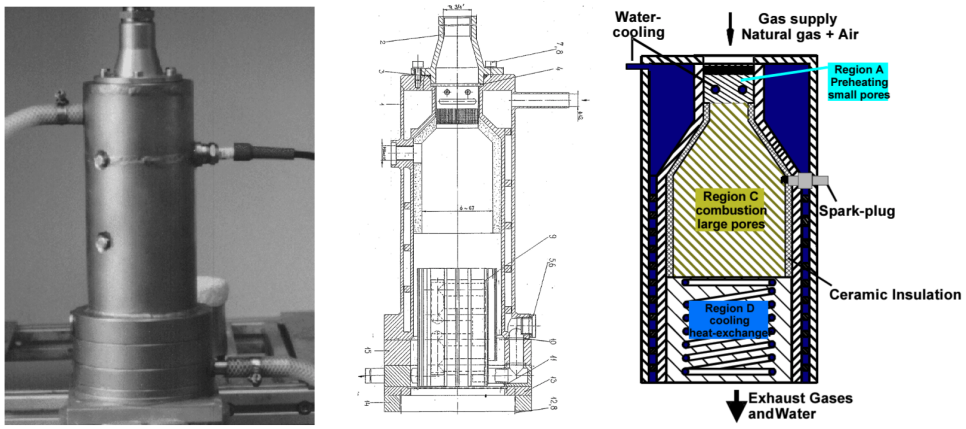

Figure 1.12. – Picture, blueprints and schematic (from left to right) of the 10 kW Porous Media Burner prototype with integrated heat exchangers developed by Durst et al. in [46].

A few years later, Malico and Pereira performed 2D numerical simulations of a porous media

integrated with a heat exchanger [122, 123]. They simulated the configuration developed by Durst et al. in [46] and compared the axial temperature profiles and pollutant emissions to those obtained in experiments. Delalic et al. [124] conducted experiments and analysis of a porous media burner with a built-in heat exchanger to be used in condensing boilers for domestic heating. They reported an increased power density with a reduction in the CO emissions and nearly zero NO_x. Dedalic et al. highlight the enhanced thermal inertia and the high efficiency achieved in the heat exchange. They suggest that PMB technology could be used to develop low cost, high-efficient compact condensing boilers in the residential sector. Further examples of integration of porous media burners with heat exchangers for household applications can be found in [125–127].

1.2.3.3. Steam reforming

Steam reforming is a method to produce syngas, $H_2 + CO$, by reacting hydrocarbon fuels with water vapor. Indeed, most of the current hydrogen production is done with this procedure [128]. When a hydrocarbon fuel is burned at a rich equivalence ratio, the endothermic reaction of steam reforming takes place in the burnt gasses which contain an important fraction of water vapor and the excess of non-reacted hydrocarbon fuel. Heat recirculating reactors extend the rich flammability limit of the mixture, allowing the combustion at ultra-rich equivalence ratios. This is why a popular application of heat recirculating burners is the production of syngas from hydrocarbon fuels [43, 129]. An experimental demonstration of the use of heat-recirculating burners to produce H_2-rich mixtures from methane is presented in [130]. Ellzey and coworkers carried out various numerical and experimental studies on the syngas production using counterflow reactors operating in ultra-rich conditions [91, 93, 94, 131]. PMBs have also been used to produce hydrogen via rich combustion of hydrocarbon fuels in [47, 109, 132, 133]. Toledo et al. [47] evaluated the use of inert porous media for steam reforming using methane, ethane, and propane as fuels. They reported the operation at equivalence ratios up to $\phi = 2.5$ and a maximum hydrogen yield of 50%. Recently, Guerrero et al. [133] considered the production of hydrogen from biogas via ultra-rich combustion in a filtration porous burner.

1.2.3.4. Other applications

- Combustion of Low Calorific value Gasses (LCG). The ability of heat recirculation to enhance the burning rate and extend the flammability limits of the mixture can also be exploited to burn fuels with low calorific value that are, otherwise, hard to oxidize. Heat recirculation can be used to stabilize the combustion of these compounds which is sometimes hindered by a fluctuating composition and by the presence of inert components [52, 134–137]. An extensive review on this application of porous media burners is provided in [138].

  Ammonia has been identified as an alternative energy vector to hydrogen for several applications [139]. However, Ammonia is a low heating value fuel and is characterized by a low flame speed and a long ignition delay. Thanks to the enhancement of the burning rate, PMBs are deemed good candidates to address the specific challenges of Ammonia combustion. Several recent experimental and numerical works have studied the combustion of $NH_3 - H_2$ in step porous burners [58, 59, 66].

- Other domestic uses. Several authors have also explored the possibility of employing porous media burners for other domestic uses such as water heating devices or cooker-top burners [140–145]. The utilization of porous media burners for cooking applications in the food industry has also be considered by some authors to replace free flame by radiant heaters and increase the efficiency of the system [146–148].

– Oxidation of Volatile Organic Components (VOC). VOC such formaldehyde and acetone are often considered as highly pollutant and the use of PMB for their oxidation has been analyzed by some authors as an effective way to reduce their harmful effect [80, 149, 150].

1.3. Research gap

In many aspects, the fundamental macroscopic behavior of flames in porous media burners is understood [63, 65, 111]. The first-order driving mechanism, heat recirculation, is well documented and its foundations are clear [43].

When it comes to modeling, Direct Pore Level Simulations (DPLS) where all the scales of the flow are resolved can in principle include conjugate heat transfer and radiation. As a result, they can provide very accurate results. However, this high predicting capacity comes at an elevated computational cost, resulting impractical for many engineering applications and burner optimization. Therefore, a considerable scientific effort is devoted to the development of low-order models such as Volume Averaged Models (VAM) [59, 67, 68].

Whereas most of the macroscopic physical mechanisms are clear, many pore-scale phenomena are yet to be understood. Because of the nonlinear nature of combustion and heat transfer, these local phenomena play a key role on the stabilization of flames and on the global performance of the burner. An illustrative example is the influence of the pore size on the local heat losses and the flame wrinkling [67–70]. Current VAMs do not generally account for these pore-scale phenomena. As a result, their predicting capacity is still too limited. It is thus crucial to improve our understanding of the complex flame-wall interactions at the pore-scale that play a key role in the combustion process. A better insight into these local mechanisms will allow us to feedback the present reduced order models, improving their accuracy. Better reduced order models will in turn permit the development of more efficient and performing burners. For that, it is necessary to access the interior of the porous matrix in order to study the behavior of flames at the pore level.

Unfortunately, experimental measurements in PMBs are mainly hindered by the lack of optical and physical access to the interior of the porous matrix. Reticulated ceramic foams are used in the majority of experimental studies [45, 58, 101]. These porous media feature a random structure and hence they are opaque, preventing the application of optical diagnostics. However, the lack of optical access is not the only problem when it comes to nonintrusive diagnostics. Many experimental techniques rely on the bandwidth filtering of light. Some techniques such as flame chemiluminescence measure the naturally emitted light from the flame at specific wavelengths. Others, such as Laser Induced Fluorescence (LIF) collect the fluorescent emission of excited radicals when they return to a lower energy state. However, owing to the elevated temperatures reached by the solid matrix, part of its black-body radiation is emitted in the visible spectrum and this can be a source of significant background noise for certain optical techniques.

Many experimental studies only report pointwise temperature measurements from thermocouples probes and stability maps (load versus equivalence ratio). Inside the burner, thermocouple probes are submitted to a strong radiative flux from the porous matrix which alters the thermal equilibrium of the thermocouple's bead. As a result, their temperature reading drifts towards the solid phase temperature, questioning their use to measure the gas phase temperature. All in all, because of the aforementioned difficulties, the use of nonintrusive diagnostics in the literature is scarce and only a few handful examples exist [69, 86, 101, 151–154].

The first example of nonintrusive diagnostics in a PMB is found in [152]. In this work, dual-pump Coherent Anti-Stokes Raman Scattering (CARS) was successfully applied to simultaneously measure the gas phase temperature and the H_2 concentration in a two-stage combustor. The schematic of the experimental setup together with the measured axial profiles of temperature and H_2 concentration are reproduced in Fig. 1.13. The upstream layer of the burner is an

Al_2O_3 flame trap with ⌀1.5 mm evenly distributed holes. The downstream stage is a SiSiC foam with very large pores. An adequate positioning of the two layers provides line-of-sight access through the ceramic foam and flame trap. The CARS laser beams overlap in a certain region of space and this is where the local temperature is measured. To reconstruct the axial profiles of temperature, the burner is axially translated using a linear stage. The authors highlight the demanding alignment requirements during the experiments. According to Kiefer et al. [152], despite the partial obstruction of the laser beams at certain axial positions, the CARS signal was always sufficiently strong to obtain reliable measurements.

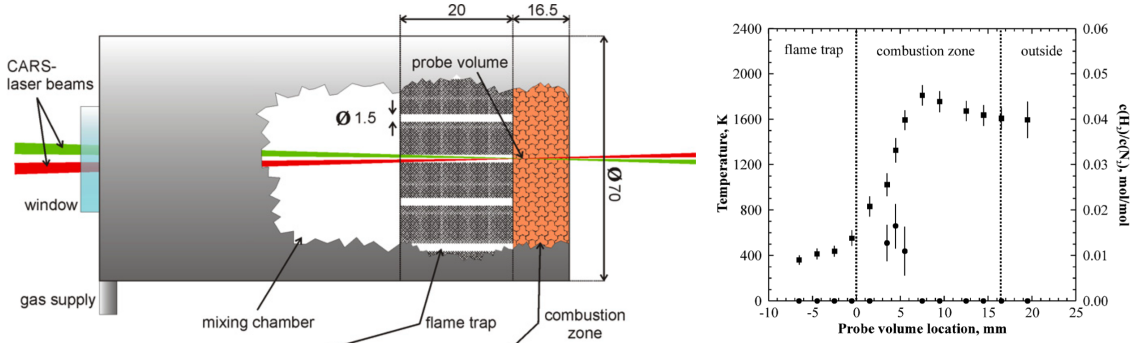

Figure 1.13. – Experimental setup used in [152, 153] to apply CARS (left) and axial profile of gas temperature and H_2 concentration obtained inside the burner (right). Reproduced from [152].

Shortly after, the same group [153] published another work where they updated their experimental apparatus and provided new results applying Dual-Pump Dual-Broadband CARS (DPDB-CARS). Their improved experimental setup allowed for the simultaneous measurement of the relative concentration of H_2 and O_2 as well as the gas temperature. They analyzed the influence of thermal load and equivalence ratio on the temperature profiles. In [153], Weikl et al. also measured the 2D temperature map inside one pore.

In [151], OH-Planar Laser Induced Fluorescence (OH-PLIF) was used to visualize the flame through a narrow slit in a two stage PMB. In the OH-PLIF technique, hydroxyl radicals are driven to an excited energy level using a laser. Then, the fluorescence emitted by the excited $OH^\star$ radicals when they relax back to a lower energy state is measured [155–157]. For a laser technique such as OH-PLIF to be applied, two orthogonal optical accesses to the interior of the porous matrix must be created. In [151], this was achieved by machining the SiSiC foam. A schematic of the experimental setup used in [151] and an example of the obtained results are reproduced in Fig. 1.14. The slit thickness is of the same order as the pore size to minimize the alteration of the burner geometry. The authors examined the evolution of the flame front position with the thermal load and the equivalence ratio. The low signal to noise ratio is one of the main challenges highlighted by the authors. The measured OH concentrations are not quantitative since it is not possible to apply local temperature and concentration corrections.

In these works, optical access is very limited and is achieved either by using very large pores or by creating narrow gaps inside the porous matrix and therefore altering the burner geometry. A notable exception is the use of X-ray tomography [101], which allowed the reconstruction of the temperature field in a multi-layer SiC burner. In [101], Krypton is added to a methane-air mixture to enhance its X-ray contrast. Then, a time-averaged reconstruction of the X-ray attenuation field is used to obtain the three-dimensional temperature field in the gas phase of a porous media burner. In this work, the transversely averaged temperature profiles are compared to a 1D Volume Averaged Model for an interface stabilized flame and a good quantitative agreement is reported.

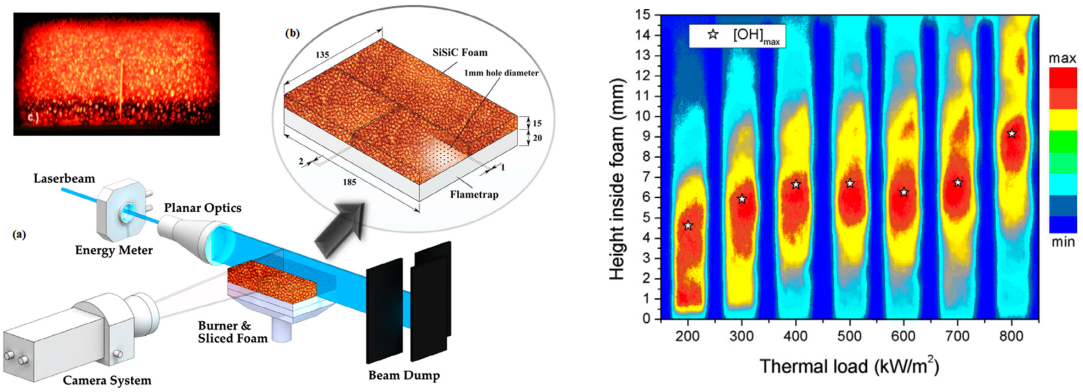

Figure 1.14. – Experimental setup used in [151] to achieve optical access to the interior of the porous burner (left) and OH distribution for various thermal loads at an equivalence ratio of $\phi = 0.71$ (right). Reproduced from [151].

The X-ray tomographic reconstruction provides insightful physical information about the temperature field and it is applicable to reticulated random topologies with an opaque structure. The technique is complex and lengthy, demanding a notable experimental effort. The burner and its structure must be mounted on a rotating platform to perform the X-ray scans and multiple scans must be carried out with and without Krypton as tracer. The molar fraction of Krypton required to obtain an acceptable signal to noise ratio is significant, $X_{\mathrm{Kr}} \simeq 30\%$, which may entail a modification of the combustion and heat transfer dynamics of the mixture. The resolving power of the tomographic reconstruction is about 200 μm so that global information is extracted rather than pore-scale details. When small pore sizes are considered the 3D fields must be weighted by the local porosity to recover the effective temperature in the gas phase. An example of the reconstructed 3D temperature field in the three-stage burner of Dunnmon et al. is presented in Fig. 1.15.

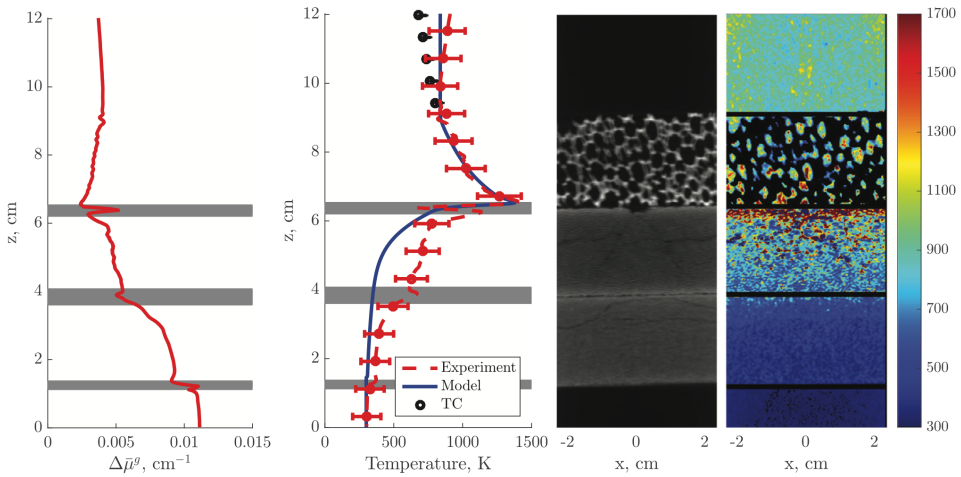

(a) 1D mean attenuation (b) 1D temperature profiles (c) Solid (d) Implied temperature

Figure 1.15. – Transversely averaged profiles of attenuation, $\Delta\overline{\mu}^g(x)$ (a) and temperature (b). (c) X-ray scan of the solid structure. (d) Vertical cross section of the reconstructed 3D temperature field. Reproduced from [101]

In a very recent work, Boigné et al. [69] combined μX-ray Computed Tomography (CT) measurements with infrared thermometry to obtain a full reconstruction of the temperature

field in both phases of the burner. Micrometric X-ray CT requires a remarkable experimental struggle since the minor micrometric motion of the porous matrix results in artifacts and spoils the measurements. For that, a significant improvement of the technique was accomplished with respect to the previous work [101]. A topology-tailored porous matrix made of SiC and featuring an *ad hoc* structure was fabricated via the replica technique to minimize the motion by thermal expansion. Measuring the gas phase temperature for a single operating point requires nearly 6 hours and produces roughly 49 Gb of data. This work represents a substantial step forward in the application of nonintrusive diagnostics. However, the technique is so complex that only a very limited number of operating points can be studied. Therefore, it becomes difficult to evaluate the influence of different parameters on flame stabilization and to extract general conclusions. The infrared thermometry measurements were performed using a Short Wavelength Infrared (SWIR) camera. The solid phase temperature measurements are later used to impose the temperature of the wall in a Direct Pore Level Simulation (DPLS) with the same burner configuration and at the same operating point. Good quantitative agreement between the spatial fields of gas phase temperature is obtained. Simulations reveal that roughly 80% of the combustion process takes place in thin adiabatic flamelets inside the porous matrix cavities.

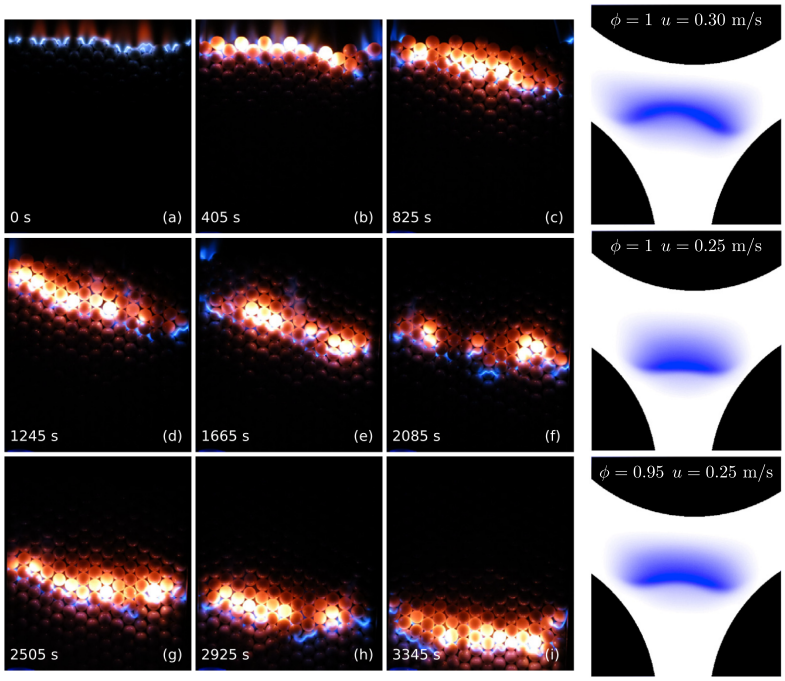

Figure 1.16. – Direct flame visualization in a single-layer packed bed structure from Fursenko et al. [158]: transition from surface to submerged combustion (left). $CH^{\star}$ chemiluminescence imaging in a 2D cylinder array in staggered configuration with controlled wall temperature from Khodsiani et al. [154]: influence of the operating conditions on the flame liftoff distance (right).

Finally, direct flame front visualizations have only been achieved in 2D configurations. Fursenko et al. [79] analyzed the pore-scale dynamics of NG-Air flames propagating inside a single-layer packed bed structure between two parallel quartz walls. In [79], optical access is granted by the use of a single layer structure. The main limitations of this approach are the low values of achievable porosity and the relatively high level of heat losses. This may render the behavior of flames not fully representative of 3D porous matrices. High speed imaging is used to investigate the dynamics of filtrating combustion waves at the pore scale. The authors report the existence of two kinds of oscillations: Flame Repetitive Extinction Ignition (FREI) and small amplitude

oscillations of the flame front at the scale of a pore. The latter are characterized by a higher frequency and do not involve a sequence of quenching and reignition phenomena. Figure 1.16 shows a combustion wave propagating in the single-layer packed bed burner of Fursenko et al. [79].

Another example of direct flame visualization is found in the work of Khodsiani et al. [154], who performed $CH^{\star}$ chemiluminescence measurements of CH_4-Air flames stabilized in a two dimensional array of cylinders with a staggered configuration. In [154], the temperature of the solid elements is imposed and the two dimensional structure grants optical access to the entire gas phase. Khodsiani et al. [154] are able to quantify the sidewall quenching distance and the flame-wall heat transfer. They report that flames can transfer up to 25% of their power towards the solid phase and that operating conditions have a strong influence on the flame liftoff distance. An example of the $CH^{\star}$ chemiluminescence imaging at the pore-scale of Khodsiani et al. [154] is shown in Fig. 1.16. The results presented in [69, 154] offer insightful information about the local structure of flames inside porous burners and report similar fractions of flame-wall heat transfer.

To the author's best knowledge these are the only examples of the application of nonintrusive diagnostics in PMC. All of them are quite recent, indicating that there is renewed interest in the combustion community for PMBs and a growing need for nonintrusive and optical diagnostics. Different research groups [69, 101, 154] are currently working on the development of nonintrusive and optical diagnostics and their results have already revealed interesting features about the stabilization of flames at the pore-level.

1.4. Objective of this thesis

In other areas of combustion science such as turbulent flames [159] or detonations [160], experimental techniques such as chemiluminescence, Mie-scattering imaging and Particle Image Velocimetry (PIV) are applied on a daily basis to analyze the behavior of flames, unveil the underpinning physical mechanisms and validate simulations [161, 162]. However, there is a very limited use of these techniques in porous media combustion. In [151], Stelzner et al. wrote:

"Achieving optical access in the porous structure is essentially a compromise between disturbing the actual phenomena taking place inside the porous structure and obtaining the required optical characteristics"

To date, because of this difficulty, the application of optical diagnostics in PMBs was very restricted. This thesis is devoted to the experimental study of porous burners. The focus is on a very specific problem that hinders the fundamental understanding of the behavior of flames inside porous media: the lack of optical access and scarcity of non-intrusive diagnostics. By combining computer generated geometries and additive manufacturing techniques, optically accessible porous media burners are produced. With this new methodology, an extensive optical access can be achieved without disturbing the physical phenomena inside the porous matrix. Optical access allows the application of various nonintrusive techniques such as $CH^{\star}$ chemiluminescence, Mie-scattering imaging and PIV that have not been applied in a 3D PMB structure before. The current approach can also be exploited to tailor the topology of the porous matrix and enables a systematic study of the influence of the different topological parameters on flame stabilization. Notably, in this work, the influence of pore size and porosity is analyzed separately. In line with the context, the specificities of hydrogen combustion are also addressed making use of the new experimental techniques presented. Overall, the thesis seeks to open new paths for the experimental study of porous media burners.

The remainder of the manuscript is organized as follows:

- **Chapter 2** presents the experimental setup including the POROSITO test rig, the mixing system, the diagnostics, the experimental procedure and the images processing. This chapter also provides a detailed description of the geometry-generation process offering technical details related to the handling of the porous matrices' CADs. Uncertainties in the experimental measurements are also quantified.
- **Chapter 3** offers an in-depth discussion on the different modeling approaches in porous media combustion and presents the 1D Volume Averaged Model developed during this thesis.
- **Chapter 4** presents the results from the article *Flame-front tracking in Porous Media Burners* [163]. In this chapter, the direct visualization of the reaction region inside the burner is used to track its position as a function of the operating conditions. Topology-tailoring is exploited to evaluate the influence of the pore size on flame stabilization. Experimental results are compared to the 1D VAM in terms of flame position, reaction region thickness and temperature profiles. The influence of the interphase heat exchange and the solid thermal properties on the model predictions is evaluated. The tracking of the reaction region is proposed as a useful model validation technique to complement temperature measurements.
- **Chapter 5** presents the results from the article *Speed-up drivers for* H_2*-enriched flames in Porous Media Burners* [164]. This chapter analyzes the influence of porosity and hydrogen enrichment on the flame stabilization. The impact of hydrogen on the operating domain and on the stabilization curves is reported for two porous burners with different porosities. The tracking of the reaction zone offers new insights regarding the stabilization of hydrogen enriched flames in PMBs.
- **Chapter 6** presents the results from the article *Mie-scattering imaging and μPIV in porous media burners with TPMS-based topologies*. This chapter demonstrates the feasibility of laser diagnostics in TPMS-based topologies. Mie-scattering imaging is first combined with $CH^\star$ chemiluminescence to investigate the heat recirculation mechanism. Then, Mie-scattering imaging and μPIV measurements are applied at the scale of a pore and used to study the structure of inlet-anchored flames for different topologies, pore-sizes and hydrogen contents.
- **Appendix A** is a verbatim reproduction of the article *Predicting flashback limits in* H_2*-enriched* CH_4*/air and* C_3H_8*/air laminar flames* [33] where 2D DNS with conjugate heat transfer and a skeletal chemistry are used to analyze the influence of H_2-enrichment on the flashback limit of slit-stabilized CH_4/Air and C_3H_8/Air flames.

1.4.1. Publications during the thesis

1.4.1.1. Works related to porous media combustion

- **Flores-Montoya. E**, Masset, P. A., Schuller, T. & Selle, L. (2024). Flame-front tracking in Porous Media Burners *Combustion and Flame*, 267, 113597.
- **Flores-Montoya. E**, Masset, P. A., Schuller, T. & Selle, L. (2024). Speed-up drivers in H_2-enriched flames for Porous Media Burners, *Proceedings of the Combustion Institute* 40, 1-4, 105666.
- **Flores-Montoya. E**, Cazin, S., Schuller, T. & Selle, L. Mie-scattering imaging and μPIV in porous media burners with TPMS-based topologies, *Combustion and Flame*, (In review).

1.4.1.2. Other works

- Pers, H., Masset, P. A., **Flores-Montoya, E.**, Selle, L. & & Schuller, T. (2024). Influence of slit asymmetry on blow-off and flashback in methane/hydrogen laminar premixed burners, *Combustion and Flame* , 263, 113413.
- **Flores-Montoya. E**, Aniello, A., Schuller, T. & Selle, L. (2023). Predicting flashback limits in H_2-enriched CH_4/Air and C_3H_8/Air laminar flames, *Combustion and Flame*, 258, 113055.
- **Flores-Montoya. E**, Muntean, V., Pozo-Estivariz, D. & Martínez-Ruiz, D. (2023). Thermoacoustic coupling regions of premixed-flames in non-adiabatic tubes, *Combustion and Flame*, 247, 112478.
- **Flores-Montoya. E**, Muntean, V., Sánchez-Sanz, M. & Martínez-Ruiz, D. (2022). Non-adiabatic modulation of premixed-flame thermoacoustic frequencies in slender tubes, *Journal of Fluid Mechanics*, 933, A50.

Chapter 2

Experimental setup

This chapter presents the experimental setup employed throughout the majority of this thesis. Firstly, the POROSITO test rig and the mixing system are described in Sec. 2.1. The major novelty of this research is the use of optically accessible Porous Media Burners (PMBs) that provide direct visualization of the flame and enable the application of optical diagnostics. Optical access is made possible by the use of special burner topologies that are generated by computer and produced via Additive Manufacturing (AM). These topologies are defined by mathematical functions and feature multiple optical pathways. Computer-defined geometries offer a full control and an accurate characterization of the geometrical parameters of the burner. Finally, this framework enables the exploration of brand-new burner designs where the geometrical parameters of the porous matrix are graded in space, opening the door to burner optimization. However, the generation of these topologies is not trivial. In this chapter, this process is thoroughly described and technical details are provided. Also, since the whole process relies on the Additive Manufacturing technique, the 3D printing technology is presented. The diagnostics, including the imaging system and the thermocouple measurements, are discussed in Sec. 2.3. The experimental procedure and the images processing are described in Sec. 2.4 and Sec. 2.5, respectively. The analysis of errors in mixture composition, burner load and inlet temperature can be found in Appendix 2.A.

Overview

2.1. The POROSITO test rig **26**
2.1.1. Burner base 26
2.1.2. Burner head 26
2.1.3. Mixing system 27
2.2. Topology-tailored burners **29**
2.2.1. Triply-Periodic Minimal Surfaces 29
2.2.2. Pore size and void fraction control 29
2.2.3. From a mathematical function to a printable CAD 31
2.2.4. Graded and swirled topologies 32
2.2.5. Optical access 33
2.2.6. Additive manufacturing technique 35
2.2.7. Inventory of porous burners 38
2.3. Diagnostics **39**
2.3.1. Imaging 39
2.3.2. Thermometry 39
2.4. Experimental procedure **40**
2.5. Images post-treatment **42**
2.6. Conclusions of the chapter **44**
2.A. Uncertainties analysis **45**
2.A.1. Load and mixture composition 45
2.A.2. Inlet temperature 46

"*Today we made no progress, but we have thought a lot.*"

Maria del Mar Montoya

2.1. The POROSITO test rig

2.1.1. Burner base

The POROSITO test rig takes up an existing experimental setup at the IMFT. The original experiment, designed and built by François Muller, was devoted to the study of porous media combustion in reticulated ceramic foams. More information about the original apparatus can be found in his PhD thesis [165]. For this work, the burner head has been replaced by the one described in Sec. 2.1.2. Since the POROSITO test rig incorporates the burner base from the previous setup, a brief description of the burner base is presented here for the sake of completeness.

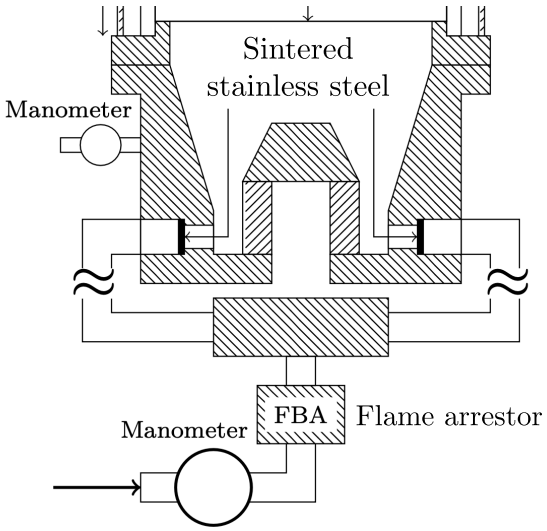

Figure 2.1. – Schematic of the burner base. Reproduced from Muller [165].

The structure of the burner base is depicted in Fig. 2.1. Premixed reactants enter the system from the bottom where a manometer is used to monitor the head loss through the burner. Because the POROSITO test rig operates in premixed regime, a flame arrestor is used to protect the mixing system from an eventual flashback. Reactants arrive at the small plenum chamber at the bottom of the burner. From there, eight tubes convey the flammable mixture towards the second plenum chamber. These tubes are evenly distributed to maximize the homogeneity of the injection. The main plenum chamber is equipped with three instrumentation accesses. One of them mounts a differential pressure sensor to measure the pressure drop through the head of the burner. The measurement range of this instrument is ± 2000 Pa and its resolution is 10 Pa. The other two are used to inject an air flow seeded with oil droplets when applying laser diagnostics.

2.1.2. Burner head

Figure 2.2 depicts the schematic of the POROSITO test rig. At the bottom, methane, hydrogen and air flow rates are imposed by the mixing system, which is described in Sec. 2.1.3. The

premixed reactants go through a convergent section and a sintered steel plate to remove flow inhomogeneities. To limit the thermal drift of the system, the straight duct section is cooled down to $T_w = 293$ K by a recirculating water bath system. Nevertheless, the radiative heat flux from the burner heats up the sintered steel plate and the fresh gasses. Two K-type thermocouples with different bead sizes are used to measure the actual temperature of the reactants, T_{in}, which is used to evaluate the laminar flame properties at each operating point. More details on the inlet temperature measurements are provided in Sec. 2.3.2.

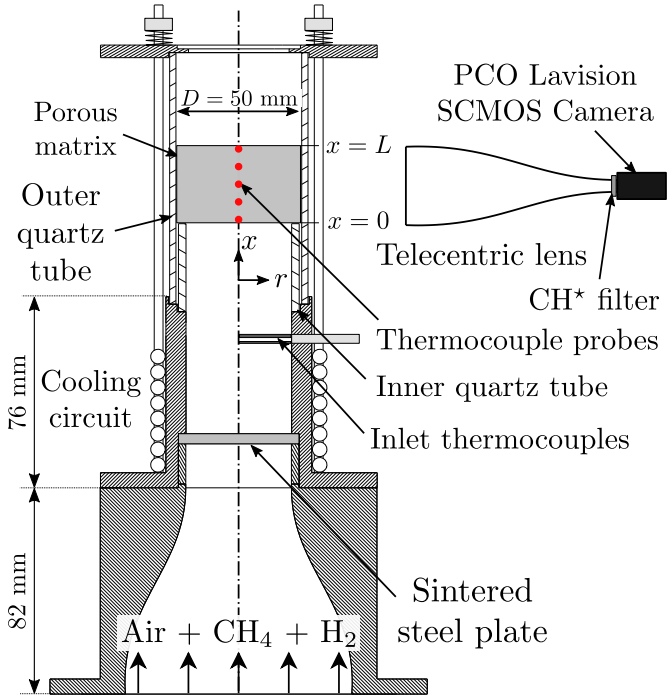

Figure 2.2. – Schematic of the POROSITO test rig.

The porous medium where flames are stabilized leans on an inner quartz tube and is enclosed by another quartz tube with inner diameter $D = 50$ mm. The diameter of the porous matrix is slightly smaller than the inner diameter of the quartz tube. This makes assembly possible and prevents quartz break due to thermal expansion. To minimize the leakage between the quartz and the burner, the quartz-to-porous gap is smaller than the pore size at room temperature conditions. Graphite joints between the different components are used for sealing and the ensemble is clamped by an upper flange. The origin of the coordinate system is located at the burner inlet. The streamwise coordinate is denoted by x and the total burner length is $L = 30$ mm. The axial coordinate is often expressed in dimensionless form by normalization with burner length. The dimensionless axial coordinate is denoted by $\xi = x/L$.

2.1.3. Mixing system

The operating point of the burner is defined by the load and the mixture composition, $Y_{k_{in}}$. The load is quantified via the thermal power, which is defined as:

$$P = \sum_f \dot{m}_f Q_f \tag{2.1}$$

where $\dot{m}_f$ and Q_f are the mass flow rate and the Lower Heating Value (LHV) of fuel $f = H_2, CH_4$, respectively. The composition, $Y_{k_{in}}$ is fixed by the hydrogen power fraction $\alpha_P = \dot{m}_{H_2} Q_{H_2}/P$ and the equivalence ratio ϕ.

Two sets of Mass Flow Controllers (MFC) are used to set the mixture composition and the burner load. Each set of MFC is used for a different load range to minimize the errors in the gas composition. The low-power set consists of three Bronkhorst ELFLOW-Base for the Air, H_2 and CH_4 flow lines. Their mass flow ranges are 45 nL/min, 5 nL/min and 3.5 nL/min, respectively. The high-power set is composed of two Voegtlin Red-y smart for the Air and H_2 lines with flow ranges of 130 nL/min and 20 nL/min, respectively; and a Bronkhorst ELFLOW-SELECT for CH_4 with flow range of 19.5 nL/min. A schematic of the pipeline arrangement in the mixing system is presented in Fig. 2.3.

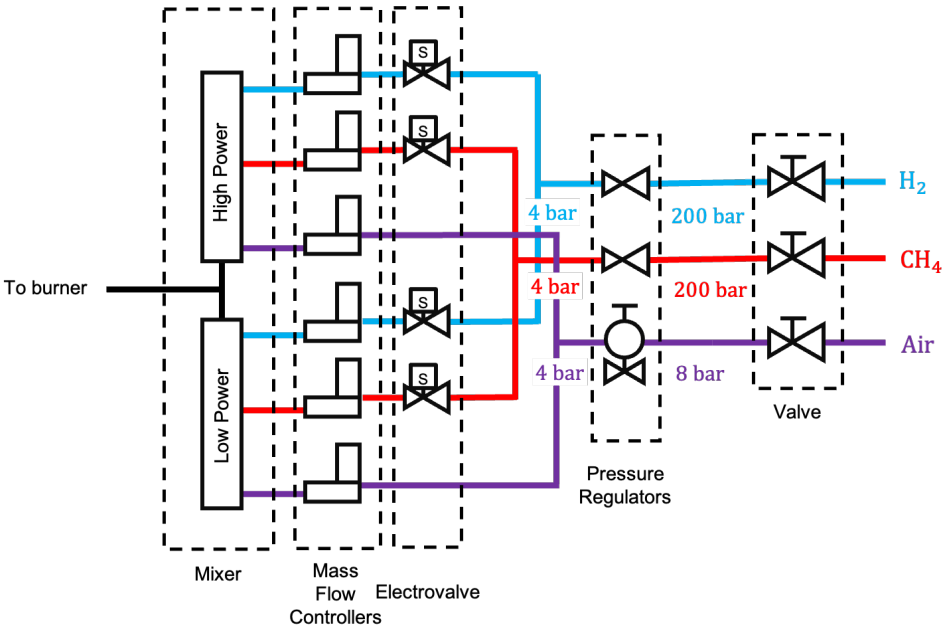

Figure 2.3. – Schematic of the mixing system.

From the MFCs specifications and the analysis of errors presented in Appendix 2.A, it is possible to estimate the uncertainties in power, δP, equivalence ratio, $\delta\phi$ and hydrogen content, $\delta\alpha_P$, for each operating point. The uncertainties of the input parameters have been calculated for an experimental database including nearly 500 stable operating points with equivalence ratios, hydrogen power fractions and powers ranging from $0.27 < \phi < 0.72$, $0\% < \alpha_P < 80\%$ and $0.75\ \text{kW} < P < 2\ \text{kW}$, respectively. The Probability Density Functions (PDFs) of the errors are represented in Fig. 2.4. The relative errors in hydrogen content and power are below 5% and 3%, respectively. The modal absolute error in equivalence ratio is $\delta\phi \simeq 0.005$.

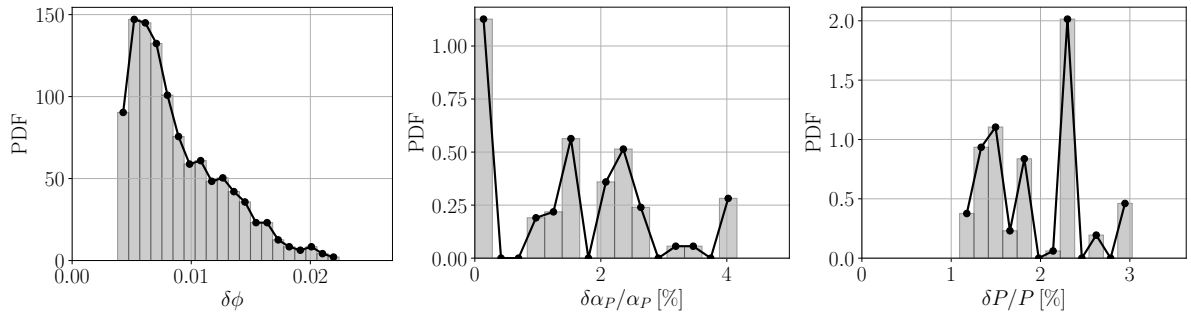

Figure 2.4. – PDF of the uncertainties in ϕ, α_P and P.

2.2. Topology-tailored burners

In this thesis, computer-defined topologies are used to build tailored PMBs. In these burners, the interface between the solid and the gas phase is defined by an implicit mathematical function. Computer-defined topologies offer several advantages with respect to random reticulated foams. Firstly, the pore size and the porosity can be independently controlled. As a result, a systematic study on the influence of these parameters on the burner's performance can be carried out. Secondly, they simplify the characterization of the topological parameters. Since a mathematical description of the fluid-solid interface is available, an accurate evaluation of parameters such as the tortuosity coefficients and the interface surface density is possible. In reticulated porous matrices, if a detailed characterization of the porous matrix is sought, X-ray tomography is required to scan a small sample of the burner geometry [58, 59, 66, 67]. The X-scan must be processed and several technicalities make this handling difficult [64]. VAMs must be fed with many numerical parameters, including several related to the burner topology. Reducing the uncertainties in the evaluation of these parameters is crucial if a reliable comparison between simulation and experimental results is sought. Finally, this framework enables new burner designs, including axially graded topologies and swirled burners. This opens the door to optimizing the burner performance via topology tailoring [117, 121].

2.2.1. Triply-Periodic Minimal Surfaces

In this work, Triply-Periodic Minimal Surfaces (TPMS) [166–168] define the fluid-solid interface of the porous matrix. These surfaces are periodic in the three directions of the space and this periodicity is characterized by a wavenumber κ_i where $i = x, y, z$. Here, for the sake of simplicity, isotropic TPMS with $\kappa_i = \kappa$ are considered. There are various families of TPMS and each of them is characterized by an implicit equation. In this work, the Diamond, Gyroid and Primitive topologies are used. In the Diamond topology, the implicit equation that defines the fluid-solid interface reads:

$$\begin{aligned}\mathcal{D}(\mathbf{x};\kappa) = s(\kappa x)s(\kappa y)s(\kappa z) + s(\kappa x)c(\kappa y)c(\kappa z) + \\ c(\kappa x)s(\kappa y)c(\kappa z) + c(\kappa x)c(\kappa y)s(\kappa z) = t\end{aligned} \tag{2.2}$$

In eq. (2.2), $s(\cdot)$ and $c(\cdot)$ stand for the sine and cosine functions. The topology equation has two input parameters, namely the wavenumber, $\kappa = 2\pi/\Lambda$ and the threshold, t. Here, Λ denotes the spatial period of the lattice. However, the use of these parameters is not convenient when dealing with PMBs. In the literature, the characterization of porous media structures is always made in terms of the pore size, d_p, and the void fraction, ϵ. Therefore, the first step is to find a mapping between the duple (d_p, ϵ) and the parameters in the TPMS equation (Λ, t).

2.2.2. Pore size and void fraction control

To begin with, the void fraction, ϵ, and the pore size, d_p, must be clearly defined. When TPMS are used to generate the geometry of a porous medium, the region of the space, Ω_s where $\mathcal{D}(\mathbf{x}, \kappa) > t$ corresponds to the solid phase and its volume is V_s. Therefore, gas phase is the region Ω_g where $\mathcal{D}(\mathbf{x}, \kappa) < t$ and its volume is V_g. The fluid-solid interface where $\mathcal{D}(\mathbf{x}, \kappa) = t$ is denoted by $\partial\Omega$. The void fraction or porosity is defined as:

$$\epsilon = V_g/(V_g + V_s) \tag{2.3}$$

For a given $\mathbf{x} \in \Omega_g$ in the gas phase, the local pore size, $d_p(\mathbf{x})$, is defined as the diameter of the largest sphere that contains $\mathbf{x}$ and is tangent to the solid phase. Note that the sphere is

not necessarily centered on $\mathbf{x}$. From this definition, we can compute the 3D field of pore size $d_p(\mathbf{x})$ in the gas phase and obtain its Probability Density Function (PDF). For an entire porous matrix, the global pore size, d_p is taken as the pore diameter for which the PDF is maximum. Figure 2.5 shows a cut of the 3D field of local pore size, $d_p(\mathbf{x})$, and its PDF in a Diamond-based porous matrix with $\epsilon = 0.8$ and $d_p \simeq 2.5$ mm. Because of the spatial periodicity of TPMS, it is possible to evaluate the lattice properties over a volume spanning for one wavelength in the three directions of space $\Omega = \Lambda \times \Lambda \times \Lambda$.

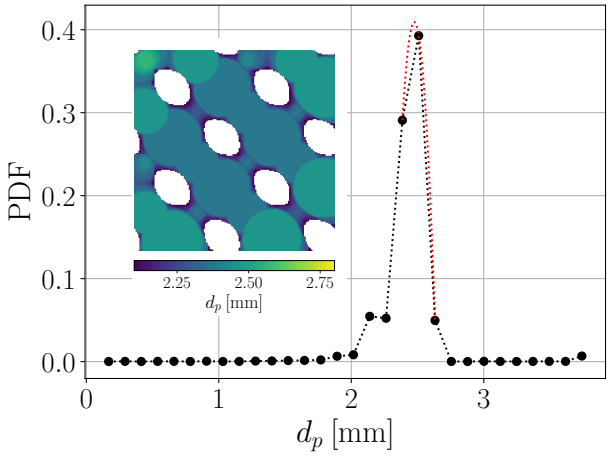

Figure 2.5. – Local pore size field, $d_p(\mathbf{x})$ and pore size PDF for a Diamond-based porous matrix with $\epsilon = 0.8$ and $d_p = 2.5$ mm.

In order to use the pore size, d_p and the porosity, ϵ as input parameters, the relationship between these quantities and the parameters of the TPMS equation, t and κ, must be established. By construction, the threshold t only depends on the void fraction, ϵ. Also, it can be shown that for a given ϵ, the pore size is proportional to the lattice spatial period $d_p \propto \Lambda$. Thus, both the threshold, t and the normalized pore size d_p/Λ are a function of ϵ only. These properties enable a direct remapping between $(d_p, \epsilon) \rightarrow (t, \Lambda)$ via the functions $d_p/\Lambda(\epsilon)$ and $t(\epsilon)$. From these functions it is possible to compute the lattice wavelength, Λ, and threshold, t, that produce a certain combination of pore size, d_p and porosity, ϵ. The remapping curves must be obtained for each family of TPMS porous matrices. They are computed numerically for a certain range of ϵ values and, then, they are interpolated for arbitrary values of porosity. Figure 2.6 shows the remapping curves for the Diamond topology. For ϵ close to the unity, the solid phase, Ω_s is a non-connected space and no porous structure can be produced.

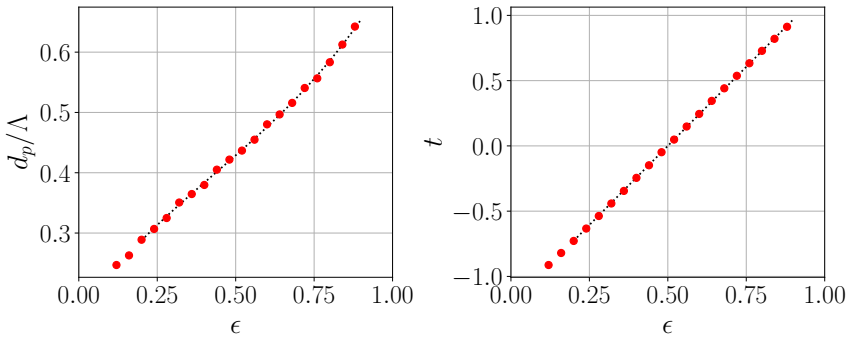

Figure 2.6. – Remapping curves for the Diamond topology.

2.2.3. From a mathematical function to a printable CAD

Upon the determination of the remapping curves, the process to generate a 3D printable Computer Aided Design (CAD) starts with the evaluation of the TPMS equation – $\mathcal{D}(\mathbf{x};\kappa)$ for a Diamond structure – over a 3D domain using a cartesian grid. The dimensions of this domain must be slightly larger than those of the burner to prevent errors in the subsequent steps. Then, an isosurface algorithm is employed to extract the exact coordinates where $\mathcal{D}(\mathbf{x};\kappa) = t$. This fluid-solid interface, $\partial\Omega$, can be triangulated and stored using the STL format at the aid of different off-the-shelf python tools. An important aspect is the choice of the mesh resolution, which must be defined in relation to the topology wavelength, Λ. In this work, a total of $n = 30$ points per wavelength are used to obtain smooth and resolved CAD files.

The next step is obtaining a closed 3D surface of the burner geometry from its fluid-solid interface. For that, a boolean operation of type intersection must be performed between the interface and a cylinder with the final dimensions of the burner. This is a critical step because many existing tools produce errors and geometrical aberrations when performing this operation. In the search for a reliable technique, different tools such as BLENDER were explored. In the end, the process was successfully automatized by using the python library PyMesh [169]. Among the different boolean operation engines available in PyMesh, CGAL [170] was used for its repeatability and reliable results. After this boolean operation, there might be some disconnected elements that must be ruled out. Upon the removal of disconnected elements, the resulting STL files are suitable for 3D printing in most cases. Figure 2.7, shows the different steps in the geometry-generation process. It is important to stress that the burner width must be slightly smaller than the inner diameter of the combustion chamber. Otherwise, the thermal expansion of the PMB can break the quartz tube. This must be taken into account at this stage of the manufacturing process.

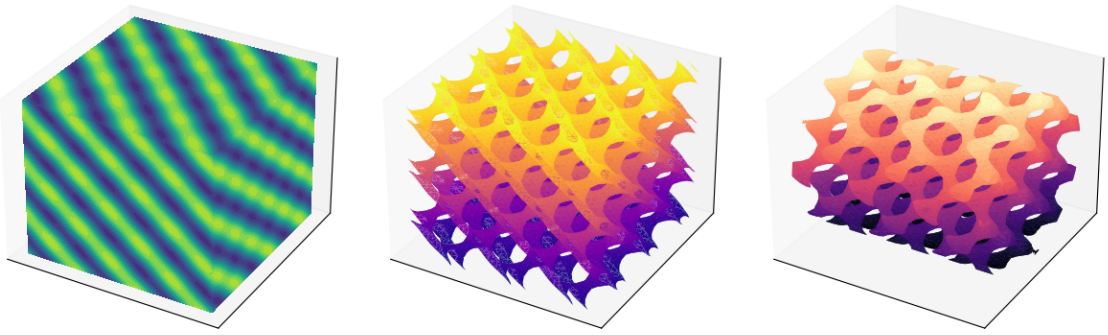

Figure 2.7. – Steps in the geometry-generation process.

Upon the above-described process, the STL files are free of geometrical errors and therefore printable. However, they feature a non-homogeneous triangle distribution which turns out to be suboptimal in terms of storage. In this respect, difficulties arise when burners with a small pore size are to be generated. Owing to the resolution requirements, the resulting files are very heavy (up to 2 Gb in binary) and 3D printing softwares cannot handle them. To deal with this technicality, these STL files are remeshed using PyMesh. The algorithm employed homogenizes the triangle distribution according to an user-specified characteristic mesh size. Typically, a characteristic mesh size of $100 - 150$ μm is used. Generally, this reduces the size of the files by more than 50% with little loss of accuracy in the geometrical representation. Figure 2.8 depicts a detail of the burner geometry before and after the remeshing operation.

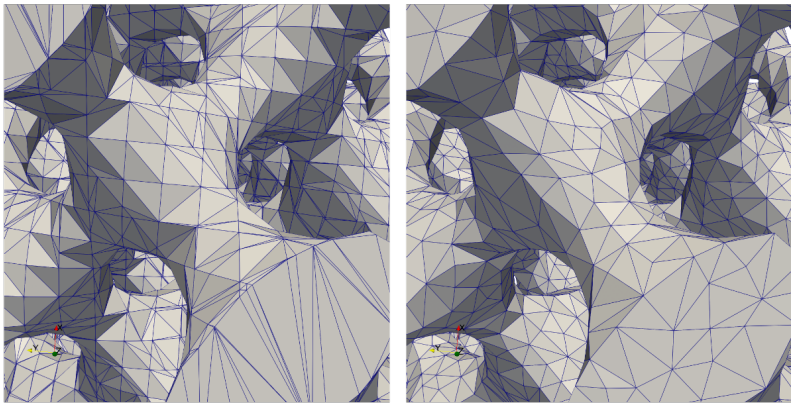

Figure 2.8. – Detail of the burner geometry before (left) and after (right) the remeshing operation.

2.2.4. Graded and swirled topologies

The use of computer-defined topologies opens the door for topology-tailoring to optimize the performance of the burner. In an axial porous burner, flames stabilize at different locations, x_f, depending on the operating conditions, i.e., close to the burner inlet in the vicinity of flashback and at the middle of the porous matrix right before blowoff. Therefore, the topological properties can be varied in the streamwise direction to extend the operating domain of the burner. In this respect, two topology-modulation strategies can be considered.

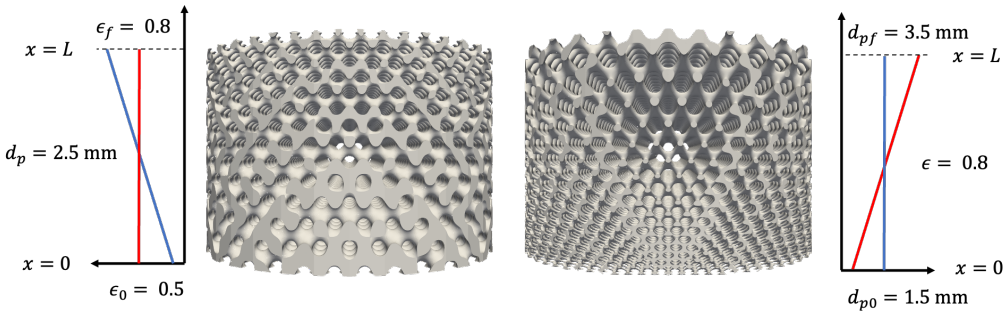

Figure 2.9. – PMBs featuring a topological gradation of porosity (left) and pore size (right).

The first strategy is based on hydrodynamic stabilization. At first order, flame stabilization is driven by the balance between the local flame speed, S_L, and the bulk flow velocity, u_B. Therefore, this approach consists in creating an axial profile of bulk velocity, $u_B(x)$ that delays flashback and blowoff occurrence. This is achieved via a decreasing longitudinal velocity profile from the inlet to the outlet of the burner. Because the bulk flow velocity is inversely proportional to the burner cross-section, this profile is obtained by imposing an increasing axial profile of porosity $\epsilon(x)$. To obtain a linear variation of porosity, $\epsilon(x) = \epsilon_0 + (\partial_x \epsilon)x$, the threshold, $t(\epsilon)$, and the normalized pore size, $d_p/\Lambda(\epsilon)$, must be computed using the topology remapping. Therefore, the TMPS equation becomes $\mathcal{D}(\mathbf{x}; \kappa(x)) = t(x)$.

The second strategy relies on flame quenching. Local flame-to-wall heat losses are directly linked to the pore size, d_p, i.e. small pores increase the local heat losses and quench the flame. This can be exploited to extend the flashback limit by introducing an axial variation of pore size, $d_p(x)$ that quenches the flame close to the burner inlet, thereby limiting its upstream propagation. To obtain a linear variation of the pore size, $d_p(x) = d_0 + (\partial_x d_p)x$, with constant porosity, ϵ, the normalized pore size $d_p/\Lambda(\epsilon)$ must be computed as a function of x and the TPMS

equation becomes $\mathcal{D}(\mathbf{x};\kappa(x)) = t$. These two topological modulation strategies are illustrated in Fig. 2.9, where two porous burners featuring an axial gradation of porosity (left) and pore size (right) are shown.

The possibilities for topology tailoring are immense. For instance, by using rotation matrices, the geometry of the burner can be swirled around its axis of symmetry:

$$\begin{bmatrix} x \\ y \\ z \end{bmatrix}_{\partial\Omega_s} = \begin{bmatrix} 1 & 0 & 0 \\ 0 & \cos(\theta) & -\sin(\theta) \\ 0 & \sin(\theta) & \cos(\theta) \end{bmatrix} \begin{bmatrix} x \\ y \\ z \end{bmatrix}_{\partial\Omega} \qquad \text{where } \theta = sx \tag{2.4}$$

Here, s is the swirl number, $\partial\Omega$ denotes a point at the fluid-solid interface, and subscript $-s$ refers to the swirled geometry. This can be used to increase the residence time of the gas inside the burner which can in turn reduce the amount of unburned gasses in very lean mixtures. Figure 2.10 shows a swirled Diamond burner with a radial variation of porosity.

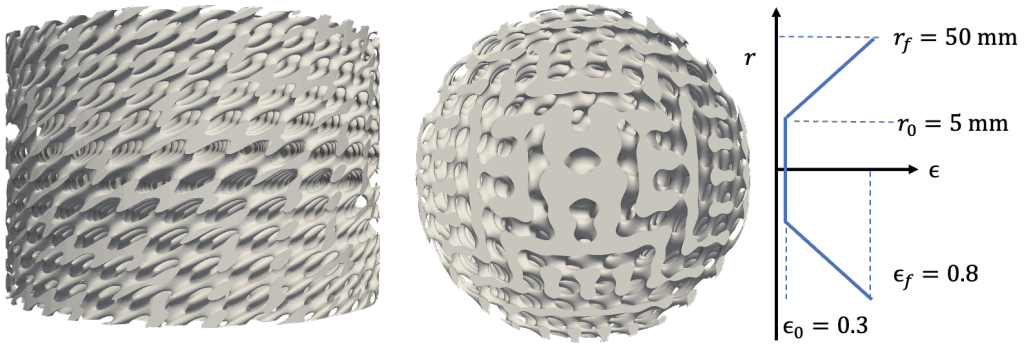

Figure 2.10. – Swirled Diamond porous medium with a radial distribution of porosity, a pore size of $d_p = 3.5$ mm and a swirl number of $s = 0.05$.

2.2.5. Optical access

So far, we have focused on the operational advantages of computer defined topologies. However, a peculiarity of TPMS-based topologies is the existence of See-Through Directions (STD) in the porous matrix consisting of multiple parallel optical pathways. These optical pathways provide extensive optical access to the interior of the solid matrix. As a result, direct visualization of the flame inside the burner is possible. Furthermore, when two of these STDs feature orthogonal and coincident optical pathways, one can be used for illumination and the other for imaging. Therefore, it is possible to apply laser diagnostics such as Particle Image Velocimetry (PIV), Planar Laser Induced Fluorescence (PLIF), or Raman Scattering.

Besides the above-mentioned Diamond topology, two other TPMS have been used in the present work to produce optically accessible burners: the Gyroid topology, where the fluid-solid interface is defined by the implicit equation:

$$\mathcal{G}(\mathbf{x};\kappa) = c(\kappa x)s(\kappa y) + c(\kappa y)s(\kappa z) + c(\kappa z)s(\kappa x) = t \tag{2.5}$$

and the Primitive topology, whose implicit equation reads:

$$\mathcal{P}(\mathbf{x};\kappa) = c(\kappa x) + c(\kappa y) + c(\kappa z) = t \tag{2.6}$$

In each topology, the optical pathways of the burner are arranged differently. Some of these

optical pathways, here called minor, are too small for practical purposes. Moreover, porosity can affect the number of usable STDs.

In the Diamond topology, there are four major and three minor STDs. Figure 2.11a sketches the arrangement of the STDs in the Diamond topology. Two of the major STDs are contained in the XZ and the XY planes and are not shown in Fig. 2.11a because they were not used in the present work. The other two major STDs – here referred to as yz and zy – are horizontal and are used here for direct flame visualization. These two STDs are perpendicular but they are not coincident so they cannot be combined to apply laser diagnostics.

A detailed view of the STD is offered in the 3D rendering of Fig. 2.11b for a Diamond-based burner with a porosity of $\epsilon = 0.8$. The represented volume extends for one wavelength, Λ, in the three directions of space. With this topology, if only one major STD is used, the optically accessible volume represents approximately 42% of the total volume, which is more than half of the gas-phase volume. Finally, the hidden volume, which is the fraction of the gas phase that cannot be seen is roughly 38% of the total volume. In contrast to previous efforts [151–153], the present technique offers an extensive optical access to the interior of the porous matrix.

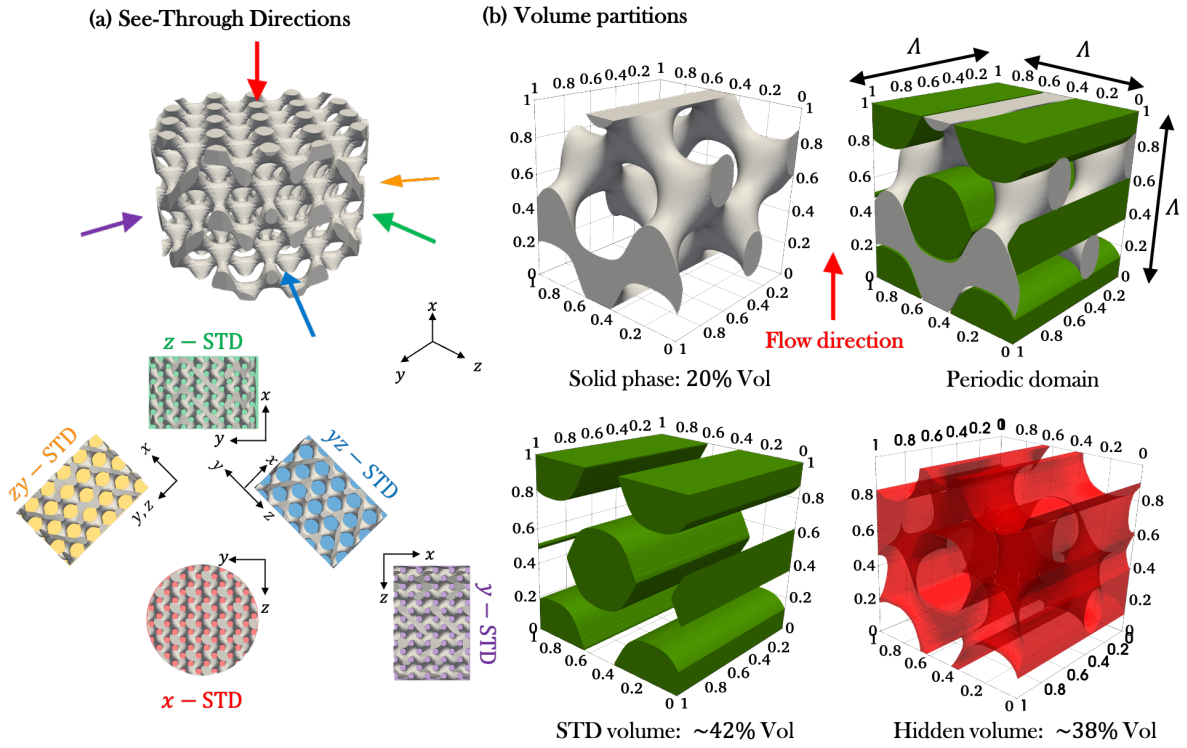

Figure 2.11. – a) Arrangement of the STDs in a Diamond-TPMS-based porous media. In this topology, the x, y and z-STD are too small for practical purposes. For direct flame visualization, the zy and the yz-STD can be used to access the interior of the porous matrix. b) 3D view of the different volume-partitions in an elementary volume. Green-colored volumes are accessible by imaging the porous medium from one of the major STDs and represent roughly 42% of the total volume. The hidden volume is depicted in red and accounts for approximately 38% of the total volume. The remaining 20% of the volume is occupied by the solid phase.

In the Gyroid topology, there are eight STDs and their arrangement is sketched in Fig. 2.12a. Again, four of the major STDs in the xyz direction were not used in this work and have been excluded from the visualization of Fig. 2.12. For direct flame visualization, the y and z-STDs offer the largest optical access to the interior of the porous matrix. However, these two STDs

do not intersect inside the burner and hence cannot be combined to apply laser diagnostics. In the yz-STD, the optical access is more limited, but these optical pathways intersect those in the x-direction. Hence, combining the optical access provided by the x-STD and the yz-STD, it is possible to apply laser diagnostics in Gyroid-based PMBs. A detailed view of the y-STD is offered in the 3D rendering of Fig. 2.12b for a Gyroid-based burner with a porosity of $\epsilon = 0.8$. Using this STD for imaging provides optical access to roughly 33% of the total volume.

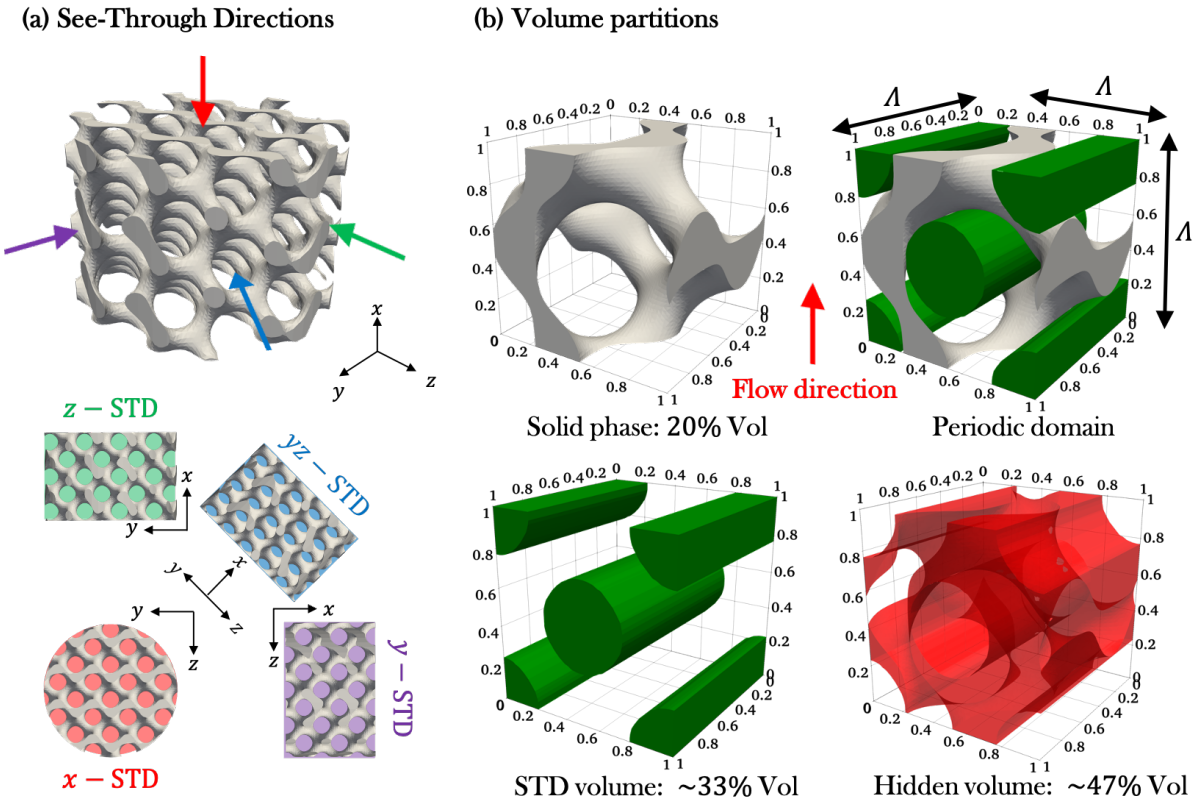

Figure 2.12. – a) Arrangement of the STDs in a Gyroid-based topology. In this geometry, the y-STD and z-STD are used for direct flame visualization. However, the optical pathways of these two STDs do not intersect inside the burner and thus cannot be combined to apply laser diagnostics. In contrast, the optical pathways of the yz-STD and x-STD are coincident and can be used for laser diagnostics. In this topology there are also four major STDs in the xyz direction but they were not used the present study. b) 3D rendering of the different volume-partitions in an elementary volume. For $\epsilon = 0.8$, the fraction of optically accessible volume using the y-STD is approximately 33% and the hidden volume is roughly 47%.

Finally, Fig. 2.13a shows the STDs arrangement in the Primitive topology. This is the simplest TPMS topology and features three major STDs, each aligned with one direction of space. These three optical pathways intersect over the volume of the pore rendering this topology suitable for laser diagnostics. The different volume partitions of Primitive-based burners have been represented in Fig. 2.13b for a porosity value of $\epsilon = 0.7$.

2.2.6. Additive manufacturing technique

In this work, porous media are 3D printed in 316L stainless steel. This alloy features a high corrosion resistance at elevated temperatures and its solidus and liquidus temperatures are

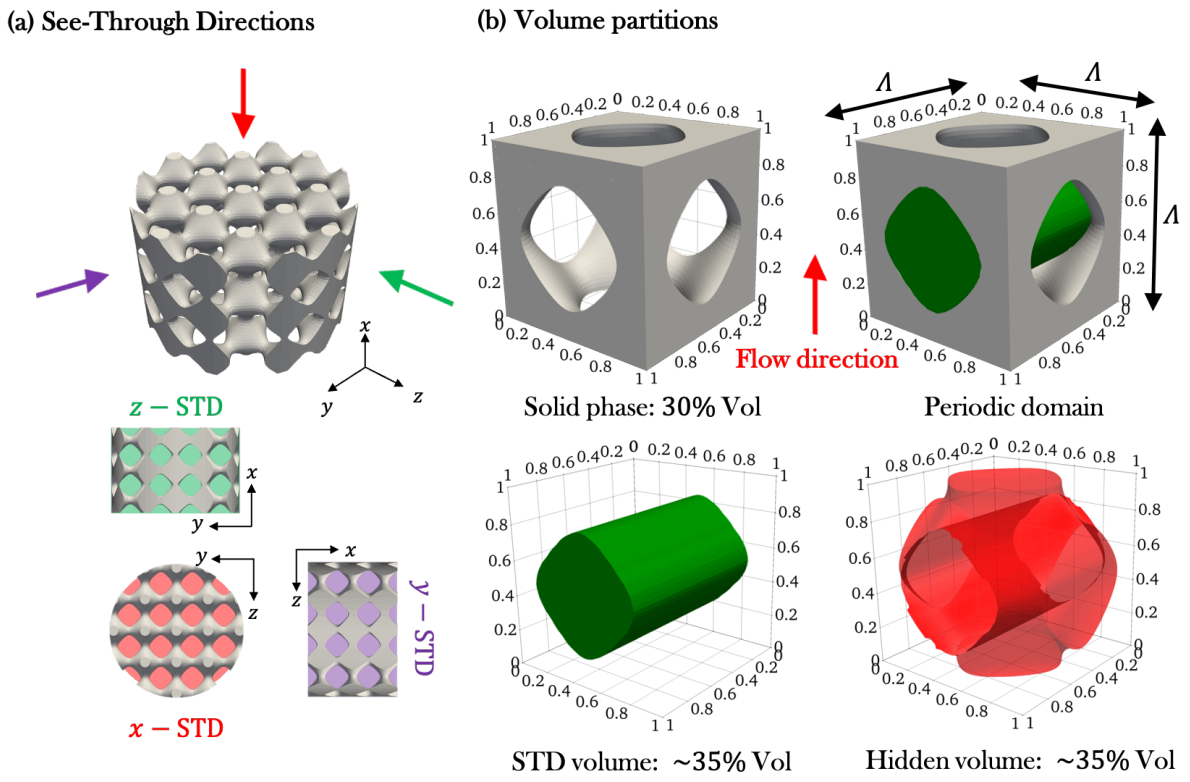

Figure 2.13. – a) Arrangement of the STDs in the Primitive topology. In this geometry, there are three STDs each aligned with one direction of space. These three STDs intersect inside the cavities of the burner and therefore can be combined to apply laser diagnostics. b) 3D view of the different volume-partitions in an elementary volume. The optically accessible volume in a $\epsilon = 0.7$ burner is approximately 35% of the total volume and the hidden fraction is roughly 35%.

1648 K and 1673 K, respectively [171]. The manufacturing technique employed is called Selective Laser Melting (SLM). In SLM, solid metal components are produced when a high intensity laser is used to melt and fuse selective regions of powder in a layer-by-layer process according to a CAD [119]. Some of the burners were manufactured by the company MIZAR Additive and some others were printed by the CIRIMAT laboratory in Toulouse. Both suppliers use the same manufacturing technique but there are small differences in the metal powder characteristics and the printing parameters. Unfortunately, for the MIZAR burners, fewer details about the manufacturing process are available. Overall, no remarkable differences could be reported in terms of printing quality, surface state and burner behavior between the two suppliers.

For the CIRIMAT burners, a SLM Phenix 3D System machine was used to produce the porous matrices. In this device, a ND-Yag 1074 nm Laser with a 300 W power is used to fuse the metal powder. In this printer, material layers are compacted upon deposition by a compression roll to reduce the porosity of the manufactured elements. The SLM process takes place inside an inert Argon atmosphere to prevent material oxidation. The metal powder used is a 3D Systems 316L Laser Form (b) with a characteristic size of 40 μm. The dimensions of the building platform are 140 $\times$ 140 mm. Figure 2.15 shows two building plates where the porous matrices have been manufactured. The MIZAR porous matrices were manufactured using a EOSM90 3D printing machine that mounts a Yb-fiber laser with a total power of 400 W. The diameter of the focused laser beam is 100 μm. The layer thickness is 40 μm and the dimensions of the building platform are 250 $\times$ 250 mm.

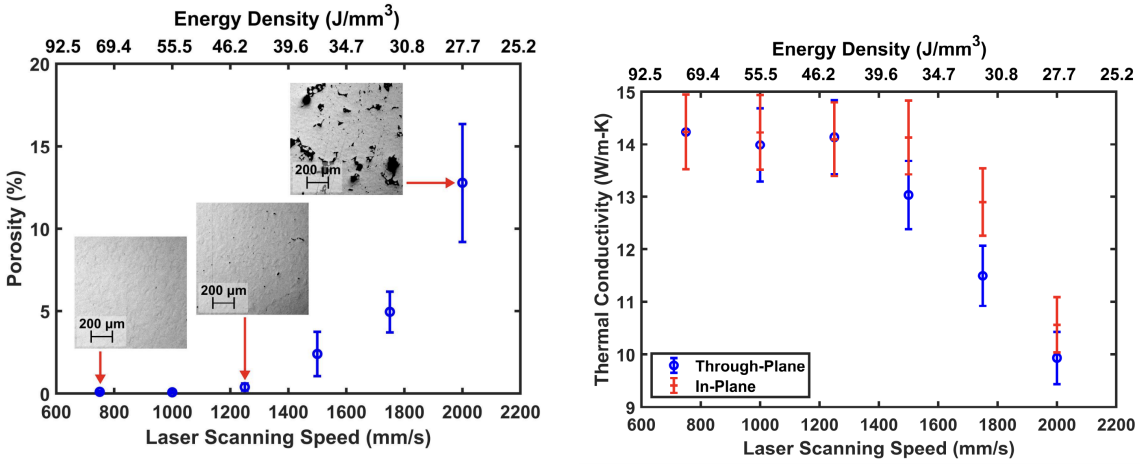

Figure 2.14. – Evolution of the 3D printed material porosity and thermal conductivity as a function of the laser scanning speed and energy density. Reproduced from Simmons *et al.* [172].

Owing to this specific manufacturing technique, the thermo-mechanical properties of the resulting solid components differ slightly from those of the bulk base material [172]. Notably, additive manufactured items have a certain level of intrinsic porosity which translates into a mildly lower density and thermal conductivity. Quantitatively, the variation of the material properties depends upon the printing parameters such as the laser scanning speed and the energy density. For example, elevated laser scanning speeds can result in differences between the in-plane and the through-plane properties of the metallic component (cf. Fig. 2.14). Among the thermo-mechanical properties of the solid phase, we are interested in the solid thermal conductivity, λ_s, since it has a direct impact on the stabilization of the flame via heat recirculation.

The CIRIMAT porous matrices were manufactured using a hexagonal scanning strategy with a 50 μm hatching and a layer thickness of 50 μm. The laser scanning speed was 1400 mm s^{-1} for the inner region and 160 mm s^{-1} at the layer contours. Likewise, a laser power of 126 W was applied to the inner region whereas a power of 54 W was used for the contours. The output energy density of the manufacturing process expressed in J mm^{-3} is given by:

$$\text{Energy density}\left[\frac{\text{J}}{\text{mm}^3}\right] = \frac{\text{Laser Power [W]}}{\text{Laser scan speed}[\frac{\text{mm}}{\text{s}}] \times \text{hatch spacing[mm]} \times \text{layer thickness[mm]}} \tag{2.7}$$

In the porous matrices, the energy density in the inner region is approximately 36 J mm^{-3}. According to the observations of [172] and [173], a level of intrinsic porosity ranging between 0 and 5 % can be expected for the printed components (see Fig. 2.14). Following Simmons et al. [172], at this scanning speed and energy density, there is just a small offset between the in-plane and the through-plane thermal conductivity (see Fig. 2.14). The through-plane thermal conductivity is expected to drop to roughly 13 W m^{-1} K^{-1}. Since the porous matrices are printed in the streamwise direction, the through-plane solid thermal conductivity must be retained. To account for the mild reduction in the thermal conductivity arising from the manufacturing process a value of $\lambda_s = 13$ W m^{-1} K^{-1} is taken for the solid thermal conductivity of the present burners.

Despite a thorough analysis of the 3D printing accuracy has not been performed, a few printed burners were scanned using X-ray Computed Tomography (XCT). From the X-ray slices of the porous matrix, a STL of the real burner geometry can be reconstructed. Overall, the 3D reconstructions from XCT scans show a good qualitative agreement with the original CAD files.

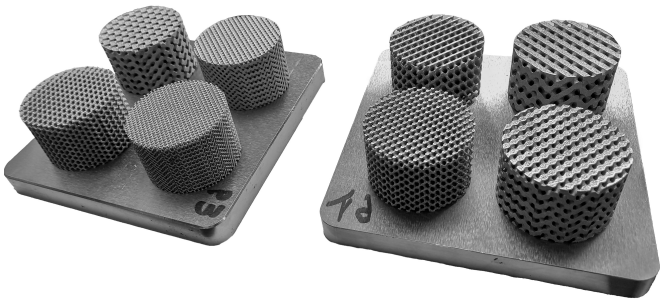

Figure 2.15. – Porous matrices on the printing plate after the additive manufacturing process.

2.2.7. Inventory of porous burners

Table 2.1 lists all the printed porous burners together with their topological parameters including the diameter, D, height, L, pore size, d_p, porosity, ϵ, interface surface density, S_v, solid and gas phase tortuosities, $\tau_{s/g}$, topology, manufacturer and number of working hours. Chapter 3 offers a detailed description of the procedure to evaluate the topological parameters of the burner from its CAD representation. The number of working hours has been estimated from the records of laboratory notebook. Since heat-up times were not always registered, the reported working time represents a conservative estimate of the real time.

Burner	Diameter D [mm]	Height L [mm]	Porosity ϵ [-]	Pore size d_p [mm]	S_v [m^{-1}]	τ_s [-]	τ_g [-]	Topology	Manufacturer	Working Time [h]
B1	50	23.5	0.6	2.23	804.7	1.769	1.430	Diamond	MIZAR	44
B2	50	30	0.8	2.87	661.9	2.515	1.190	Diamond	MIZAR	45
B3	50	30	0.5	2.00	823.5	1.582	1.582	Diamond	MIZAR	19
B4	50	30	0.8	2.41	754.2	2.515	1.190	Diamond	MIZAR	34
B5	100	75	0.6	2.23	804.7	1.769	1.430	Diamond	MIZAR	0
B6	50	30	0.8	2.5	729.1	2.515	1.190	Diamond	CIRIMAT	30
B7	50	30	0.5	2.5	658.8	1.582	1.582	Diamond	CIRIMAT	32
B8	50	30	0.8	1.5	1215.2	2.515	1.190	Diamond	CIRIMAT	26
B9	50	30	0.5	1.5	1098.0	1.582	1.582	Diamond	CIRIMAT	31
B10	50	30	0.8	3.5	520.8	2.515	1.190	Diamond	CIRIMAT	33
B11	50	30	0.5	3.5	470.6	1.582	1.582	Diamond	CIRIMAT	32
B12	50	30	0.8	x-Graded	NA	NA	NA	Diamond	CIRIMAT	0
B13	50	30	x-Graded	2.5	NA	NA	NA	Diamond	CIRIMAT	0
B14	50	30	r-Graded	3.5	NA	NA	NA	S-Diamond	CIRIMAT	0
B15	50	30	r-Graded	3.5	NA	NA	NA	S-Gyroid	CIRIMAT	0
B16	50	30	0.8	2.5	772.8	2.431	1.198	Gyroid	CIRIMAT	18
B17	50	30	0.5	2.5	591.2	1.600	1.600	Gyroid	CIRIMAT	0
B18	100	60	0.8	3.5	520.8	2.515	1.190	Diamond	CIRIMAT	0
B19	100	60	0.5	3.5	470.6	1.582	1.582	Diamond	CIRIMAT	0
B20	50	30	0.7	3.5	615.4	2.237	1.265	Primitive	MIZAR	33
B21	50	30	0.7	2.5	861.6	2.237	1.265	Primitive	MIZAR	14
B22	50	30	0.8	3.5	552.0	2.431	1.198	Gyroid	MIZAR	21

Table 2.1. – List of printed PMBs and their topological properties. Prefix -S in the topology nomenclature indicates a swirled topology and NA stands for Non-Available data.

2.3. Diagnostics

2.3.1. Imaging

A LaVision Imager sCMOS camera is used to visualize the flame inside the porous matrix. Image resolution is 2560 × 2100 px, pixel size is 6.5 μm and images bit-depth is 16 bits. The camera is fitted with an Edmund Optics band-pass filter with a 4.0 Optical Density (OD), a bandwidth of 10 nm and a central wavelength of $\lambda = 430$ nm. As depicted in Fig. 2.16, the imaging system is aligned with one of horizontal see-through directions of the burner and collects the line-of-sight integrated $CH^{\star}$ radical emission from the flame. The filter allows us to identify the reaction region and to partly remove the black body radiation from the solid, which takes place primarily in the IR and low-frequency visible range.

Due to perspective distortion, if a conventional lens is used, only the optical pathway aligned with the axis of the camera is completely cleared. To circumvent this issue, the camera is fitted with an Opto Engineering Telecentric lens TC4M-64. This lens features a working distance of 182 mm and a field of view of approximately 60×44 mm given the dimensions of the camera sensor. Telecentric (TC) lenses remove perspective distortion providing an orthogonal projection of imaged objects. Thanks to TC lens, a cleared optical access is obtained for all the visual pathways aligned with the observation see-through direction. Hence, it is not necessary to translate the camera when the position of the flame in the burner changes. Perspective removal combined with the parallel horizontal see-through directions of the PMB topology yield direct optical probing of the flame. Figure 2.17 compares the visualization of the flame using the present setup and a conventional imaging system. Unfortunately, despite the use of a TC lens, the curvature of the quartz tube causes some distortion of the image at the burner edge owing to light refraction. This reduces the effective visualization through the optical pathways on the sides of the porous matrix.

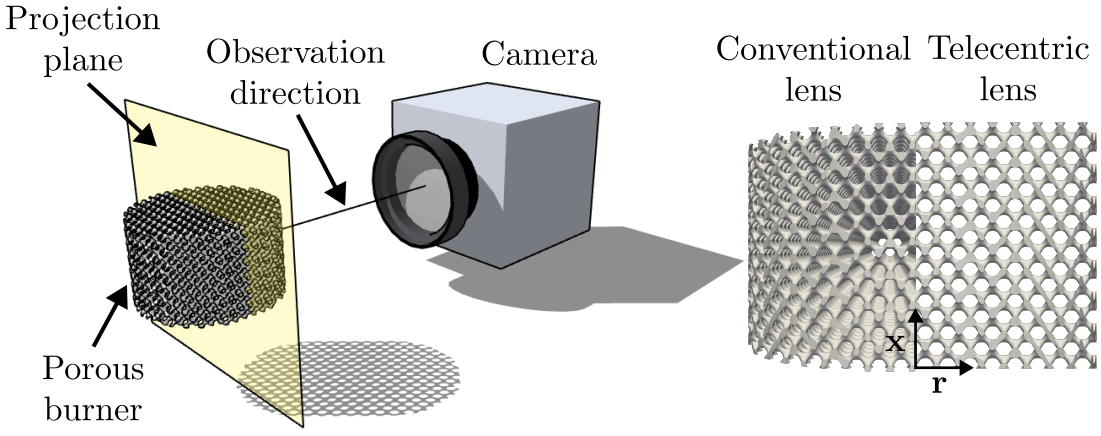

Figure 2.16. – Schematic of the camera alignment and effect of perspective removal on the STD visualization.

2.3.2. Thermometry

The see-through directions of the burner are used to insert thermocouple probes that are placed along the symmetry axis of the burner at different longitudinal positions, $\xi_i = x_i/L$. N-type thermocouples with a 0.5 mm sheath diameter are used to measure the temperature inside the burner. Temperature readings are used to reconstruct the axial temperature profile. The spacing between the thermocouple probes is imposed by the porous matrix periodicity. In the

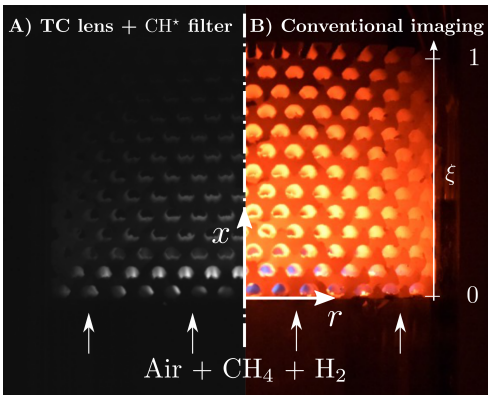

Figure 2.17. – Comparison between flame visualization using CH* chemiluminescence and a TC lens (A) and using a conventional imaging setup.

Diamond topology, there are two optical pathways per wavelength. Therefore, the uncertainty in the thermocouples positioning is $\pm\Lambda/2$. Inside the burner, thermocouple probes are submitted to a significant radiative heat flux from the solid matrix. The temperature of the thermocouple is given by the convective-radiative equilibrium of the thermocouple's bead at a given location. As a result, temperature readings lie somewhere between the solid and the gas phase temperatures whenever a thermal unbalance between the phases exists.

Two K-type thermocouples with different bead sizes are used to measure the reactants' inlet temperature T_{in} right before they enter the porous matrix. These thermocouples are submitted to the thermal radiation flux emitted by the hot solid matrix which alters their thermal balance and can result in an overestimation of the inlet temperature. Following [174], these two temperature measurements are combined to override the effect of thermal radiation on the energy balance of the thermocouple. The details of this correction can be found in Appendix 2.A together with its associated uncertainty analysis. After this correction, the uncertainty in the inlet temperature measurement is $\delta T_{in} \simeq 10$ K. A National Instruments (NI) Data Acquisition (DAQ) equipped with a thermocouple module is used to sample and digitize the analog measurements. An in-house Labview program allows us to monitor in real time and record the temperature readings inside the burner.

2.4. Experimental procedure

The burner is operated at fixed power, P, and hydrogen content, α_P, and its stability domain is explored by varying the equivalence ratio in steps of $\Delta\phi = 0.02$. Close to the blowoff and flashback limits, the step is reduced to $\Delta\phi = 0.01$. In methane-air flames, the flashback limit was rarely reached since the burner maximum operating temperature was usually attained before. When the operating point of the burner is changed, temperature monitoring is used to ensure that a steady state is reached. The evolution of temperatures over time allows us to assess the degree of steadiness in the system and to define a criterion for thermal convergence. Thermal convergence, and thus steadiness, is assumed when the variation of temperatures over two minutes is smaller than 1 K. PMC experiments are characterized by long transient times which can last for several minutes. This is because the characteristic time of the system is imposed by the diffusion time in the solid phase. Provided the lengthscale of the system, $L \simeq 30$ mm, and the thermal diffusion coefficient of the solid phase, $D_{T_s} = \lambda_s/\rho_s c_s \simeq 5 \times 10^{-6}\,\mathrm{m^2\,s^{-1}}$ the diffusion characteristic time is given by:

$$t_{s_{\mathrm{diff}}} \propto L^2/D_{T_S} \simeq 180\,\mathrm{s} \tag{2.8}$$

which provides an order-of-magnitude estimation of the transient times of the system. In practice, convergence times typically range between 5 and 15 minutes but can rise to nearly 30 minutes in the vicinity of blowoff. Figure 2.18 shows the time evolution of temperature readings inside the burner when the operating point is changed by modifying the mixture equivalence ratio ϕ.

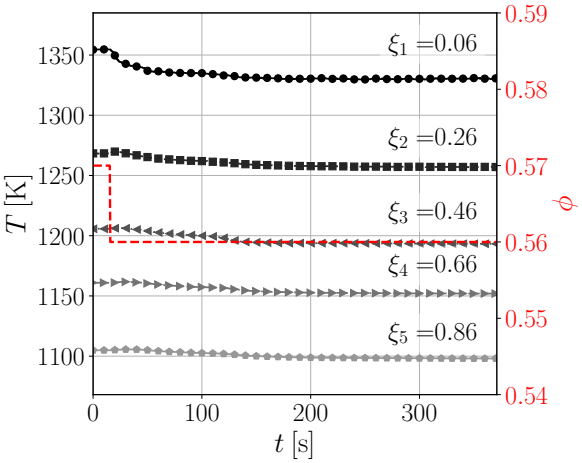

Figure 2.18. – Time-evolution of the temperature readings inside the burner when the operating point is changed by reducing the mixture equivalence ratio ϕ. $\xi_i = x_i/L$ denotes the normalized position of the i thermocouple. Measured temperatures are generally in the range $1000 < T < 1500$ K.

For each operating point, once thermal equilibrium is reached, the mass flow controllers and thermocouples signals are recorded and averaged for over two minutes and an image of the flame inside of the burner is taken with an exposure time of 2 s. Finally, a back-lighting placed behind the burner is employed to generate a mask that is used in the post processing stage to remove reflections of CH* signal on the burner surface. From images, the transversely averaged $\mathrm{CH}^\star(x)$ profile is computed, which is assumed to be proportional to the heat release rate and it is used to compute the flame position inside the PMB. The flame position, x_f, is given by the location of the $\mathrm{CH}^\star(x)$ maximum. This allows tracking the flame as a function of the operating conditions. The details of this post-processing can be found in Sec. 2.5.

For each operating point, the measured inlet temperature, T_{in} and the mixture composition defined by α_P and ϕ are used to compute the properties of the corresponding 1D adiabatic premixed flame: the laminar burning velocity, S_{L_0}, the adiabatic flame temperature, T_{ad}, the flame thickness, $\delta_T = (T_{ad} - T_{in})/\max(\partial T/\partial x)$, the inlet gas density, ρ_{in}, and the Zeldovich number, Ze. More specifically, the Zeldovich number is computed as, $\mathrm{Ze} = E(T_{ad} - T_{in})/RT_{ad}^2$, where R is the universal gas constant and E is the activation energy, calculated from:

$$E = -2R\partial[\ln(\rho_{in}S_L)]/\partial(1/T_{ad}) \tag{2.9}$$

The derivative in eq. (2.9) is computed from two one-dimensional flames by performing small variations in the N_2 molar fraction while keeping the equivalence ratio and inlet temperature constant. These calculations are performed using Cantera and the detailed kinetic scheme UCSD (57 species and 268 reactions) with mixture-averaged transport coefficients. Finally, temperatures are normalized as $\theta = (T - T_{in})/(T_{ad} - T_{in})$.

2.5. Images post-treatment

This section describes the procedure to extract the axial CH* profile and to compute the flame position from chemiluminescence images. Overall, the post-treatment method is very robust and requires only minor adjustments when the pore size is changed.

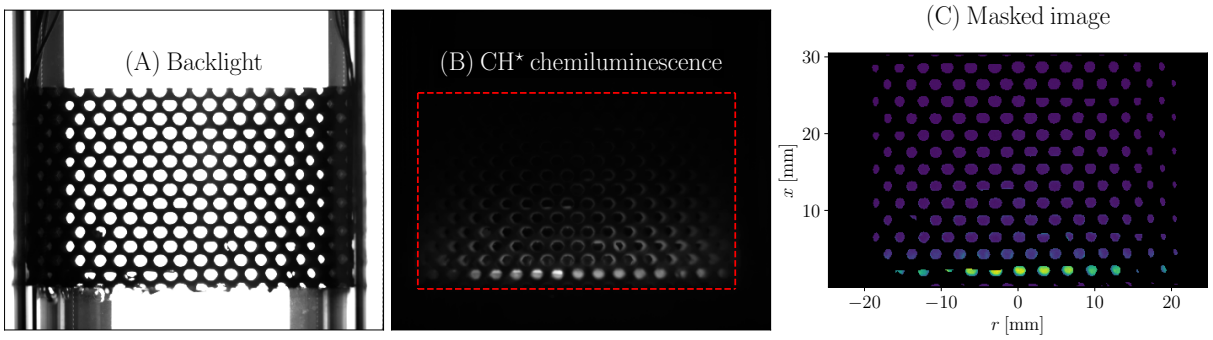

Figure 2.19. – (A) Backlight image. (B) CH* chemiluminescence signal. (C) Masked and cropped image.

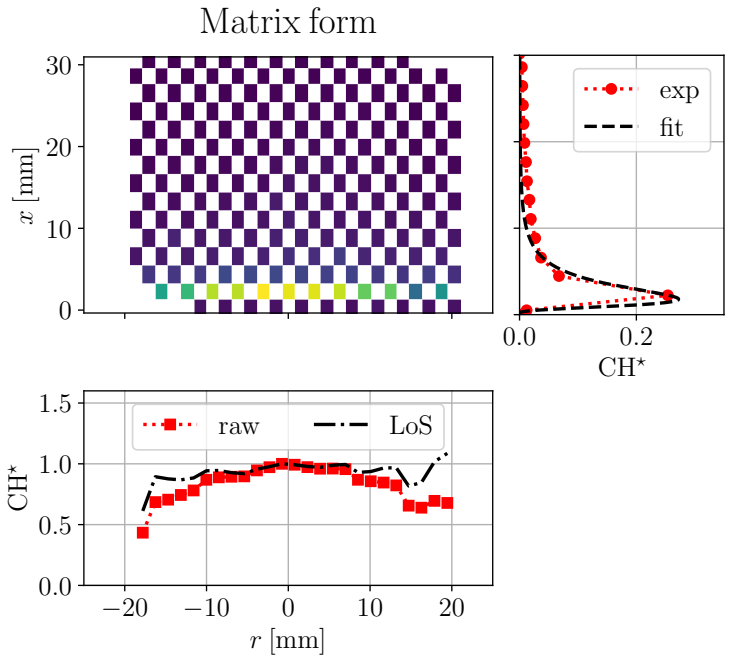

Figure 2.20. – Matrix form of the CH* chemiluminescence image that is used to compute the axial and radial profiles of CH* luminosity.

When projected onto the camera sensor, the optical pathways of the burner generate a two-dimensional array of spots. This is illustrated in Fig. 2.19a where a backlight image is shown. In Fig. 2.19a the loss of visualization surface caused by light refraction on the sides can be appreciated. The CH* emission by the flame is integrated along the optical pathways and collected by the sensor. Figure 2.19b shows a CH* chemiluminescence image where the row of bright spots indicates the overall position of the flame. To rule direct reflections out, the backlight image is binarized and used to mask the CH* chemiluminescence signal. The masked

image of Fig. 2.19c is transformed into a matrix representation where each element stores the surface-weighted average of the CH* intensity on each spot. By weighting the average by the surface, the influence of occasional artifacts in the images and the effect of radial deformation by refraction are removed. This matrix form is used to compute the radial and axial profiles of CH* and it is shown in Fig. 2.20. The axial CH* profile is computed as the transverse average of the elements of this matrix. This raw profile is plotted in Fig. 2.20 with red dotted lines and its resolution is given by the spacing between the pores. Since the CH* signal often spans over more than one row of optical pathways, the raw axial profile is fitted by a betaprime distribution to smooth the flame-front detection [175]. The fitted CH* profile is represented with black dashed lines in Fig. 2.20. The position of the flame front, x_f, is given by the location of the CH$^\star(x)$ maximum. The whole procedure to compute the flame position from images is schematized in Fig. 2.21.

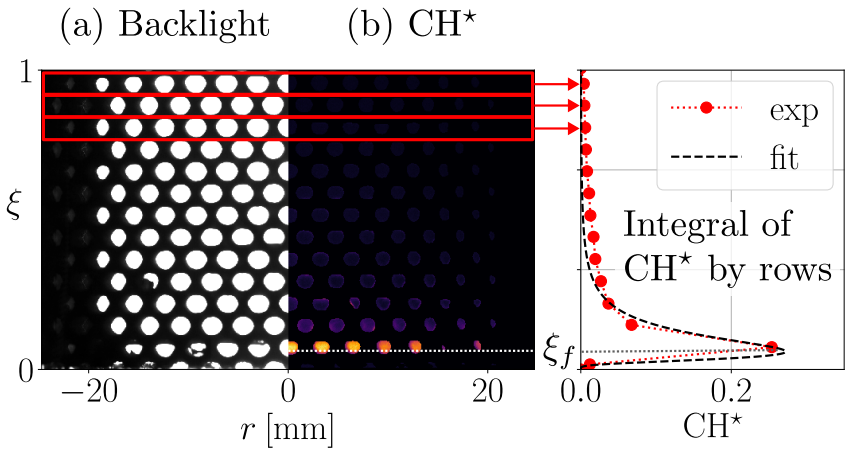

Figure 2.21. – Procedure to compute the axial profile of CH* and the flame position $\xi_f = x_f/L$.

The raw radial profile of CH* is plotted with red dotted lines and square markers in Fig. 2.20. In this radial profile, there is a reduction in the intensity of the CH* signal towards the edges of the burner. This lack of radial homogeneity is due to the line-of-sight integration of the CH* emission. The integration path is maximal at the central optical pathways and reduces towards the burner sides. The raw profile can be corrected by normalizing the radial distribution with the length of the integration path at each radial position. This correction is somewhat rudimentary because it assumes a transverse homogeneity of the signal. Nonetheless, the corrected radial profiles plotted with dash-dot black lines in Fig. 2.20 are rather uniform, indicating that the assumption holds. The radial homogeneity of the CH* profiles suggests that the comparison with a 1D model is reasonable.

2.6. Conclusions of the chapter

In this chapter, the experimental setup used during the most part of this thesis has been presented. The test rig, mixing system, diagnostics, experimental procedure and images processing have been extensively described and the experimental uncertainties have been characterized. In this work, computer-generated geometries are combined with additive manufacturing techniques to produce tailored PMBs. This methodology offers several advantages with respect to reticulated foams:

- Full control and accurate characterization of topological parameters
- New burner designs such as graded or swirled topologies that can be used to optimize the performance of the system.

However, this framework is here exploited in a novel manner to produce optically accessible burners. Optical access enables direct flame visualization and opens the door to apply laser diagnostics. The procedure to generate the burner geometry has been thoroughly described and a detailed analysis of the optical properties of the different topologies has been presented. The manufacturing process has been described and its influence on the thermo-mechanical properties of the porous matrices has been analyzed. Topology tailoring is a promising optimization tool for PMBs and future work must be devoted to the exploration of the multiple possibilities offered by this methodology.

2.A. Uncertainties analysis

2.A.1. Load and mixture composition

Symbol	a	R	p_{std}	T_{std}	W_{H_2}	W_{CH_4}	W_{O_2}	W_{N_2}	Q_{H_2}	Q_{CH_4}
Units	[-]	[J/kg/K]	[atm]	[K]	[kg/kmol]	[kg/kmol]	[kg/kmol]	[kg/kmol]	[MJ/kg]	[MJ/kg]
Value	3.76	8.314	1	273	2	16	32	28	121	50

Table 2.2. – Numerical constants

Set	Gas	Model	Pressure drop ΔP [bar]	Flow range $\dot{m}_k$ [nL/min]	Error $\delta\dot{m}_k$ [nL/min]
LP	Air	Bronkhorst ELFLOW BASE	2	45	± 0.450
	H_2			5	± 0.050
	CH_4			3.5	± 0.035
HP	Air	Voegtlin Red-y smart		130	$\pm(0.39 + 0.5\%\dot{m}_{Air})$
	H_2			20	$\pm(0.06 + 0.5\%\dot{m}_{H_2})$
	CH_4	Bronkhorst ELFLOW SELECT		19.05	$\pm(0.019 + 0.5\%\dot{m}_{CH_4})$

Table 2.3. – MFC specifications

This section presents the analysis of errors in P, ϕ and α_P from the uncertainties in the MFC mass flow rates. The power load is computed as:

$$P = \dot{m}_{H_2} Q_{H_2} + \dot{m}_{CH_4} Q_{CH_4} \tag{2.10}$$

where, Q_f is the Lower Heating Value (LHV) of fuel f and $\dot{m}_f$ is the fuel mass flow rate. Neglecting the uncertainties in the fuels LHVs, the error in P, denoted by δP, as a function of the uncertainty in the mass flow rate measurements $\delta\dot{m}_f$ is:

$$\delta P = \sqrt{\left(\frac{\partial P}{\partial \dot{m}_{H_2}}\Big|_{\dot{m}_{CH_4}} \delta\dot{m}_{H_2}\right)^2 + \left(\frac{\partial P}{\partial \dot{m}_{CH_4}}\Big|_{\dot{m}_{H_2}} \delta\dot{m}_{CH_4}\right)^2} \tag{2.11}$$

leading to:

$$\delta P = \sqrt{(Q_{H_2}\delta\dot{m}_{H_2})^2 + (Q_{H_2}\delta\dot{m}_{CH_4})^2} \tag{2.12}$$

The hydrogen power fraction α_P represents the fraction of power generated by hydrogen combustion and is defined as:

$$\alpha_P = \frac{\dot{m}_{H_2} Q_{H_2}}{\dot{m}_{H_2} Q_{H_2} + \dot{m}_{CH_4} Q_{CH_4}} = \frac{\dot{m}_{H_2} Q_{H_2}}{P} \tag{2.13}$$

In the same fashion, the uncertainties in the hydrogen power fraction can be expressed as a function of the hydrogen and methane mass flow rates and their associated uncertainties:

$$\delta\alpha_P = \sqrt{\left(\frac{\partial \alpha_P}{\partial \dot{m}_{H_2}}\Big|_{\dot{m}_{CH_4}} \delta\dot{m}_{H_2}\right)^2 + \left(\frac{\partial \alpha_P}{\partial \dot{m}_{CH_4}}\Big|_{\dot{m}_{H_2}} \delta\dot{m}_{CH_4}\right)^2} \tag{2.14}$$

where:

$$\frac{\partial \alpha_P}{\partial \dot{m}_{H_2}}\Big|_{\dot{m}_{CH_4}} = \frac{\dot{m}_{CH_4} Q_{CH_4} Q_{H_2}}{P^2} \qquad \frac{\partial \alpha_P}{\partial \dot{m}_{CH_4}}\Big|_{\dot{m}_{H_2}} = \frac{-\dot{m}_{H_2} Q_{CH_4} Q_{H_2}}{P^2} \tag{2.15}$$

The global equivalence ratio of the mixture is given by:

$$\phi = \frac{\frac{O}{F}\Big)_{st}}{\frac{O}{F}} = \frac{\chi_{CH_4} - \frac{\alpha}{2}(2\chi_{CH_4} - 1)}{\frac{\dot{n}_{O_2}}{\dot{n}_{CH_4} + \dot{n}_{H_2}}} \tag{2.16}$$

where $\chi_{CH_4} = 2$ is the stoichiometric ratio of methane, α is the hydrogen molar fraction in the fuel defined as:

$$\alpha = \frac{\dot{n}_{H_2}}{\dot{n}_{H_2} + \dot{n}_{CH_4}} \tag{2.17}$$

and $\dot{n}_k$ is the molar flow of species k. Molar flows $\dot{n}_k$ can be computed as:

$$\dot{n}_{H_2} = \dot{m}_{H_2}/W_{H_2}, \qquad \dot{n}_{CH_4} = \dot{m}_{CH_4}/W_{CH_4}, \qquad \dot{n}_{O_2} = \frac{\dot{m}_{Air}}{W_{O_2} + aW_{N_2}} \tag{2.18}$$

where W_k is the molar mass of species k and $a = 3.76$ is the molar ratio of nitrogen to oxygen in air. Introducing eq. (2.17) and eq. (2.18) into eq. (2.16), one can express the equivalence ratio ϕ as a function of the mass flow rates of air, methane and hydrogen, $\phi(\dot{m}_k)$. Neglecting the errors in the constants values, the uncertainty in the equivalence ratio can be computed as:

$$\delta\phi = \sqrt{\sum_k \left(\frac{\partial \phi}{\partial \dot{m}_k}\Big|_{\dot{m}_{j\neq k}} \delta\dot{m}_k \right)^2} \tag{2.19}$$

where the partial derivatives of ϕ are given by:

$$\frac{\partial \phi}{\partial \dot{m}_{Air}}\Big|_{\dot{m}_{H_2},\, \dot{m}_{CH_4}} = -\frac{\left(W_{CH_4}\dot{m}_{H_2} + 4W_{H_2}\dot{m}_{CH_4}\right)\left(W_{N_2}a + W_{O_2}\right)}{2W_{CH_4}W_{H_2}\dot{m}_{Air}^2} \tag{2.20}$$

$$\frac{\partial \phi}{\partial \dot{m}_{H_2}}\Big|_{\dot{m}_{Air},\, \dot{m}_{CH_4}} = \frac{W_{N_2}a + W_{O_2}}{2W_{H_2}\dot{m}_{Air}} \tag{2.21}$$

$$\frac{\partial \phi}{\partial \dot{m}_{CH_4}}\Big|_{\dot{m}_{Air},\, \dot{m}_{H_2}} = \frac{2\left(W_{N_2}a + W_{O_2}\right)}{W_{CH_4}\dot{m}_{Air}} \tag{2.22}$$

For any given combination of $(\dot{m}_k, \delta\dot{m}_k)$ the above-presented formulas provide the uncertainty in the power, hydrogen power fraction and equivalence ratio. The values of the constants used throughout this thesis are gathered in Tab. 2.2. The specifications of the different MFCs, including their measurement error, $\delta\dot{m}_k$, are reported in Tab. 2.3.

2.A.2. Inlet temperature

When a thermocouple is used to measure the temperature of a stream in an environment with hot solid walls, it is submitted to a significant radiation heat flux. In these conditions, its temperature reading, T_b drifts away from the flow temperature, T_g. As proposed in [174], if the equivalent temperature of the surrounding environment is denoted by T_∞, the equation for the thermal equilibrium of the thermocouple bead reads:

$$h(T_g - T_b) = \epsilon_b \sigma_B (T_b^4 - T_\infty^4) \tag{2.23}$$

where h is the heat exchange coefficient, ϵ_b is the thermocouple bead emissivity and σ_B is the Stephan-Boltzmann constant. The heat exchange coefficient is expressed as $h = \lambda_g \mathrm{Nu}/D_b$ where D_b is the diameter of the thermocouple's bead, λ_g is the gas thermal conductivity and Nu is a Nusselt number. The latter is a function of the Reynolds and the Prandtl number and its generic expression is:

$$\mathrm{Nu} = cRe^m Pr^{1/3} \tag{2.24}$$

where c and m depend on the geometry and on the flow regime. Manipulating eq. (2.23) we can express the difference of temperature between the flow and the thermocouple's bead as:

$$\Delta T_{b-g} = \frac{\epsilon_b \sigma_B}{\lambda_g c Pr^{1/3}} \left(\frac{\nu}{u_g}\right)^m D_b^{1-m} (T_b^4 - T_\infty^4) \tag{2.25}$$

The exponent m depends on the range of Reynolds numbers but is always smaller than the unity. Hence, for an imposed environment temperature T_∞, the smaller the diameter of the thermocouple bead is, the closer to the actual flow temperature its reading is. Thus, in the presence of strong radiation fluxes, it is convenient to use thermocouples with small bead sizes.

In principle, eq. (2.25) could be applied to correct the thermocouple measurement in a hot environment. However, the equivalent surrounding temperature T_∞ is hard to estimate in a complex configuration. This problem can be circumvented by using two thermocouple probes with different bead sizes. The two probes must be placed side by side and as close as possible so that they are exposed to approximately the same local flow temperature and radiation flux. If the temperature readings of two thermocouple probes with diameters D_{b_1} and D_{b_2} are denoted by T_{b_1} and T_{b_2}, respectively, one can write:

$$T_g = \frac{h_2 T_{b_2} - h_1 T_{b_1}}{h_2 - h_1} + \frac{\epsilon_b \sigma_B}{h_2 - h_1} (T_{b_2}^4 - T_{b_1}^4) \tag{2.26}$$

Notice that, since the kinematic viscosity, the thermal conductivity and the flow velocity vary with the temperature, the problem must be solved iteratively.

In this work, the measurement of the gas temperature is used to estimate the inlet temperature of the reactants, T_{in}. Therefore, T_g is replaced by T_{in} from now on. The Reynolds number can be directly computed from the total mass flow rate as:

$$Re_{D_b} = \frac{\dot{m} D_b}{A\mu} \tag{2.27}$$

The uncertainty in the inlet temperature correction from eq. (2.26) can be estimated using:

$$\delta T_{in} = \sqrt{\left(\frac{\partial T_{in}}{\partial \dot{m}} \delta \dot{m}\right)^2 + \left(\frac{\partial T_{in}}{\partial T_{b1}} \delta T_{b_1}\right)^2 + \left(\frac{\partial T_{in}}{\partial T_{b2}} \delta T_{b_2}\right)^2 + \left(\frac{\partial T_{in}}{\partial \epsilon_b} \delta \epsilon_b\right)^2} \tag{2.28}$$

In the error propagation we have only retained the contributions of the mass flow rate, the thermocouples measurements and the uncertainty in the bead emissivity ϵ_b. In eq. (2.28), the partial derivatives are given by:

δT_b [K]	ϵ_b [-]	$\delta\epsilon_b$ [-]	c [-]	m [-]	D_{b_1} [mm]	D_{b_2} [mm]
2.5	0.15	0.1	0.683	0.466	0.5	1

Table 2.4. – Numerical parameters for the calculation of δT_{in}. Constants c and m are taken from [176].

$$\frac{\partial T_{in}}{\partial \dot{m}} = \frac{D_{b_1} D_{b_2} \epsilon_b \sigma_B m \left(-T_{b_1}^4 + T_{b_2}^4\right)}{Pr^{1/3} \dot{m} c \lambda_g \left(-D_{b_1} \left(\frac{D_{b_2}\dot{m}}{A\mu}\right)^m + D_{b_2} \left(\frac{D_{b_1}\dot{m}}{A\mu}\right)^m\right)} \tag{2.29}$$

$$\frac{\partial T_{in}}{\partial T_{b1}} = \frac{D_{b_2} \cdot \left(4 D_{b_1} T_{b_1}^3 \epsilon_b \sigma_B + Pr^{1/3} c \lambda_g \left(\frac{D_{b_1}\dot{m}}{A\mu}\right)^m\right)}{Pr^{1/3} c \lambda_g \left(-D_{b_1} \left(\frac{D_{b_2}\dot{m}}{A\mu}\right)^m + D_{b_2} \left(\frac{D_{b_1}\dot{m}}{A\mu}\right)^m\right)} \tag{2.30}$$

$$\frac{\partial T_{in}}{\partial T_{b2}} = \frac{D_{b_1} \cdot \left(4 D_{b_2} T_{b_2}^3 \epsilon_b \sigma_B + Pr^{1/3} c \lambda_g \left(\frac{D_{b_2}\dot{m}}{A\mu}\right)^m\right)}{Pr^{1/3} c \lambda_g \left(D_{b_1} \left(\frac{D_{b_2}\dot{m}}{A\mu}\right)^m - D_{b_2} \left(\frac{D_{b_1}\dot{m}}{A\mu}\right)^m\right)} \tag{2.31}$$

$$\frac{\partial T_{in}}{\partial \epsilon_b} = \frac{D_{b_1} D_{b_2} \sigma_B \left(T_{b_1}^4 - T_{b_2}^4\right)}{Pr^{1/3} c \lambda_g \left(-D_{b_1} \left(\frac{D_{b_2}\dot{m}}{A\mu}\right)^m + D_{b_2} \left(\frac{D_{b_1}\dot{m}}{A\mu}\right)^m\right)} \tag{2.32}$$

For the same dataset as for Sec. 2.1.3, we have computed the temperature correction as the difference between T_{in}, estimated with eq. (2.26), and the temperature measured by the thermocouple with a smaller bead diameter, T_{b_1}. In this calculation, the numerical parameters gathered in Tab. 2.4 were employed and Sutherland law was used to compute the dynamic viscosity. Similarly, the uncertainty in the inlet temperature of, δT_{in}, has been computed using eq. (2.28) for this experimental database. Results are represented in Fig. 2.22 as under the form of a PDF.

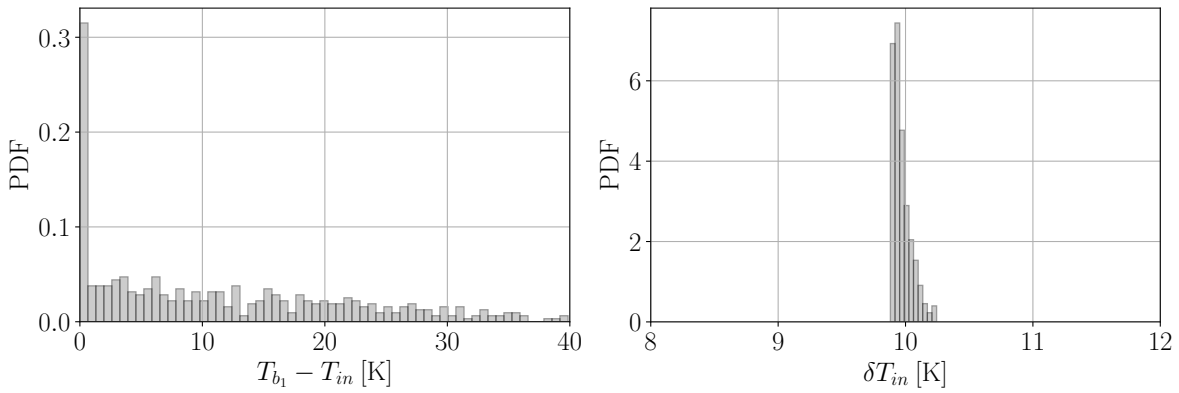

Figure 2.22. – PDF of the temperature correction $T_{b_1} - T_{in}$ (left). PDF of the inlet temperature error δT_{in} (right).

Figure 2.22 indicates that, in most cases, the temperature reading of the smallest thermocouple can be directly used as the inlet temperature value. However, for a few operating points, the temperature differences can be significant and hence it is convenient to apply the correction of eq. (2.26). Regarding the uncertainty in the estimation of the inlet temperature, δT_{in}, it is observed that the error is almost uniform and equal to 10 K. Hence, a reference uncertainty of $\delta T_{in} \simeq \pm 10$ K is retained for the inlet temperature measurements. The most significant

contribution to the inlet temperature error is due to the uncertainty in the thermocouples' measurements, δT_b. The correction of eq. (2.28) is almost insensitive to the emissivity when applied to our database. Therefore, errors in the emissivity value have a negligible impact on the temperature correction.

Chapter 3

Volume Averaged Model

In this chapter, a literature review of the different modeling approaches in Porous Media Combustion (PMC) is presented. In Sec. 3.1, various recent theoretical and numerical works are reviewed and the main current challenges in PMC modeling are highlighted.
Section 3.2 presents the 1D Volume Averaged Model (VAM) developed during this thesis. The model equations are detailed and the submodels for interphase heat exchange, dispersion and radiation are described. VAM results, and hence their agreement with experiments, are very sensitive to the effective parameters and submodels.
In an effort to increase the confidence on the numerical results, several correlations for the interphase heat exchange term from the literature have been collected and compared. The strong dependence of VAM results to this term and the large dispersion observed among the different correlations motivate the sensitivity analysis of this submodel in Chapter 4.
In the same vein, a rigorous evaluation of the model constants is presented here. In computer-defined topologies, an accurate characterization of the topology-dependent parameters can be performed using the CAD of the porous matrix geometry.

Overview

3.1. Modeling approaches in Porous Media Combustion 52
3.1.1. Theoretical models 52
3.1.2. Direct Pore Level Simulations 53
3.1.3. Volume averaged models 55
3.2. Volume Averaged Model 56
3.2.1. Conservation equations 56
3.2.2. Effective diffusive fluxes 57
3.2.3. Interphase heat exchange 57
3.2.4. Heat losses 61
3.2.5. Boundary conditions 61
3.3. Evaluation of model constants 62
3.3.1. Topological parameters 62
3.3.2. Material-dependent parameters 63
3.4. Conclusions of the chapter 65

"*PhD students are like ideal gases, they expand when you release the pressure.*"

Laurent Selle

3.1. Modeling approaches in Porous Media Combustion

The modeling of porous media burners is very complex due to the wide variety of physical phenomena at play. Some of them such as chemical kinetics and heat transfer are very sensitive to small temperature variations. In these burners, the pore-size, d_p is comparable to the flame thickness δ_T, so flame-wall interactions have a direct influence on the stabilization of the flame. Most models share a series of common assumptions: perfectly premixed reactants, transparent gas phase, and negligible pressure drop through the porous matrix. When isobaric combustion is assumed, the momentum equation is not explicitly solved. This is a good hypothesis for small Reynolds numbers, which is the case of the majority of studies. Typically, the solid energy equation is written separately from the gas energy equation and both are coupled via an interphase heat exchange term. This modeling approach is termed as two equations model. When the heat exchange between the phases tends to infinite they are in thermal equilibrium and a one-equation model can be used to describe the thermal state of the system. In PMC, chemistry modeling is a major concern. In some applications, heat recirculation is exploited to operate at very low equivalence ratios in order to reduce pollutant emissions. In ultra-lean conditions, the burner temperature is relatively low. In PMBs, the thermal stabilization of the flame is driven by the sensitivity to preheating. Thus, the kinetic scheme must be able to capture the influence of temperature on the species kinetics over a wide range of operating temperatures. Overall, the existing modeling strategies can be classified into theoretical, Direct Pore-Level Simulations (DPLS) and Volume Averaged Models (VAMs).

3.1.1. Theoretical models

The theoretical foundations of porous burners were established after the seminal works of [83, 111, 177, 178]. In [83], Takeno and Sato presented a theoretical model for an excess enthalpy flame within a semi-infinite highly-conductive solid matrix. This model was derived in the limit $\lambda_s \gg \lambda_g$ so that the temperature of the solid phase is uniform and equal to T_{ad}. In [179], Deshaies and Joulin solved the semi-infinite problem in the limit of large activation energy. This work showed that there is a direct relationship between the mass flow rate $\dot{m}$ and the position of the flame ξ_f in the porous medium. The model of Takeno and Sato [178] was extended to account for finite-length solid matrices in [178]. This study revealed the existence of a critical mass flow rate, $\dot{m}_c$, that defines the blowoff limit of the burner. For $\dot{m} < \dot{m}_c$, two solutions with different solid matrix temperatures exist. In [111], it was shown that the two branches of the stabilization curve have different stability properties. Notably, the upstream branch is stable since perturbations in the flame position are counterbalanced by variations in the burning rate. In contrast, in the downstream branch, these perturbations tend to be amplified by changes in the flame speed. These first works bring to light some of the distinctive properties of heat recirculating burners: multiplicity of solutions, super-adiabatic temperatures and enhanced burning rates.

For flames stabilized inside infinite porous media, the works of Pereira et al. [60–62] present a thorough characterization of the problem in different asymptotic limits. First, it is shown that the presence of the solid matrix leads to an additional characteristic lengthscale in the problem: the solid-phase diffusion distance, l_s, where there is a thermal non-equilibrium between the gas and the solid. This lengthscale adds to those of freely propagating flames, namely, the

fluid-phase diffusion distance associated to the flame thermal thickness, l_g, and the chemical reaction region, l_r, directly linked to the Zeldovich number. In [60], Pereira et al. develop an asymptotic model for a stationary flame stabilized in an adiabatic infinite porous media in the limit of scale separation $l_r \ll l_g \ll l_s$. In the model of Pereira et al., the flame speed enhancement and the maximum superadiabatic temperature are found to decrease with the equivalence ratio. However, the hypotheses made in its derivation restrict the application of this model to moderately lean flames only. In a later work, Pereira et al. [61] used asymptotic expansion to derive a theoretical model in the case of intense interphase heat transfer, a situation that is obtained at very lean mixtures and small pore sizes. Under these conditions, the fluid and solid phase are in thermal equilibrium at the solid-diffusion lengthscale. Therefore, a one-equation model for the energy conservation equation suffices to describe the thermal state of the system in this region. This analysis reveals the existence of a lean flammability limit for premixed combustion in inert porous media. In this framework, the flame velocity and the maximum superadiabatic temperature are found to increase with the equivalence ratio. Finally, an analytical model for intermediate values of the interphase heat transfer parameter is developed by Pereira et al in [62]. This study unifies under a common framework the previous theories derived for two opposite asymptotic limits [60, 61]. Their results reveal the existence of a critical equivalence ratio that maximizes the nondimensional superadiabatic temperature showing that there is an upper limit for superadiabaticity.

More recently Masset et al. [63] carried out a theoretical analysis of the combustion of $\mathrm{Le} = 1$ fuels in inert porous media. They showed that the infinite problem boils down to two dimensionless parameters that define the combustion regime: the reduced mass flow, $r_{\dot{m}}$, and the ratio of conductivities, r_λ. Depending on these two governing parameters, three different combustion regimes can be identified: decoupled, hyperdiffusive and intermediate. In [63], the analytical problem in the decoupled regime is solved for both infinite and finite porous media. In the hyperdiffusive regime, the speed-up is found to be independent of $r_{\dot{m}}$ and to converge towards $(1 + r_\lambda^{-1})^{1/2}$. The theoretical model derived for the decoupled regime is found to capture the trends of a 1D-VAM with variable transport coefficients and detailed kinetics for a wide range of $r_{\dot{m}}$ and r_λ values. Finally, in [180], Kurdyumov et al. presented an asymptotic analysis for the combustion of premixed flames in inert porous media with uniform solid temperature. This study focuses on the multiplicity of steady-state solutions and their stability, which is analyzed using time-dependent simulations.

Theoretical models are key to understanding the underlying physical mechanisms at play and provide insight into the stability of solutions, the characteristic lengthscales, the combustion regimes and the governing parameters. From theory, it is known that in homogeneous PMBs there is a relationship between the burning rate and the flame position inside the porous matrix. One of the contributions of this thesis is to exploit this distinctive property of heat recirculating burners for model validation. However, theoretical and asymptotic models usually require strong assumptions such as constant transport coefficients and adiabaticity. As a result, they usually do not provide quantitative results.

3.1.2. Direct Pore Level Simulations

On the other side of the spectrum there are Direct-Pore-Level Simulations (DPLS) where the reactive Navier-Stokes equations are numerically solved at the pore scale [67–70, 100, 181, 182]. This framework resolves all flow scales and can in principle incorporate skeletal kinetics, heat diffusion in the solid, conjugate heat transfer and radiation. Over time, thanks to the increase in computational resources, the level of detail in DPLS and the size of the simulated systems have largely increased. For example, recent advances in tomographic scanning techniques have enabled detailed 3D reconstructions of actual ceramic foams used in PMC experiments. Thanks

to X-ray tomography, the geometrical details of the porous medium are accounted for and a more realistic description of the interstitial flow is achieved [67–69, 182].

Sahraoui and Kaviani [70] carried out 2D-DPLS of premixed methane-air flames stabilized inside different porous media geometries including in-line/staggered arrangements with discrete and/or connected square rods. They compared the results of the numerical simulations with a two-equation volume averaged model. Sahraoui and Kaviani found that the connectivity of the solid matrix and the configuration (inline vs staggered) have a strong impact on the flame speed enhancement. Connected solid elements in staggered configuration lead to larger flame speeds. Reductions in the pore size and the equivalence ratio are also shown to have a positive impact on the burning rate. The comparison with the volume averaged solver indicates that the two-equation model overpredicts the increase in the flame speed by as much as 20%. This work reveals that pore-level details have a strong impact on the performance of the burner at the macroscopic scale, questioning the accuracy of the averaged equations.

Hackert et al. [100] performed 2D pore-resolved simulations for methane-air flames stabilized inside two simplified porous geometries: a honeycomb structure consisting of multiple parallel plates and an array of non-connected cross-flow plates. Their model incorporates solid-to-solid radiative heat transfer and a Monte Carlo method is used to compute the view factors between the solid elements. Their results show good agreement with experiments of Min and Shin [65] in terms of gas/solid temperature profiles, burning rates and radiant output. Hackert et al. observed that flames are highly two-dimensional at the pore scale highlighting the limitations of the 1D volume averaged modeling framework. Their results also hint towards strong geometrical dependence of the interphase heat exchange coefficient, h_V.

Ferguson et al. [181] presented 2D-DPLS with conjugate heat transfer between the solid and the gaseous phase. In this work, the solid phase is modeled by a network of isothermal cylinders connected via conductive but fully-permeable elements. On the fluid phase, fully compressible reactive Navier-Stokes equations with detailed chemistry are solved. Their results reveal the existence of stationary solutions for a range of flow rates in single-layered burners.

In [68], reactive 3D-DPLS in sponge-like porous structures are compared to experiments and a 1D-VAM for different burner geometries. This is one of the first works performing DPLS in a realistic 3D geometry obtained via X-ray tomographic reconstruction of a SiSiC ceramic foam. The authors observed that the 1D VAM underpredicts the flame thickness and the burning velocity. As explained by Bedoya et al. [68], in the 1D model the source terms are computed using the average gas temperature $\dot{\omega}(\langle T_g \rangle)$. However, in the DPLS there are important transverse variations of temperature. When the source term from the DPLS is averaged, $\langle \dot{\omega}(T_g) \rangle$, large discrepancies are observed between $\langle \dot{\omega}(T_g) \rangle$ and $\dot{\omega}(\langle T_g \rangle)$. This is due to the local variations of temperature at the pore level and the non-linear dependence of the Arrhenius equation with temperature. Based on the DPLS results, the authors propose a combustion model where a statistical description of the source terms is made. The combustion model incorporates the temperature probability density function and an expression to estimate the temperature fluctuations from the mean profiles is provided for model closure.

More recently, Masset et al. [67] performed 3D DPLS with conjugate heat transfer and detailed chemistry in various random and lattice-based porous structures. In this work, similar stabilization properties are observed between reticulated and lattice-based geometries. These detailed simulations are compared to a 1D-VAM whose effective coefficients are estimated from DPLS as in [68]. Strong discrepancies are observed in terms of burning rates and spatially-averaged profiles. Thin wrinkled flame fronts spanning across several pores are observed in direct contradiction to the upscaling hypotheses of volume averaging. Following the analysis of Bedoya et al. [68], the authors show that 1D models implicitly assume the commutation of averaging operators with nonlinear terms. A correction for the reaction rates based on the DPLS results is proposed. This correction includes a flame surface Γ_w and a dispersion diffusion Γ_d factor to

account for the wrinkling of the flame front and to override the influence of dispersion effects on the local burning rate.

3.1.3. Volume averaged models

Despite their accuracy, the large computational cost of DPLS makes them impractical for engineering applications and burner optimization. More affordable simulations are sought and the so-called Volume Averaged Models (VAMs) offer a relevant alternative between theoretical models and DPLS [45, 68, 101, 112, 113, 117, 122, 183, 184]. In VAMs, equations are averaged over a Representative Elementary Volume (REV) with a characteristic lengthscale l, which must satisfy two conditions:

$$d_p \ll l \ll L \qquad \text{and} \qquad \Delta_l \psi \ll \Delta_L \psi \tag{3.1}$$

where d_p is the characteristic pore size, L is the system lengthscale of the system and ψ is a generic variable. These models are generally one-dimensional, yet some remarkable attempts of developing multi-dimensional VAMs can be found [122]. So far, adiabaticity was a common assumption but the latest models include a sink term in the solid phase equation to incorporate radial heat losses by radiation [58, 59]. Upon the averaging process of the equations, effective properties and transport coefficient arise [76]. These effective coefficients are incorporated to model certain physical phenomena such as dispersion that take place at the pore level scale and whose multidimensional and geometry-dependent nature is partially lost in the averaging process. Provided the sensitivity of the model to some of these effective coefficients, part of the modeling efforts is exclusively devoted to come up with accurate and representative submodels for some of these physical phenomena [59, 67, 68, 185–187]. The estimation of the dispersion distance, the radiation extinction coefficient, the tortuosity and the interphase heat exchange coefficient from DPLS is nowadays a state-of-the-art procedure.

Model accuracy is not the only concern, as pointed out by many authors [67, 68, 70, 100], DPLS results question the relevance of VAMs assumptions. In these works, it is observed that because of the small thickness, δ_T, of hydrocarbon flames, eq. (3.1) does not strictly hold. Recently, Bedoya et al. and Masset et al. [67, 68] have proposed different corrections for the source terms to account for flame wrinkling and local temperature gradients at the pore scale. Regarding experimental validation, temperature measurements are generally compared to VAM results in two-staged burner configurations where the flame stabilizes at the interface between two porous layers. However, in this burner configuration, the position of the flame is nearly fixed. For an imposed flame position, it is relatively easy to obtain a good agreement between the temperature fields. It suffices to reasonably estimate the heat transport coefficients and the global heat losses of the system. Therefore, this validation methodology may bias the comparison with the model.

One of the objectives of the present work is to test the ability of current VAMs to predict the position of the flame and the blowoff limit in a single-layer PMB. In contrast to the step-burner design, this burner configuration does not impose the position of the flame. Therefore, there is a two-way coupling between the location of the reaction region and the burning rate. Consequently, predicting the position of the flame as a function of the mass flow rate is arguably more difficult than capturing the temperature field for an imposed flame position. To establish this comparison it is necessary to localize the position of the reaction region inside the burner. This is now possible thanks to the novel experimental setup combining optically accessible PMBs and $CH^\star$ chemiluminescence imaging presented in Chapter 2. The experimental results will be confronted to the 1D VAM presented in Sec. 3.2. Despite the detailed description of the model made in Sec. 3.2, the purpose of this work is not to make a contribution to VAM modeling. The model presented here is state-of-the-art and the reason for such a careful evaluation of the various parameters is to show that this is not the cause for the deviation from the experimental results.

3.2. Volume Averaged Model

3.2.1. Conservation equations

The open source code CANTERA [188] has been modified to be coupled with the VAM equations for the solid phase. The expressions for the diffusive fluxes have been modified to incorporate the effective transport coefficients and supplementary terms have been added to the original equations in one-dimensional form. For the sake of readability, averaging operands have been dropped from the notation. A rigorous derivation of the VAM equations can be found in [76]. The 1D volume-averaged equations for species and energy conservation in the gaseous and solid phases read [68, 112, 185]:

$$\epsilon\,\rho_g\,\partial_t Y_k + \epsilon\rho_g u_g \partial_x Y_k + \partial_x\left(\epsilon J_k^{\text{eff}}\right) = \epsilon\dot{\omega}_k \tag{3.2}$$

$$\epsilon\,\rho_g c_{p_g}\partial_t T_g + \epsilon\rho_g c_{p_g} u_g \partial_x T_g + \epsilon\left[\sum_k c_{p_g,k} J_k^{\text{eff}}\right]\partial_x T_g + \partial_x\left[\epsilon\mathcal{T}_g^{\text{eff}}\right] - h_V\left(T_s - T_g\right) = \epsilon\dot{\omega}_T \tag{3.3}$$

$$\partial_t\left[(1-\epsilon)\rho_s c_{p_s} T_s\right] + \partial_x\mathcal{T}_s^{\text{eff}} - h_V\left(T_g - T_s\right) = -\dot{q}_{\text{loss}} \tag{3.4}$$

where Y_k are the species mass fractions and T_g and T_s the gas and solid temperatures, respectively. In eqs. (3.2)-(3.4), ϵ denotes the local porosity, ρ_g the gas density, c_{p_g} the mixture-averaged specific heat, $c_{p_g,k}$ the $k^{th}-$species heat capacity and u_g the gas velocity. In the solid phase equation, eq. (3.4), ρ_s and c_{p_s} denote the solid density and heat capacity, respectively. The terms $\dot{\omega}_T$ and $\dot{\omega}_k$ represent the heat release rate and the mass production rate of species k per unit volume respectively. The detailed kinetic scheme GRIMECH 3.0 [189] with mixture-averaged transport coefficients is used to model the chemistry of methane/hydrogen-air flames. The computational domain extends from the burner inlet at $x = 0$ to its outlet at $x = L$. Unsteady terms are written here for the sake of completeness but are only used in Cantera for transient computation of steady states. In other words, the solid thermal capacity and density can influence convergence of the solver but do not affect the solution. Automatic and recursive grid refinement is employed to find a stationary solution for the above-presented equations. Figure 3.1 represents the 1D-numerical setup. A generic solution with a flame stabilized at ξ_f is shown. Note that the position of the flame corresponds to the location of the heat release rate peak. The solid and gas temperatures are depicted with dotted and solid lines, respectively.

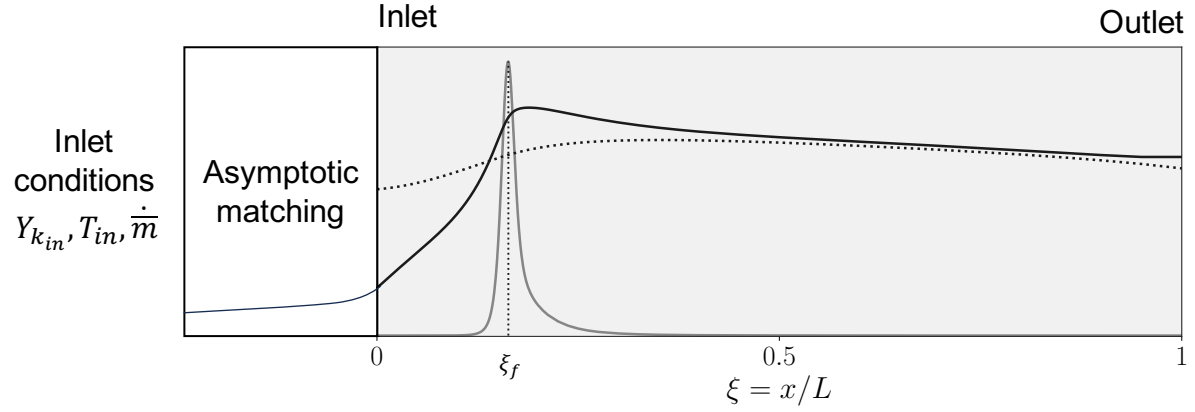

Figure 3.1. – Numerical setup

3.2.2. Effective diffusive fluxes

In the gas phase, the effective diffusive fluxes for mass and heat are written as:

$$J_k^{\text{eff}} = -\rho_g \frac{W_k}{W}(D_k/\tau_g + D^{\text{dis}})\partial_x X_k \tag{3.5}$$

$$\mathcal{T}_g^{\text{eff}} = -\lambda_g^{\text{eff}}\partial_x T_g = -\left[\lambda_g/\tau_g + \rho_g c_{p_g} D^{\text{dis}}\right]\partial_x T_g \tag{3.6}$$

In eq. (3.5) and eq. (3.6), W_k and X_k stand for the species molar mass and molar fraction, D_k is the mixture-averaged diffusion coefficient of species k and W is the mean molar mass of the mixture. In a quiescent fluid inside a porous media, the presence of obstacles increases the effective path-length for diffusion. This phenomenon is known as tortuosity and reduces the effective diffusion at the macroscopic scale. To incorporate this effect, the mass diffusion coefficient of species k, D_k, and the thermal conductivity, λ_g are weighted by a tortuosity coefficient, τ_g.

Dispersion effects refer to the rise in the macroscopic diffusivity of species and heat owing to the meandering nature of the interstitial flow. In the intricate flow within the porous matrix cavities, a series of phenomena such as velocity gradients, flow tortuosity and recirculation zones increase the effective diffusivity at a macroscopic scale. In VAMs, these effects are typically bundled in a dispersion diffusion coefficient D^{dis} which adds to the intrinsic diffusivity for mass/temperature of the gaseous phase. Dispersion effects have been shown to scale with the mean velocity in the cavities, u_g, and the pore size, d_p [190]. Usually, the scaling law $D^{\text{dis}} \sim d_p u_g/2$ is assumed as a formal expression for the dispersion coefficient. Nonetheless, some studies [67, 68] have refined this dispersion model by substituting the pore size d_p by a dispersion distance l_{dis} which is fitted from cold flow DPLS. This approach allows incorporating the topological details of the porous matrix in the dispersion model. Here, for the sake of simplicity the dispersion coefficient is written as:

$$D^{\text{dis}} = \frac{u_g d_p}{2} \tag{3.7}$$

Entrance effects upon dispersion coefficient are modeled via a relaxation distance of two pore sizes where dispersion diffusivity increases from zero to its nominal value [191]. In the solid phase, the effective temperature flux reads:

$$\mathcal{T}_s^{\text{eff}} = -\lambda_s^{\text{eff}}\partial_x T_s = -\left[(1-\epsilon)\lambda_s/\tau_s\partial_x T_s + \lambda_s^{\text{rad}}\right]\partial_x T_s \tag{3.8}$$

where effective thermal conductivity in the solid includes a tortuosity coefficient and a radiation term. If the porous medium is assumed to be optically thick, solid-to-solid radiation can be modeled using the Rosseland approximation [68, 117, 185]:

$$\lambda_s^{\text{rad}} = 16\,\sigma_B\,T_s^3/(3\,\beta) \tag{3.9}$$

where σ_B is the Stephan-Boltzmann constant and $\beta = 3(1-\epsilon)/d_p$ is the effective radiative extinction coefficient [192].

3.2.3. Interphase heat exchange

The interphase heat exchange between the gas and the solid is modeled via a volumetric interphase heat coefficient which represents the power transferred between the two phases per unit volume and unit temperature jump:

$$h_V = \lambda_g S_v \text{Nu}/d_p \tag{3.10}$$

Here, S_v denotes the interphase surface per unit volume and Nu is a Nusselt number. Generally, this Nusselt number is a function of the porosity, ϵ, the pore-based Reynolds number, $Re = u_g d_p/\nu$ and the Prandtl number $Pr = \mu c_{p_g}/\lambda_g$.

Many empirical and theoretical correlations have been proposed to model Nu in this framework [68, 176, 186, 187, 193, 194]. Hereafter, a review of these correlations is presented and their expressions are provided. Note that because they have been derived for different geometrical configurations, each of them is normalized in a different fashion. The Nusselt number is denoted by $\mathrm{Nu}^\star$ whenever a normalization different to eq. (3.10) is used. Later on, these correlations have been rewritten under a uniform normalization using geometrical relationships for each porous geometry.

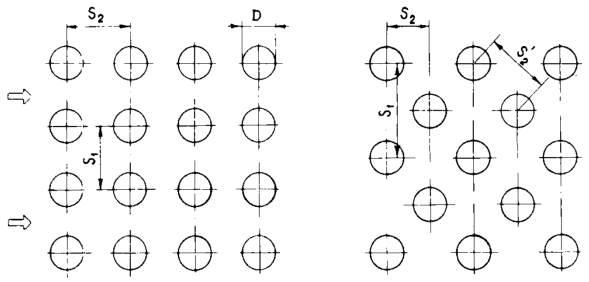

Figure 3.2. – Inline (left) and staggered (right) configurations in tube banks from [176].

In [176], Zukauskas performs an exhaustive analysis of the fluid-solid heat exchange in a flow through a two dimensional array of cylinders for a wide range of Re and Pr numbers (cf. Fig. 3.2). This work collects numerous experimental measurements and proposes several correlations for the Nusselt number in various configurations and flow regimes. Here, we retain the interphase heat transfer correlation for inline and staggered banks of circular rows, which reads:

$$\mathrm{Nu}^\star = \frac{h_v D}{S_v \lambda_g} = 0.021 Re_D^{0.84} Pr^{0.36} \tag{3.11}$$

In eq. (3.11), D is the tube diameter and Re_D is the D-based Reynolds number. In the staggered configuration of Fig. 3.2(right), if $S_1 = S_2 = S$, the relationship between the tube diameter, D, and the tube spacing S, is given by:

$$D = 2S\sqrt{(1-\epsilon)/\pi} \tag{3.12}$$

For high porosities, if $S \simeq d_p$ is assumed, eq. (3.12) allows us to rewrite eq. (3.11) as a function of the pore size d_p and the pore-based Reynolds Re.

Later on, Wakao et al. [193, 195] derived the following correlation for the interphase heat exchange in closely packed beds with a particle diameter d:

$$\mathrm{Nu}^\star = \frac{h_v d}{S_v \lambda_g} = 2 + 1.1\, Re_d^{0.6} Pr^{1/3} \tag{3.13}$$

where Re_d is the particle diameter-based Reynolds number. In packed bed structures, the interstitial size is directly proportional to the particle size $d_p = \sigma d$. The proportionality constant, σ is smaller than one and depends on the packing structure. In a close packing of equal spheres with a face-centered cubic structure it is approximately $\sigma \simeq 0.50$ and it increases for less dense structured packings and random packings.

One of the most broadly used formulations for the interphase heat transfer coefficient is that of [194]. In this experimental work, Younis and Viskanta measured the interphase heat transfer

in a laminar flow through various alumina foams as a function of the Reynolds number and for different pore sizes, d_p. Then, the experimental results are fitted by an empirical correlation that depends on the pore size-to-matrix length ratio, d_p/L. This expression, used in the VAMS from [112, 113, 183] reads:

$$\mathrm{Nu}^\star = \frac{h_V d_p^2}{\lambda_g} = 0.819\left(1 - 7.33\frac{d_p}{L}\right) Re^{0.36\left(1+15.5\frac{d_p}{L}\right)} \quad 5.1 < Re < 564 \tag{3.14}$$

A numerical correlation obtained from two-dimensional simulations of a flow over an array of square rods in staggered configuration was proposed by Kuwahara et al [186]:

$$\mathrm{Nu}^\star = \frac{h_v D_s}{S_v \lambda_g} = 1 + \frac{4(1-\epsilon)}{\epsilon} + \frac{1}{2}\sqrt{1-\epsilon}\, Re_{D_s}^{0.6} Pr^{1/3} \tag{3.15}$$

Here, D_s is the solid characteristic size. In the geometry evaluated by Kuwahara et al. [186], there is a direct relationship between D_s and the spacing between the solid obstacles, H:

$$\epsilon = 1 - \left(\frac{D_s}{H}\right)^2 \quad \rightarrow \quad Re_{D_s} = \sqrt{1-\epsilon} Re_H \tag{3.16}$$

If we assume that $d_p \simeq H$, eq. (3.16) allows rewriting the heat exchange correlation from Kuwahara et al. [186] under the present notation. This correlation was obtained by fitting the simulation results for multiple values of the porosity $0.2 < \epsilon < 0.9$ and over a Reynolds number range of $10^{-2} < Re < 10^3$. In [196], Saito et al. performed 2D DNS simulations in the same porous geometry as Kuwahara et al. [186] with a similar numerical setup. They evaluated the interphase heat exchange coefficient in their simulations and compared their results to the correlation of eq. (3.19). An excellent quantitative agreement was found at low Reynolds number and for several porosities.

Next, Saito and De Lemos [187] derived a new correlation for the interphase heat exchange coefficient for turbulent flows in the canonical configuration of two-dimensional array of square rods in staggered configuration. The Nusselt number expression is:

$$\mathrm{Nu}^\star = \frac{h_v D}{S_v \lambda_g} = 0.08\left(\frac{Re_D}{\epsilon}\right)^{0.8} Pr^{1/3} \tag{3.17}$$

which is valid for turbulent flows with $1 \times 10^4 < Re_D/\epsilon < 2 \times 10^7$ and porosities ranging from $0.2 < \epsilon < 0.9$.

Finally, the correlation proposed by Bedoya et al. in [68] is presented. This correlation is fitted from non-reacting 3D DPLS for various Reynolds and Prandtl numbers. The expression for the dimensionless heat exchange coefficient is:

$$\mathrm{Nu}^\star = \frac{h_v d_h}{S_v \lambda_g} = 3.7 Re_{d_H}^{0.38} Pr^{0.25} \tag{3.18}$$

where $d_h = 4\epsilon/S_v$ is the hydraulic diameter of the porous matrix.

Table 3.1 gathers all the above-described correlations rewritten under the uniform notation of eq. (3.10). Note that because of the disparity of configurations and the lack of an exact correspondence among the various geometries, some hypotheses regarding the geometrical parameters have been made. Figure 3.3 displays the evolution of the Nusselt number with the Reynolds number using these correlations for a reference porous matrix with $\epsilon = 0.8$, $d_p = 2.5$ mm, $S_v = 750$ m^{-1} and $L = 30$ mm. The Prandtl number is fixed to $Pr = 0.71$. Each correlation is evaluated within its domain of validity. The correlation of Saito and De Lemos [187], only valid

$\mathrm{Nu} = h_V d_p / S_v \lambda_g$	Domain	Ref.
$0.021 \left(2\sqrt{(1-\epsilon)/\pi}\right)^{-0.16} Re^{0.84} Pr^{0.36}$	$1 < Re < 10^6$	Zukauskas [176]
$\frac{2}{\sigma} + 1.1\,\sigma^{-0.4} Re^{0.6} Pr^{1/3}$	$3 < Re < 10^5$	Wakao et al. [193, 195]
$\frac{0.819}{d_p S_v}\left(1 - 7.33\frac{d}{L}\right) Re^{0.36\left(1+15.5\frac{d}{L}\right)}$	$5.1 < Re < 564$	Younis and Viskanta [194]
$\frac{1}{\sqrt{1-\epsilon}} + \frac{4\sqrt{1-\epsilon}}{\epsilon} + \frac{1}{2}\left(\sqrt{1-\epsilon}\,Re\right)^{0.6} Pr^{1/3}$	$10^{-2} < Re < 10^3$	Kuwahara et al. [186]
$\frac{0.08}{\sqrt{1-\epsilon}}\left(\frac{\sqrt{1-\epsilon}}{\epsilon} Re\right)^{0.8} Pr^{\frac{1}{3}}$	$10^4 < Re < 2 \times 10^7$	Saito and De Lemos [187]
$3.7\frac{d_p S_v}{4\epsilon}\left(\frac{4\epsilon}{d_p S_\nu} Re\right)^{0.38} Pr^{0.25}$	$10 < Re < 500$	Bedoya et al. [68]

Table 3.1. – Heat exchange correlations and domain of validity under a uniform notation

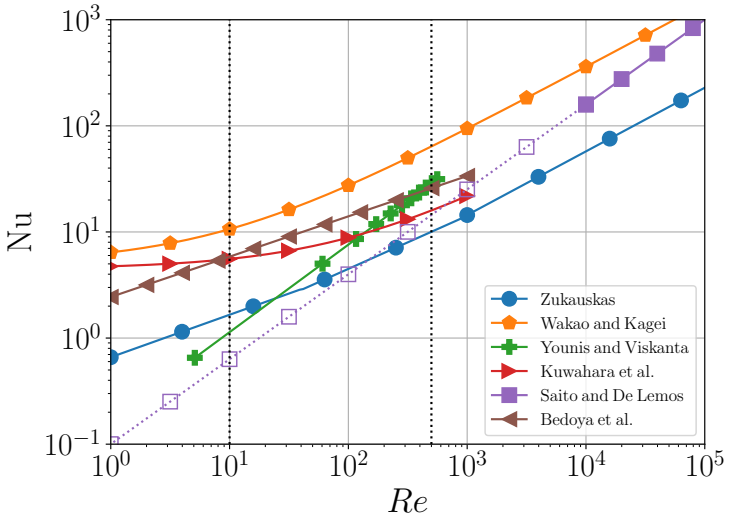

Figure 3.3. – Comparison between the different Nusselt number correlations. Evolution of the Nusselt number, Nu, with the Reynolds number, Re, in different interphase heat exchange models.

for $Re > 10^4$, has been extrapolated to lower Reynolds numbers. This is indicated with empty symbols and a dotted line. In the present experiments, the pore-based Reynolds number is in the range $10 < Re < 500$. This region has been outlined in Fig. 3.3 with black dotted lines.

There is a reasonable agreement among the different correlations regarding the scaling of the Nusselt number with the Prandtl number. In all the submodels for the interphase heat coefficient, the Nusselt number scales approximately as $\mathrm{Nu} \propto Pr^{1/3}$. In contrast, larger discrepancies exist for the exponent of the Reynolds number, which is found to depend on the flow regime. At high Re the scaling with the Reynolds number is closer to $Re^{0.7-0.8}$ whereas at low Reynolds, the exponent is between $0.4 - 0.6$. In the region of interest $10 < Re < 500$, the envelope for the Nusselt number is defined by the correlations of Wakao et al. [193, 195] and Zukauskas [176].

At low Re numbers, there is a large dispersion among the different correlations. In this work, the correlation derived in [186] for laminar flows over an array of squared rods is employed,

which reads:

$$\mathrm{Nu} = \frac{1}{\sqrt{1-\epsilon}} + \frac{4\sqrt{1-\epsilon}}{\epsilon} + \frac{1}{2}\left(\sqrt{1-\epsilon}\,Re\right)^{0.6} Pr^{1/3} \tag{3.19}$$

This correlation is chosen for its good agreement with those of [68] and [197] and because it was validated for a wide range of Re and ϵ. Because of the strong sensitivity of the flame position to this submodel and the large dispersion in the Nusselt number values, the influence of the interphase heat transfer correlation is addressed in Sec. 4.2.4.

3.2.4. Heat losses

Finally, in the same spirit as [59], a heat loss term is included in the solid phase energy equation to account for radiative losses through the burner walls:

$$\dot{q}_{\mathrm{loss}} = 4\eta\Xi\sigma_B(T_s^4 - T_{\mathrm{amb}}^4)/D \tag{3.20}$$

Here, Ξ is the solid phase emissivity, η is the quartz transmissivity and $T_{\mathrm{amb}} = 300$ K is the ambient temperature.

3.2.5. Boundary conditions

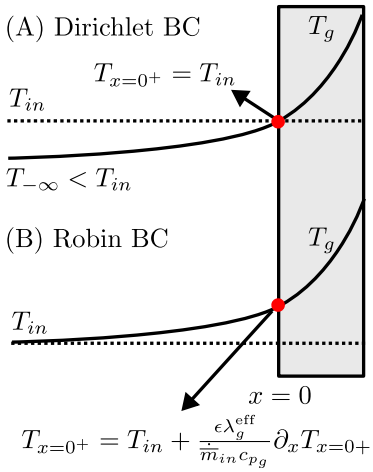

Figure 3.4. – Inlet temperature error induced by the use of Dirichlet boundary conditions.

At the burner inlet, the mass flux, $\dot{\overline{m}}_{in}$, mixture composition, $Y_{k_{in}}$, and temperature, T_{in}, are imposed as follows:

$$\dot{\overline{m}}_{in} - \epsilon\rho_g u_g\big|_{x=0^+} = 0 \tag{3.21}$$

$$\dot{\overline{m}}_{in} Y_{k_{in}} - \epsilon\rho_g u_g Y_k\big|_{x=0^+} - \epsilon J_k^{\mathrm{eff}}\big|_{x=0^+} = 0 \tag{3.22}$$

$$\dot{\overline{m}}_{in} T_{in} - \epsilon\rho_g u_g T_g\big|_{x=0^+} + \epsilon\frac{\lambda_g^{\mathrm{eff}}}{c_{p_g}}\partial_x T_g\big|_{x=0+} = 0 \tag{3.23}$$

Note that, to avoid a discontinuous treatment of the fluid domain, the equations are only solved inside the porous domain. In this framework, using Dirichlet boundary conditions to impose the gas phase temperature at the inlet ($x = 0^+$) is not correct because it does not account for the preheating of the mixture upstream of the burner $-\infty < x < 0^-$. This is illustrated in Fig. 3.4. This problem can be solved with an asymptotic matching of the solution. Using

Robin-type boundary conditions, it is possible to match the solution at the inlet of the porous domain with the solution of a convective-diffusive equilibrium in the gas phase upstream of the burner $-\infty < x < 0^-$. This allows accounting for the preheating of the reactants upstream of the burner. A similar reasoning can be applied for species diffusion.

At the outlet, $x = L$, zero temperature and species gradients are imposed in the gas phase. In the solid phase, radiative heat losses are prescribed on the sides of the domain, $x = x_b$:

$$\Xi\,\sigma_B\left[T_s^4|_{x=x_b} - T_\infty^4\right] = \pm\lambda_s^{\text{eff}}\partial_x T_s\Big|_{x=x_b} \tag{3.24}$$

where $x_b = 0$ or L and the sign is given by the direction of the boundary (inlet $+$, outlet $-$).

3.3. Evaluation of model constants

The VAM presented above must be fed with several numerical values that depend on the topology and material of the porous matrix. It is known that these models are very sensitive to the evaluation of the effective properties. Thus, it is important to carefully quantify the geometrical and material properties of the porous burner. Thanks to the mathematical description of the geometry and its spatial periodicity, the calculation of the geometrical parameters is straightforward, in contrast to random structures where a 3D scan of the porous matrix is required.

3.3.1. Topological parameters

Topological parameters include the void fraction, ϵ, the pore size, d_p, the interphase surface density, S_v, and the solid/gas phase tortuosities, τ_s and τ_g, respectively. The definition of the pore size and the porosity was addressed in Chapter 2. Here, the focus is on the interface surface density, S_v, and the tortuosity coefficients, τ. Topological parameters are computed numerically from a binarized voxel representation of the porous matrix geometry. Thanks to the periodicity of the lattice, the evaluation can be made over an elementary periodic unit. The 3D volume with dimensions $\Lambda \times \Lambda \times \Lambda$ is discretized using a cartesian grid with a resolution of $n = 80$ steps per wavelength. The interface surface density, S_v, is defined as the area of the fluid-solid interface per unit volume. It can be directly computed from the STL representation of the fluid-solid interface surface, $\partial\Omega$. The tortuosity of each phase is computed following [198, 199] as:

$$\tau_{s,g} = \frac{D^{\text{int}}}{D^{\text{eff}}}\Upsilon_{s,g} \tag{3.25}$$

where D^{int} is the intrinsic diffusivity, $\Upsilon_{s,g}$ is the phase volume fraction and D^{eff} is the effective diffusivity. To compute D^{eff}, 3D numerical simulations of Fickian diffusion are run using the python tools PORESPY and OPENPNM [200, 201]. In these simulations, a concentration jump ΔX_A for species A is imposed along one direction. Then, the molar flux at the outlet is computed and the effective diffusion coefficient is obtained as:

$$D^{\text{eff}} = \frac{J_A L}{\Delta X_A} \tag{3.26}$$

where J_A is the molar flux (mole per unit area and per unit time), L is the diffusion distance and ΔX_A is the jump of concentration across the distance L. Tortuosity is not an isotropic quantity so it is important to impose the concentration jump in the streamwise direction of the burner. Figure 3.5 represents two XZ-cuts of the A species concentration field in Fickian diffusion simulations for the gas and solid phases used to compute the phase tortuosity. In TPMS-based

topologies, the phase tortuosity is a function of the porosity ϵ but it is independent of the pore size, d_p.

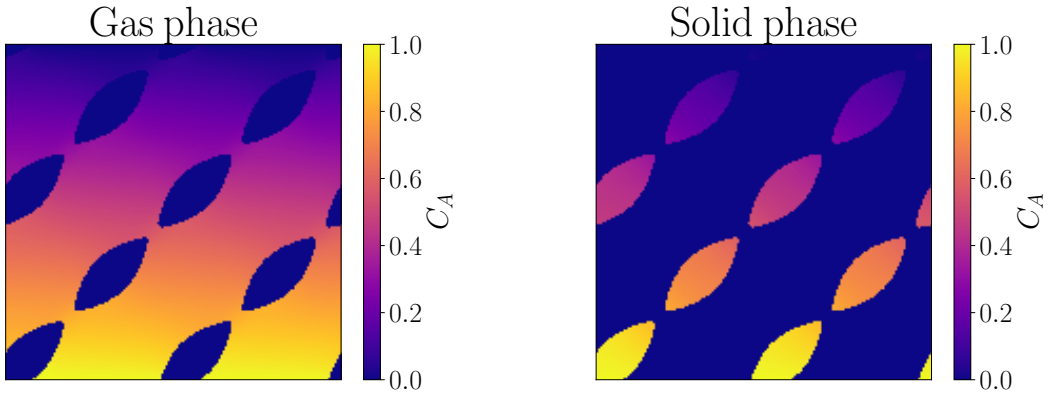

Figure 3.5. – XZ-cut of the A species concentration field in Fickian diffusion simulations for the gas (left) and the solid (right) phases in a Diamond topology with $\epsilon = 0.8$. These simulations are used to extract the phase tortuosity.

3.3.2. Material-dependent parameters

Material-dependent parameters include the solid thermal conductivity, λ_s, the solid emissivity Ξ and the quartz transmissivity, η. The influence of the manufacturing process on the solid thermal conductivity was addressed in Chapter 2. Here, we focus on the emissivity and the quartz tube transmissivity.

For the solid emissivity Ξ, a number of experimental and numerical works have studied the emissive properties of 316L samples under different pressures, temperatures, surface states and oxidation conditions [202–205]. There is a vast disparity in the emissivity values depending on the surface roughness and the level of oxidation of the samples. Due to the manufacturing process and the extreme operating conditions of the burner, their surface is oxidized and rough. Given the typical temperatures measured inside the burner ($1000 - 1300$ K), we can estimate the emissivity to fall within $0.6 < \Xi < 0.7$. Henceforth, a value of $\Xi = 0.65$ is retained for the emissivity of the solid phase. The influence of this parameter on the model predictions is addressed in Sec. 4.A.

Quartz transmissivity, η_{λ_r}, depends upon the light wavelength, λ_r. Typically, quartzs are fully transparent ($\eta_{\lambda_r} = 1$) within the wavelength range 150 nm $< \lambda_r <$ 3000 nm and opaque elsewhere ($\eta_{\lambda_r} = 0$). The total transmissivity, $\eta(T)$, is thus a function of the temperature of the solid and can be computed as:

$$\eta(T) = \left(\int \pi \eta_{\lambda_r} B(\lambda_r,\, T) \mathrm{d}\lambda_r \right) \Big/ \left(\sigma_B T^4 \right) \tag{3.27}$$

where $B(\lambda_r,\, T)$ is the spectral radiance as a function of temperature. For solid temperatures between 800 K $< T_s <$ 1400 K the transmissivity varies almost linearly between $0.14 < \tau < 0.52$.

Figure 3.6 shows the spectral transmissivity of the quartz, η_{λ_r}, the correlation between the spectral radiance and the transmissivity, and the total transmissivity of the quartz as a function of temperature, η.

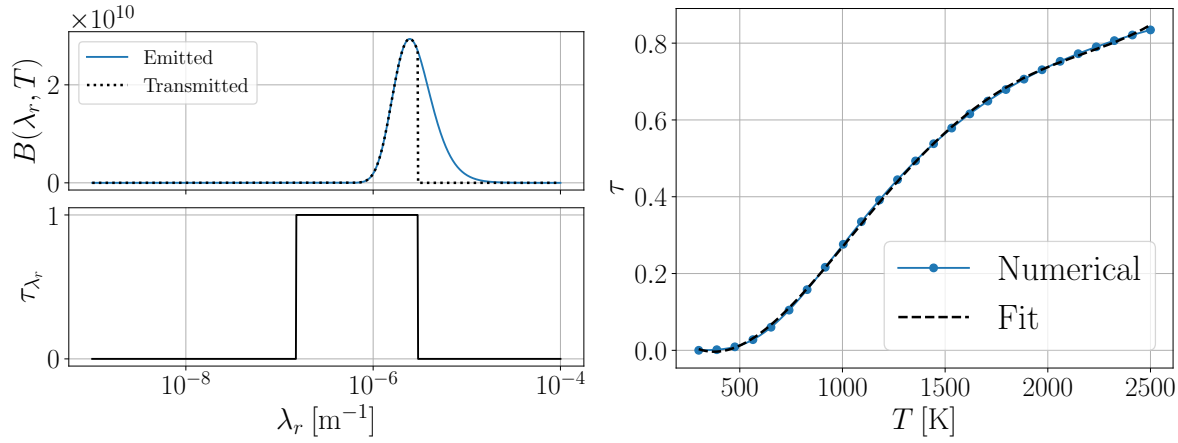

Figure 3.6. – Correlation between the radiative emission of a black body for $T_s = 1180$ K and the quartz transmissivity as a function of the wavelength. Total quartz transmissivity as a function of the temperature of the radiation source, T, computed as the integral of the curve.

3.4. Conclusions of the chapter

This chapter has been devoted to the modeling of PMC. First, a review of the state of the art in PMC models has been presented. The limitations of 1D models were already pointed out in [70] and several recent works have highlighted the contradictions between the VAM hypotheses and the DPLS results [67, 68]. However, due to the elevated computational cost of DPLS, VAMs represent the only viable modeling strategy for engineering applications and burner optimization. Therefore, it is necessary to refine current VAMs to improve their accuracy and predicting capacity.
In Sec. 3.2, a 1D two-equation nonadiabatic VAM with detailed chemistry has been presented. In the spirit of [59] a systematic literature review has been conducted to incorporate the most widely-used sub-models for dispersion, interphase heat transfer and thermal radiation. It has been noticed that there are large discrepancies among the existing correlations for the heat exchange coefficient. Because of its strong impact on the solution, the influence of this term on the stabilization of the flame is addressed in Chapter 4. It is known that VAMs are very sensitive to the model parameters. For this reason, in Sec. 3.3, a rigorous evaluation of the geometry-dependent parameters has been carried out making use of the analytical description of the porous geometry.
Some minor paths for improvement have been identified for the evaluation of model constants in future works:

- Computing the effective radiative extinction factor β from the CAD of the burner geometry to improve the description of heat transfer by radiation.
- Incorporate a temperature-dependent solid conductivity $\lambda_s(T_s)$.
- Estimate the dispersion characteristic length, l_{dis}, and the entrance relaxation distance for dispersion effects from cold DPLS.

In Chapter 4, a comparison between this VAM and the experimental results is established in terms of flame position, reaction zone thickness and temperature profiles.

Chapter 4

Flame-front tracking in PMBs

This chapter corresponds to the article **"Flame-front tracking in Porous Media Burners"** by E. **Flores-Montoya, P. A. Masset, T. Schuller and L. Selle**, Combustion and Flame, 267, 113597, (2024).

Abstract
The experimental setup presented in Chapter 2 is used to visualize the flame inside an optically accessible Porous Media Burner (PMB). As a result, the flame front position inside the burner can be tracked as a function of the operating conditions. Flame tracking is used to analyze the influence of the pore size on the stabilization of lean premixed CH_4-Air flames. $CH^\star$ chemiluminescence and temperature measurements reveal nearly one-dimensional sub-adiabatic flames featuring an axially spread-out reaction region. In this respect, the localization of the heat release rate provides a significant addition for the validation of Volume Averaged Models (VAMs). A comparison between the 1D-VAM from Chapter 3 and the experimental results is proposed in terms of flame position, reaction-zone thickness and temperature profile. The model captures fairly well the thermal state of the system as in many previous studies, but exhibits significant deviations for the flame position and its thickness. Scrutinizing the various model parameters, the positioning of the flame inside the burner is found to be extremely sensitive to the interphase heat exchange term. These comparisons call for improvement in combustion models for porous media and suggest that pointwise temperature measurements in multi-stage burners are insufficient for the validation of 1D-VAM if an accurate characterization of the operating domain of the burner is sought.

Overview

4.1. Introduction **68**
4.2. Results & Discussion **68**
4.2.1. Stability domain 68
4.2.2. Axial profiles of $CH^\star$ and temperature 69
4.2.3. Flame-front tracking 71
4.2.4. Sensitivity to the interphase heat exchange submodel 73
4.3. Conclusions of the chapter **74**
4.A. Influence of solid phase properties **75**

"*That's a second order problem*"

Thierry Schuller

4.1. Introduction

In this chapter, a new validation method for VAMs is proposed. This method consists in the tracking of the reaction zone inside the burner as a function of the operating conditions. It relies on a basic principle of heat recirculating burners: the relationship between the flame position and the burning rate in a homogeneous porous medium. To accomplish the tracking of the reaction region in experiments, the optically accessible burners presented in Chapter 2 are employed. These are made possible by the combination of computer-defined topologies and AM techniques. The topologies used here feature see-through directions that enable direct flame-front visualization and hence the tracking of its position. The novel experimental setup presented in Chapter 2 uses a telecentric lens to measure the axial distribution of $CH^\star$ chemiluminescence. Topology tailoring offers a systematic control of the geometrical parameters of the porous matrix, which is exploited here to assess the influence of the pore-size on flame stabilization.

The results are compared with the 1D-VAM presented in Chapter 3, where the effective properties and model parameters are evaluated from the mathematical definition of the geometry. A direct comparison in terms of flame front position, reaction region thickness and temperature profiles is performed. The results point out several shortcomings in the state-of-the-art VAMs and may call for a revision of the diagnostics currently used for validation.

4.2. Results & Discussion

As a preliminary remark, many studies comparing experimental results and 1D-VAM numerical solutions are performed with two-layer PMBs with different pore sizes. The stage with smaller pores is placed upstream so that the flame cannot flashback and is often stabilized at the junction between the two layers. This reduces the coupling between the flame front position and the heat recirculation so that it is arguably a less stringent validation than the PMBs with homogeneous properties used in the present work.

In this chapter, three PMBs with a Diamond topology, a porosity, $\epsilon = 0.8$, and different pore sizes are considered. Their topological parameters are gathered in Tab. 5.1. The submerged combustion of CH_4/Air flames is analyzed in terms of operating domain, stabilization curves, performance and axial profiles of temperature and heat release rate.

Table 4.1. – Topology-dependent parameters.

d_p [mm]	ϵ	S_v [m^{-1}]	τ_g	τ_s
1.5		1215		
2.5	0.8	729	1.19	2.52
3.5		521		

4.2.1. Stability domain

Figure 4.1 plots the experimental points evaluated in this study in the $P - \phi$ map. The blowoff, flashback and high temperature limits are indicated with dotted, solid and dashed lines,

respectively. The shadowed region delimits the estimated boundaries of the burner operating domain. Dashed areas on the upper right corners indicate unexplored regions due to thermal constraints. The blowoff limit is unaltered when the pore size is reduced from $d_p = 3.5$ mm to 2.5 mm but is shifted towards higher equivalence ratios when d_p is decreased to 1.5 mm. This greatly impacts the burner operating range at the lowest pore size.

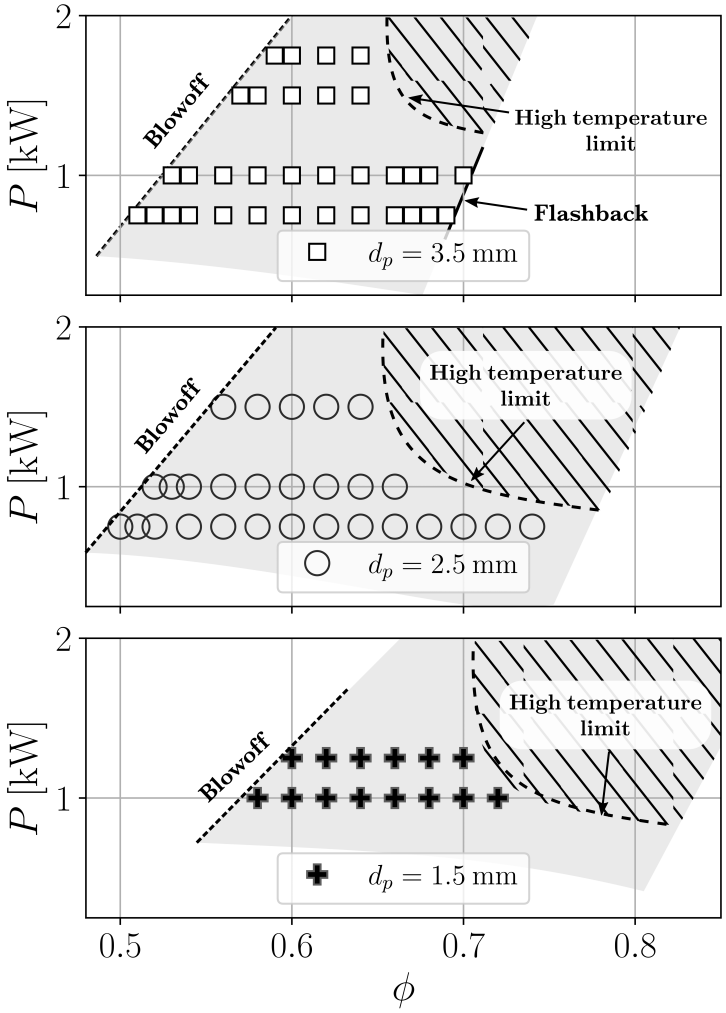

Figure 4.1. – Operating domain of the PMBs for different pore sizes, d_p, spanned by power, P, and equivalence ratio, ϕ.

4.2.2. Axial profiles of $CH^\star$ and temperature

Figure 4.2 illustrates how the new method presented here allows the determination of the flame front position. Three flames at the blowoff limit with $P = 1$ kW stabilized in PMBs with different pore sizes are shown. In Fig. 4.2A, line-of-sight integrated $CH^\star$ chemiluminescence images are presented. In these direct visualizations, white dotted lines indicate the interpolated flame position. In Fig. 4.2B, the axial profiles of $CH^\star$ and the beta-prime fit of the experimental curve are plotted in red dotted lines and black dashed lines, respectively. The solid blue line is the normalized heat release rate profile computed with the VAM solver for the same operating conditions. Finally, in Fig. 4.2C, the experimental and numerical normalized temperature profiles are depicted. At the blowoff limit, flames are observed approximately in the middle of the porous matrix. For the $d_p = 3.5$ mm and $d_p = 2.5$ mm PMBs, the flame spreads over two and

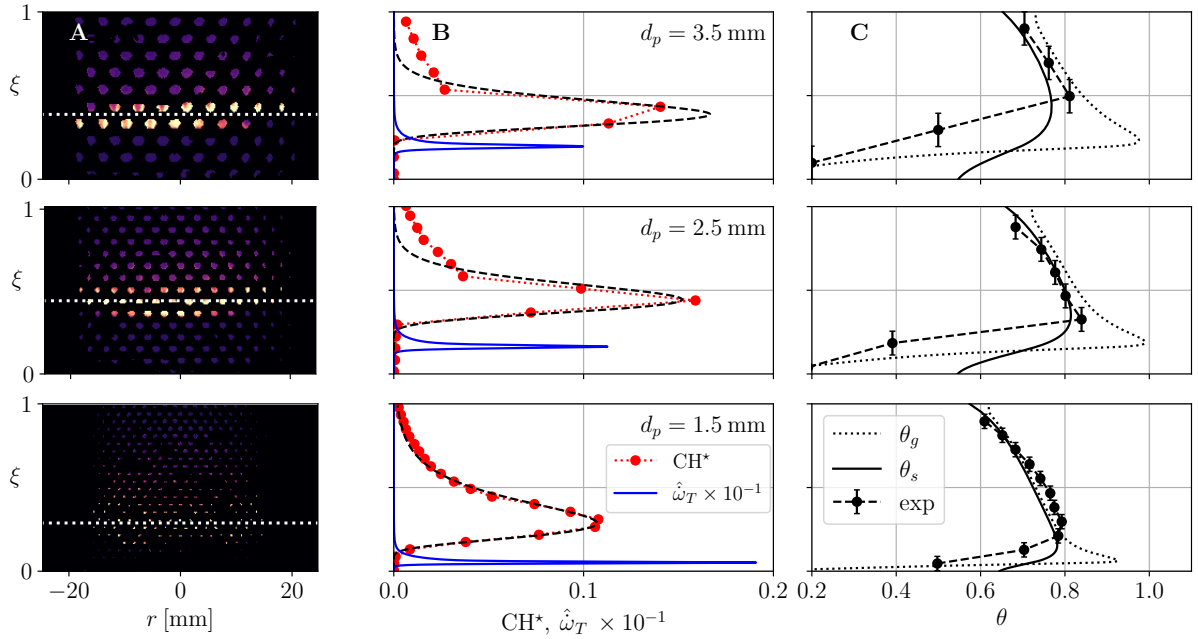

Figure 4.2. – Flame structure for cases at the blowoff limit with $P = 1$ kW. A) LoS integrated CH* chemiluminescence images. B) Profiles of CH* from the experiments and normalized heat release rate $\hat{\omega}_T$ from simulations. C) Experimental and computed normalized temperature profiles. Results in (B) and (C) are presented as a function of $\xi = x/L$. Temperatures are normalized as $(T - T_{in})/(T_{ad} - T_{in})$.

three pore rows respectively. However, the width of the reaction region remains approximately constant. When the pore size is reduced to $d_p = 1.5$ mm the width of the flame front increases and the reaction zone is distributed over 5 to 6 pore rows. Regardless of the pore size and the burner load, there is limited radial deformation of the reaction region so that the comparison with 1D simulations seems quite reasonable.

There are large discrepancies between the heat release rate profiles computed using the VAM and the experimental CH* distribution in Fig. 4.2B. Both the width and the position of the peak are not well predicted by the model. In experiments, the width of the reaction region is several times larger than in simulations. DPLS [67] have shown wrinkled flames distributed over several pores as a result of local anchoring effects. Owing to the line-of-sight integration of the CH* signal, such a flame front would appear to be thickened with the present experimental setup. Therefore, we cannot infer whether the thickening results from a local broadening of the reaction region or from the spatial averaging of a thin wrinkled flame front. Nevertheless, it appears that additional modeling efforts are needed in VAMs to predict the extent and position of the reaction region. It is reiterated that unlike in two-layer PMBs with different pore sizes, here the flame is not preferentially anchored at the interface. This allows for a two-way coupling between combustion and heat recirculation, which arguably makes it a more stringent validation case for VAMs.

Regarding the temperature profiles, there is a fair agreement between the measurements and the model in Fig. 4.2C. The offset in the flame position between the model and the experiments yields significant errors upstream of the flame but the maximum temperatures and the temperature gradients at the outlet show a reasonable agreement. This indicates that, overall, thermal losses are well modeled in the simulations. Interestingly, despite the blatant disagreement in the heat-release rate profiles, the fair agreement observed in the temperature profiles suggests that this variable is actually less sensitive to changes in the inlet mass flow rate.

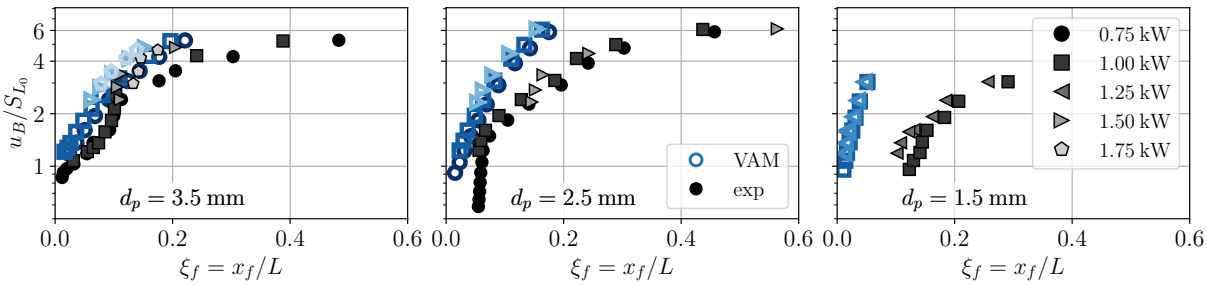

Figure 4.3. – Flame speed-up, u_B/S_{L_0}, versus flame position, $\xi_f = x_f/L$, for different powers, P, and pore sizes, d_p. The h_V correlation presented in Kuwahara et al. [186] is used as interphase heat exchange submodel.

4.2.3. Flame-front tracking

The evolution of the flame position with the operating conditions is now analyzed. For each experiment, bulk flow velocity is computed as, $u_B = \dot{m}/\rho_{in} A\epsilon$, where $A = \pi D^2/4$, $\dot{m}$ is the total mass flow rate and ρ_{in} is the density at the inlet temperature, T_{in}. This value is normalized by the flame speed of the 1D unstretched adiabatic flame at the inlet conditions, $S_{L_0}(\phi, T_{in})$. The ratio, u_B/S_{L_0}, quantifies the increase in mass consumption rate per flame unit surface and is called here the flame speed-up. As for the experiments, the position of the flame in the burner, x_f, is defined by the location of the heat release rate maximum. In the simulations, when the flame is so close to the inlet that the heat release rate is non-zero on the boundary condition, the case is considered to be a flashback. In practice, flashback can be influenced by entrance and boundary layer effects as well as by local pore-anchoring. Therefore, accurately predicting its occurrence is complex and out of the scope of the present work. Here, the focus is on the overall agreement between the observed and computed flame positions for a given mass flow rate.

Figure 4.3 shows the speed-up, u_B/S_{L_0}, versus the dimensionless flame position, $\xi_f = x_f/L$, at different powers for the three burners. When the flames are close to the inlet, $u_B/S_{L_0} \simeq 1$, which is consistent with the limited preheating. Because of thermal losses, the speed-up can even be smaller than unity near $\xi = 0$. As the bulk to flame velocity ratio is increased, the position of the flame is shifted towards the burner outlet. The speed-up reaches a maximum value at approximately $\xi \simeq 0.5$. At this point, a further increase of u_B/S_{L_0} leads to blowoff. This is, to the authors' best knowledge, the first tracking of the flame front position as a function of the burner operating conditions. These experimental observations confirm the theoretical predictions obtained with analytical models for finite porous media [63, 178]. The flame position is found to be independent of the thermal power for the range reported in this study. Interestingly, despite sub-adiabatic temperatures are measured inside the burner, the mass consumption rate per unit surface of the flame increases by nearly a factor six at blowoff in the $d_p = 2.5$ mm burner. This ratio is reduced to approximately three in the $d_p = 1.5$ mm case. For the experimental results at hand, the speed-up at blowoff is found to decrease when the pore size is reduced. Concerning the flame positioning, a fairly good agreement between the model and the experiments is obtained for $d_p = 3.5$ mm. However, near blowoff differences between the model and the experimental results significantly increase. As the pore size is decreased, the agreement between the experimental results and the model progressively degrades. At $d_p = 1.5$ mm, the predicted flame position is completely off the experimental observations. Interestingly, in the VAM results shown in Fig. 4.3, the influence of the thermal power on the position of the flame is also marginal and qualitatively similar to experiments.

In experiments, the pore size plays a major role in flame stabilization influencing both the position and the width of the reaction zone. This strong influence does not seem to be captured

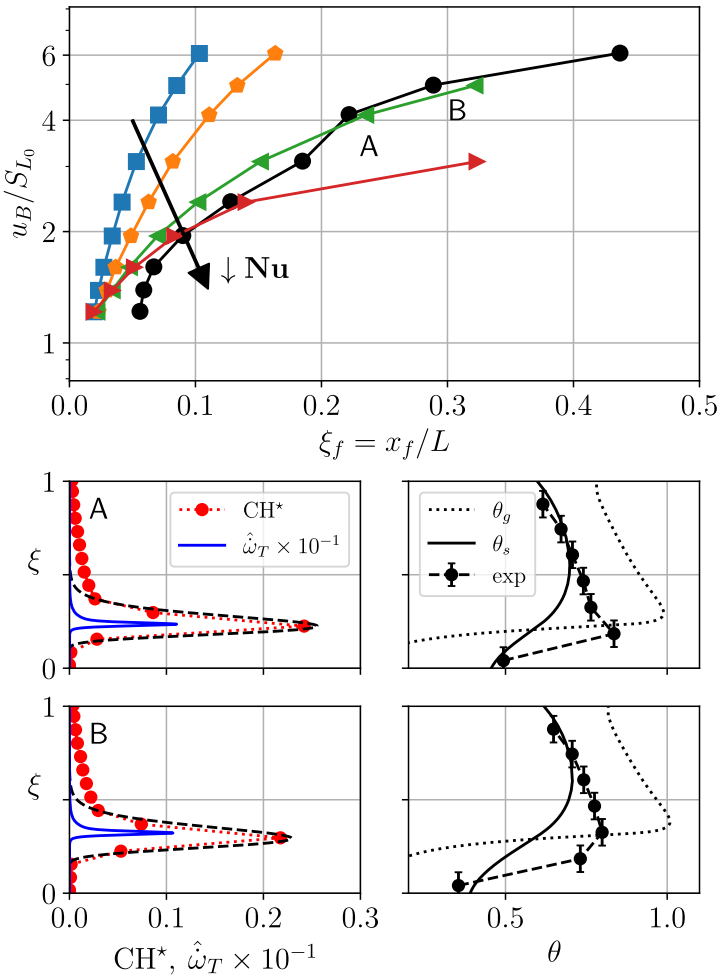

Figure 4.4. – Influence of the interphase heat exchange term on the VAM results for 1 kW flames stabilized in the $d_p = 2.5$ mm burner: experimental results; Wakao and Kagei [195]; Kuwahara et al. [186]; Saito and De Lemos [187]; Zukauskas [176]. The experimental and numerical axial profiles are compared for points A and B.

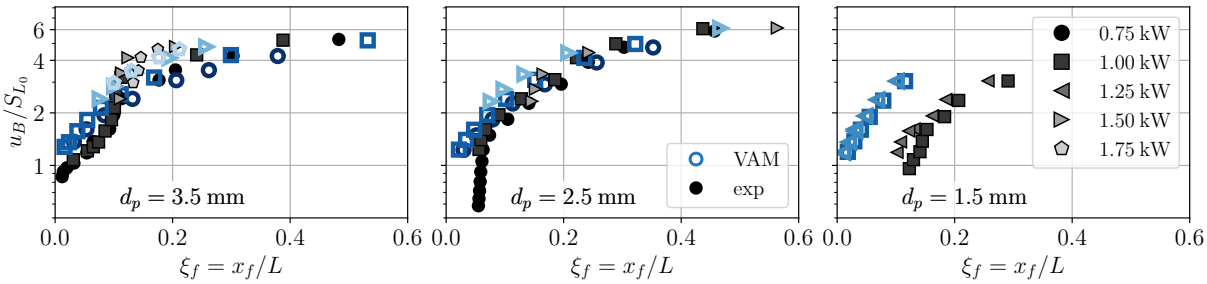

Figure 4.5. – Flame speed-up, u_B/S_{L_0}, versus flame position, $\xi_f = x_f/L$, for different powers, P, and pore sizes, d_p. The h_V correlation presented in Saito and De Lemos [187] is used as interphase heat exchange submodel.

by the model where the stabilization curves in Fig. 4.3 are marginally affected by changes in d_p. Unfortunately, in its present form, CH* chemiluminescence measurements only provide the macroscopic behavior of the flame inside the burner. The present results show that d_p has a

remarkable influence on the stabilization of flames but due to the lack of pore level details we can only speculate about the underlying mechanisms. Recently, Boigné et al. [69] performed 3D DPLS and reported that nearly 80% of the combustion process takes place in a flamelet mode where the flame front is locally adiabatic. However, this may not be the case at small pore sizes and this dependency on d_p is not modeled in VAMs. Because combustion and heat transfer are highly nonlinear processes, local phenomena at the pore scale can have a strong impact on the macroscopic behavior. This point requires further investigations and must be addressed in future works both experimentally, via pore-resolved diagnostics, and numerically, via DPLS.

4.2.4. Sensitivity to the interphase heat exchange submodel

In an effort to identify paths for improvements of the simulations, the sensitivity to the interphase heat transfer model is now discussed. To this end, the position of the flame is computed using several correlations from the literature [176, 186, 187, 193]. Numerical results are compared to experiments in Fig. 4.4 for 1 kW flames with varying ϕ in the $d_p = 2.5$ mm burner. As the Nusselt number decreases, flames stabilize further downstream for a given flow rate. When the correlation of [187] is employed, the current 1D model accurately predicts the flame position. As shown in Fig. 4.5, the use of this correlation improves the numerical predictions for $d_p = 2.5$ mm and $d_p = 3.5$ mm. However, it does not perform as well for the $d_p = 1.5$ mm burner.

In Fig. 4.4, the axial profiles of $CH^\star$ and temperature from experiments are compared to the heat release rate and temperature distributions from the 1D-VAM for two mass flow rates. These two cases are labeled with A and B and their equivalence ratios are $\phi = 0.54$ and $\phi = 0.53$, respectively. The heat release rate profiles show an excellent agreement in terms of mean flame position. However, the model still fails to predict the thickness of the reaction region. Furthermore, the numerical results show large differences between the solid and the gas phase temperatures in Fig. 4.4, suggesting the operation in the so-called decoupled regime [64]. It is pointed out that the correlation from [187] was derived and validated for turbulent flows with $10^4 < Re < 10^7$ while in the present experiments, the pore-based Reynolds number falls within $20 \lesssim Re \lesssim 120$. This strongly questions the use of the correlation and might indicate some kind of error compensation between the submodels. This question should be addressed in future works since it has a major impact on the blowoff limit of the burner. Further efforts must also focus on the thickening of the reaction region and the influence of the pore size, which are not well retrieved by the 1D model. To complement this sensitivity analysis, the influence of solid material properties on the model results is evaluated in 4.A. It is shown that they have a marginal impact on the model predictions when compared to the interphase heat transfer term.

4.3. Conclusions of the chapter

In this chapter, the direct visualization of the reaction region inside a porous medium has permitted its tracking as a function of the operating conditions. Flame-front tracking enables a a better confrontation between experiments and simulations. The combustion of lean methane-air flames has been analyzed for three PMBs with different pore sizes. The experimental results show nearly one-dimensional sub-adiabatic flames featuring a thickened reaction region.
Comparisons are carried out with the 1D VAM with detailed chemistry and including radial heat losses presented in Chapter 3. Effective parameters have been evaluated by making use of the exact description of the burner geometry and correlations from the literature. Neither the width nor the position of the reaction zone are accurately predicted by the VAM, especially for small pore sizes. In contrast, heat losses are well estimated and a reasonably good agreement is obtained for the temperature profiles. Finally, the effect of the interphase heat exchange term on the positioning of the flame has been shown to have a strong impact on the flame position. In many studies, VAMs are typically validated using pointwise temperature measurements in multi-stage burners where the flame usually stabilizes at the interface between two layers. The results presented here show that a qualitative agreement between the temperature profiles can be achieved if global heat losses are well characterized. In contrast, predicting the flame position inside the burner, which is necessary for accurate description of the blowoff limit, is much more challenging. The present work highlights that current VAMs exhibit high sensitivity to the modeling of the heat exchange term, failing to accurately predict both the flame thickness and the impact of the pore size.

4.A. Influence of solid phase properties

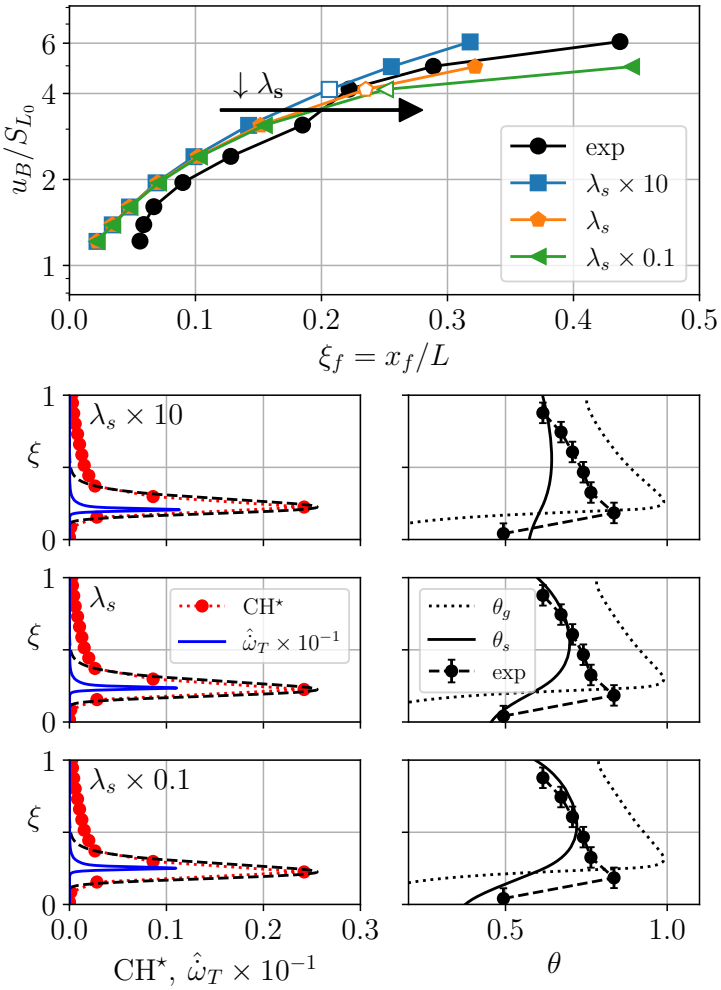

Figure 4.6. – Influence of solid conductivity, λ_s, on the VAM results for 1 kW flames stabilized in the $d_p = 2.5$ mm burner. A comparison between the experimental and the numerical profiles at different values of λ_s is offered for the points labeled with white markers.

In VAMs, there are many effective parameters and submodels and it is out of the scope of the present work to perform an exhaustive parametric analysis of their cross-influences. Instead, our approach has been to focus on a parameter that combines a large variability and a strong influence on the results, i.e. the Nusselt number, and to perform the most rigorous characterization possible of the rest. For example, geometrical parameters can be evaluated with good accuracy when computer-defined topologies are used. Therefore, it is less likely that they are at the origin of discrepancies between the model and the experiments. To complement the results of Sec. 5.3, the influence of the thermal properties of the solid is further discussed. Notably, the impact of the thermal conductivity, λ_s, and the emissivity, Ξ, on flame stabilization is examined.

In Fig. 4.6, the speed-up curves from experiments are compared to the model results for different values of the thermal conductivity λ_s. Results are presented for 1 kW CH_4-Air flames with varying ϕ stabilized in the $d_p = 2.5$ mm burner. The VAM is evaluated using the interphase heat exchange correlation from [187]. Results in Fig. 4.6 show that a ten-fold increase/decrease of the solid thermal conductivity has only a slight influence on the macroscopic behavior of the

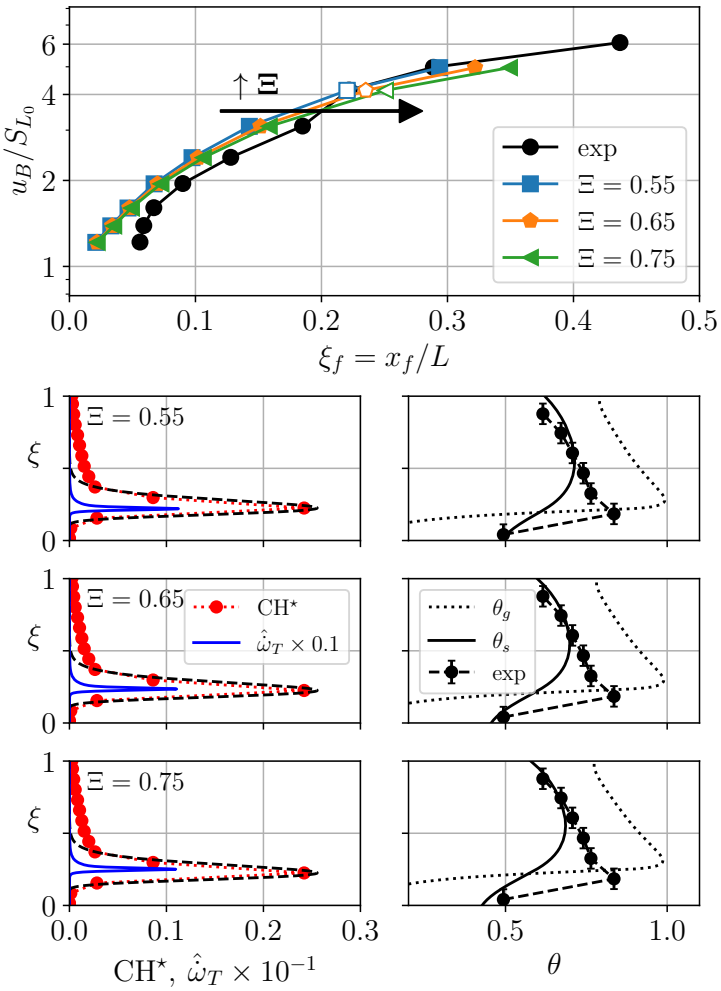

Figure 4.7. – Influence of solid emissivity, Ξ, on the VAM results for 1 kW flames stabilized in the $d_p = 2.5$ mm burner. A comparison between the experimental and the numerical profiles at different values of Ξ is offered for the points labeled with white markers.

flame.

For example, at $\phi = 0.54$ (labeled as A in Fig. 4.4 and indicated with white markers in Fig. 4.6), a decrease in the mean Nusselt number from Nu $\simeq$ 6.5 [186] to Nu $\simeq$ 1.5 [187] (more than a four-fold reduction) drives a 3.72 mm change in the flame position. In contrast, a ten-fold reduction of the thermal conductivity from $\lambda_s = 130$ W m^{-1} K^{-1} to 13 W m^{-1} K^{-1} only shifts the position of the flame by 0.87 mm. This indicates that the model is only weakly sensitive to the solid thermal conductivity. A detailed comparison between the numerical and experimental axial profiles is presented at the bottom of Fig. 4.6 for the three points with white markers ($\phi = 0.54$). These flames feature the same speed-up, $u_B/S_{L_0} \simeq 4$, but different solid thermal conductivity, $\lambda_s = 1.3$, 13 and 130 W m^{-1} K^{-1}. As expected, at higher values of λ_s the solid temperature profile is flatter, but this has only a minor impact on the positioning of the flame and on the heat release rate and gas temperature profiles.

Let us now analyze the influence of the solid matrix emissivity, Ξ, on flame stabilization. This parameter scales the axial and radial heat losses by thermal radiation. The thermal conductivity is fixed to its reference value, $\lambda_s = 13$ W m^{-1} K^{-1}, and the model is run for different values of the solid emissivity Ξ = 0.55, 0.65 and 0.75. It is recalled that a value of Ξ = 0.65 is used

for the results presented in Sec. 5.3. As for the previous analysis, we consider 1 kW CH_4-Air flames with different equivalence ratios stabilized in the $d_p = 2.5$ mm PMB. Figure 4.7 compares the stabilization curves and the axial profiles for different values of the solid emissivity, Ξ. At $\phi = 0.54$, increasing the emissivity from 0.55 to 0.75 only shifts the location of the flame approximately 0.91 mm downstream. The numerical and experimental axial profiles for the three points with white markers are represented at the bottom of Fig. 4.7. It can be noticed that increasing the solid emissivity translates in mild reductions on the solid phase temperature, but this has marginal impact on the heat release rate and gas temperature profiles.

These results show that solid material properties have a smaller impact on flame stabilization than the heat exchange term. This reinforces the applied methodology and justifies the analysis presented in Sec. 4.2.4 for the Nusselt number correlations.

Chapter 5

Speed-up drivers for H_2-enriched flames

This chapter corresponds to the article **"Speed-up drivers for H_2-enriched flames in Porous Media Burners"** by **E. Flores-Montoya, P. A. Masset, T. Schuller and L. Selle**, Proceedings of the Combustion Institute, 40, 1-4, 105666 (2024).

Abstract
In this chapter, the influence of porosity and hydrogen enrichment on the stabilization of premixed CH_4-Air flames in Porous Media Burners (PMBs) is addressed. Flame stabilization is analyzed via direct flame-front tracking, which is made possible by the novel experimental apparatus presented in Chapter 2. Topology tailoring is here exploited to study the influence of porosity on the performance of the burner. Flame front tracking reveals a different stabilization trend in highly H_2-enriched flames. A comparison with a theoretical model is used to remove the effect of preheating and focus on other fuel properties. This suggests a flame-speed enhancement mechanism driven by Lewis number effects in Le < 1 mixtures. Together with recent 3D Direct Numerical Simulations, these results provide evidence that preferential diffusion effects are key in the stabilization of flames in PMBs. These phenomena, not considered in state-of-the art 1D-Volume Averaged Models, remain crucial for the design of efficient PMB using hydrogen as a fuel.

Overview

5.1. Introduction **80**
5.2. Controlled flashback **80**
5.3. Results & Discussion **82**
5.3.1. Influence of porosity 82
5.3.2. Influence of H_2-enrichment 84
5.4. Conclusions of the chapter **88**

"*Patiente is the mother of science.*"

Maria del Mar Montoya

5.1. Introduction

The storage of excess renewable energy in the form of hydrogen is a viable path for the reduction of CO_2 emissions. The subsequent use of H_2 as a fuel requires addressing specific challenges such as flame stabilization and NO_x mitigation. In the present chapter, heat-recirculating burners are considered for their ability to address these issues. Owing to their outstanding properties [45], PMBs are well suited to achieve a low-NO_x carbon-free flame via lean hydrogen combustion.

Surprisingly, few works have addressed the combustion of pure hydrogen-air mixtures in PMBs [206, 207]. Other studies have considered the effects of hydrogen enrichment on canonical fuels such as methane and natural gas [55, 56] and on alternative energy vectors such as ammonia [58, 59]. Hydrogen addition was found to have a remarkable impact on burner operation, shifting the stability map towards lower equivalence ratios [55]. The aforementioned studies focus on the evolution of the burner operating range and report changes in the temperature profiles and in pollutant emissions. However, they do not specifically address the stabilization mechanisms of these flames and how they are affected by hydrogen blending. Recent DNS have shown that preferential diffusion effects play a key role in the stabilization of H_2 flames in PMBs [76, 182]. This effect is not specifically taken into account in 1D models such as those used for PMBs [206].

Moreover, the geometrical parameters of the porous structure are known to have a direct impact on the combustion properties [117, 121]. However, the influence of the matrix porosity, ϵ, is rarely assessed in experimental studies. Generally, variations of ϵ are small and in most cases are a side effect of the utilization of different foams rather than a controlled parameter. Computer-designed geometries allow the independent variation of pore size, d_p and void fraction, ϵ. Here, we address the influence of porosity on the burner performance by comparing two PMBs with the same pore size and different porosities, $\epsilon = 0.5$ and $\epsilon = 0.8$. The influence of hydrogen enrichment on the burner operating domain and on flame stabilization is also analyzed. The tracking of the flame position as a function of the operating conditions allows us to compare the stabilization of CH_4-Air flames and H_2-enriched flames. For these flames, our results indicate stabilization mechanisms other than heat recirculation, which are not accounted for in present 1D models.

5.2. Controlled flashback

In this thesis, the focus is on the submerged combustion regime, where the flame is stabilized inside the PMB and there is an intense coupling between combustion and heat transfer. However, submerged flames cannot be stabilized directly from cold start, a transient starting process is required to achieve this regime. The starting of PMBs is an overlooked topic in the literature. Generally, flames are first stabilized on top of the burner in the surface combustion regime. When multi-staged configurations are used, the transition from surface to submerged combustion is straightforward. Usually, ceramic foams with a small pore size are used for the upstream stages. This way, the upstream porous matrix acts as flame arrestor, quenching the flame and ensuring stability during the process. However, in single-staged configurations the transition from surface to submerged combustion is challenging. In CH_4-Air flames, the progressive reduction of the

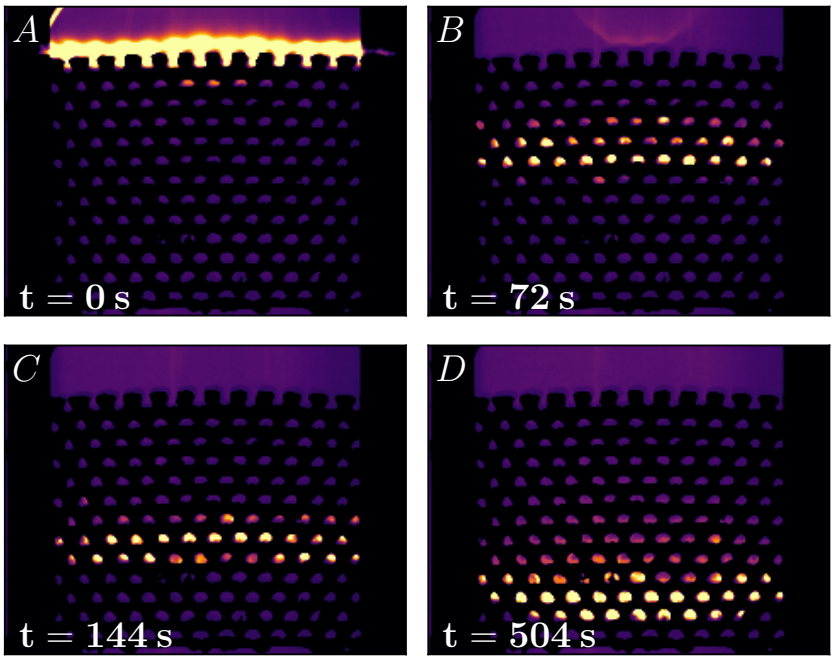

Figure 5.1. – $CH^{\star}$ chemiluminescence imaging of a *Controlled flashback* transient. (A) Ignition with CH_4-Air at $\phi = 0.6$. (B) Hydrogen addition to trigger transition to submerged combustion. (C) Removal of hydrogen. (D) Steady state in thermal equilibrium is reached.

bulk to flame speed ratio often causes Flame Repetitive Extinction and Ignition (FREI) and is likely to result in flashback. Ceramic porous matrices feature a low resistance to thermal shocks [101, 121]. As a result, the burner operating conditions must be varied extremely slowly to prevent breakage. This imposes long transient times, further increasing the complexity of the starting process. Here, we propose a time-efficient method to achieve this transition that is made possible by the use of metallic burners. The procedure is detailed below.

First, a CH_4-Air flame is stabilized on top of the burner in the surface combustion regime. Typically, the burner is started with a 0.8 kW CH_4-Air flame at $\phi = 0.6$. Then, to achieve submerged combustion conditions, a small fraction of hydrogen is temporarily added so as to pull the flame inside of the porous matrix. For $\epsilon = 0.8$ matrices, an increase of the hydrogen content to $\alpha_P = 20\,\%$ generally suffices to trigger the transition. The flame front is tracked live as it performs a *controlled flashback* across the porous matrix (see Fig. 5.1). In the sequence of Fig. 5.1 snapshots are labeled with the elapsed time from the start of the transient phase. Note that a relatively fast transition can be achieved without matrix breakage. The enhanced thermal shock resistance has proven to be a major advantage of metallic PMBs when compared to their ceramic counterparts. Their improved durability largely simplifies burner operation by reducing the risk of fracture and hence the laboratory time. Continuous surveillance is needed during the transient phase in order to prevent a flashback once the flame is close to the inlet. When the flame reaches the bottom of the burner, hydrogen content, α_P, power, P, and equivalence ratio, ϕ are re-adjusted and set to a known stable operating point. The system is then allowed to reach thermal equilibrium.

5.3. Results & Discussion

In this chapter, two different PMBs with the same pore size and different porosity, ϵ, are analyzed. Their topological parameters, including the solid and gas phase tortuosities, τ_s and τ_g, and the interphase volumetric surface, S_v, are gathered in Tab. 5.1.

Table 5.1. – Topological parameters of the PMBs.

d_p [mm]	ϵ	S_v [m^{-1}]	τ_g	τ_s
2.5	0.5	659	1.58	1.58
2.5	0.8	729	1.19	2.52

Figure 5.2 depicts three 1 kW CH_4–Air flames with distinct equivalence ratios stabilized in the $\epsilon = 0.8$ PMB. Post-treated images are presented in the left column, where the interpolated flame position is indicated with a white dotted line. On the right, the experimental profiles of $CH^\star$ and their beta-prime fit are displayed in red dotted and black dashed lines, respectively. Additionally, solid blue lines represent the normalized temperature profiles acquired via the thermocouples. Near the flashback limit, flames stabilize close to the burner inlet, as illustrated in the lower plot of Fig. 5.2. As the equivalence ratio is decreased, flames gradually shift downstream, stabilizing at higher $\xi = x/L$ values. At the blowoff limit, top plot of Fig. 5.2, flames stabilize approximately in the middle of the burner. Note that the flame front is reasonably flat across the transverse direction, which suggests that a one-dimensional model is a reasonable first approximation.

5.3.1. Influence of porosity

The influence of porosity on the PMB performance is now examined for CH_4-Air mixtures. Figure 5.3 shows the experimental points in the $P - \phi$ map for the two burners considered. The blowoff and high-temperature limits are marked with dashed and dash-dot lines, respectively. The shaded region outlines the estimated boundaries of the burner's operating domain. Dashed areas in the upper right corners denote unexplored regions due to thermal constraints of the material. In these zones, the elevated temperatures reached inside the PMB can lead to severe deformation of the porous structure. Figure 5.3 shows that the stability domain of the burner is directly affected by ϵ. When the porosity is lowered from $\epsilon = 0.8$ to $\epsilon = 0.5$, the operating domain is shifted towards higher equivalence ratios. This can be explained by an analysis of the kinematic balance between the flow velocity, u_B, and the local flame speed, S_L. When the porosity is reduced, the effective burner section is reduced by the same factor and velocities inside the porous matrix increase for an imposed mass flow rate. Therefore, in order to ensure a kinematic balance between the flow and flame velocities, higher values of S_L are required. The local flame speed can be enhanced either by increasing the recirculation efficiency, η_{rec}, or by operating at larger equivalence ratios, ϕ. *Ceteris paribus*, recirculation efficiency decreases with porosity [63]. However, porosity variations also drive changes in other parameters such as the specific exchange surface, S_v, which directly scales the heat exchange term, h_v. Thus, predicting its influence is not straightforward in practice.

In PMBs, heat recirculation enables increasing the mass consumption rate per flame unit surface. This increase is quantified by the flame speed-up, defined as the ratio between the bulk velocity in the PMB, computed as $u_B = \dot{m}/(\rho_{in} A \epsilon)$, and the laminar burning velocity at inlet conditions, $S_{L_0}(\phi, T_{in})$. Here, $\dot{m}$ and $A = \pi D^2/4$ denote the total mass flow rate and the burner section, respectively. In finite PMB, the speed-up is a function of the position of the flame in the burner [63]. Our novel experimental setup allows measuring the evolution of the speed-up with the flame position, x_f, and comparing it to theoretical predictions. Figure 5.4 displays the

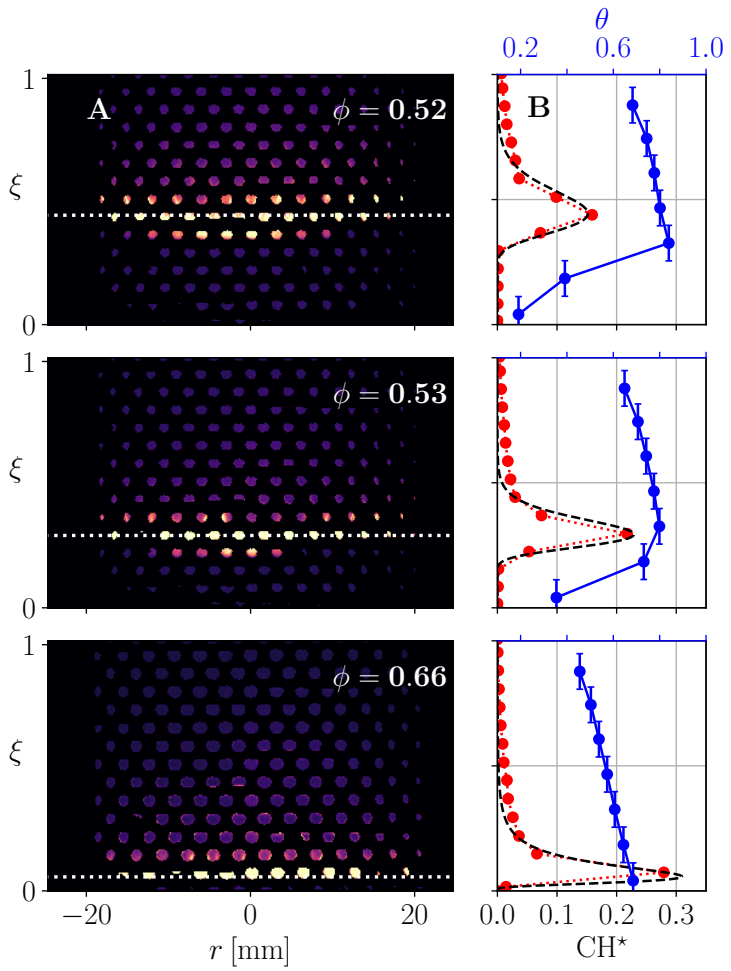

Figure 5.2. – A) Line-of-sight integrated CH⋆ signal for three 1 kW CH_4-Air flames at different equivalence ratios. B) Profiles of CH⋆ and normalized temperature, $\theta = (T - T_{in})/(T_{ad} - T_{in})$, as a function of the axial position, $\xi = x/L$.

results for CH_4-Air flames with different powers for the two burners under investigation. For $u_B/S_{L_0} \simeq 1$, flames stabilize in the vicinity of the burner inlet, $\xi = 0$. Due to heat losses, some of these flames can feature a speed-up smaller than unity. Unfortunately, the overheating limit of the burner was here reached before flashback occurrence and thus the u_B/S_{L_0} at flashback is not available for CH_4-Air flames. When u_B/S_{L_0} is increased, the flame is progressively pushed towards the burner outlet. u_B/S_{L_0} is maximum around $\xi_f \simeq 0.5$ and a further increase in the bulk to laminar flame speed ratio leads to blowoff. At the blowoff limit, the flame speed-up rises to approximately $u_B/S_{L_0} \simeq 7$ in both burners. For the limited power range reported here, the burner load does not affect the flame stabilization in terms of $u_B/S_{L_0}(\xi_f)$. Overall, ϵ is found not to alter the speed-up at blowoff but it has an impact on the shape of the $u_B/S_{L_0}(\xi_f)$ curve. In periodic structures, local anchoring effects can result in discrete jumps of the flame front position. In the $\epsilon = 0.5$ PMB, the discretization of the flame position, ξ_f, is more relevant and results in a different shape of the speed-up stabilization curve. This explains the larger spreading of experimental points around $\xi_f \simeq 0.2$ in the $\epsilon = 0.5$ burner.

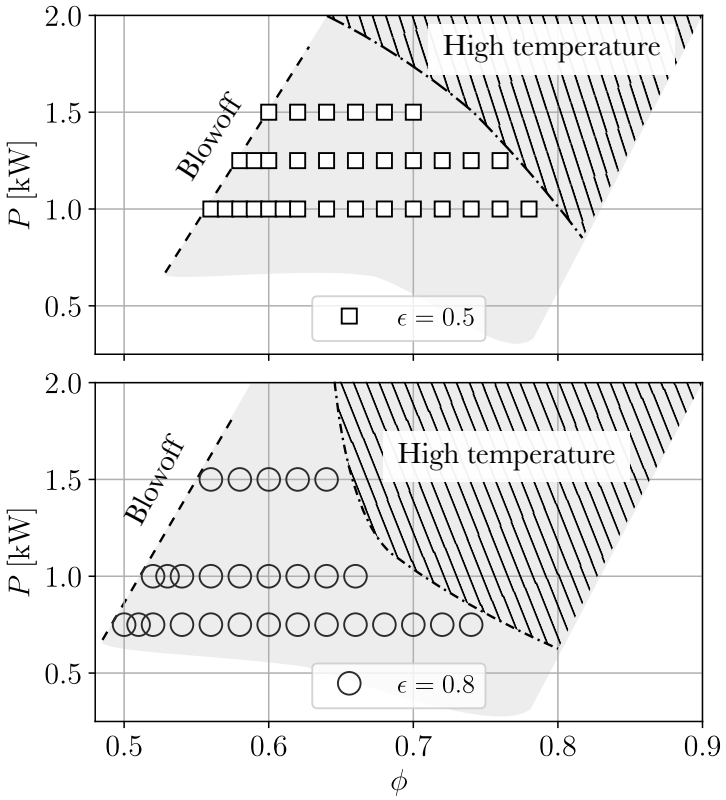

Figure 5.3. – Operating domain spanned by power, P, and equivalence ratio, ϕ, for CH_4-Air flames in PMBs with different porosities $\epsilon = 0.5$ and $\epsilon = 0.8$.

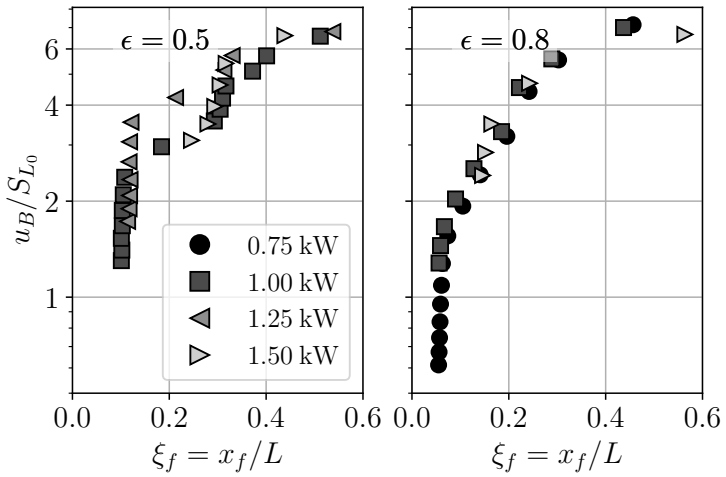

Figure 5.4. – Flame speed-up, u_B/S_{L_0}, versus flame position, $\xi_f = x_f/L$, at various powers for two porosities, ϵ.

5.3.2. Influence of H_2-enrichment

The influence of hydrogen enrichment on flame stabilization is now discussed. The operating domain of the $\epsilon = 0.8$ burner spanned by Power, P, and equivalence ratio, ϕ is displayed in Fig 5.5a. The blowoff, flashback and high temperature limits are indicated with dotted, solid and dashed lines, respectively. For the sake of clarity, no shadowed regions are included here. Different markers are used for each hydrogen power fraction, α_P. Note that the $\alpha_P = 0\%$

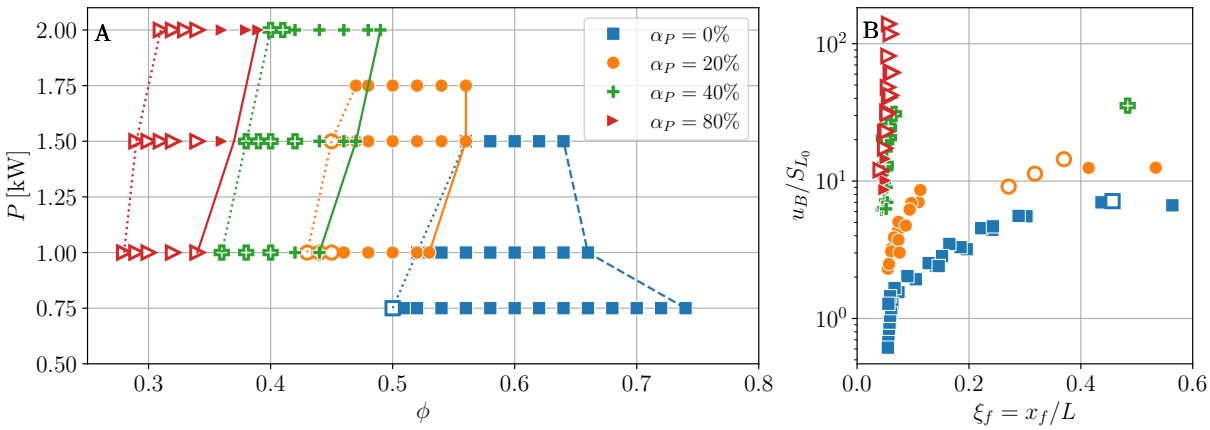

Figure 5.5. – A) Operating domain of the $\epsilon = 0.8$ burner for different hydrogen power fractions, α_P, in the $P - \phi$ space. B) Flame speed-up, u_B/S_{L_0}, versus normalized flame position, $\xi_f = x_f/L$, for different powers and hydrogen contents.

points in Fig. 5.5a are those of Fig. 5.3 with $\epsilon = 0.8$. Empty markers denote operating points where the laminar burning velocity S_{L_0} is lower than $0.5\,\mathrm{cm\,s^{-1}}$. For those operating points, combustion in the absence of heat recirculation is virtually impossible. Safety considerations make of combustion beyond flammability limit a major asset of PMBs for practical applications. Hydrogen content has a first order impact on the operating equivalence ratios. As shown in Fig. 5.5a, the operating domain of the burner is shifted towards lower equivalence ratios for increasing values of α_P. As a rule of the thumb, the operating equivalence ratio ϕ is reduced by $\Delta\phi = 0.1$ every time the hydrogen power fraction is doubled. In the $\epsilon = 0.5$ PMB (not shown here), operating domains are slightly shifted towards higher equivalence ratios but the overall behavior is the same. In Fig. 5.5b, the speed-up u_B/S_{L_0} is plotted against the flame normalized position for different powers and hydrogen contents, α_P. The addition of hydrogen has a direct impact on the flame stabilization. A H_2-enrichment of $\alpha_p = 20$ % results in an upward displacement of the stabilization curve, but the overall behavior remains roughly the same. A larger increase in the hydrogen content to $\alpha_P = 40$ % drives a substantial change in the stabilization trend of the flame. For increasing u_B/S_{L_0} ratios, highly H_2-enriched flames remain attached to the burner inlet, anchoring to the first row of pores at roughly $\xi_f \simeq 0.05$. Then, when a critical speed-up is reached, these flames are blown off the burner. As the H_2 content is increased, the stabilization curve $u_B/S_{L_0}(\xi_f)$ becomes very stiff. This is a significantly different behavior than that usually predicted by Volume Averaged Models (VAMs) and theory and it was also observed in 3D DNS [76, 182]. Note that the mass consumption rate per flame unit surface can rise to nearly $u_B/S_{L_0} \simeq 140$ for $\alpha_P = 80$ %. The $u_B/S_{L_0}(\xi_f)$ stabilization curves display a similar trend in the $\epsilon = 0.5$ burner. Hydrogen flames feature larger Zeldovich numbers and are thus more sensitive to preheating than methane flames. However, in H_2-enriched flames, the different stabilization trends observed in Fig. 5.5b suggest the existence of flame speed enhancement mechanisms other than preheating. To dig deeper into this question we compare the flame mass consumption rate observed in experiments, u_B, to the flame speed-up predicted by the asymptotic model of [63], S_{L_P}. In this theoretical model, heat recirculation is the sole flame-stabilization mechanism and mixture sensitivity to preheating is accounted for via the Zeldovich number. Hence, variations in u_B/S_{L_P} with the hydrogen content hint towards the existence of other stabilization mechanisms. To compute S_{L_P} we impose the flame position observed in experiments, ξ_f and evaluate the theoretical model. Model parameters are computed as follows: topology dependent parameters are extracted from Tab. 5.1; gas constants such as density, ρ_{in}, specific heat, c_{p_g}, thermal conductivity, λ_g, and viscosity, μ, are

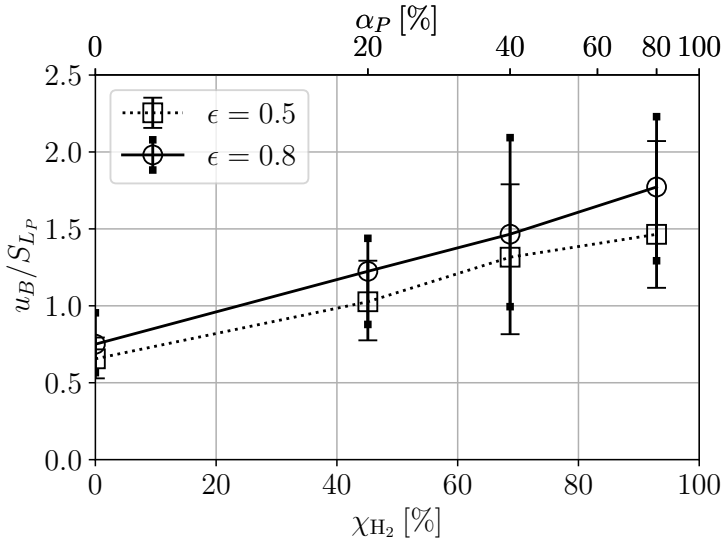

Figure 5.6. – Evolution of the ratio between the experimental and the theoretical speed-up, u_B/S_{L_P}, with the H_2 content.

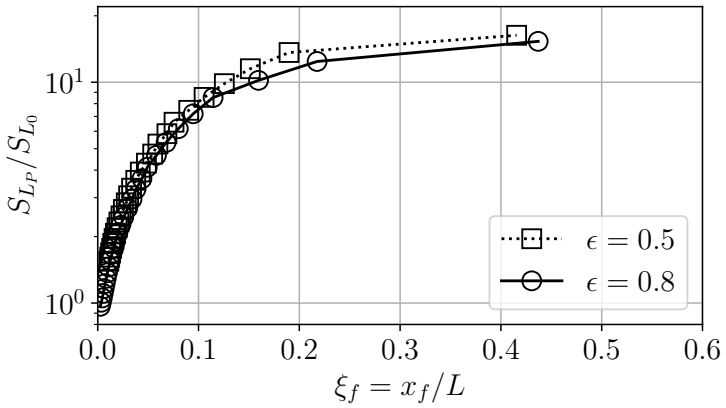

Figure 5.7. – Theoretical speed-up, S_{L_P}/S_{L_0}, versus flame position, ξ_f, for 1 kW CH_4-Air flames in the two burners with different porosity, ϵ.

evaluated at the fresh gases temperature, T_{in}, and computed using the UCSD kinetic scheme; the interphase heat transfer coefficient is $h_v = S_v \lambda_g \mathrm{Nu}/d_p$, where the Nusselt number Nu is calculated using the correlation presented in [68] and the pore-based Reynolds and Prandtl numbers are defined as, $Re = \rho u_B d_p/\mu$ and $Pr = c_{p_g}\mu/\lambda_g$, respectively. A solid thermal conductivity of $\lambda_s = 13$ W m^{-1} K^{-1} is assumed and radiative thermal losses at the burner ends are taken into account. In this asymptotic model [63], different expressions can be used to evaluate the flame speed ratio as a function of heat recirculation $S_{L_P}/S_{L_0}(\eta_{\mathrm{rec}})$. Here, the speed-up correlation developed by [60] is chosen.

Results are plotted in Fig. 5.6 as a function of the hydrogen molar fraction in the fuel, χ_{H_2}, for both burners. For each hydrogen content, u_B/S_{L_P} is averaged over the whole dataset and the vertical lines correspond to the maximum and minimum values. For CH_4-Air flames, the u_B/S_{L_P} ratio should be equal to one but the obtained values are about 0.7. This means that speed-ups measured in the experiment are smaller than those predicted by the asymptotic model. These differences can be attributed to the numerous simplifications made in the derivation of the asymptotic model. Strong assumptions such as constant transport coefficients and zero radial heat losses hinder quantitative predictions. However, these modeling limitations are expected to

affect all flames rather equally, regardless of the fuel composition. Despite the fact that the model does not include radial heat losses, it does account for in/outlet losses by radiation. Switching them on/off only shifts the curves in Fig. 5.6 downwards by $2-7\%$ but does not affect the trends. Thus, when comparing u_B/S_{L_P} ratios for different hydrogen contents the error should remain constant. In other words, if preheating is the sole mechanism responsible for flame speed-up, the u_B/S_{L_P} ratio should be independent of the mixture composition. Figure 5.6 reveals that the ratio between the observed and the predicted speed-up increases with the hydrogen molar fraction. Despite the significant dispersion in the results, the trend is clear and this supports the idea that a mechanism different from preheating affects flame speed-enhancement in H_2-enriched flames. Note that in Fig. 5.6, the u_B/S_{L_P} ratio is also mildly affected by the porosity ϵ. This is because its influence on the speed-up is not quantitatively captured by the model. Changing the porosity affects other topological parameters that have a strong impact on h_v. Thus, the influence of porosity on simulations is, to a certain extent, encapsulated in h_v. The evaluation of the asymptotic model with different off-the-shelf correlations for the Nusselt number affects the predicted speed-ups yet it does not alter the conclusions drawn from Fig. 5.6. For the sake of comparison, Fig. 5.7 shows the theoretical speed-up curves for 1 kW CH_4-Air flames in the two burners with different porosity ϵ. The comparison between Figs. 5.7 and 5.4 confirms the overall qualitative agreement despite the over-prediction by the model. It has been checked that the kinetic mechanism is not at the origin of these discrepancies, which are very likely due to the underestimation of heat losses in the theoretical model.

For non-unity Lewis-number fuels such as H_2, preferential diffusion effects are known to play a major role in flame stabilization [208]. Recent 3D-DNS [76, 182] revealed that the formation of locally enriched pockets caused by flame-front curvature has a strong impact on flame stabilization in PMBs. Therein, it was shown that hydrogen flames can accommodate larger mass flow rates by stretching and increasing their surface without moving downstream. Here, flame front tracking has revealed a different stabilization trend in highly H_2-enriched flames. Then, the influence of the Zeldovich number has been removed via normalization by the theoretical flame speed S_{L_P}. Variations in the u_B/S_{L_p} ratio with hydrogen content suggest the existence of other flame speed enhancement mechanisms different from preheating in H_2-enriched flames. These results reinforce the claim that Lewis number effects must be taken into account for an accurate evaluation of the flame speed-up.

5.4. Conclusions of the chapter

In this chapter, flame-front tracking has been used to study the influence of porosity and H_2-enrichment on flame stabilization in PMBs. The analyzed porosity variation was found to alter the operating equivalence ratios, ϕ, but did not affect the blow-off limit in terms of speed-up, $u_B/S_{L_0}(\xi_f)$. A comparison with the theoretical model presented in [63] reveals that quantifying the influence of porosity is challenging. This is because theoretical predictions are very sensitive to the modeling of the heat exchange term, h_v, which is in turn influenced by porosity variations. Moreover, H_2 enrichment is found to shift the operating domain towards lower equivalence ratios and to alter the flame stabilization. Qualitative differences between the stabilization of CH_4-Air and H_2-enriched flames suggest the existence of different stabilization mechanisms for non-unity Lewis-number fuels. Comparison with a theoretical model allows separating the sensitivity to preheating and brings to light other stabilization mechanisms. Variations of the u_B/S_{L_P} ratio with the hydrogen content point out the existence of other flame speed enhancement mechanisms in H_2-enriched flames. The present experimental results are consistent with recent observations made in 3D-DNS of premixed H_2-Air flames that could stabilize and accommodate large flow rates while being anchored at the inlet. Therein, preferential diffusion effects were shown to play a major role on flame stabilization in PMBs. These experiments provide further evidence that these phenomena need to be modeled if an accurate description of the burning rate is sought. Future work must address these modeling tasks and seek pore-level diagnostics to unveil the details of flame stabilization in PMBs.

Chapter 6

Pore-scale laser diagnostics

This chapter is based on the article **"Mie-scattering imaging and μPIV in porous media burners with TPMS-based topologies"** by **E. Flores-Montoya, S. Cazin, T. Schuller and L. Selle** (submitted to Combustion and Flame).

In this chapter, Mie-scattering imaging, $CH^\star$ chemiluminescence and μPIV are applied in various optically accessible Porous Media Burners (PMBs). The 3D printed PMBs used in this chapter feature optical pathways that are both orthogonal and coincident, so that one can be used for illumination and the other for imaging. This enables the application of laser diagnostics in fully 3D structures whilst avoiding altering the geometry of the porous medium. These techniques are applied in homogeneous porous burners where the position of the flame is determined by the operating conditions. First, flame topography from Mie-scattering images is combined with $CH^\star$ chemiluminescence imaging to analyze the influence of the flame position on the preheating distance of the reactants. Then, Mie-scattering imaging and μPIV measurements are used to study the structure of inlet-anchored flames for different topologies, pore-sizes and hydrogen contents. The topology is found to have a major impact on the interstitial flow and flame stabilization. A new topological parameter, namely the linear porosity, is proposed to quantify the influence of local hydrodynamic effects on flame stabilization.

Overview

6.1. Introduction **90**
6.2. Experimental setup **91**
6.2.1. Seeding system 92
6.2.2. The POROSITO test rig 92
6.2.3. Laser-suited PMBs 94
6.2.4. Influence of seeding 95
6.3. Mie-Scattering in a PMB **96**
6.3.1. Preliminary considerations 96
6.3.2. Results 99
6.4. PIV measurements at the scale of a pore **100**
6.4.1. Diagnostics setup 100
6.4.2. Calibration process 101
6.4.3. Experimental procedure 103
6.4.4. Images processing 103
6.4.5. Results 103
6.5. Influence of the burner topology **108**
6.6. Conclusions of the chapter **111**
6.A. Supplementary material **112**

"*Do it fast first, then you'll do it right.*"

Laurent Selle

6.1. Introduction

The mechanism of heat recirculation in PMBs is well understood [60–64] and the macroscopic behavior of flames within porous matrices has been extensively documented [39, 59, 65, 66]. However, there is still limited knowledge about many pore-scale phenomena such as the thermal quenching, preferential diffusion effects and flame wrinkling [67–69]. These local phenomena have a critical impact on the macroscopic behavior of the system and its performance. Low order models such as Volume Averaged Models (VAMs) do not incorporate the modeling of all these local phenomena, which results in a poor accuracy [67, 68, 70]. Improving the predicting power of current VAMs could help designing more efficient and fuel-flexible combustion devices. For that, it is crucial to gain understanding into the complex flame-wall interactions at the pore level so that the appropriate upscaling parameters and emerging properties are incorporated into current models. A deeper understanding of these processes can be achieved via advanced diagnostic techniques such as Planar Laser Induced Fluorescence (PLIF) [151], Coherent Anti-Stokes Raman Scattering (CARS) [152, 153] and X-ray Computed Tomography [69, 101].

In the literature, there are only a few examples of pore-level diagnostics [86, 151–153]. One of the first examples of pore-level diagnostics is found in [152, 153], where CARS is used to measure the gas phase temperature and the H_2 concentration in a two-stage reactor. Later on, [151] carried out OH-PLIF measurements to visualize the flame front through a narrow slit in a PMB. In these studies, optical access is limited and achieved either by using very large pores or by creating narrow gaps inside the porous matrix, thus altering the burner geometry. A notable exception is the use of X-ray tomography [101], which allowed the reconstruction of the temperature field in a multi-layer SiC burner. This technique has also been used in combination with infrared thermometry [69] to obtain a full reconstruction of the temperature field in both phases of the burner at a micrometric scale. However, μX-ray tomography is very complex and requires the addition of Krypton to enhance the X-ray contrast. Recently, direct visualization of the flame front was achieved in a 2D configuration where optical access was provided by quartz walls and a single-layer packed-bed configuration [79]. Another example of direct flame visualization is found in the work of [154], who performed chemiluminescence measurements in a 2D array of cylinders with a staggered configuration.

One of the main difficulties is the availability of an optical pathway to the interior of the porous medium. However, TPMS-based topologies usually have see-through directions with extensive optical access to the interior of the porous matrix without disturbing the geometry. This was demonstrated in [163] where topology tailoring was combined with Additive Manufacturing (AM) techniques to produce optically accessible burners. So far, the extensive optical access offered by TPMS-based topologies has been used to obtain line-of-sight integrated $CH^\star$ chemiluminescence images. This has allowed the direct visualization of the flame inside the burner and the tracking of the reaction zone as a function of the operating conditions. Flame-front tracking has been proposed as an useful input for model validation and has revealed different stabilization trends in H_2-enriched flames [163, 164]. However, the technique offers limited information about the flame structure inside the pores because some of the pore-level details are lost in the line-of-sight integration process.

In this chapter, the optical access provided by TPMS-based topologies is leveraged to apply two laser diagnostics at the scale of the pore: flame topography from Mie-scattering imaging and Micro Particle Image Velocimetry (μPIV).

Mie-scattering imaging is a broadly-extended planar flow-imaging technique in reactive flows [162, 209–211]. In these diagnostics, the flow is seeded with small particles and the change in the seeding density across the flame front is used to obtain the boundary between the fresh reactants and the burned products. Mie-scattering is used as a flame surface detection technique that provides comparable results to those of $CH^\star$ chemiluminescence and OH-PLIF. It can be used to compute the fractal dimension of turbulent flames and to perform a 3D-tomographic reconstruction of the flame surface [212]. However, Mie-scattering has never been applied in the context of porous reactors. This work represents the first experimental demonstration in a PMB and will bring to light how this diagnostic can be exploited to study the heat recirculation mechanism.

PIV is probably the most widespread non-intrusive experimental technique in fluid mechanics [213–217] and it has been applied to porous media flows in a wide variety of configurations [218–223]. Nonetheless, PIV measurements in porous media have only been conducted in non-reactive flow conditions so far. Overall, we can distinguish two main approaches. On the one hand, we find PIV measurements in regular 2D structures that aim to reproduce the flow conditions found in realistic 3D porous media. To replicate the flow conditions found in porous media, a set of rods perpendicular to the bulk flow direction are arranged in a regular configuration [219, 220, 224, 225]. This solution provides full optical access to the fluid phase but is limited to two-dimensional porous structures. The technique permits the variation of the void fraction by adjusting the cross-section area of the rods and their spacing. This approach was combined with AM to produce a transparent fractured porous media structure in [221].

In other cases, the technique is applied in packed bed configurations [218]. In 3D packed bed structures, the lack of optical access must be compensated using a transparent solid phase. However, in this case, differences between the refractive index of the solid and fluid phase can produce image distortion [223]. As a result, the refractive index of the fluid phase has to be tuned to match that of the solid. To do so, a mixture of fluids with different refractive indices has to be prepared with high accuracy. Whereas cross-flow arrays of rods are limited by the two-dimensional nature of the porous structure, packed-beds are limited in terms of porosity range, with achievable porosities narrowing down to $\epsilon \simeq 0.36 - 0.42$.

In this chapter, 2D velocity fields are measured in a TPMS-based porous medium in reactive flow conditions and at the pore-scale. Owing to the small scale of the system and the steadiness of the flow, μPIV post-processing techniques can be applied [226, 227]. In contrast to previous examples of PIV measurements in porous media, here the optical access is granted by the see-through directions of the porous structure so it is not required to use a transparent solid matrix. The main drawback of TPMS topologies is the lack of full optical access to the fluid phase in the laser plane and the partial loss of information.

The remainder of the chapter is organized as follows. Section 6.2 describes the experimental setup with a focus on the modifications with respect to Chapter 2. In Sec. 6.3, Mie-scattering imaging and $CH^\star$ chemiluminescence are applied at the macroscopic scale across the stability domain of the burner. Section 6.4 presents the results of μPIV measurements at the pore scale combined with flame topology for inlet-anchored flames. Section 6.5 analyzes the influence of the porous structure on flame stabilization based on macro and microscale diagnostics and, finally, Sec. 6.6 outlines the conclusions of the chapter.

6.2. Experimental setup

Experiments are performed in the POROSITO test rig presented in Chapter 2. Yet a thorough description of the experimental setup and procedure were made in Chapter 2, the diagnostics presented in this chapter require several modifications of the apparatus. For both Mie-scattering and μPIV, the flow must be seeded with small flow tracers. This implies at least the incorporation of an aerosol generator in the air flow pipeline. Other modifications include the removal of

thermocouple probes located inside the porous structure to avoid reflections. In this section, the changes in the experimental setup with respect to Chapter 2 are described in detail.

6.2.1. Seeding system

The air line is bypassed right after the air mass flow controller and part of the air stream flows through the seeding system. The rest is premixed with the fuel and injected normally into the burner bulk stream. The air seeded with particles is re-injected at the plenum section, before the convergent. The seeding density is adjusted by controlling the mass flow rate on each air stream with two needle valves. The seeding particles are micrometric oil droplets produced with an air nebulizer. The mineral oil Edwards Ultragrade Performance 15 was used in this study. The oil vaporization temperature is $T_v = 225°$. As shown by [228], this kind of seeding system produces a seeding of oil droplets with a mean droplet diameter of 2.63μm. A major drawback of the present seeding system is the manual control of the seeding density. Therefore, the operator of the experimental setup is in charge of maintaining the homogeneity between experimental realizations. Despite this limitation, a good repeatability in the experiments was obtained as shown in Sec. 6.2.4. Low seeding densities have been used to limit the intrusiveness of the measurements on the combustion process. This question is also addressed in Sec. 6.2.4, where the impact of the seeding particles on flame stabilization is quantified. In Mie-scattering imaging, the low seeding density can be overcome using long exposure times. In μPIV measurements it was necessary to average the velocity field over a large number of snapshots, which is the standard approach in μPIV experiments [214].

6.2.2. The POROSITO test rig

Figure 6.1 shows different views of the POROSITO test rig. In the schematic of 6.1a, the front view of the burner is depicted. Premixed reactants seeded with oil droplets enter the burner from the bottom and go through a convergent section. In order to have a homogeneous laminar flow a multi-layer homogenization system is placed at the outlet of the convergent. This homogenization system replaces the previous one, which consisted of a sintered steel plate. Sintered steel plates render a flat laminar velocity profile but prevent the passage of oil droplets and hence the application of laser diagnostics. The multi-layer homogenization section includes a perforated plate, a layer of packed bed spheres, a honeycomb section and several micrometric grids between these elements. The straight-duct section is cooled down to $T_w = 293$ K by a recirculating bath and two K-type thermocouples are used to measure the reactants inlet temperature right before the porous matrix, T_{in}. These thermocouples have different bead sizes and their readings are combined following the methodology of [174] to correct for thermal radiation. After this correction, the uncertainty in the inlet temperature value is ± 10 K. The inlet temperature correction is thoroughly described in Sec. 2.28.

This inlet temperature is later used to evaluate the flame properties such as the adiabatic flame temperature, T_{ad}, the laminar burning velocity S_{L_0}, the flame thickness $\delta_T = (T_{ad} - T_{in})/\max(\partial_x T)$. It is recalled that the hydrogen power fraction, $\alpha_P = \dot{m}_{\mathrm{H}_2} Q_{\mathrm{H}_2}/P$, is used to quantify the proportion of H_2 in the fuel. Here, P denotes the total thermal power, $\dot{m}_{\mathrm{H}_2}$ the hydrogen mass flow rate and Q_{H_2} its lower heating value. Inlet temperature measurements are also used to assess the steadiness of the system in these experiments.

Two different laser systems have been used for macroscopic flame topography and μPIV. Lasers are mounted on a movable platform that allows for both lateral (z-axis) and vertical displacement (x-axis). They are equipped with a LaVision sheet optics that transforms the laser beam into a laser sheet with a small divergence angle. In the flame topography experiments, a COHERENT VERDI G with a maximal output power of 20 W, a beam propagation ratio $M^2 < 1.1$, and a 532 nm wavelength has been used. With this device, the laser sheet thickness measured using

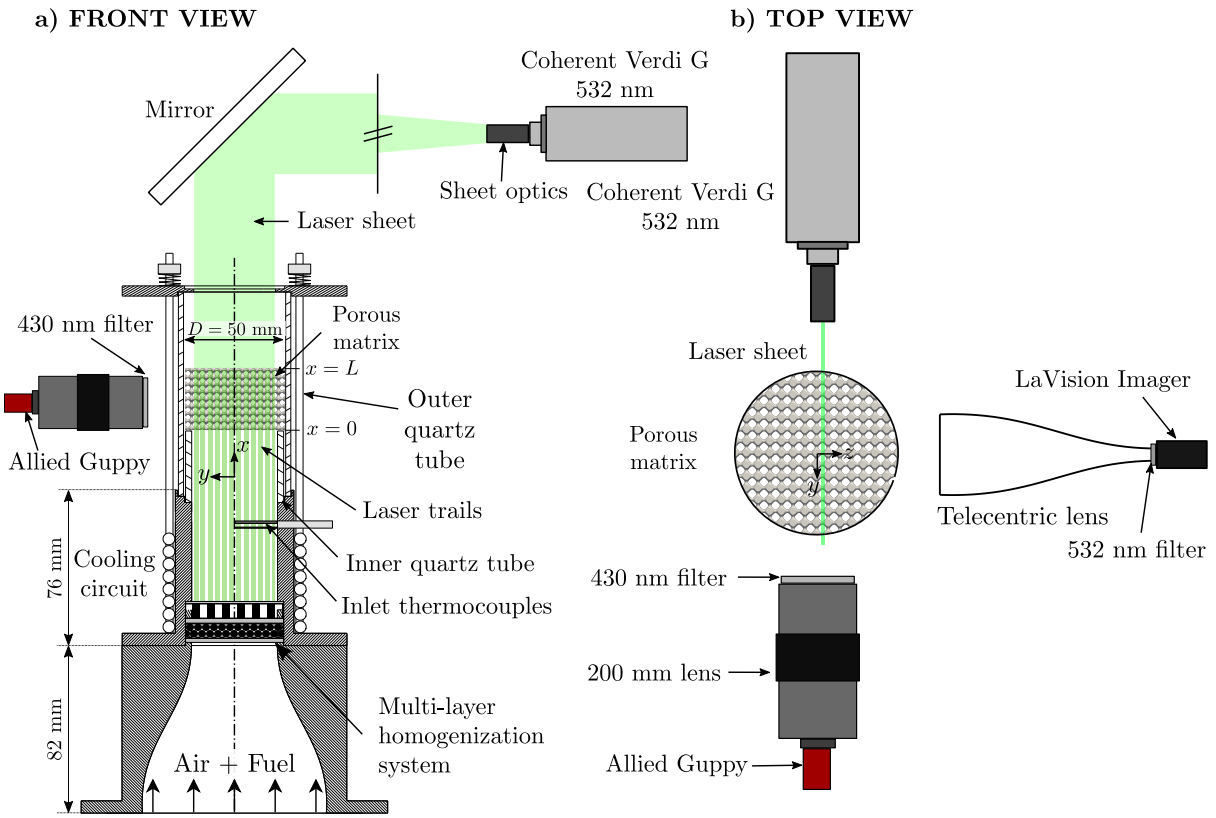

Figure 6.1. – Experimental setup of the POROSITO test rig.

photosensitive paper was $\lesssim 1$ mm. The laser system used in μPIV experiments is described in Sec. 6.4.1. The laser sheet enters the porous medium from the top. For that, a mirror is installed above the burner. A slit injector is used to protect the mirror from the hot combustion products via film cooling. The orientation and the positioning of the laser sheet must be carefully adjusted in these experiments. A fine tuning of the laser plane orientation is achieved by rotating the mirror with two orthogonal high-precision goniometers. The translation of the laser sheet in the z-direction (cf. Fig. 6.1) is adjusted with a micrometric linear stage. As the laser sheet traverses the vertical optical pathways, a characteristic pattern of laser trails is formed upstream of the burner inlet (cf. Figs. 6.1 and 6.4). When the laser plane lies at the center of the pore, the width of these trails is maximal and this can be used to finely tune the z-position of the laser.

The top view of the experimental setup depicted in Fig. 6.1b illustrates the arrangement of the cameras and the laser. Simultaneous Mie-scattering and CH* chemiluminescence images are captured from the two horizontal see-through direction of the burner. The camera Allied-Vision Guppy F-146B is placed in the y-direction. This device mounts a 1388×1038 px sensor with a pixel size of $4.65\,\mu$m and a bitdepth of up to 12 bits. The Allied Guppy camera is used to capture the line-of-sight integrated emission of CH* radicals. For that, the imaging system is fitted with a 200 mm lens and a filter. The bandpass filter has an optical density of 4 and features a central wavelength and a bandwidth of 430 nm and 10 nm, respectively. The exposure time is fixed to 1 s and the gain is adjusted to achieve a good signal-to-noise ratio. Compared to the previous setup [163, 164], the lack of a telecentric lens increases the perspective distortion and reduces the optical access at the burner edges. However, it is still possible to track the position of the flame from CH* chemiluminescence images. Also, here the focus is on the central rows of pores where the distortion due to perspective is smaller. A LaVision Imager SCMOS camera is placed in the z-direction, orthogonal to the laser plane. The resolution of these images is 2560×2160 px

and their bitdepth is 16 bits. The size of the sensor pixels is 6.5 μm. This camera is fitted with a telecentric lens for perspective removal and a bandpass filter. The central wavelength and bandwidth of the filter are 532 nm and 10 nm, respectively. The LaVision Imager collects the scattering of the laser light from the seeding particles in the laser sheet. The exposure time is varied between experimental realizations to achieve a good signal to noise ratio depending on the scattering intensity. Typical exposure times are approximately 200 ms.

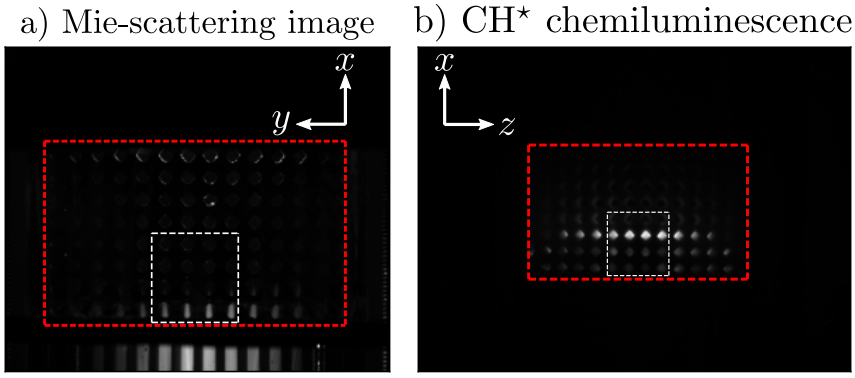

Figure 6.2. – Raw Mie-scattering (a) and CH* chemiluminescence (b) images. The red dotted line indicates the limits of the porous matrix. The focus of the analysis is on the window outlined with white dotted lines in the middle of the burner.

In Fig. 6.2a and b, raw Mie-scattering and CH* chemiluminescence images are shown, respectively. The limits of the porous matrix are indicated with red dotted lines. In the Mie-scattering images, the laser trails can be observed upstream of the burner inlet. The focus of the analysis is on the central window outlined with white dotted lines. Backlight images are generated for both views so that a mask can be applied during the processing of images.

6.2.3. Laser-suited PMBs

In this chapter, five different PMBs have been analyzed. Their topological parameters are gathered in Tab. 6.1. Burners B1 and B2 have a Primitive-based topology with a volumetric porosity of $\epsilon = 0.7$ and different pore sizes. Burner B3 features a porosity of $\epsilon = 0.8$ and has a Gyroid-based topology. The TPMS equation for each topology and the lattice parameters are described in Sec 2.2. These two topologies have orthogonal see-through directions with optical pathways that intersect inside the burner. Therefore, the volume where they overlap can be studied with laser techniques if one of the optical pathways is used for imaging and the other for illumination. This is why we term these topologies as laser-suited. Burners B4 and B5 feature a Diamond topology and different porosities. These burners are not laser-suited and are used here only to compare their macroscopic stabilization properties with those of the Primitive topology in Sec. 6.5. A detailed analysis of the optical properties of this topology is presented in [163].

Table 6.1. – Topological parameters of the different PMBs.

Burner	Topology	ϵ [–]	d_p [mm]	τ_g [–]	τ_s [–]	S_v [m^{-1}]
B1	Primitive	0.7	3.5	1.265	2.237	615.5
B2	Primitive	0.7	2.5	1.265	2.237	861.6
B3	Gyroid	0.8	3.5	1.198	2.431	552.0
B4	Diamond	0.5	3.5	1.581	1.581	470.6
B5	Diamond	0.8	3.5	1.190	2.515	520.8

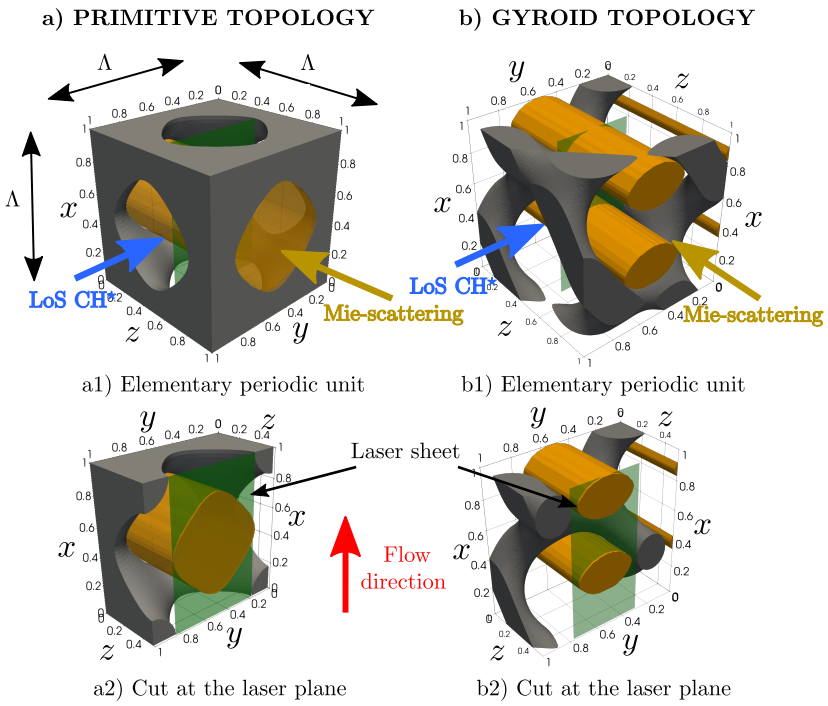

Figure 6.3. – Arrangement of the see-through directions in the Primitive (a1) and Gyroid (b1) topologies. The x-direction is used for laser illumination, and the y and z-directions are used to collect the CH* emission of the flame and the Mie-scattering of particles, respectively. a2 and b2 show the intersection between the laser plane and the see-through direction volume for the Primitive and the Gyroid topology, respectively.

In Fig. 6.3, a 3D rendering of the elementary periodic unit is depicted for the Primitive (a) and the Gyroid (b) topologies. The axes have been normalized with the lattice wavelength, Λ. Following the axes of Fig. 6.3, the x direction is used for laser illumination, y is used to collect the line-of-sight integrated emission of CH* radicals and z is used to visualize the light scattering from the particles in the laser sheet. Figures 6.3a2 and 6.3b2 show a cut at $z = \Lambda/2$. This cut allows visualizing the intersection surface between the laser sheet and the horizontal see through direction. This intersection surface corresponds to the observable area per square wavelength, Λ^2, inside the burner. Yet both topologies allow for laser diagnostics, the observation window is appreciably larger in the Primitive (45.9% of the surface) topology than in the Gyroid (17.5%).

To illustrate the challenges of these experiments various pictures of the burner and the laser sheet are represented in Fig. 6.4. Figures 6.4a and b, show the burner during operation. Here, due to its elevated temperature the solid matrix is emitting part of its black body radiation in the visible spectrum. Figure 6.4b shows the laser trails that are visible upstream of the burner inlet via the scattering of light. Note that these trails cannot be seen downstream because of the evaporation of oil droplets inside the burner. Finally, Fig. 6.4c offers a lateral view of the laser sheet passing through the vertical optical pathways.

6.2.4. Influence of seeding

The presence of oil droplets in the reactants can have an influence on the combustion dynamics. To minimize the intrusiveness of these diagnostics, the total mass fraction of the seeding particles and their size must be limited. As demonstrated by [228], with the present seeding system the mean droplet diameter is less than 3 μm, which complies with the diameter requirements for the

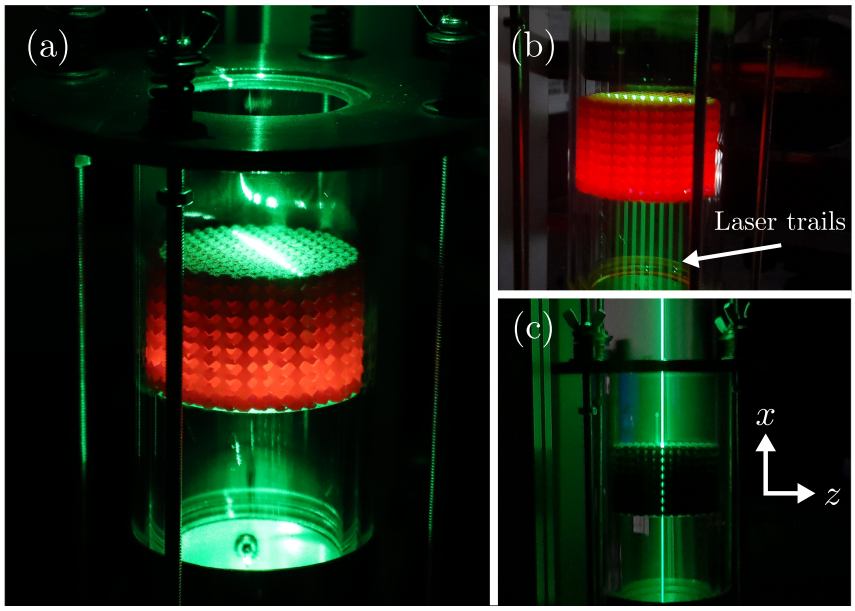

Figure 6.4. – Pictures of the experimental setup during operation (a and b). The characteristic scattering trails are clearly visible in (b).

seeding particles [212]. To check that the seeding densities employed do not significantly alter the chemical kinetics, we have quantified the influence of the seeding on the behavior of the flame inside the burner. Figure 6.5 compares the stabilization curves with and without seeding particles in burner B1. The stabilization curve represents the evolution of the speed-up as a function of the flame position $\xi_f = x_f/L$, where L is the length of the burner. The flame position, x_f, can be directly computed from $CH^\star$ chemiluminescence images as described in Sec. 2.5. The speed-up is defined as the ratio between the actual burning rate, u_B, and the flame speed of a 1D adiabatic flame, $S_{L_0}(T_{in}, \phi)$. The bulk velocity, u_B, is computed as, $u_B = \dot{m}/\rho_{in} A \epsilon$, where $\dot{m}$ is the total mass flow rate, ρ_{in} is the density of the mixture at the inlet temperature, T_{in}, $A = \pi D^2/4$ is the cross-section area of the burner and ϵ is the porosity of the matrix.

In these experiments, a 1 kW methane-air flame is first stabilized at the burner inlet and then the equivalence ratio is progressively reduced at constant power. With this procedure, the speed-up increases as the equivalence ratio is reduced and the flame progressively moves towards the burner outlet. This operation has been performed twice in the presence of seeding droplets and once in the absence of seeding. When the speed-up, u_B/S_{L_0} is plotted against the flame position, ξ_f, the stabilization curves show a good agreement considering the experimental uncertainties. This indicates that the influence of the seeding particles on flame stabilization is marginal and that a good repeatability is obtained.

6.3. Mie-Scattering in a PMB

6.3.1. Preliminary considerations

To the authors' best knowledge, flame topography from Mie-scattering images has not been applied in a PMB. Therefore, several preliminary considerations about this technique must be made before analyzing the results. In a reactive flow, oil droplets evaporate shortly after the surrounding flow reaches the particles' vaporization temperature, here denoted by T_v. In the Mie-scattering images, the evaporation of oil droplets results in a sharp evaporation front. In conventional free flames, Fig. 6.6a, the gas preheating distance is provided by the balance

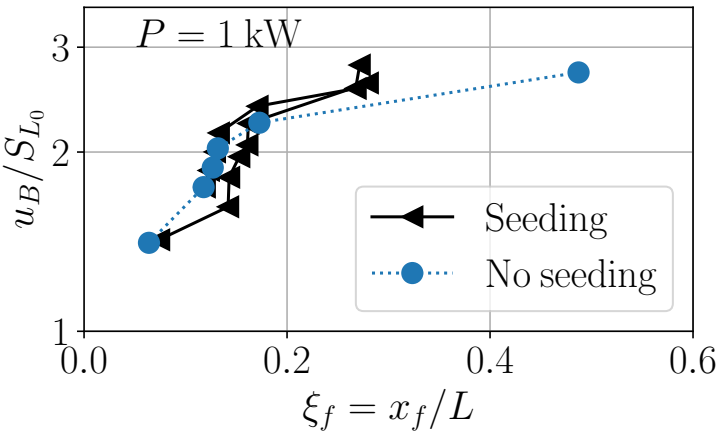

Figure 6.5. – Influence of the seeding on flame stabilization. The stabilization curve represents the speed-up, u_B/S_{L_0}, as a function of the dimensionless position of the flame $\xi_f = x_f/L$.

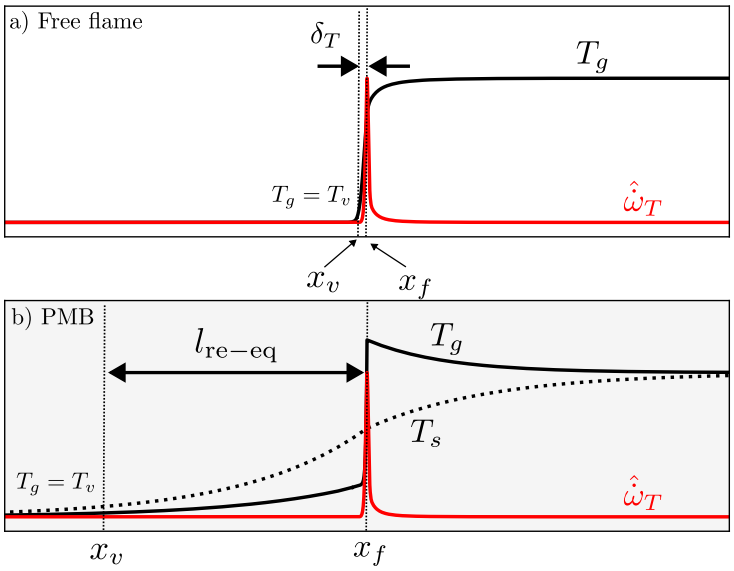

Figure 6.6. – Evaporation, x_v, versus reaction front, x_f, in an adiabatic free flame (a) and in a PMB (b).

between convection and diffusion and is equal to the flame thickness, $\delta_T \sim D_T/S_L$. Therefore, the location of the evaporation front, x_v is approximately at a distance δ_T from the reaction region. In locally adiabatic flames, this distance is of the order of hundreds of microns, which is generally very small compared to the scale of many combustion systems. Hence, in practice, the evaporation and the reaction front are overlapping. This is why Mie-scattering images are typically used to infer the location of the flame front position in unsteady turbulent flows [162, 209–212].

However, in PMBs, owing to the presence of the solid matrix, the preheating of reactants occurs over a larger distance that is often referred to as re-equilibration distance and is here denoted by $l_{\mathrm{re-eq}}$ (cf. Fig. 6.6b). A comprehensive analysis of the characteristic lengthscales in a porous reactor can be found in the works of [60, 63]. From asymptotic analyses [60, 63, 64], it is known that this lengthscale is directly related to the interphase heat exchange term, h_v and the solid thermal conductivity, λ_s. Therefore, in a PMB the evaporation, x_v, and the reaction front,

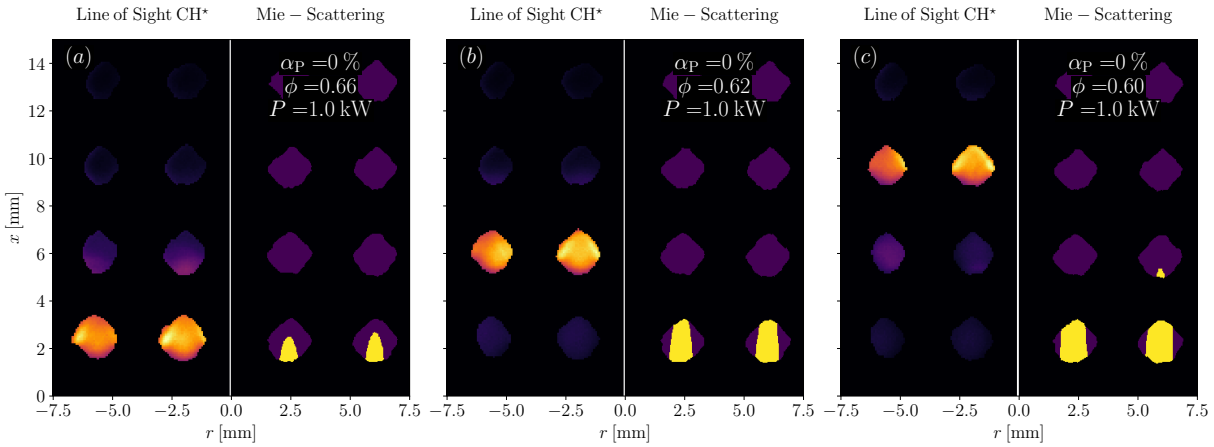

Figure 6.7. – Comparison between Line of Sight integrated CH* chemiluminescence and binarized Mie-Scattering images for 1 kW CH_4/Air flames with different equivalence ratios ϕ: (a) $\phi = 0.66$, (b) $\phi = 0.62$ and (c) $\phi = 0.60$.

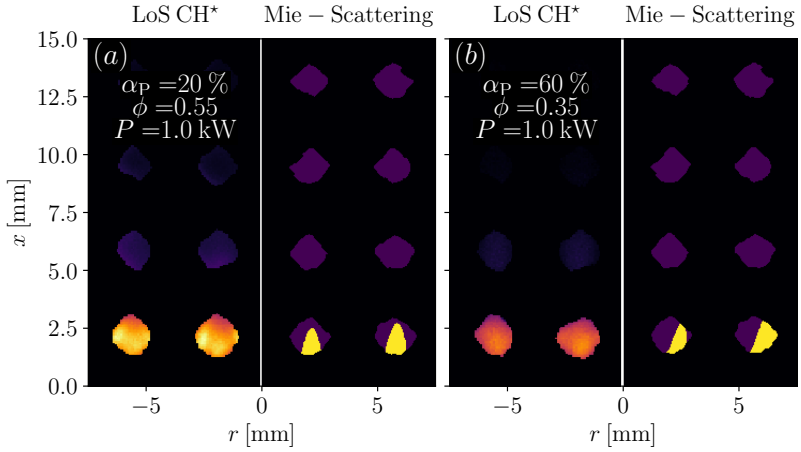

Figure 6.8. – Transition from a symmetrical to an asymmetrical stabilization in a 1 kW inlet-anchored flame when the H_2 content is increased from $\alpha_P = 20\%$ to $\alpha_P = 60\%$. Equivalence ratios are (a) $\phi = 0.55$ and (b) $\phi = 0.35$.

x_f, are not necessarily at the same location. In this respect, Mie-scattering images only indicate the position of the temperature isoline corresponding to the oil evaporation temperature, which is approximately $T_v \simeq 500$ K in the present case. Furthermore, because of the small scale of the system and the droplets evaporation dynamics, it is necessary to analyze the spatial uncertainties of this technique. Following the time-scale analysis of [229] we can estimate the vaporization time, t_v, of an oil droplet as:

$$t_v \sim \rho_d a^2/(\rho_f D_{T_f}) \tag{6.1}$$

where subscripts $-d$ and $-f$ denote the droplets and fluid properties. Upon numerical evaluation using the droplets characteristic size and the air and oil properties, a characteristic evaporation time of roughly 0.2 μs has been estimated. Thus, for flow velocities ranging from 0.5 m/s and 2 m/s the uncertainty in the positioning of the T_v isoline lies between 0.1 and 0.4 mm.

6.3.2. Results

In this section, the stabilization of CH_4-Air flames inside B1 is analyzed by combining the results from Mie-scattering and $CH^\star$ chemiluminescence images. In Figs. 6.7 and 6.8 only the first four rows of pores in the middle of the burner are represented. The zoomed window comprises the region of the burner where a steady combustion process can be sustained in stable conditions [63, 111], i.e. from the burner inlet $x = 0$ to $x = L/2$. This zone is indicated with a white dotted box in the raw images of Fig. 6.1.

In Fig. 6.7, three CH_4-Air flames stabilized inside the burner are shown. For each case, the left side represents the line-of-sight integrated $CH^\star$ signal and the right side shows the binarized Mie-Scattering image. The yellow region indicates the presence of particles and hence fluid temperatures below $T_v = 500$ K. This region is referred to as the cold gasses region. The cases presented in Fig. 6.7 feature the same thermal power, $P = 1$ kW, and different equivalence ratios, ϕ. In Fig. 6.7a, the flame with $\phi = 0.66$ is stabilized at the burner inlet. Note that the evaporation front and the $CH^\star$ signal are located in the same row of pores. When the flame is stabilized close to the burner inlet, the preheating of the reactants occurs at the gas diffusion scale. As a result, the evaporation front is close to the flame front and outlines the flame shape. Here, a conical flame is observed inside the porous matrix cavities. It can also be noticed that the $CH^\star$ signal is more intense on the sides of the pore, which is coherent with the conical shape observed in Mie-scattering images. The lack of symmetry in the $CH^\star$ chemiluminescence images can be explained by perspective distortion since this camera is fitted with conventional optics.

When the equivalence ratio is reduced to $\phi = 0.62$ the flame stabilizes at the second row of pores (Fig. 6.7b). Again, the presence of brighter regions on the sides of the pore in the $CH^\star$ image can be observed. This suggests that the shape of the flame is similar to that of Fig. 6.7a. At this flame location, the vaporization of oil droplets takes place between the first and the second row of optical pathways. The separation between the evaporation front and the reaction region indicates that there is a significant preheating of the reactants due to the heat exchange with the hot solid matrix. This image illustrates the mechanism of heat recirculation in PMBs. It must be noticed that the cold gas zone vanishes on the sides of the optical pathway, revealing that oil droplets evaporate faster close to the solid wall. The high aspect ratio of the cold gasses zone suggests that there are large transverse temperature gradients at the pore-level, which is consistent with the observations of [70] in 2D-DPLS. Finally, Fig. 6.7c represents a 1 kW CH_4-Air flame at the blowoff limit. In this case, the 500 K isoline is located more than one pore upstream of the flame front. The total preheating distance is approximately $l_{\mathrm{re-eq}} \gtrsim 4$ mm so that there is an important scale separation between the gas diffusion scale $l_{\mathrm{diff}} \simeq \delta_T$ and the re-equilibration distance, $l_{\mathrm{re-eq}}$. Therefore, in this burner and at these operating conditions the hypothesis of decoupled combustion regime seems reasonable [64].

Figure 6.8 illustrates the existence of two different stabilization modes inside the porous matrix. In Fig. 6.8, two H_2-enriched flames stabilized at the burner inlet are shown. These flames feature the same power, $P = 1$ kW, but different composition (different hydrogen content, α_P and equivalence ratio, ϕ). When the hydrogen content of the mixture is increased, the equivalence ratio must be adjusted in order to avoid a flashback. At $\alpha_P = 20\,\%$ (cf. Fig. 6.8a), a symmetric conical flame is observed within the matrix cavities. In Fig. 6.8b, a flame with $\alpha_P = 60\,\%$ stabilizing in an asymmetric way inside the pores is represented. Note that it is not possible to tell the difference between the asymmetric and the symmetric flame from the line-of-sight integrated chemiluminescence images. However, thanks to Mie-scattering imaging, it is possible to recognize two different anchoring modes inside a porous burner. It is important to clarify that the asymmetric stabilization has also been observed at smaller hydrogen contents and it is out of the scope of the present work to dig into the underlying mechanisms of this symmetry breaking. The asymmetric stabilization of H_2 flames in PMBs was also reported in

the DPLS of [76].

Mie-scattering images offer a new way of studying the stabilization of flames in PMBs. These results reveal that Mie-scattering images can be used to study the flame shape when flames are stabilized at the burner inlet. This is because, at this location, the preheating of the fresh gasses occurs at the gas diffusion lengthscale. As in locally adiabatic flame fronts, the offset between the reaction zone and the evaporation front is of the order of the flame thickness. When the position of the flame is shifted downstream, the interphase heat exchange preheats the reactants and the evaporation front moves away from the reaction region. Since low vaporization temperature oil droplets are used, the distance between the flame front and the evaporation front can be used to estimate the re-equilibration distance between the solid and the gas phase. Yet a systematic characterization of the re-equilibration distance is not presented here, the proposed technique can be used to analyze and compare the characteristic lengthscales, the combustion regime and the recirculation efficiency of different porous matrices.

6.4. PIV measurements at the scale of a pore

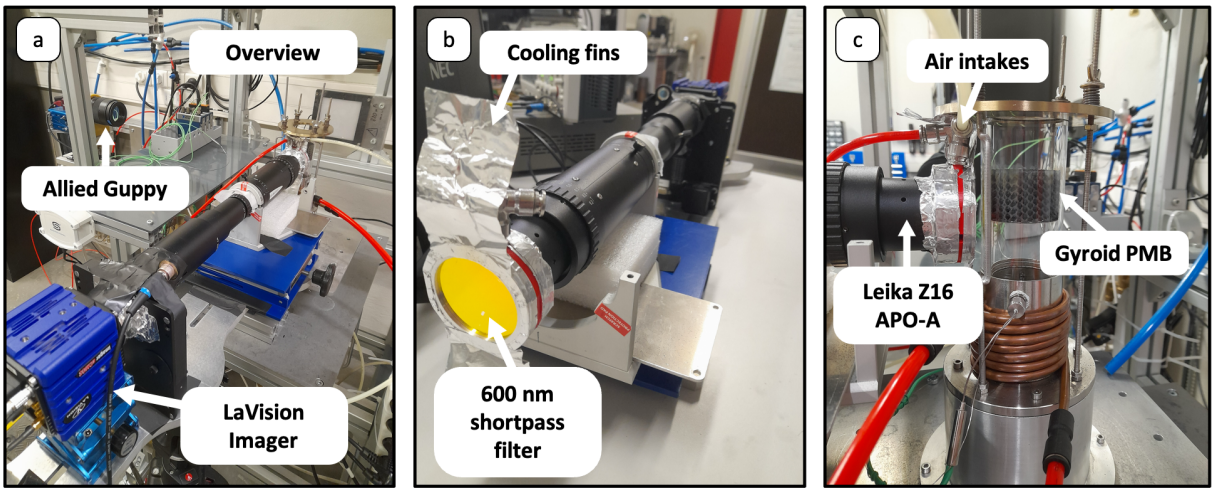

Figure 6.9. – Overview of the experimental setup for the μPIV experiments. a) Global positioning of the cameras with respect to the experiment. b) Detail of the optics cooling system. c) Positioning of the macroscope with respect to the burner.

6.4.1. Diagnostics setup

In the μPIV experiments, the continuous laser source is replaced by a double pulsed Nd:YAG Quantel Twins Ultra. The energy and wavelength of the laser pulses are 30 mJ and 532 nm, respectively. A digital synchronizer is employed to trigger the camera and the laser shots. The synchronizer clock is set to a frequency of 10 Hz. Every 100 ms, two laser pulses are delivered with a time span of Δt. For each operating point, Δt is adjusted according to the bulk flow velocity so as to keep a constant particle displacement between frames across the experiments. Typical values of Δt are around 15 μs. A delay generator is used to accurately tune the camera shooting window with respect to the laser pulses. The synchronization of all these time signals is monitored using an oscilloscope and a photodiode is used to measure the laser pulses. With the double-pulsed source, a laser sheet thickness of 1.6 mm has been measured at the burner inlet using a CMOS Beamage-4M camera. Given the small scale of the pores and the thickness of the laser sheet, the illumination source can be considered to be volumetric [214, 227]. This

means that the whole depth of the optically accessible region of Fig. 6.3 is illuminated. In this respect, the measurement plane is defined by the depth of field of the optics.

The telecentric lens is substituted by a Macroscope Leika Z16 APO-A with a working distance of approximately 40 mm. For the optics configuration used in these experiments (zoom and aperture), a focus depth between 460 and 560 μm has been measured using a Ronchi-Ruling image. Because of its short working distance, the first surface of this optics is very close to the burner and it is submitted to an intense thermal radiative flux. To refrigerate the lens and prevent its damage, an *ad hoc* tooling attached to the optics' front is used to cool it down. This cooling system houses a shortpass filter with a cutoff wavelength of 600 nm and is fitted with two air intakes and several lateral outlets. A cold air flow is established within the narrow gap between the optics' front element and the filter. This cold stream of air does not affect the thermal equilibrium of the burner. To dissipate as much heat as possible, the optics cooling tool is equipped with aluminum cooling fins. Various pictures of the arrangement of the cameras and the experiment as well as of the optics cooling system are offered in Fig. 6.9.

Mie scattering results have shown that when the flame is stabilized at the burner inlet, the evaporation front is very close to the reaction zone and this can be used to infer the shape of the flame. For this reason, during these experiments flames have been kept anchored to the first row of pores so we can obtain the velocity field close to the flame front. Figure 6.10 illustrates how the vertical and horizontal see-through directions are combined in these experiments. The schematic is presented for burner B3 with Gyroid topology, a pore size of $d_p = 3.5$ mm and a porosity of $\epsilon = 0.8$. Thanks to the macroscopic lens, it is possible to zoom in one of the central pores of the porous matrix (cf. Fig. 6.10c). The top and front views of Fig. 6.10a and b, respectively, illustrate how the vertical and horizontal see-through directions are combined in these experiments. This pore is illuminated by the laser from the top of the burner using a vertical see-through direction and imaged through the corresponding horizontal optical pathway. In Fig. 6.10c, a detailed view of the imaged pore has been represented. In this plot, the Mie scattering image obtained from μPIV results is superimposed with the streamlines of the velocity field and a mask generated by computer using the CAD of the porous geometry. The Mie-scattering image and the velocity field correspond to a cold flow realization and the procedure to obtain them is detailed in Sec. 6.4.4. In the μPIV images, a local coordinate system is used, (x^*, y^*). The x^* axis is oriented in the streamwise direction and the origin of the system is approximately at the center of the pore. Note that the direction of the y^* axis is inverted with respect to the convention presented in Fig. 6.1.

6.4.2. Calibration process

The calibration process for μPIV experiments is illustrated in Fig. 6.11, Fig. 6.12 and Fig. 6.13 for the three laser-suited burners analyzed: B1, B2 and B3, respectively. From the left to the right, the backlight image, the scale picture and a snapshot of the cold flow μPIV sequence have been represented. Figure 6.11 corresponds to burner B1 (Primitive topology with $\epsilon = 0.7$ and $d_p = 3.5$ mm). In Fig. 6.12, these three visualizations are displayed for burner B2 (Primitive based with $d_p = 2.5$ mm and $\epsilon = 0.7$). Owing to the smaller size of the pores we have chosen to keep the zoom approximately constant and to image the inlet of the burner as well. Finally, Figure 6.13 shows the backlight image, the scale picture and a cold flow snapshot for burner B3 (Gyroid topology with $\epsilon = 0.8$ and $d_p = 3.5$ mm). In the cold flow snapshots, the low density of the particles seeding can be noticed. Such a low seeding density is characteristic of μPIV experiments.

The first step of the calibration process is the alignment of the camera with the z-axis of the optical pathway. Because of the lack of references, the small scale of the system and the inaccessibility, an alignment based on geometrical criteria is not possible. When the light from

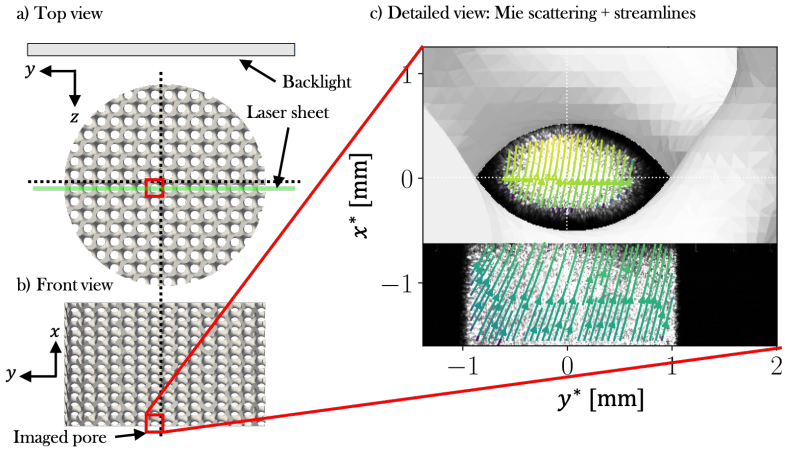

Figure 6.10. – Schematic of the μPIV experiments. a) Top view of the burner, the laser sheet and the backlight. b) Front view of the burner. The target pore is at the burner inlet in the center of the porous matrix. c) Detailed view of the pore: Mie-scattering image, streamlines and computer-generated mask. Note that local axes, (x^*, y^*) are used in μPIV images.

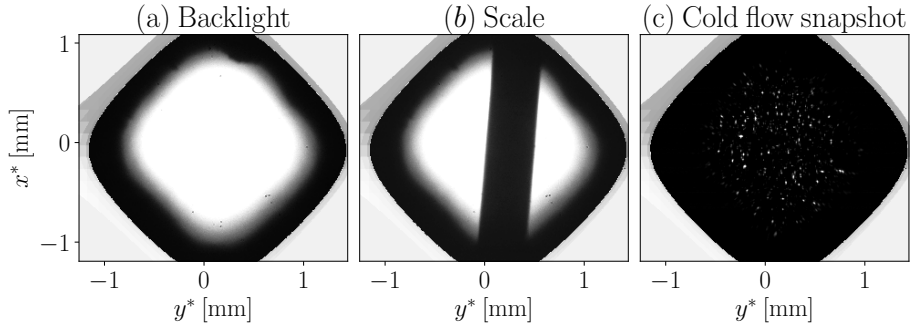

Figure 6.11. – B1: Primtive-based burner with $d_p = 3.5$ mm and $\epsilon = 0.7$.

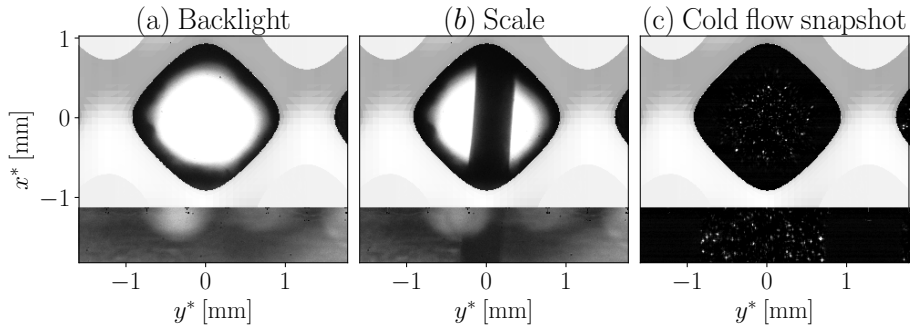

Figure 6.12. – B2: Primtive-based burner with $d_p = 2.5$ mm and $\epsilon = 0.7$.

the backlight traverses the pore, it generates a diffuse bright region with the shape of the optical pathway on the camera sensor (cf Fig. 6.11a). The brightness and the size of this *footprint* are maximal when the camera is aligned with the z-axis of the pore. This criterion is here used to finely adjust the positioning and the orientation of the optics.

Then, the scale factor of the images must be determined. For that, a thin wire is inserted through the vertical optical pathway that intersects with imaging see-through direction at the

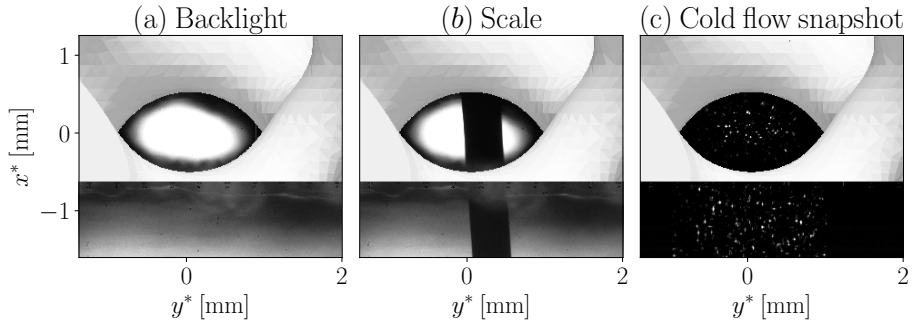

Figure 6.13. – B3: Gyroid-based burner with $d_p = 3.5$ mm and $\epsilon = 0.8$.

pore of interest. The focus of the camera is adjusted to obtain a sharp edge in the wire backlighting. Because the working distance of the optics is fixed, the focal plane is modified by translating the imaging system along the axis of the pore (z-direction). Figure 6.11b, shows a picture of the pore with the backlight on and the wire in. This image is used to determine the scale of the pixels provided that the wire diameter is 0.5 mm. Finally, the focal plane is corrected using a cold air flow seeded with particles (cf. Fig. 6.11). The z-position of the camera is adjusted so as to maximize the number of particles in focus. Because the optical pass of the lens is kept constant, this operation does not affect the scaling factor of the images.

6.4.3. Experimental procedure

Upon the calibration process, the experiment is started and the input parameters are adjusted to stabilize a flame inside the burner. It is reiterated that, during these experiments, flames are kept anchored to the burner inlet, stabilizing at the first row of pores. The position of the flame inside the burner is monitored via $CH^\star$ chemiluminescence images captured from the y-axis see-through direction. For each operating point, once thermal convergence is achieved, the mass flow controllers and inlet temperature readings are registered and averaged over two minutes. Then, the flow is seeded with particles, the laser is started and 500 snapshots of the flow field are captured at a 10 Hz rate. Each snapshot contains two frames of the flow field.

6.4.4. Images processing

In the post processing stage, images are first scaled and then a time-averaged background removal filter is applied. From this pre-processed sequence two results are obtained. On the one hand, the maximum intensity registered by each pixel over the whole μPIV sequence is extracted. This generates a Mie-scattering image that is used to analyze the shape of the flame. This Mie-scattering image is also employed to define a mask for the μPIV calculations. Finally, the velocity field, $\mathbf{u}(x^*, y^*) = (u, v)$, is computed using the sum of the cross-correlation peaks over the whole sequence [227]. The cross-correlation is computed using a window size of 128 px with an overlap of 87 %. This is standard processing technique in μPIV experiments and relies on the steadiness of the laminar flow. This post-processing methodology is used to compensate for the commonly low seeding density in microfluidic systems. It has been verified that the statistical convergence of the velocity field requires averaging over at least 200 snapshots.

6.4.5. Results

As shown in Sec. 6.3.2, the shape of the flame can only be reported for inlet-anchored flames. Therefore, the analysis is focused on the influence of perturbations in load and mixture compo-

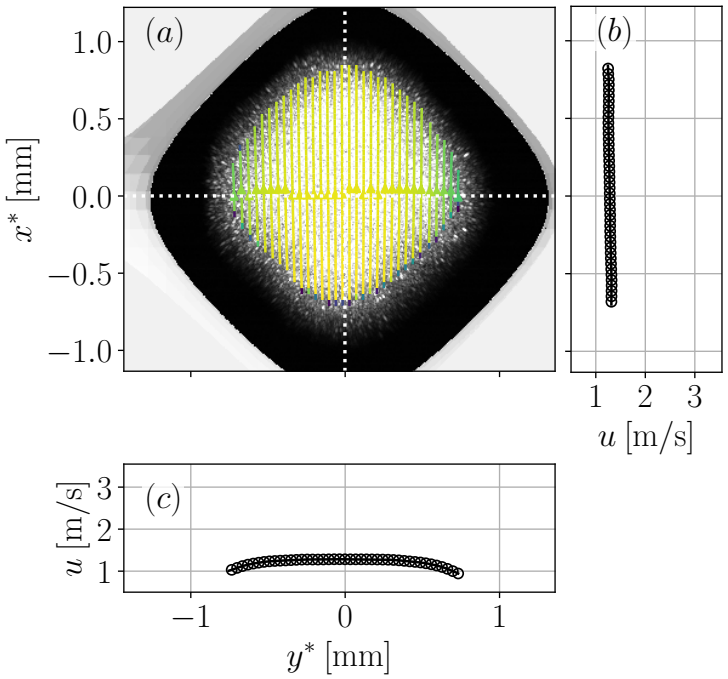

Figure 6.14. – a) Flow streamlines and Mie-scattering image from μPIV measurements in non-reactive conditions. b) Longitudinal profile of axial velocity, $u(x^*)$. c) Transverse profile of axial velocity $u(y^*)$.

sition on the stabilization of inlet-anchored flames.

Table 6.2. – Equivalence ratio ϕ resulting in an inlet-anchored flame for each burner and H_2 content. The operating point defined by $P = 1$ kW, and the combinations of α_P and ϕ from this table determine the reference operating condition for each burner in the μPIV experiments.

Burner	$\alpha_p = 0\%$	$\alpha_p = 20\%$	$\alpha_p = 60\%$
B1	0.66	0.55	0.37
B2	–	0.60	0.40
B3	0.66	0.50	0.25

For each burner and hydrogen content, the equivalence ratio, ϕ, that results in a 1 kW inlet-anchored flame is determined to define a reference operating point. Table 6.2 collects the equivalence ratios of the reference operating points for each burner and H_2 content. Then, perturbations in power, $\Delta P = \pm 0.2$ kW, and equivalence ratio, $\Delta\phi = \pm 0.02$, have been introduced around this reference flame to analyze their impact on its structure. In the primitive burner with $d_p = 2.5$ mm (B2) it was not possible to stabilize CH_4-Air flames.

To guide the interpretation of the results, two μPIV results in non-reactive and reactive flow conditions are presented for B1 in Fig. 6.14 and Fig. 6.15, respectively. For non-reactive flow conditions, Fig. 6.14a shows the flow streamlines and the Mie-scattering image, Fig. 6.14b depicts the longitudinal velocity profile of axial velocity, $u(x^*)$, and Fig. 6.14c represents the transverse profile of streamwise velocity, $u(y^*)$. The horizontal and vertical white dotted lines indicate the location of the velocity profiles. Figure 6.15 provides the same results for a reactive flow case. In the Mie-scattering images obtained in non-reactive flow conditions like the one shown Fig. 6.14a for B1, particles are not observed close to edges of the optical pathway. This loss of effective visualization surface is caused by the presence of out-of-plane defocused walls.

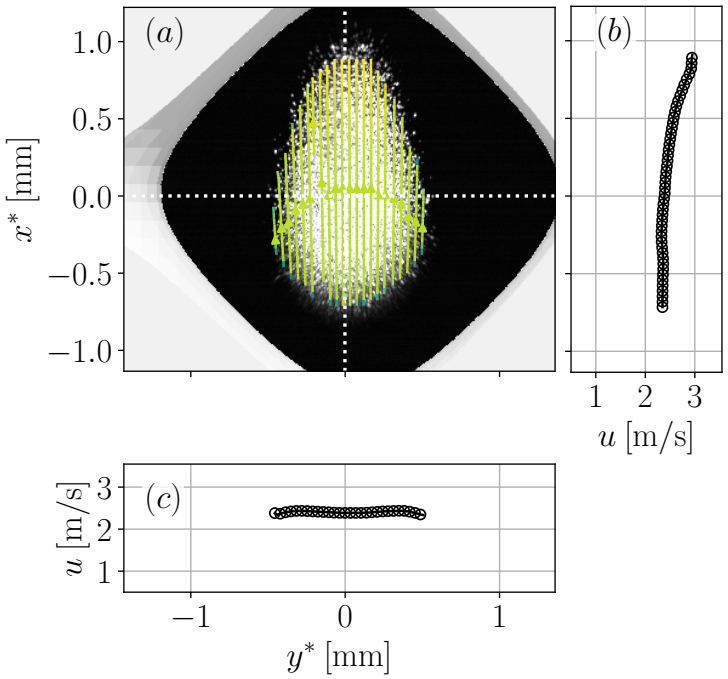

Figure 6.15. – a) Flow streamlines and Mie-scattering image from μPIV measurements in reactive flow conditions. b) Longitudinal profile of axial velocity, $u(x^*)$. c) Transverse profile of axial velocity $u(y^*)$.

Actually, Mie-scattering images in cold flow conditions outline the real limits of the observable region inside the pores.

In the reactive μPIV case (cf. Fig. 6.15), the vaporization front indicates that a conical flame is stabilized inside the pore. The shape of this flame is in agreement with the results presented in Sec. 6.3.2. Regarding the axial distribution of velocity, $u(x^*)$, in the non-reactive flow case the velocity profile is nearly flat (cf. Fig. 6.14b). Conversely, in the reactive flow μPIV measurement of Fig. 6.15b, the streamwise velocity increases in the axial direction by approximately 25%. This acceleration is due to the preheating of the reactants along the pore. Note that in the reactive case of Fig. 6.15, the velocity field is only available in the unburned gas region. The resolution of the velocity profiles is $\Delta x = 17.4$ μm and for the sake of readability a marker is used every two samples in the velocity profiles of Fig. 6.14 and Fig. 6.15.

First, the influence of power, P, on the flame structure is examined for burner B1 (Primitive topology and $d_p = 3.5$ mm). The hydrogen content and the equivalence ratio are fixed to $\alpha_P = 20\%$ and $\phi = 0.55$, respectively, and the power is varied from $P = 0.8$ kW to 1.2 kW. The Mie-scattering images and the streamlines of these flames are shown in Fig. 6.16a-c. Figure 6.16d shows the axial velocity profiles, $u(x^*)$ along the white dotted lines for cases (a)-(c). When the power is augmented, the evaporation front is pushed downstream and the flame surface increases. The velocities measured in the fresh gasses region display a coherent trend with the increase in burner load. The axial velocity profiles reveal a remarkable acceleration in the streamwise direction owing to the preheating of the reactants. The combination of preheating and increase in the flame surface permits attaining larger local consumption rates when the power is increased.

A similar analysis is now presented for burner B2 with the same topology as B1 and a smaller pore size, $d_p = 2.5$ mm. Figure 6.17a-c shows three H_2-enriched flames with $\phi = 0.60$ stabilized at the inlet of burner B2. The hydrogen content is $\alpha_P = 20\%$ and the power varies from $P = 0.9$ to $P = 1.2$ kW. Because of flame extinction, it was not possible to stabilize a flame with a power of 0.8 kW at $\phi = 0.60$. As for the previous case, Fig. 6.17d displays the axial velocity profiles

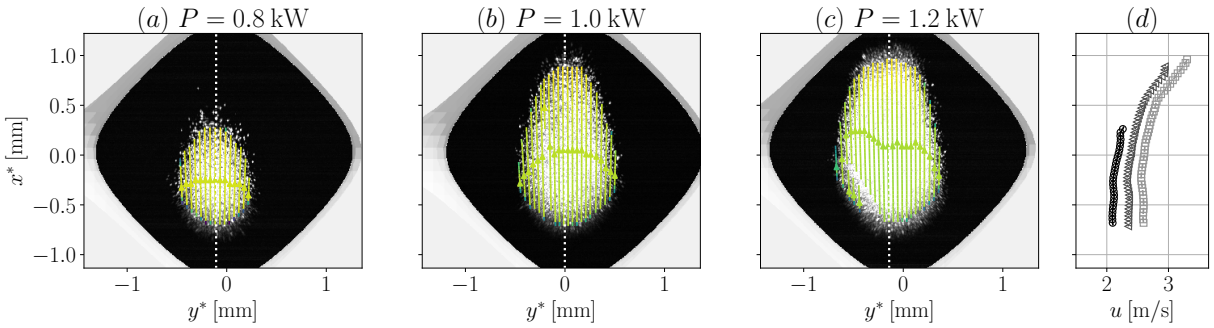

Figure 6.16. – Influence of power, P, on the flame structure in burner B1. The hydrogen content is $\alpha_P = 20\%$ and the equivalence ratio is $\phi = 0.55$. For these flames the speed-ups are: (a) $u_B/S_{L_0} = 1.86$, (b) $u_B/S_{L_0} = 2.42$ and (c) $u_B/S_{L_0} = 2.97$. The axial velocity profiles, $u(x^*)$, along the white dotted lines are represented in (d) for cases (a) —○— , (b) ····◁·· and (c) --⊟- .

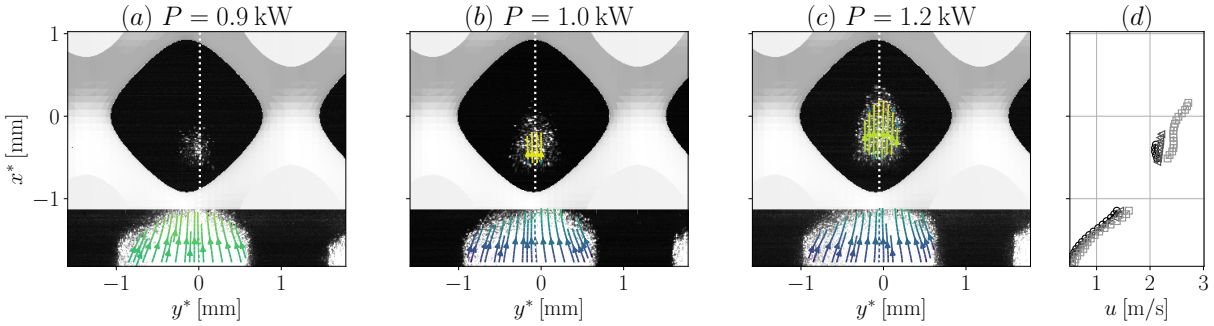

Figure 6.17. – Influence of power, P, on the flame structure in burner B2. The hydrogen content is $\alpha_P = 20\%$ and the equivalence ratio is $\phi = 0.60$. For these flames the speed-ups are: (a) $u_B/S_{L_0} = 1.21$, (b) $u_B/S_{L_0} = 1.42$ and (c) $u_B/S_{L_0} = 1.66$. The axial velocity profiles, $u(x^*)$, along the white dotted lines are represented in (d) for cases (a) —○— , (b) ····◁·· and (c) --⊟- .

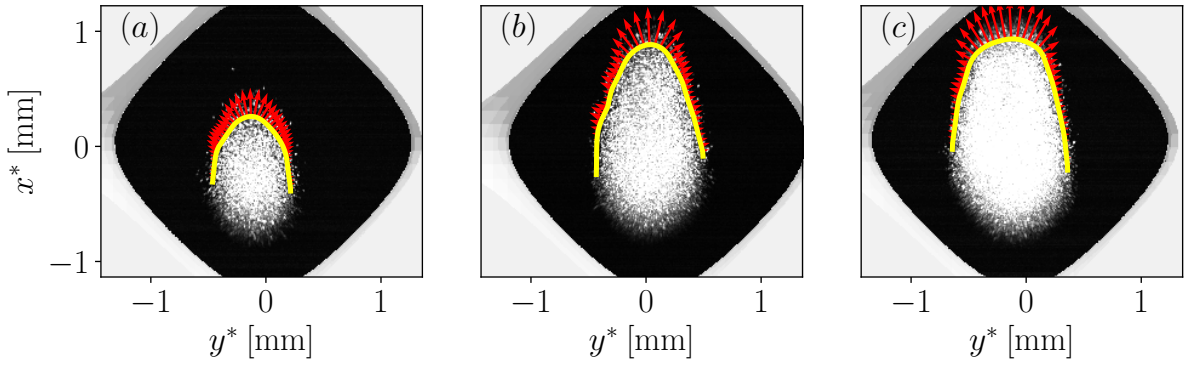

Figure 6.18. – Mie-scattering images for three H_2-enriched CH_4-Air with $\phi = 0.55$, $\alpha_P = 20\%$ and different powers: (a) $P = 0.8$ kW, (b) $P = 1.0$ kW and (c) $P = 1.2$ kW. The evaporation front is indicated with a yellow line and the red arrows represent the magnitude and direction of the local consumption speed, S_C.

at increasing powers. At $P = 0.9$ kW (cf. Fig. 6.17a) the evaporation front is located at the bottom of the pore because this flame is close to the flashback limit. Indeed, the evaporation front extends beyond the burner inlet as indicated by the absence of particles on the sides of the

laser trail. When the load of the burner is increased, the evaporation front is shifted downstream and the fresh gasses zone grows. At $P = 1.2$ kW, the Mie-scattering image reveals a conical flame shape. The axial velocity profiles on the right of Fig. 6.17 show an important acceleration of the flow from freestream conditions towards the burner inlet. This acceleration is confirmed by the convergence of the streamlines at the inlet of the burner. This velocity field suggests that, as for slit-stabilized flames [32, 33, 230], hydrodynamic effects have a first order impact on the stabilization of the flame in this burner. When the pore size is reduced, the surface-to-volume ratio inside the pores increases. Yet it is not possible to quantify the flame-to-wall heat losses with the present diagnostics, a decrease in the pore size is expected to increase the flame quenching. This would explain why higher equivalence ratios, and thus higher local flame speeds and temperatures, are required to stabilize a flame at the inlet when the pore size is reduced.

The information from Mie-scattering images and μPIV can be combined to obtain the local consumption speed at the flame front. From Mie-scattering, the evaporation front defined by the implicit curve $f_v(x_v^*, y_v^*) = 0$ can be extracted. From the evaporation front, the normal vectors are computed as $\mathbf{n} = -\nabla f_v / |\nabla f_v|$. This allows us to evaluate the velocity flux across this line as $S_c = \mathbf{u} \cdot \mathbf{n}$. Since the evaporation front $f_v(x_v^*, y_v^*)$ is very close to the flame front $f_v(x_v^*, y_v^*) \simeq f_f(x_f^*, y_f^*)$ the velocity S_c represents a first-order estimation of the local consumption speed at the flame front. Moreover, because the evaporation temperature of the oil droplets is known, it is possible to estimate the density of the fluid at the evaporation front location ρ_{T_v}. This allows the normalization of the consumption speed by the densities ratio $S_C = \rho_{T_v}/\rho_{in} S_c$ to override the influence of preheating. The evaporation front, $f_v(x_v^*, y_v^*)$ and the magnitude

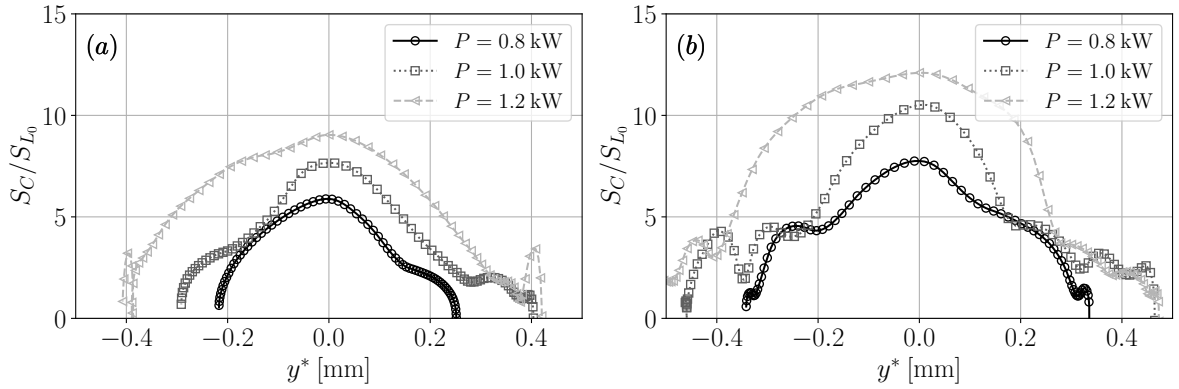

Figure 6.19. – Evolution of the consumption speed S_C along the flame front for different powers in CH_4-Air flames with $\phi = 0.66$ (a) and in H_2-enriched CH_4-Air flames with $\alpha_P = 20\%$ and $\phi = 0.55$ (b).

and direction of the local consumption speed $S_C \cdot \mathbf{n}$ have been represented in Fig. 6.18 for three H_2-enriched CH_4-Air flames with $\alpha_P = 20\%$ stabilized in B1. These flames feature the same equivalence ratio, $\phi = 0.55$, and different powers. A similar result is shown in Fig. 6.27 for CH_4/Air flames with $\phi = 0.6$. The local consumption speed, S_C, from the flames shown in Figs. 6.27 and 6.18 has been extracted and plotted against the y^* coordinate in Figs. 6.19a and b, respectively. In Fig. 6.19, the local consumption speed S_C is normalized by the laminar burning rate S_{L_0}. The results represented in Fig. 6.19 show that the normalized local consumption speed, S_C/S_{L_0} increases with the hydrogen content. This is here attributed to the higher sensitivity to preheating of H_2-enriched flames.

The analysis of the influence of perturbations in power and mixture composition on the flame structure is completed by the results presented in 6.A.

6.5. Influence of the burner topology

In this section, the influence of the topology on the performance of the burner, the stabilization of the flame and the interstitial flow is analyzed. As a preliminary remark, it is advanced that there are only minor differences between the Gyroid (B3) and the Diamond (B4 and B5) topology in terms of macroscopic flame stabilization and operating domain. Therefore, the discussion presented down below is focused on the comparison between the Primitive geometry and the other two. In particular, B1 is compared to B4 and B5 in terms of operating domain and stabilization curves. These burners feature the same pore size and different porosities. Then, the velocity fields of B2 and B3 are compared at the pore-level in cold flow conditions to analyze the differences in the interstitial flow.

First, significant qualitative differences have been observed during the experiments between Primitive and Diamond-based burners, including:

- Difficulty to achieve a smooth transition from surface to submerged combustion.
- In Primitive-based burners, the stabilization of the flame is more discretized, as if only a few anchoring locations were possible.

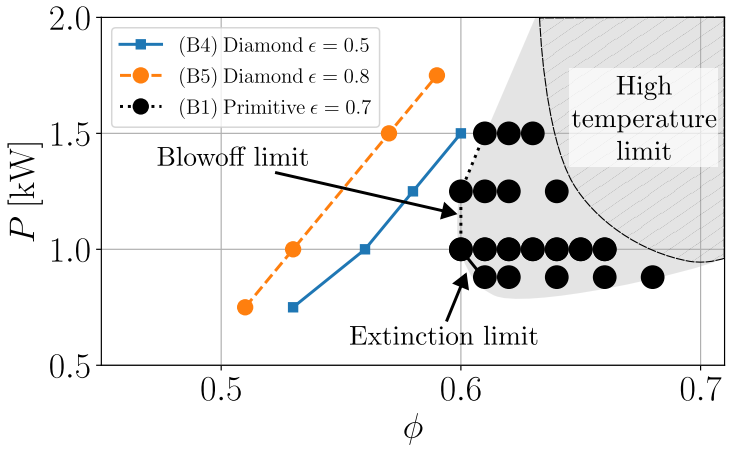

Figure 6.20. – Stability domain of burner B1 spanned by power, P, and equivalence ratio, ϕ for CH_4/Air flames. Blowoff limits of burners B4 and B5 in the $P - \phi$ map.

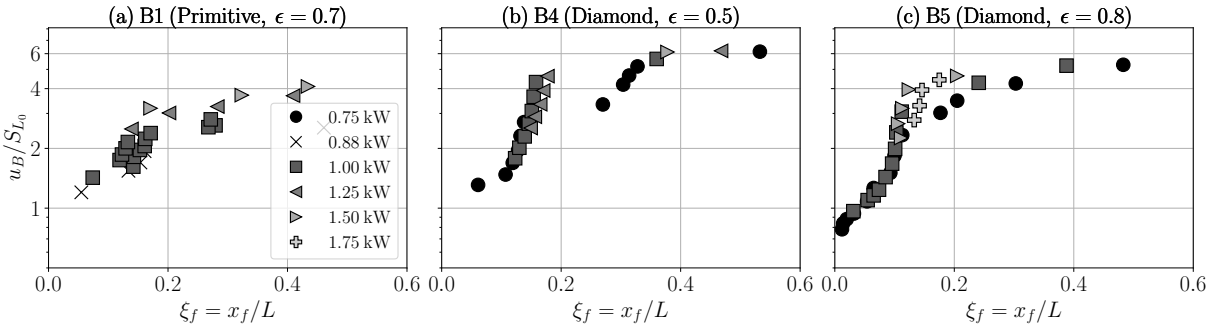

Figure 6.21. – Evolution of the speed-up, u_B/S_{L_0}, with the flame location $\xi_f = x_f/L$, in Primitive and Diamond-based burners with the same pore size $d_p = 3.5$ mm and different porosities.

Figure 6.20 shows the stability map for CH_4-Air flames in B1. The operation at high power and equivalence ratio is limited by the low melting point of the burner material. In Fig. 6.20,

the black dotted line indicates the blowoff limit of the burner which corresponds to the leftmost points of the stability map. For the sake of comparison, the blowoff limits of burners B4 and B5 are depicted in blue and orange lines, respectively. It must be noticed that Diamond-based burners (B4 and B5) are capable of sustaining combustion at both leaner mixtures and lower powers. This result shows that the topology has a strong influence on the operating domain of the burner. Flame stabilization is now analyzed in terms of speed-up and flame location. In Fig. 6.21, the speed-up, u_B/S_{L_0}, is plotted against the flame position, $\xi_f = x_f/L$, estimated from CH* chemiluminescence images for B1 (a), B4 (b) and B5 (c). The results presented in Fig. 6.21 reveal significant differences in performance between these two topologies. In B1, the maximum achievable speed-up is approximately 4 whereas in the Diamond topology is almost 6 for both porosities (B4 and B5). This implies that changes in the geometrical configuration of the porous structure can increase the performance of the burner by roughly 50%.

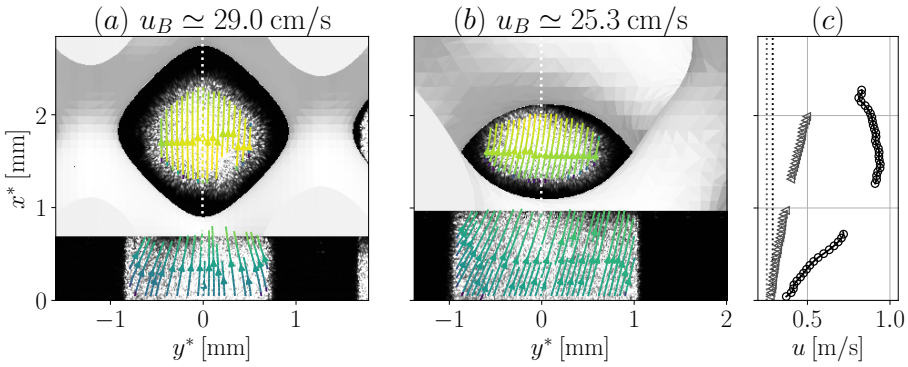

Figure 6.22. – Streamlines and Mie-scattering image in non-reactive flow conditions for burners B2 (a) and B3 (b). The axial velocity profiles, $u(x^*)$, along the white dotted lines are represented in (c) for cases (a) —○— and (b) ···◁··· .

Finally, Figs. 6.22a and b show two μPIV results in cold flow conditions for burner B2 and B3, respectively. On the right of Fig. 6.22, the axial velocity profiles along the white dotted lines are represented. Figures 6.22a and b are labeled with the corresponding bulk flow velocity, which is computed from the total mass flow rate, $\dot{m}$, the inlet density, ρ_{in}, the burner section, A, and the volumetric porosity ϵ. This velocity value is indicated with a vertical dotted line in the velocity profiles. The axial profiles of Fig. 6.22 show that the local velocity increases with respect to u_B along the x^* axis in both burners. However, the acceleration of the flow is higher in the Primitive topology, with a peak of velocity at the burner inlet that is almost three times larger than the mean bulk velocity u_B. μPIV measurements indicate that there are notable differences between the interstitial flow configuration of these two topologies.

The explanation for such remarkable differences in the interstitial flow can be found in Fig. 6.23 where the evolution of the linear porosity, ε, over one wavelength, Λ, is plotted as a function of the streamwise coordinate, x, for the three TPMS topologies evaluated in this work. The linear porosity $\varepsilon(x)$ is computed as the cross-stream surface of the gas phase divided by the total transverse surface. Note that this quantity depends on the direction in which it is evaluated. In Fig. 6.23, the represented TPMS topologies feature the same volumetric porosity $\epsilon = 0.7$, which is indicated with a black dotted line. In the Diamond and Gyroid topologies, the variations of the linear porosity, ε around the volumetric value ϵ are small. In contrast, in the Primitive topology there are large deviations in the linear porosity with respect to ϵ. In isothermal conditions, the mean gas velocity at a given streamwise location, $u_g(x)$, is inversely proportional to the cross-section area and hence to the linear porosity ε. Therefore, strong variations of ε result in significant axial velocity gradients. In the Primitive topology, the important variations of the linear porosity are responsible for the acceleration of the flow observed in Fig. 6.22 at the burner

inlet. This interstitial flow configuration may also explain the discretized stabilization of the flame in this burner.

These results have shown that the lattice structure can play a key role on the performance and the stability domain of the burner. The topology of the burner has a direct impact in various physical phenomena that influence flame stabilization. It affects the dispersion effects and hence the effective diffusivity [68, 76]. It also modifies the view factors between solid elements and thus the radiation extinction coefficient [59, 68]. Finally, it alters the interphase surface density, which modulates the convective heat exchange between the phases [70]. The influence of the topology on these phenomena is already quantified in the VAMs via the topological parameters of in Tab. 6.1. Here, thanks to μPIV measurements at the pore scale it has been shown that the topology can have a strong influence on the interstitial flow. The velocity field inside the cavities of the porous matrix determines the contribution of hydrodynamic effects on the flame stabilization. A statistically homogeneous velocity field reduces the impact of local pore-anchoring phenomena on the stabilization of the flame and smooths the macroscopic response of the burner. This must be borne in mind when it comes to performing DPLS in regular porous geometries, since they may not be fully representative of random structures. The linear porosity, ε can be used as an indicator of the relevance of these local pore anchoring phenomena.

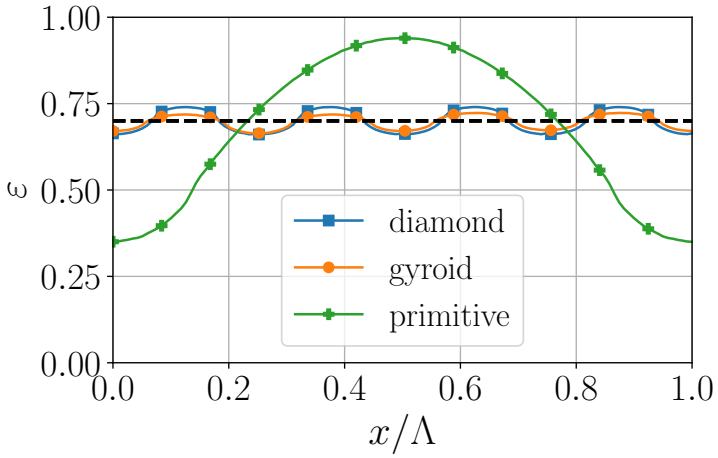

Figure 6.23. – Evolution of the linear porosity in the streamwise direction for the three TPMS structures. These three topologies feature the same volumetric porosity $\epsilon = 0.7$, indicated with a black dotted line.

6.6. Conclusions of the chapter

In this chapter, the optical access granted by TPMS-based porous matrices has been exploited to apply two different laser diagnostics: Mie-scattering imaging and μPIV.
First, Mie-scattering imaging and $CH^\star$ chemiluminescence have been applied at a macroscopic scale over the whole operating range of the burner: from inlet anchored flames to the blowoff limit. It has been observed that when flames are stabilized at the burner inlet, the vaporization front can be used to infer the topology of the flame. This is because the preheating of the reactants takes place at the gas diffusion scale. Mie-scattering imaging has revealed the existence of a symmetric and an asymmetric stabilization mode in a PMB. When the position of the flame is shifted downstream, fresh gases undergo a significant preheating before reaching the flame front as a result of heat recirculation. Hence, the vaporization temperature of the oil droplets is reached far upstream the flame front. The offset between the vaporization and the flame front can be used to experimentally quantify the re-equilibration distance. In future works, the use of seeding particles with different evaporation temperatures could be used to obtain different temperature iso-contours in the burner.
Mie-scattering imaging has been combined with μPIV to simultaneously obtain the shape of the flame and the velocity field in the fresh gasses region at the pore scale for three different burners. Owing to the experimental limitations, only inlet-anchored flames could be analyzed. This technique has been used to study the influence of topology, pore size, power and hydrogen content on the flame structure. By combining the information from Mie-scattering images and μPIV measurements, it has been possible to compute the local consumption speed of various flames. It has been observed that the flame surface increases to accommodate larger mass flow rates and that the local consumption speed, S_C, increases with the hydrogen content. Overall, these results demonstrate the feasibility of PIV measurements in TPMS structures and open new paths for the application of non-intrusive optical diagnostics in PMBs. The technique is complex due to the stringent alignment and positioning requirements, the small scale of the system and the inaccessibility. The calibration of the cameras, laser and mirror is extremely sensitive and small perturbations can cause an important misalignment. Another challenge specific to μPIV measurements in reactive flows is the need to refrigerate the optics. The major drawback of the current setup is the use of low vaporization temperature particles. Yet this feature was exploited in Sec 6.3.2 to estimate the re-equilibration distance, it is a limiting factor in PIV. Firstly, it only provides the velocity field in the unburned gas region. Secondly, it restricts the analysis to inlet-anchored flames. Finally, as a result of the evaporation dynamics of particles, there is some uncertainty in the localization of the evaporation front. At high flow velocities, this uncertainty may be non-negligible due to the small scale of the system. Future improvements of this technique will include a 2D calibration of the images using a chessboard pattern and the use of solid particles. However, this may involve important experimental challenges including the adhesion to the burner walls, the clustering of particles and the potential clogging of the burner.
Finally, the influence of the topology on flame stabilization has been examined. A comparison between the Primitive and the Diamond topologies has been established in terms of operating domain and stabilization curves. Some qualitative differences observed during the experiments have also been reported. The analysis of the velocity field at the pore-level reveals the existence of large axial velocity gradients in the Primitive topology. This can be explained by the significant variations of linear porosity in the streamwise direction. The linear porosity profile configures the interstitial flow and influences the contribution of hydrodynamic effects to the stabilization of the flame. This result brings to light the impact of interstitial flow configuration on the macroscopic behavior of the burner and claims for a further development of pore-scale diagnostics.

6.A. Supplementary material

This Appendix presents supplementary results from the μPIV experiments that complement analysis presented in Sec 6.4.5. In Fig. 6.24 the influence of power on the stabilization of the flame is presented for burner B3 (Gyroid topology, $d_p = 3.5$ mm). These flames feature a H_2-enrichment of $\alpha_P = 20\%$ and an equivalence ratio of $\phi = 0.5$. In this case, the vaporization front displays an asymmetric shape inside the imaged optical pathway. As in B2 (Fig. 6.17), the evaporation line extends beyond the burner limits, suggesting that these flames are close to flashback. The most noticeable change in the flame structure is observed when the power is increased from 1 kW to 1.2 kW and the vaporization front is shifted towards the wall. If the axial velocity profiles of Fig. 6.17d and Fig. 6.24d are compared, it is found that the local velocities measured in B3 are nearly 50% smaller than those measured in B2. This suggests that local flame anchoring owing to hydrodynamic effects is less important in B3 than in B2.

Figure 6.25 displays the Mie-scattering images and the streamlines for three flames with the same power and different equivalence ratios, ϕ, stabilized in burner B1 (Primitive-structure with $d_p = 3.5$ mm). In these flames, the total mass flow rate is very similar and the flame speed increases with the equivalence ratio. As the velocity ratio, u_B/S_{L_0} reduces, the flame surface decreases, indicating that there is a correlation between these two phenomena. The variations of the flame surface observed in Fig. 6.25 are less pronounced than those observed in Fig. 6.16 for variations of the power.

The effect of H_2-enrichment on the flame topology is shown in Fig. 6.26 where three flames with varying hydrogen contents are stabilized at the inlet of burner B1. These flames feature a thermal power of $P = 1$ kW and their equivalence ratio has been adjusted to obtain an inlet-anchored flame. At $\alpha_P = 60\%$, the evaporation front is shifted towards the sides of the pore, which is compatible with the characteristic flame tip opening observed in lean hydrogen flames [231] and a stretching of the flame front. However, given the uncertainties in the positioning of the evaporation front (cf. Sec. 6.3.1) and the limitations of the experimental technique, we prefer to be cautious in the interpretation of these results.

Figure 6.27 depicts the Mie-scattering image, the evaporation front and the consumption speed vectors, $S_C \cdot \mathbf{n}$, for three CH_4-Air flames stabilized in B1. These flames feature the same equivalence ratio, $\phi = 0.6$, and powers ranging from $P = 0.8$ kW (a) to $P = 1.2$ kW (c).

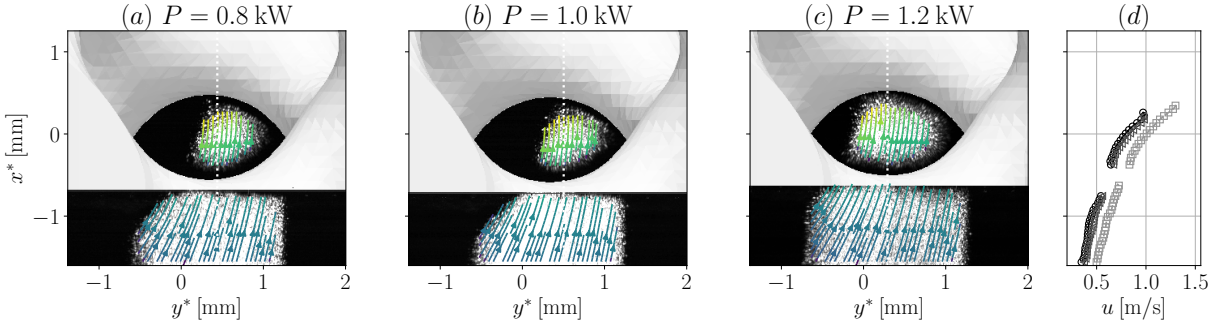

Figure 6.24. – Influence of power, P, on the flame structure in burner B3. The hydrogen content is $\alpha_P = 20\%$ and the equivalence ratio is $\phi = 0.50$. For these flames the speed-ups are: (a) $u_B/S_{L_0} = 2.04$, (b) $u_B/S_{L_0} = 2.52$ and (c) $u_B/S_{L_0} = 4.66$. The axial velocity profiles, $u(x^*)$, along the white dotted lines are represented in (d) for cases (a) —○— , (b) ····◁·· and (c) - -□- .

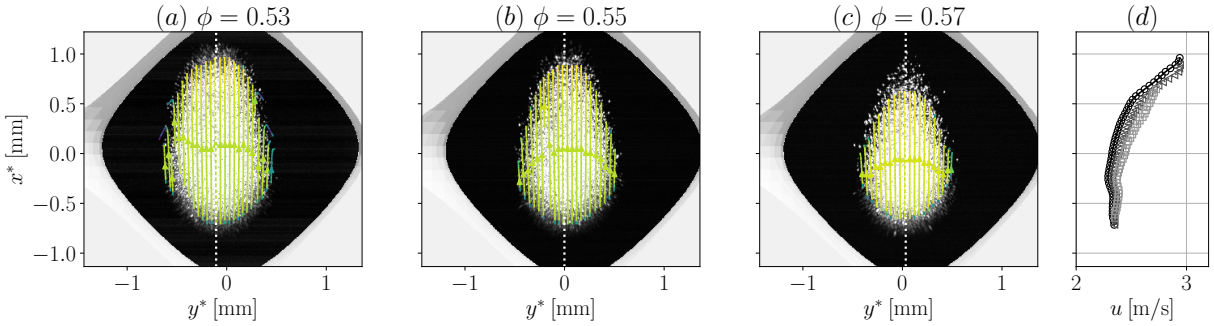

Figure 6.25. – Influence of equivalence ratio, ϕ, on the flame structure in burner B1. The hydrogen content is $\alpha_P = 20\%$ and the power is $P = 1$ kW. For these flames the speed-ups are: (a) $u_B/S_{L_0} = 2.99$, (b) $u_B/S_{L_0} = 2.41$ and (c) $u_B/S_{L_0} = 2.03$. The axial velocity profiles, $u(x^*)$, along the white dotted lines are represented in (d) for cases (a) —○— , (b) ····◁···· and (c) - -⊟- .

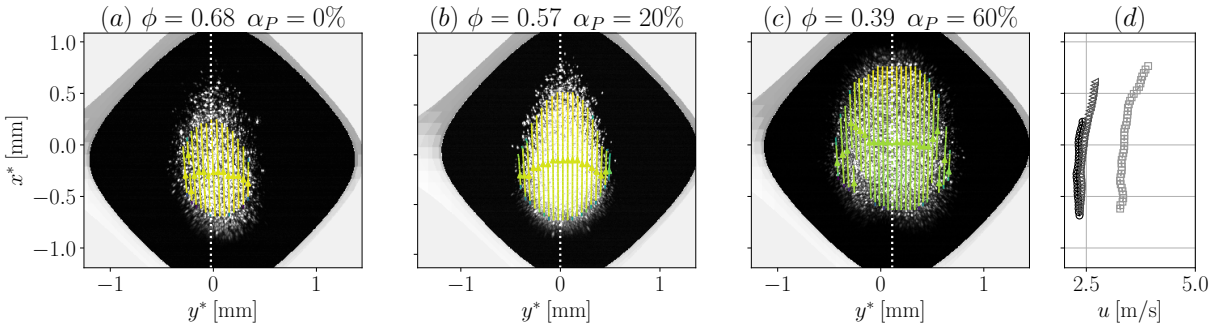

Figure 6.26. – Influence of hydrogen content on the flame structure in burner B1. In these flames, the power is $P = 1$ kW and equivalence ratio is adjusted to obtain an inlet-anchored flame. For these flames, the speed-ups are: (a) $u_B/S_{L_0} = 1.57$, (b) $u_B/S_{L_0} = 2.03$ and (c) $u_B/S_{L_0} = 8.21$. The axial velocity profiles, $u(x^*)$, along the white dotted lines are represented in (d) for cases (a) —○— , (b) ····◁···· and (c) - -⊟- .

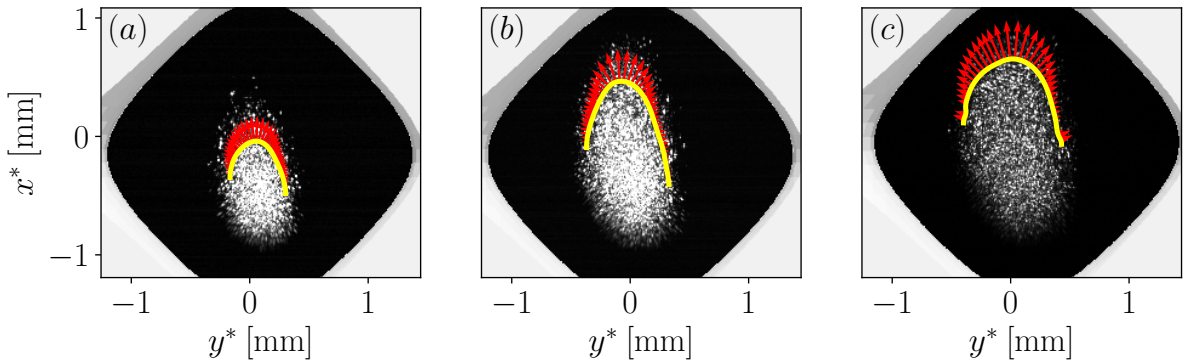

Figure 6.27. – Mie-scattering images for three CH_4-Air with $\phi = 0.66$ and different powers: (a) $P = 0.8$ kW, (b) $P = 1.0$ kW and (c) $P = 1.2$ kW. The evaporation front is represented with a yellow line and the red arrows indicate the magnitude and direction of the consumption speed S_C.

Conclusions and future research directions

Conclusions

Porous Media Burners are characterized by a unique combination of properties such as high-power density, broad turndown ratio, fuel-flexibility, ultra low NO_x emissions, high-radiant efficiency, and quiet operation. Their ability to stabilize flames over a wide range of burning rates and the possibility of optimizing the burner via topology tailoring could be exploited to achieve fuel-flexibility. Thus, they are promising candidates to decarbonize combustion processes in both industrial and domestic applications.

Despite the main driving mechanism of PMBs, i.e. heat recirculation, being understood, the intricate flame-wall interactions at the pore-level are still not well-characterized. Local phenomena such as flame wrinkling, stretch, quenching and preferential diffusion effects have a strong influence on flame stabilization and hence on the burner's performance. Now and in the foreseeable future, Direct Pore Level Simulations will remain computationally expensive, making it impractical to simulate a full scale system. Therefore, it is crucial to improve current Volume-Averaged Models (VAMs) to increase their accuracy and predicting capacity. For that, a deeper understanding of the pore-scale phenomena is essential and this can be achieved through experimental investigations using advanced diagnostic techniques. These methods provide valuable insights into local heat losses, flame wrinkling and preferential diffusion effects at the pore level, enabling the refinement of existing models. The integration of these detailed experimental observations into VAMs could enhance their predictive capabilities and reliability.

In this work, a novel strategy to achieve optical access to the interior of the porous matrix has been proposed. By combining computer-defined topologies with additive manufacturing, it is possible to produce optically accessible burners. Optical access allows the application of nonintrusive diagnostics such as chemiluminescence imaging and laser techniques. Another advantage of the current methodology is the independent control of the different topological parameters of the porous matrix, which allows for a systematic study of their influence on flame stabilization. Finally, the present approach could be used to enlarge the stability domain and optimize the performance of the burner via topology tailoring.

The combination of optically accessible burners with $CH^\star$ – chemiluminescence and a telecentric lens provides direct optical probing of the reaction zone inside the burner across its entire operating range. This enables the tracking of the flame front as a function of the operating conditions of the burner. This technique allows the confrontation of experiments and model results in terms of flame positioning, reaction zone thickness and axial temperature profiles. In homogeneous burners, there is a direct relationship between the flame position and the burning rate. This distinctive property can now be exploited for model validation to complement the widely-used temperature measurements.

In the first place, flame-front tracking from $CH^\star$ chemiluminescence imaging has been used to analyze the stabilization of CH_4-Air flames in PMBs with different pore sizes. These results have shown that current VAMs are not able to retrieve neither the position nor the thickness of the reaction zone in PMBs. It has also been observed that VAMs are very sensitive to the modeling of the interphase heat exchange term. Changing the interphase heat exchange term allows us to improve the predictions of the model. However, the inconsistencies regarding the domain of validity of the heat exchange correlation hint towards an error compensation. Regardless of

the interphase heat transfer submodel, the accuracy of the VAM significantly degrades at small pore sizes, indicating that the influence of this parameter on the combustion process is not well captured. The pore size directly affects the local adiabaticity of the flame. The interpretation of the results that is made here is that it is necessary to develop a combustion model that takes into account thermal quenching phenomena. Finally, the present results have brought to light that pointwise temperature measurements may not be a suitable validation tool for VAM models. According to the observations, achieving a reasonable agreement for the temperature field is possible if a relatively good characterization of the thermal problem is made. This is an issue specially for step burner configurations, where the position of the flame is nearly fixed at the interface between the two foams. Conversely, predicting the position of the flame in the burner as a function of the operating conditions is a more stringent validation method. This is because there is two-way coupling between the burning rate and the temperature field.

Secondly, the flame-front tracking methodology has been used to analyze the influence of hydrogen enrichment on flame stabilization. Hydrogen enrichment alters all the flame properties namely the flame speed, the adiabatic flame temperature, the flame thickness, the sensitivity to preheating and the stretch resistance. As hydrogen is added to the mixture, the operating domain of the burner is displaced towards lower equivalence ratios. The tracking of the reaction region reveals different stabilization trends in highly H_2-enriched flames. Whereas methane/air flames can reach speed-ups of ~ 10, H_2-enriched flames exhibit speed-ups of ~ 100. In addition, at high H_2 contents, flames remain anchored to the burner inlet for increasing mass flow rates. When the sensitivity to preheating is removed, the flame speed-ups are still found to increase with the hydrogen content. These observations suggest the existence of different stabilization mechanisms in non-equidiffusive flames. Preferential diffusion effects and stretch resistance are known to have a strong influence on the stabilization of laminar flames, but they are not taken into account in current VAMs [33]. Again, pore-level phenomena seem to be essential to explain the macroscopic stabilization trends. An accurate description of the stabilization of H_2 flames in PMBs will require the incorporation of these phenomena to the modeling.

In the last chapter of this dissertation the optical access provided by TPMS-based porous matrices has been leveraged to implement two laser diagnostics: Mie-scattering imaging and Micro Particle Image Velocimetry (μPIV). $CH^\star$ chemiluminescence and Mie-scattering imaging have been applied across the burner's operating range to analyze the stabilization modes of the flame and the preheating distance of the reactants. It has been shown that the offset between the vaporization front and reaction zone could be used to quantify the re-equilibration distance as a function of the operating conditions.

Additionally, Mie-scattering imaging has been combined with μPIV to study the structure of inlet anchored flames and the velocity field in the unburned gas region at the pore scale. Various laser-suited burners have been analyzed and the influence of topology, pore size, mass flow rate, and hydrogen content on flame stabilization has been evaluated. It has been found that the burner topology has a strong impact on the stability domain of the burner and its performance. The pore-scale velocity fields show that the topology has a crucial impact on the interstitial flow which is in turn responsible for the variations in the stabilization properties across the different topologies. It is proposed that the linear porosity of the matrix could be used to characterize the contribution of hydrodynamic effects to flame stabilization. Overall, these findings underscore the need for further development of pore-scale diagnostics.

Future research directions

Develop a combustion model
The results of this dissertation indicate that pore-scale phenomena have a critical impact on flame stabilization and hence on the performance of the reactor. The predicting power of current VAMs is strongly constrained by the lack of upscaling parameters to model certain flame-wall interactions at the pore-level. It is thus essential to refine current combustion models to incorporate the interactions between combustion and heat transfer processes at the pore scale. Future investigations must seek to integrate the influence of the pore size on the local non-adiabaticity of the flame. In the same fashion, further efforts must be devoted to the incorporation of preferential diffusion effects and stretch resistance into the model, to characterize the unique stabilization properties of hydrogen flames. Present VAMs do not include upscaling parameters to account for the influence of hydrodynamic effects and flame wrinkling on the flame behavior. Improved combustion models will enhance predictive capabilities and guide the design of more efficient and sustainable PMBs.

Graded topologies
Investigate the impact of graded topologies on the stability domain and performance of the burner. Future research should focus on designing and testing PMBs with spatially-varying topological parameters to optimize heat transfer, flame stabilization, and fuel flexibility. Topology tailoring is probably the greatest advantage of porous media burners over other combustion technologies since it allows for an extensive optimization of the burner. Because graded topologies may be the key to achieve a fuel-flexible porous burner, this is also one of the primary research directions.

Improving PIV measurements
Explore the use of solid particles in μPIV measurements. In this work, a seeding of oil droplets with a low vaporization temperature has been employed. This has allowed the visualization of the different characteristic scales in a heat recirculating burner and can be used to quantify the preheating distance. However, this represents a considerable experimental limitation when it comes to μPIV measurements. On the one hand, it only provides the velocity field in the fresh gas region. On the other hand, it restricts the analysis of the flame structure to inlet-anchored flames. The use of solid particles would permit the study of the flame structure at different locations, enabling integral velocity measurements. Enhanced PIV capabilities can provide deeper insights into hydrodynamic stabilization effects, flame wrinkling and their impact on the combustion process.

Other nonintrusive techniques: PLIF and Raman Scattering
Extend the application of nonintrusive diagnostics to other techniques such as Planar Laser-Induced Fluorescence (PLIF) and Raman Scattering to study the combustion in PMBs. PLIF can be used to analyze the flame front structure while Raman Scattering can offer insights into gas temperature field and the mixture composition. The present work has presented a new way to obtain an extensive optical access in a 3D burner structure, which could facilitate the application of these diagnostics. Integrating these techniques with existing diagnostic methods would enable a more comprehensive understanding of combustion dynamics and flame-wall interactions in PMBs.

Material influence
A major practical challenge of porous burners is the matrix durability. Therefore, it is necessary to consider the use of different materials to increase the burner durability without restricting

its operating domain. In this work, metallic burners have been used for their enhanced thermal shock resistance, but they limit the operation to lean equivalence ratios. While ceramic burners can withstand higher temperatures, they are brittle and break under thermal shocks. This is especially critical in 3D printed components, owing to the presence of residual internal stresses resulting from the manufacturing process. Future works must consider new materials for the solid phase such as MAX Phases, that combine the elevated thermal shock resistance of metals and the high melting point of ceramics. Also, the influence of the solid phase properties such as the emissivity and the thermal conductivity on heat recirculation, radiation-efficiency and burner's performance should be the subject of future studies.

Increasing TRL

Focus on increasing the Technology Readiness Level (TRL) of PMBs to facilitate their transition from research to commercial applications. This involves integrating PMBs in other systems such as heat exchangers, scaling up experimental studies, optimizing design and manufacturing processes, conducting long-term performance tests, and demonstrating the reliability and efficiency of PMBs in real-world conditions. Collaboration with industry partners like Bulane will be essential to address practical challenges and accelerate the adoption of PMBs in various sectors.

Appendices

Appendix A

Predicting flashback limits in H_2-enriched CH_4/air and C_3H_8/air laminar flames

Novelty and significance statement

1. Definition and application of hybridization strategies to systematically study the effect of hydrogen enrichment and mitigate the downsides of hydrogen admixture in conventional fuels.
2. Observation of two flashback regimes and dynamics in H_2-enriched CH_4/Air and C_3H_8/Air flames.
3. The volume- and diffusion-based effective Lewis number, are found to be controlling parameters in the transition from one flashback regime to the other. A critical value $Le_c = 0.5$ for the effective Lewis number defines the flashback tipping point and can be used to prevent abnormal flashback.

Author Contribution

E. Flores-Montoya: numerical simulations, analysis, writing: original draft.
A. Aniello: analysis, writing: revision and edition.
T. Schuller: analysis, writing: revision and edition.
L. Selle: supervision, conceptualization, analysis, writing: final version.

A.1. Introduction

There is a strong push towards the use of hydrogen as a low-carbon fuel [10, 232], which can also act as a storage for excess in renewable electricity production [6] via Power-to-Gas (PtG) strategies [11, 12]. The use of pure hydrogen in combustion devices usually requires the development of new burner designs but it is also possible to blend it with conventional fuels, for example via direct injection in Natural Gas (NG) pipelines [13]. It is generally accepted that hydrogen contents of up to 20% in volume can be accommodated by the existing end-use systems with minor adjustments [233]. A number of experimental studies on the impact of hydrogen blending into NG for end-use applications have evaluated the performance of appliances such as cook-top and oven burners under increasing hydrogen contents [22–25]. In these studies, flashback is found to be the major limitation for hydrogen blending, which can damage the system and is a major safety issue.

Domestic heating accounts for around 65% of final energy consumption of the residential sector in Europe [234, 235]. Premixed combustion systems such as condensing boilers are widely employed for heating purposes. However, limiting the hydrogen content to $\sim$ 20% in volume

corresponds to a 7% reduction of the CO_2 emissions per energy unit, which does not allow for a significant decarbonization. Broadening the capacity to accommodate hydrogen of the current domestic appliances could not only boost the use of hydrogen as an energy carrier but also yield a significant reduction of CO_2 emissions.

The deployment of hydrogen requires laminar Fuel Flexible Burners (FFB) that can operate safely and efficiently over a wide range of hydrogen content in the fuel [26, 27]. FFB pose a series of technical challenges that arise from the significant differences in combustion properties between hydrogen and hydrocarbon fuels. First, hydrogen flames feature larger burning velocities and a broader flammability range [17]. Moreover, the difference between its thermal and mass diffusivity makes lean hydrogen flames prone to thermo-diffusive instabilities [**?**]. This affects the local burning rate and has a direct impact on flame stabilization. In a recent experimental investigation for two laminar premixed burners used in domestic condensing boilers [35], different flashback and blow-off regimes are reported depending on the hydrogen content and equivalence ratio. The burner wall temperature is also found to be a critical parameter. Finally, hydrogen blending significantly reduces the auto-ignition time [17, 236]. As a result, auto-ignition induced flashback can occur as reported in [31].

The stabilization of premixed flames is mainly driven by the ratio of the flame speed, S_L, and the inlet bulk velocity, U_B. Outside of a given range, there is either flashback or blow-off. Blending hydrogen into hydrocarbon fuels increases S_L thereby promoting flashback if U_B is not increased. It has been observed that hydrogen reduces the turn-down ratio (i.e. the ratio between the maximal and the minimal operating power) of most burners, which is a challenge for the development of FFB. Consequently, there is a need for fundamental understanding of flame stabilization mechanisms in premixed laminar burners operating with fuel blends.

The seminal work of [237] provides the first flashback theory for premixed laminar conical flames. When the diameter of the tube, D, is large compared to the flame thermal thickness δ_T, the bulk velocity at flashback U_B^F is proportional to $DS_L/6\delta_T$. The work of [238] further extends the critical velocity gradient theory by accounting for the velocity profile and a parabolic flame speed distribution near the wall. The results are expressed in terms of Peclet numbers for the jet (Pe_j) and flame (Pe_f). Relations between these two dimensionless numbers at flashback are provided for two scenarios: fully ($Pe_f > 2$) and non-fully ($Pe_f < 2$) developed flame speed on the tube axis. The theoretical relations are found to successfully collapse a large number of experimental data for ethylene-air, acetylene-oxygen and NG-air mixtures.

The stabilization of laminar premixed flames anchored to flame holders and bluff bodies has been addressed in a number of recent experimental and numerical studies. In [239], the influence of the flame-holder radius on the anchoring mechanisms at blow-off and flashback is analyzed. Several stabilization regimes were reported and the presence of a recirculation zone for large flame-holder radius was found to broaden the blow-off limit. [230] identified heat losses, stretch and preferential diffusion effects as the main mechanisms for flame stabilization behind bluff bodies for H_2-enriched methane-air flames. The contribution of each mechanism to the anchoring of the flame is evaluated via flame stretch theory, and the resulting model predicts the flame displacement velocity. Both [239] and [230] compare the numerical results to experiments and report good agreement.

In a numerical parametric study, [30] proposed an improved model for flashback prediction in hydrogen-air flames. It is first shown that the local stretch rate, K, at the flame base correlates well with the near-wall velocity gradient, g. One can then estimate the local displacement speed as $S_D = S_L + g\mathcal{L}_M$ where $\mathcal{L}_M$ is the Markstein length. Replacing S_L by S_D in the Lewis and Von Elbe model allows the prediction of flashback for a large variety of cases including equivalence ratio variations and different burner geometries. The influence of the wall temperature on the flashback dynamics for hydrogen enriched methane-air flames was analyzed by [240]. Flashback propensity is found to increase with the burner wall temperature and hydrogen content of the

mixture. Finally, the work of [208] analyzes the effect of the fuel Lewis number on the stabilization mechanisms of lean-limit laminar flames stabilized on a bluff body. Two different blow-off regimes are therein identified depending on the fuel Lewis number.

With regard to the flashback mechanism, a number of experimental and numerical studies for boundary layer stabilized flames and turbulent swirled burners have reported the presence of reverse flow regions upstream of the flame leading edge [241–243]. The formation of these reverse flow pockets questions the validity of the boundary layer flashback model from [237], which is based on the hypothesis that the flame does not affect the incoming flow. Overall, these backflow regions are found to increase the flashback velocity. According to [242], in the presence of stable reverse flow pockets, the flashback limit is determined by the thermal quenching of the reaction inside the backflow zone due to strain and heat losses to the wall.

Despite this significant body of work, there is still a lack of practical guidelines to evaluate how the power turn-down ratio of a laminar burner varies as the hydrogen content in the fuel is increased. The objective of this study is therefore to provide a criterion that can predict a priori how the flashback limit of a given laminar burner evolves with hydrogen content depending on the original hydrocarbon admixture nature. First, in Sec. A.2, the reference flames and selected strategies for hydrogen addition are presented. Then Sec. A.3 describes the numerical methods and configuration and the main results are discussed in Sec. A.4.

A.2. Theoretical background: hybridization strategies

The considered fuel blend F, is a mixture of hydrogen and a generic hydrocarbon fuel:

$$\mathrm{F} = \alpha \mathrm{H_2} + (1-\alpha)\mathrm{C_mH_n}, \tag{A.1}$$

where α is the molar fraction of hydrogen in F. The global combustion of F with air in lean conditions can be written:

$$\begin{aligned} \alpha \mathrm{H_2} + (1-\alpha)\mathrm{C_mH_n} + \\ \frac{1}{\phi}\left(\psi - \frac{\alpha}{2}\left(2\psi - 1\right)\right)\left(\mathrm{O_2} + a\mathrm{N_2}\right) \longrightarrow \\ m(1-\alpha)\mathrm{CO_2} + \left(\frac{n}{2}(1-\alpha) + \alpha\right)\frac{n}{4}\mathrm{H_2O} + \\ a\frac{1}{\phi}\left(\psi - \frac{\alpha}{2}(2\psi-1)\right)\mathrm{N_2} + (\frac{1}{\phi} - 1)\left(\psi - \frac{\alpha}{2}(2\psi-1)\right)\mathrm{O_2}. \end{aligned} \tag{A.2}$$

where ϕ is the equivalence ratio, $a = 3.76$ the molar ratio of nitrogen to oxygen in air and $\psi = m + n/4$. It is also useful to define the fraction of thermal power provided by hydrogen:

$$\alpha_P = \frac{\alpha W_{\mathrm{H_2}} Q_{\mathrm{H_2}}}{\alpha W_{\mathrm{H_2}} Q_{\mathrm{H_2}} + (1-\alpha) W_{\mathrm{C_mH_n}} Q_{\mathrm{C_mH_n}}}, \tag{A.3}$$

where W_k and Q_k denote the molar mass and the Lower Heating Value of fuel k, respectively. Incidentally, α_P is also equal to the reduction in CO_2 mass emissions obtained by replacing the combustion of $\mathrm{C_mH_n}$ with the combustion of the hydrogen enriched fuel blend F.

The addition of hydrogen in the fuel changes virtually all the characteristics of the flame (speed, thickness, adiabatic temperature, etc.) as well as the thermal power of the system. When α is varied, one can simultaneously alter the equivalence ratio, ϕ, in order to conserve some of these properties. The power can be set independently via the total mass flow rate but one has to bear in mind that this will affect the bulk flow velocity through the burner, U_B, and

therefore the flashback limit.

Most domestic boilers powered with natural gas are designed to operate at a roughly constant equivalence ratio over the whole power range. However, in a context where the hydrogen content in the fuel is imposed by external factors (e.g. drop in the gas network, variable local hydrogen production), FFB may need to modulate the air-to-fuel ratio to optimize combustion over their whole operating range. In this context, a *hybridization strategy* determines how the properties of the fresh mixture are varied when hydrogen is added to the fuel. For a given thermal power there is a single free parameter, which is the relation between the equivalence ratio, ϕ, and the hydrogen content, α_P. The relation $\phi(\alpha_P)$ can be used to keep certain properties of the flame or the system constant as the hydrogen content is increased. Several options are considered:

- The adiabatic temperature T_{ad}. Whether the system be a heating device or an engine, the temperature of the burned gasses is a first-order parameter on the performance and robustness of the apparatus. One may wish to conserve this quantity or at least to keep it bounded.
- The flame thermal thickness, here defined as $\delta_T = (T_{ad} - T_u)/\max(\partial T/\partial x)$ [96]. It is a major parameter in all theories on flashback limits so one strategy would be to keep it constant.
- The laminar burning velocity S_L. In conventional flame stabilization theories, its ratio with the bulk velocity drives the flame length as well as flashback and blowout limits [237].

The theory of [237] states that the flashback limit expressed in terms of U_B/S_L scales with the ratio D/δ_T. According to this model, for an iso–S_L hybridization strategy, the ratio U_B/S_L at flashback would vary as the inverse of the flame thermal thickness, δ_T. In contrast, at constant δ_T, the ratio U_B/S_L should be constant. Therefore, in the iso–δ_T strategy, deviations in the value of U_B/S_L at flashback shed light on the influence of parameters that are not considered in the classical flashback theory of Lewis and Von Elbe. Consequently, the iso–δ_T and the iso–T_{ad} strategies are considered in this work.

Figure A.1 shows the evolution of T_{ad} and δ_T versus ϕ and α_P for a one-dimensional unstretched adiabatic methane-hydrogen-air laminar flame. These maps were generated using the Cantera software and an Analytically Reduced Chemistry (ARC) scheme presented in Sec. A.3. Iso-lines are drawn in Fig. A.1, corresponding to the two considered *hybridization strategies* labeled iso–T_{ad} and iso–δ_T, respectively. While keeping T_{ad} constant yields modest variations in equivalence ratio, keeping the flame thickness constant requires a strong reduction of ϕ as H_2 is added to the fuel mixture.

A reference operating condition $\phi_0 = \phi(\alpha_P = 0)$ should then be chosen. Typical values for natural gas burners of domestic boilers are in the range $0.7 < \phi_0 < 0.8$ in order to keep NOx emissions low. In this study, the chosen value is $\phi_0 = 0.75$ for propane. For methane, the value of ϕ_0 is set so that the adiabatic flame temperature is the same as that of propane. The reference conditions and the associated flame characteristics are summarized in Tab. A.1.

Fuel	ϕ_0	δ_T [μm]	S_L [cm s^{-1}]	T_{ad} [K]
C_3H_8	0.750	482	26.20	1976
CH_4	0.785	546	26.07	1979

Table A.1. – Properties of one-dimensional unstretched adiabatic C_3H_8 and CH_4 flames at the reference operating point $\alpha_P = 0$.

Once this point has been chosen, one can extract from Fig. A.1 the values of ϕ, T_{ad}, S_L and δ_T versus α_P for the two *hybridization strategies* investigated. Figure A.2 presents the variation of

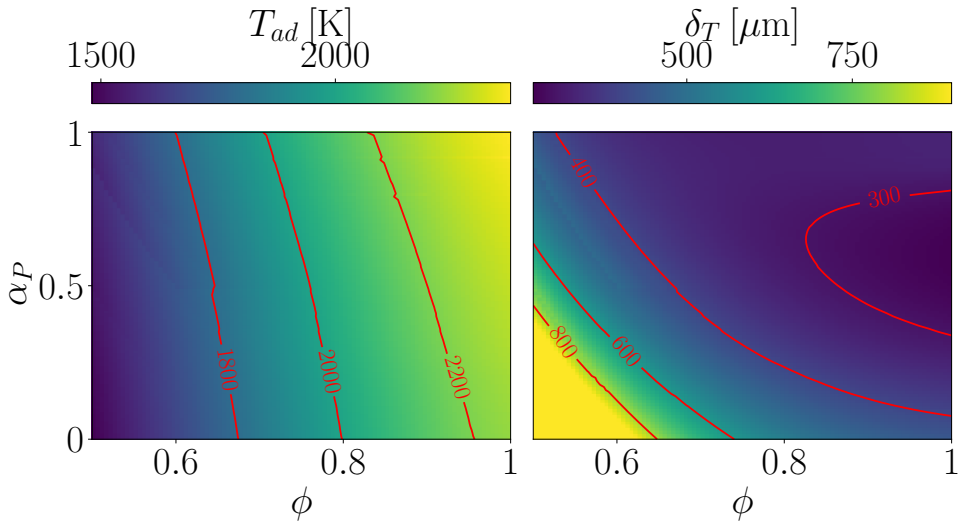

Figure A.1. – Adiabatic flame temperature T_{ad} and flame thermal thickness δ_T maps for a one-dimensional premixed laminar flame of methane-hydrogen-air as a function of the mixture global equivalence ratio, ϕ, and the hydrogen content expressed as a power fraction, α_P.

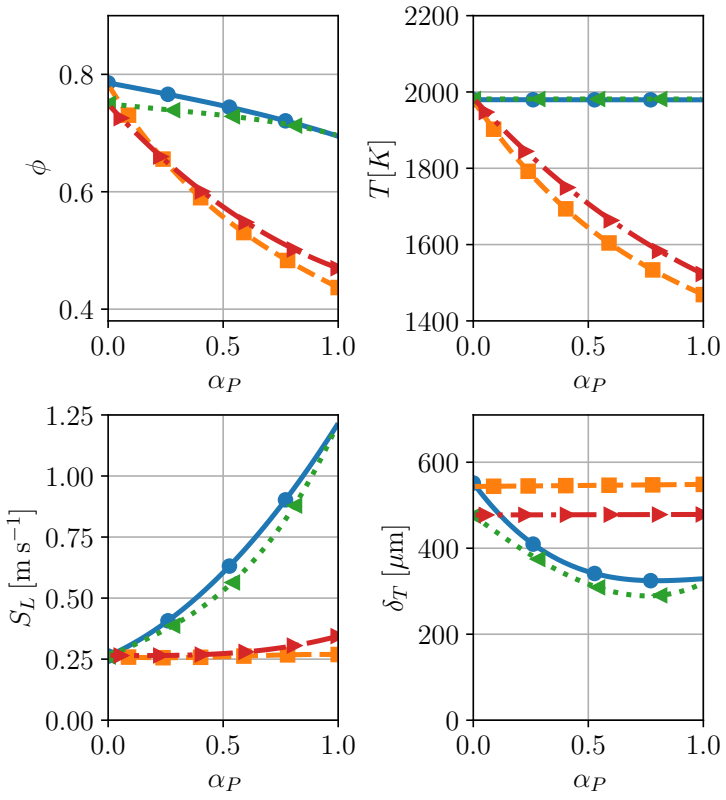

Figure A.2. – Evolution of equivalence ratio ϕ, laminar burning velocity S_L, thermal thickness δ_T and adiabatic flame temperature T_{ad} versus hydrogen content α_P for the two fuel blends under investigation CH_4/H_2 and C_3H_8/H_2 and the iso–T_{ad} and the iso–δ_T hybridization strategies. : iso–T_{ad} – CH_4; : iso–δ_T – CH_4; : iso–T_{ad} – C_3H_8; : iso–δ_T – C_3H_8.

these quantities with the hydrogen content, α_P, for C_3H_8 and CH_4. Regarding the evolution of ϕ and as anticipated from Fig. A.1, while the iso–T_{ad} strategy does not yield a reduction below $\phi = 0.7$, the iso–δ_T requires the equivalence ratio to be reduced as low as 0.45 for pure H_2. Consequently, the adiabatic flame temperature plunges by almost 500 K for the iso–δ_T strategy. This strong variation will affect the burner temperature and consequently the flashback limits. Conversely, while the flame speed is mildly increased in the iso–δ_T strategy, it is multiplied by a factor 5 for the iso–T_{ad} case between $\alpha_P = 0$ and $\alpha_P = 1$. This will surely directly alter the flashback limits. Finally, the flame thermal thickness is reduced by a factor two in the iso–T_{ad} case.

A.3. Numerical setup

Two-dimensional numerical simulations are now used to determine the flashback limits of methane-hydrogen and propane-hydrogen blends for increasing hydrogen content in a premixed laminar burner. In this Section, the solvers, computational domain and numerical procedure are described.

A.3.1. Solvers and coupling strategy

The reacting flow is computed using the AVBP software developed by Cerfacs, which solves the compressible Navier-Stokes equations on unstructured meshes. Conjugate heat transfer between the fluid and solid is accounted for via coupling with the AVTP code, which solves the Fourier equation in the solid. This allows accounting for the influence of the burner temperature on the flame stabilization via the preheating of the fresh gases. Radiative heat transfer is not considered in this study. This may not be a strong limitation for domestic burners but in some industrial applications, flames can be very sooty and radiation has a strong contribution to the thermal state of the system. Radiation from the solid remains as an overall loss, which is unaccounted for. This implies that the burner temperature is overestimated in the present simulations, which therefore represent a worse-case scenario in terms of flashback.

Both AVBP and AVTP solvers are unsteady and exchange boundary conditions periodically. AVTP prescribes the solid temperature while AVBP imposes the heat flux from the gaseous phase. This strategy is known as Neumann-Dirichlet coupling and the conditions for its stability are well known [244]. In this work, the objective is to compute steady states until flashback so that the two codes can be de-synchronized in time. This means that between two coupling events, due to the the slow heat transfer controlled by diffusion in the solid phase, the time advancement in the solid is much larger than that in the fluid. This methodology has been extensively validated and successfully applied to the complex case of a gas-turbine blade [245]. More details about the numerics can be found in Appendix A.A.

A.3.2. Mesh and boundary conditions

The two-dimensional fluid domain depicted in Fig. A.3 allows the stabilization of a laminar flame on a thin slit, which is representative of domestic boiler burners. The geometrical parameters of the burner, namely the slit width $d = 1$ mm, the wall length $w = 1$ mm and the wall thickness $e = 0.5$ mm are kept constant. The total length of the fluid domain is $4h$, with $h = d + w$. Boundary conditions are set using the NSCBC formalism [246]. The velocity $\mathbf{u}_{in}$, temperature, T_{in}, and mixture composition, Y_{in}^k, are set at the inlet and the pressure p_{out} is imposed at the outlet section. No-slip boundary conditions are applied on the inert solid surface. Finally, periodic boundary conditions are applied to the sides. The inlet temperature is set at $T_{in} = 300$ K and the outlet pressure is $p_{out} = 101325$ Pa.

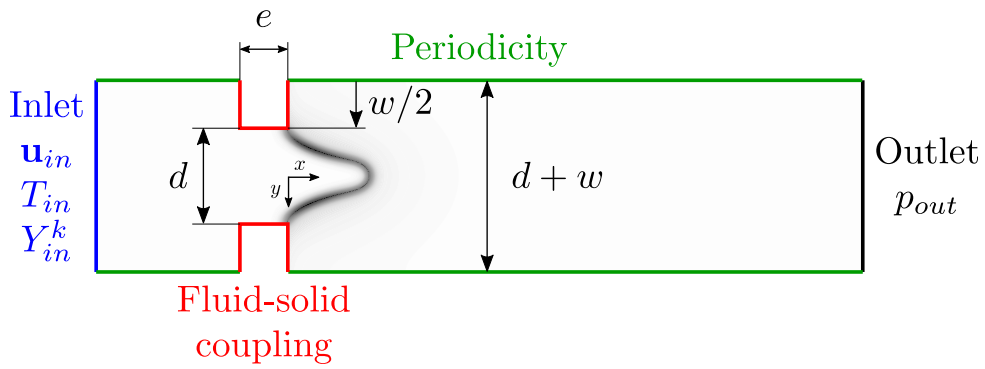

Figure A.3. – Sketch of the fluid domain, its geometrical parameters, and the applied boundary conditions.

The mesh characteristic size is 20 μm in the fluid and solid domains. This resolution ensures a minimum of 14 points within the flame thermal thickness in the worst case scenario, i.e. the C_3H_8/H_2 fuel blend, $\alpha_P = 80\%$ and iso–T_{ad} strategy. The ARC scheme developed in [247] was used to model the kinetics of methane-hydrogen and propane-hydrogen fuel blends. It involves 22 transported species, 173 reactions and 12 species in quasi-steady state.

A.3.3. Flashback limit determination

For a given hydrogen fraction α_P, the equivalence ratio ϕ is adjusted according to the fuel blend and the hybridization strategy, which determines the reactants composition Y^k_{in}. For each mixture, a stationary flame at thermal equilibrium with the solid wall is computed. Then, the inlet velocity is reduced in steps corresponding to a decrease of the thermal power by 125 W/m. The flashback limit of a given α_P and ϕ is defined as the smallest power for which a steady flame can be obtained. This minimal power is designated as flashback limit and denoted by P_f.

A.4. Results and Discussion

This section is devoted to the analysis of the flames at the flashback limit. Their structure is first examined in order to identify the physical parameters driving the onset of flashback. Then, the dynamics of the flame during flashback is presented.

A.4.1. Flame front structure

Figure A.4 shows the normalized fields of heat release rate at the flashback limit, for H_2-enriched propane-air flames in the iso–T_{ad} and iso–δ_T hybridization strategies. The heat release rate $\dot{\omega}_T$ is normalized by the maximum value in the corresponding one-dimensional unstretched adiabatic flame with the same inlet conditions, $\dot{\omega}^0_T$. All cases are labeled with the hydrogen content α_P and the equivalence ratio, ϕ. The corresponding figure for H_2-enriched methane-air flames can be found in Appendix A.B. Additionally, the flame front is highlighted via a dotted line, defined as the coordinates (x_f, y_f) where:

$$\left(\mathbf{u} \cdot \nabla \dot{\omega}_T\right)_{x_f,\, y_f} = 0 \tag{A.4}$$

In this expression, $\mathbf{u}$ and $\dot{\omega}_T$ denote the local velocity and heat release rate respectively. In order to avoid a mathematical indetermination near the walls where the velocity is null, the

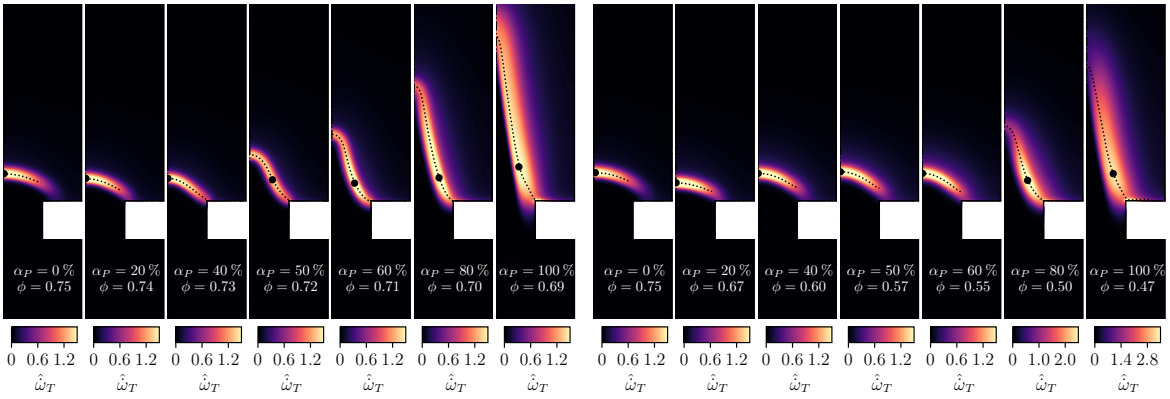

(a) hybridization strategy: iso–T_{ad} (b) hybridization strategy: iso–δ_T

Figure A.4. – Normalized heat-release rate for propane-hydrogen-air flames with increasing hydrogen content α_P.

dotted line is stopped at 85% of $\dot{\omega}_T^0$. This criterion is somewhat arbitrary but does not alter the following qualitative interpretation. Finally, on each flame, the location of the maximum heat release rate is marked with a large filled circle.

In the iso–T_{ad} strategy (Fig. A.4(a)), the flame height at the flashback limit is roughly constant until $\alpha_P \sim 40\%$ but then increases rapidly. There is a five-fold increase in flame height between pure propane and pure hydrogen, which means that flashback occurs at higher values of U_B/S_L. Now scrutinizing the location of maximum heat release rate indicated by the large filled circle, it is centered on the slit for $\alpha_P < 40\%$ and is displaced to the side with higher hydrogen enrichment. Interestingly, its height above the slit does not change much when α_P is increased, which is a somewhat unexpected feature. Regarding the iso–δ_T strategy (Fig. A.4(b)), the flame height at flashback first decreases between $\alpha_P = 0$ and 20%, followed by a marginal increase until $\alpha_P = 60\%$ and a steep increase. Variations in the distance to the wall of the heat release maxima are slightly more pronounced with respect to the iso–T_{ad} strategy but this is primarily due to the initial decrease in the flame height for small hydrogen enrichment.

The anchoring of the flame at the edge of the slit is now discussed. Without hydrogen, the flame root is detached from the wall by approximately one flame thickness but as α_P is increased, it re-attaches to the wall. This qualitative difference can be partly attributed to the local enrichment discussed below. The re-attachment occurs at different values of α_P for the two hybridization strategies: $\alpha_P \geq 40\%$ in the iso–T_{ad} case (Fig. A.4(a)) versus $\alpha_P \geq 80\%$ for the iso–δ_T (Fig. A.4(b)). This difference can be attributed to the reduction of the flame thickness in the iso–T_{ad} strategy, resulting in a reduction of the side-wall quenching distance. The cases with methane shown in Fig. A.11 of Appendix A.B display a similar trend.

An analysis of the spatial equivalence ratio distribution is intended to shed light on the variations in flame height and heat release rate distribution. The local equivalence ratio is computed as in [208] via:

$$\Phi = \left(\frac{Z_C + Z_H}{Z_O}\right) \Bigg/ \left(\frac{Z_C + Z_H}{Z_O}\right)_{st} \tag{A.5}$$

where Z_k denotes the atomic mass fraction of atom k and subscript 'st' stands for stoichiometric conditions. Figure A.5 shows the distribution of local equivalence ratio, normalized by the inlet equivalence ratio, Φ_{inlet}, which highlights the local deviations driven by thermodiffusive effects. The effect of hydrogen addition on methane and propane flames for the iso–T_{ad} strategy is

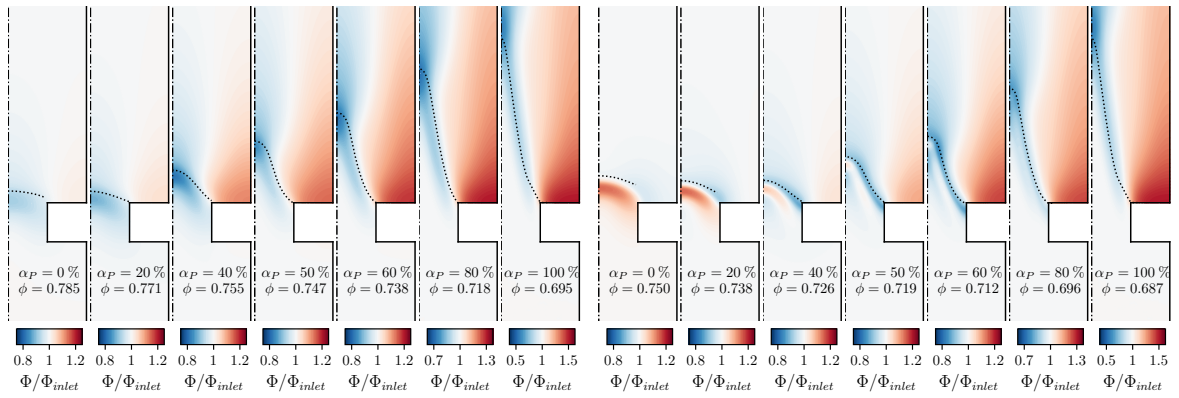

(a) Methane: iso–T_{ad} strategy

(b) Propane: iso–T_{ad} strategy

Figure A.5. – Local equivalence ratio, Φ, normalized by its inlet value for flames with increasing hydrogen content, α_P, for the iso–T_{ad} hybridization strategy.

presented in Fig. A.5. The results are qualitatively similar for the iso–δ_T case. For CH_4 (cf. Fig. A.5(a)), the fuel Lewis number at $\alpha_P = 0$ is unity so that the normalized local equivalence ratio is roughly constant. As hydrogen is added, Φ reduces on the centerline where the flame is curved towards the fresh gasses and increases at the flame base, which has the opposite curvature. This is a typical effect for lean mixtures and is attributed to the small Lewis number of hydrogen Le = 0.316 [231]. For C_3H_8 (cf. Fig. A.5(b)) the fuel Lewis number is Le = 1.884, which causes a 20% increase in Φ near the centerline at $\alpha_P = 0$. As the hydrogen content is increased, the effect is compensated by its small Lewis number, with a turning point around $\alpha_P = 50\%$, which corresponds to the increase in flame height. These results suggest that the driving mechanism for the alteration of the flashback limit is the change in fuel Lewis number.

A.4.2. Modeling the flashback limit

Figure A.6(a) depicts the evolution of the thermal power at flashback versus α_P for H_2-enriched methane-air and propane-air flames under the two hybridization strategies. This defines the minimal operating power of the burner as a function of α_P. The iso–T_{ad} strategy is discussed first. It is intended to maintain the burnt gas temperature and, therefore, not to affect the thermodynamic cycle of the system as the hydrogen content of the fuel is increased. However Fig. A.6(a) shows that with this strategy, the flashback power increases by an order of magnitude when α_P is varied from zero to one. This prevents the operation at low powers for high hydrogen-content and drastically reduces the burner turn-down ratio, should the iso–T_{ad} strategy be chosen. Moving on to the iso–δ_T strategy, the power at flashback is roughly constant until $\alpha_P = 0.6$ but then increases by up to a factor of 5. In the theoretical framework of [237], because the ratio D/δ_T is constant in the iso–δ_T strategy, this would attribute the change in flashback limit to the increase in flame speed.

Overall, Fig. A.6(a) shows that the hybridization strategy has a great influence on the flashback limit and that it is similar for both fuels. Because both strategies fail at preserving the flashback limit, one must investigate the evolution of other parameters. In order to remove the influence of the flame speed, the evolution of the normalized bulk velocity U_B/S_L versus α_P is presented in Fig. A.6(b).

This ratio remains roughly constant until $\alpha_P = 0.4$ for the iso–T_{ad} strategy and $\alpha_P = 0.6$ for the iso–δ_T strategy. This is similar to the observed evolution of the flame lengths in Fig. A.4. This

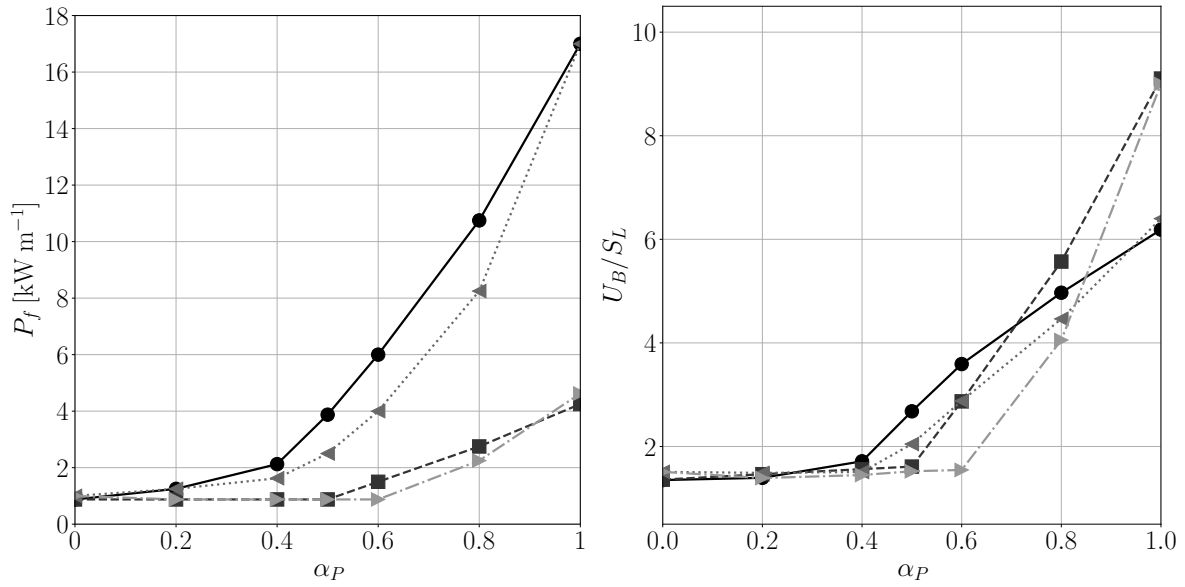

(a) Thermal power at flashback.

(b) U_B/S_L at flashback.

Figure A.6. – Evolution of the flashback limit for the different fuel blends and hybridization strategies. —●— : CH_4/H_2 iso–T_{ad}; --■-- : CH_4/H_2 iso–δ_T; ···◀··· : C_3H_8/H_2 iso–T_{ad}; -·-▶-·- : C_3H_8/H_2 iso–δ_T.

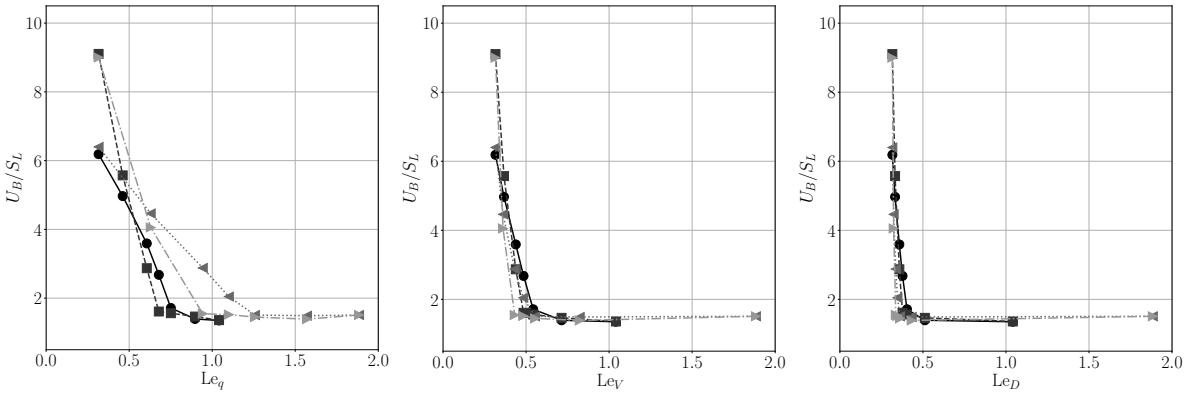

(a) Heat-release-rate averaged Eq. (A.6)

(b) Volume-averaged Eq. (A.7)

(c) Diffusion-based Eq. (A.8)

Figure A.7. – Normalized bulk velocity versus effective Lewis number, at the flashback limit for different fuel blends and hybridization strategies. —●— : CH_4/H_2 iso–T_{ad}; --■-- : CH_4/H_2 iso–δ_T; ···◀··· : C_3H_8/H_2 iso–T_{ad}; -·-▶-·- : C_3H_8/H_2 iso–δ_T.

result indicates that the theoretical framework of [237] remains valid for low hydrogen content but as anticipated from Fig. A.5, past a certain value of α_P, local deviations in equivalence ratio caused by non-unity Lewis number affect the flashback limit.

A criterion for the deviation from the theory of Lewis and Von Elbe, which would not depend on the hybridization strategy is now sought. In the case of multi-fuel blends, various effective-Lewis-number formulations have been proposed to evaluate thermo-diffusive effects [248–250]. A formulation based on the heat-release rate was proposed by [248]:

$$\mathrm{Le}_q = 1 + \frac{\sum_{i=1}^{f} q_i(\mathrm{Le}_i - 1)}{\sum_{i=1}^{f} q_i} \tag{A.6}$$

where $q_i = Q_i Y_u^i / c_p T_u$ is the normalized heat-release rate, Q_i is the fuel lower heating value per mass unit, Y_u^i is the i-fuel mass fraction, c_p is the specific heat capacity and T_u is the temperature of the reactants. This formulation has been used for example in the analyses conducted in [250–253]. A second formulation, based on a volume-weighted average was proposed by [249] and reads:

$$\mathrm{Le}_V = \sum_{i=1}^{f} x_i \mathrm{Le}_i \tag{A.7}$$

where $x_i = X_i / \sum_{i=1}^{f} X_i$ is the i-fuel volume fraction in the fuel blend $i = 1, \ldots, f$. Finally, a diffusion weighted formulation was proposed by [250]:

$$\mathrm{Le}_D = \frac{D_T}{\sum_{i=1}^{f} x_i D_{i,\,\mathrm{N_2}}} \tag{A.8}$$

where $D_{i,\,\mathrm{N_2}}$ is the molecular diffusion coefficient of fuel species i in N_2. These formulations have been systematically compared in various related works [250, 254, 255]. The volume-weighted average proposed by [249] was shown to be well suited to describe the evolution of the Markstein length for H_2/CH_4 and H_2/C_3H_8 blends [254]. [250] found that the diffusion based formulation, Le_D, yielded better predictions of the flame height in premixed turbulent H_2/CH_4/Air flames for different pressure levels. Similarly, [255] reported that the diffusion-based formulation was able to better capture stretch effects on spherical expanding flames for hydrogen enriched CH_4/Air mixtures.

The evolution of U_B/S_L at the flashback limit versus these three formulations for the effective Lewis number is represented in Fig. A.7.

Regarding the heat-release-rate averaged formulation (cf. Eq. A.6), Fig. A.7(a) shows that as Le_q decreases, the flashback limit is pushed to higher values of U_B/S_L but all fuels and hybridization strategies have a different behavior. The volume-averaged effective Lewis number deduced from Eq. (A.7) and shown in Fig. A.7(b) provides a good collapse of all the curves. Above $\mathrm{Le}_V \gtrsim 0.5$ the flashback limit in terms of U_B/S_L is unchanged but for $\mathrm{Le}_V < 0.5$, there is a strong increase in the minimum value of U_B/S_L that can be sustained. Finally, the diffusion-based formulation determined with Eq. (A.8) and presented in Fig. A.7(c) achieves an even tighter collapse of all cases, indicating that there might be some generality in the choice of these variables. From a practical perspective, the value of $\mathrm{Le} \simeq 0.5$ for the volume-averaged or diffusion-based effective Lewis number is a tipping point in the flashback behavior of these flames.

It was observed in Fig. A.4 that the increase in flame length is concomitant with the deviation of the location of maximum heat release rate away from the symmetry axis of the flame. This phenomenon is further studied in Fig. A.8, which plots the dimensionless transverse coordinate of the position of the heat release rate maxima, y/d, versus Le_D. As for the flashback limit, Le_D is a variable that yields a collapse of the curves for all cases: for $\mathrm{Le}_D > 0.5$, the maximum heat release rate is at the flame tip while for $\mathrm{Le}_D < 0.5$ all cases bundle around $y/d = 0.3$. Because the flow velocity decreases for increasing y/d and the local equivalence ratio simultaneously increases (cf. Fig. A.5), this explains why flashback occurs at higher values of U_B/S_L for these cases. This effect is quantified by computing the evolution of the displacement speed, S_D, along the flame front:

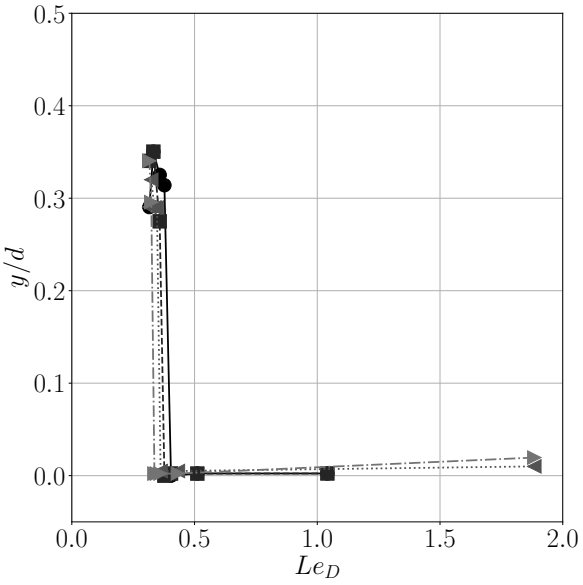

Figure A.8. – Evolution of the normalized lateral position of the maximum heat release rate versus diffusion-based Lewis number, Le_D, for all cases. —●— : CH_4/H_2 iso–T_{ad}; --■-- : CH_4/H_2 iso–δ_T; ···◀··· : C_3H_8/H_2 iso–T_{ad}; -·▶-· : C_3H_8/H_2 iso–δ_T.

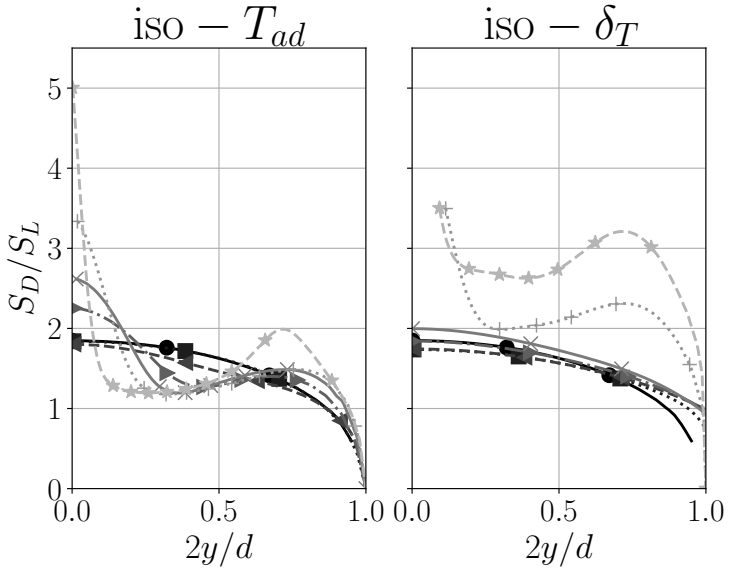

Figure A.9. – Evolution of the normalized displacement velocity S_D/S_L versus the dimensionless transverse coordinate $2y/d$ for H_2-enriched methane-air flames in the iso–T_{ad} (left) and the iso–δ_T (right) hybridization strategies. —●— : $\alpha_P = 0\%$; ···■··· : $\alpha_P = 20\%$; --◀-- : $\alpha_P = 40\%$; -·▶-· : $\alpha_P = 50\%$; —×— : $\alpha_P = 60\%$; ···+··· : $\alpha_P = 80\%$; --★-- : $\alpha_P = 100\%$.

$$S_D = \frac{\rho}{\rho_u}\mathbf{u}\cdot\mathbf{n}, \tag{A.9}$$

where $\mathbf{n}$ denotes the unit vector normal to the flame front and ρ is the local density. The displacement speed, S_D, is a measure of the local mass consumption of the flame front [96]. Figure A.9 shows the evolution of the displacement speed, S_D, normalized by the laminar burning

velocity, S_L, versus the dimensionless transverse coordinate, $2y/d$, for all hydrogen-methane-air flames. For small hydrogen content, the profiles collapse and the maxima is on the symmetry axis. Conversely, for sufficiently high values of α_P, the displacement speed of the flame front develops a local maxima in the vicinity of the flame base. This change in the mass consumption profile along the flame front is responsible for the increase in flashback propensity when the critical Lewis number is reached. Similar observations and conclusions can be drawn for the hydrogen-propane-air flames as shown in Fig. A.12 of Appendix A.B.

A.4.3. Flashback dynamics

This section is devoted to the analysis of the flame dynamics during a flashback event. Flashback is the result of an unstable feedback loop between the solid, which heats up when the flame gets closer and the flame, which approaches the solid as it heats up. In principle, the numerical simulation of a flashback event would require the synchronization of the combustion and heat transfer solvers [256]. On the one hand, the physical time of this coupling scales with the characteristic time of heat diffusion in the solid, which can be estimated as $t_s = e^2/\alpha \simeq 27.5$ ms, where α is the thermal diffusion coefficient of the solid and e is the thickness of the wall. On the other hand, the flame propagation through the burner slit is a much faster phenomenon with a time-scale of the order of $t_f = e/S_L$, which for the considered cases lies between $0.4 \lesssim t_f \lesssim 2$ ms. Consequently, there is a clear separation of time scales allowing us to assume that the solid has a constant – yet nonuniform – temperature during the flashback. Because it is also quite unlikely that the increase in temperature of the burner while the flame is flashing back would drastically affect its dynamics, with the intent to save CPU time, the following procedure is chosen in this work. The initial condition corresponds to the last stable flame that could be obtained with desynchronized coupling, i.e. the flames presented in Sec. A.4.1. The temperature of the solid wall is fixed and the inlet velocity is progressively reduced until the flame propagates upstream.

This methodology is now applied to two representative cases: one below and one above the critical threshold of $\mathrm{Le}_V = 0.5$. These flames are respectively $\alpha_P = 20$ % and $\alpha_P = 60$ % for the CH_4/H_2 and the C_3H_8/H_2 blends with the iso–T_{ad} hybridization strategy. Figure A.10 shows the flame front dynamics during flashback.

In Fig. A.10(a), the flame remains symmetric during flashback and the fastest point is the flame tip, corresponding to the location of the maximum heat-release rate when $\mathrm{Le}_V > 0.5$ (cf. Fig. A.8). However, as exemplified in Fig. A.10(b), when $\mathrm{Le}_V < 0.5$ there is a symmetry breaking and the fastest point in the flame front lies now on the side, which is again consistent with the displacement of the location of maximum heat-release rate for high hydrogen content. A similar behavior is observed for the C_3H_8/H_2 flames in Fig. A.13 presented in Appendix A.B.

Such breaking of symmetry in flame shape has already been reported in numerical simulations [257–261]. For example in [257, 258], the stabilization of hydrogen-air flames in micro and meso-scale channels with imposed wall temperature profile was shown to be asymmetric for sufficiently large inlet velocities. The transition is found to correspond to the formation of two local maxima of H radical in the flame front. In [259–261], it is shown that symmetry breaking for flames propagating in narrow tubes allows them to burn more intensively and makes them more robust to quenching.

A.5. Conclusion

A numerical study on the influence of hydrogen enrichment on methane-air and propane-air flames has been performed. First, the concept of hybridization strategy has been introduced and various hybridization schemes have been considered to set the fresh mixture composition. These strategies define how the fuel-air ratio must be adjusted when the hydrogen content in the fuel

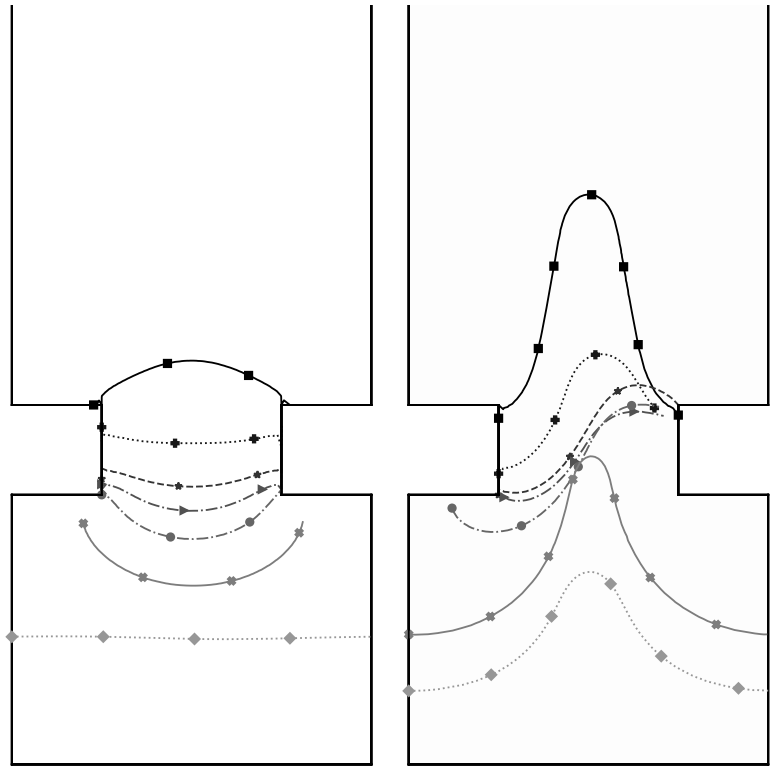

(a) $\alpha_P = 20$ % (b) $\alpha_P = 60$ %

Figure A.10. – Flame front evolution during flashback for the CH_4/H_2 blends with the iso–T_{ad} hybridization strategy. Time step between snapshots is 1.01 ms in a) and 0.45 ms in b).

is varied in order to preserve the adiabatic flame temperature or the flame thermal thickness. Secondly, two-dimensional direct numerical simulations with conjugate heat transfer have been used to determine the flashback limits of hydrogen-enriched methane-air and propane-air flames in a premixed laminar burner for the two hybridization strategies.

Upon the determination of flashback limits, two different flashback regimes have been identified as the hydrogen content in the combustible admixture is varied. These two flashback regimes are shown to be well correlated with the fuel effective Lewis number based on the volume fraction, Le_V, or the mass diffusion coefficient, Le_D. A critical effective Lewis number of $\mathrm{Le}_c = 0.5$ is found to be the tipping point in the flashback limit for all cases. For values above Le_c the flashback velocity of the flame scales with the laminar burning velocity and the maximum of heat release rate is located on the flame symmetry axis. In contrast, for values below Le_c the flame flashback velocity does not scale with the laminar burning velocity and the U_B/S_L ratio increases with the hydrogen content in the fuel. Besides, the flame front features two symmetric local maxima of heat release rate on the flame sides. These results indicate that flashback propensity of hydrogen flames is promoted by preferential diffusion effects and not exclusively linked to their increased flame speed.

Finally, the dynamics of flashback in these two regimes is studied for two representative cases. The simulations reveal two different possible flashback dynamics: a bulk symmetric flashback for low hydrogen contents and an asymmetric flashback for high hydrogen contents.

Acknowledgments

This work was granted access to the HPC resources of IDRIS under the allocation A0132B10627 made by GENCI. The PhD of Enrique Flores Montoya is funded by the company Bulane and the Occitanie Region in the framework of the *Défi Clé Hydrogène Vert*. The financial support of the European Research Council under the European Union's Horizon 2020 research and innovation program Grant Agreement 832248, SCIROCCO is also acknowledged.

A.A. Solvers and models

In the gaseous phase ($-g$ subscript), the compressible reactive Navier-Stokes parallel solver AVBP is used with the Lax-Wendroff scheme. The governing partial differential equations equations in AVBP are:

$$\frac{\partial \rho_{g,k}}{\partial t} + \nabla \cdot (\rho_{g,k}\mathbf{u}) + \nabla \cdot \mathbf{J_k} - \dot{\omega}_k = 0 \tag{A.10}$$

$$\frac{\partial \rho_g \mathbf{u}}{\partial t} + \nabla \cdot (\rho_g \mathbf{u}\mathbf{u}) + \nabla \cdot \left[P\underline{\underline{\mathbf{I}}} - \underline{\underline{\tau}}\right] = 0 \tag{A.11}$$

$$\frac{\partial \rho_g E}{\partial t} + \nabla \cdot (\rho_g E \mathbf{u}) + \nabla \cdot \left[\mathbf{u} \cdot \left(P\underline{\underline{\mathbf{I}}} - \underline{\underline{\tau}}\right) + \mathbf{q}\right] - \dot{\omega}_T^0 = 0 \tag{A.12}$$

where ρ_g is the gas density, $\mathbf{u}$ is the velocity field, E is the total non-chemical energy per mass unit, and $\underline{\underline{\tau}}$ is the viscous stress tensor in a compressible Newtonian flow. The fluid is a mixture of k perfect gases and volume forces such as gravity are neglected. Species diffusion is computed by using the Hirschfelder and Curtis approximation:

$$\mathbf{J_k} = -\rho_g \left(D_k \frac{W_k}{W} \nabla X_k - Y_k \mathbf{V^c} \right) \tag{A.13}$$

where D_k, W_k, X_k and Y_k denote the k species diffusion coefficient, molar mass, molar fraction and mass fraction respectively. The correction velocity $\mathbf{V^c}$ ensures mass conservation:

$$\mathbf{V^c} = \sum_{k=1}^{N} D_k \frac{W_k}{W} \nabla X_k \tag{A.14}$$

The heat flux, $\mathbf{q}$, is computed as the sum of the Fourier heat flux with a conductivity, λ_g, and the flux related to preferential diffusion of the sensible species enthalpies $h_{s,k}$:

$$\mathbf{q} = -\lambda_g \nabla T_g + \sum_k \mathbf{J_k} h_{s,k} \tag{A.15}$$

Transport is simplified assuming constant Prandtl ($\mathrm{Pr} = 0.662$) and species Schmidt numbers (Sc_k):

$$\mathrm{Sc}_k = \mathrm{Pr} \cdot \mathrm{Le}_k \tag{A.16}$$

so that the Lewis number, Le_k, of individual species is also constant. The assumption of constant Lewis number has proven to yield accurate results in non-equidiffusive premixed reacting flows [262, 263]. The heat release per unit volume $\dot{\omega}_T^0$ is given by the formation enthalpies [96]:

$$\dot{\omega}_T^0 = -\sum_k \Delta h_k^{f,0} \dot{\omega}_k \tag{A.17}$$

Finally, the variation of dynamic viscosity with temperature is computed using a power law:

$$\mu = \mu_{\text{ref}} \left(\frac{T_g}{T_{\text{ref},\,\mu}} \right)^{n_\mu} \tag{A.18}$$

For the present mixture, adapted values are $\mu_{\text{ref}} = 1.707 \times 10^{-5}\,\text{kg m}^{-1}\,\text{s}^{-1}$, $T_{\text{ref},\,\mu} = 288$ K and $n_\mu = 0.695$.

In the solid phase, the solver AVTP [264] is used to integrate Fourier's heat equation:

$$\rho_s c_{p_s} \frac{\partial T_s}{\partial t} - \nabla \cdot (\lambda_s \nabla T_s) = 0 \tag{A.19}$$

Spatial discretization uses second-order Galerkin diffusion scheme, and time integration is performed with an implicit first-order forward Euler scheme. The inversion of the system is achieved through a parallel matrix-free conjugate gradient method [265]. Solid density, thermal conductivity and heat capacity are $\rho_s = 7.869 \times 10^3\,\text{kg m}^{-3}$, $\lambda_s = 33\,\text{Wm}^{-1}\text{K}^{-1}$ and $c_s = 461\,\text{J kg}^{-1}\text{K}^{-1}$ respectively. The two softwares AVBP and AVTP are coupled through the CWIPI library [264]. At the gas/solid boundary, $\mathcal{A}_{gs}$, AVTP imposes the temperature and AVBP the energy flux, so that:

$$\lambda_g \nabla T_g \cdot \mathbf{n_{gs}} = \lambda_s \nabla T_s \cdot \mathbf{n_{gs}}, \text{ and } T_g = T_s \text{ on } \mathcal{A}_{gs} \tag{A.20}$$

where $\mathbf{n_{gs}}$ is the unit normal vector oriented from the gas toward the solid.

A.B. Additional figures

Figure A.11 shows the normalized fields of heat release rate at the flashback limit, for H_2-enriched methane-air flames in the iso–T_{ad} and iso–δ_T hybridization strategies. The heat release rate $\dot{\omega}_T$ is normalized by the maximum value in the corresponding one-dimensional unstretched adiabatic flame with the same inlet conditions, $\dot{\omega}_T^0$. All cases are labeled with the hydrogen content α_P and the equivalence ratio, ϕ

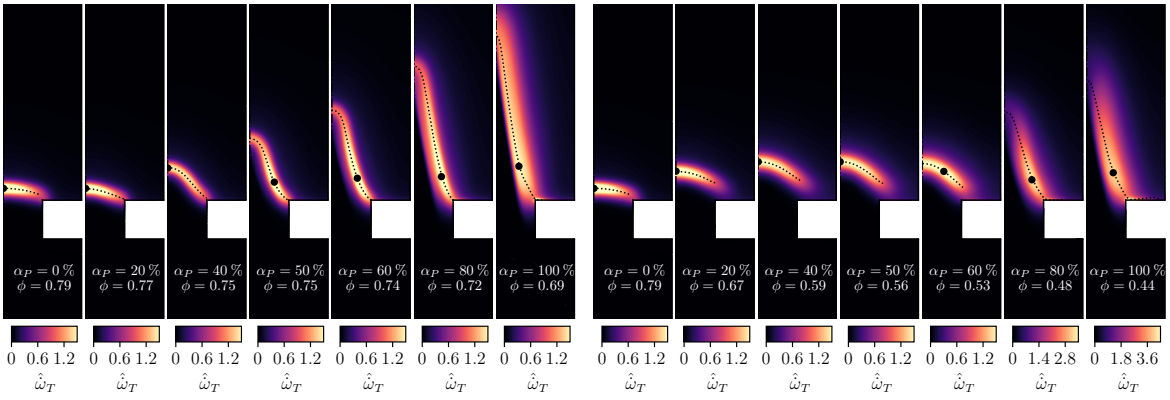

(a) hybridization strategy: iso–T_{ad}

(b) hybridization strategy: iso–δ_T

Figure A.11. – Normalized heat-release rate for methane-hydrogen-air flames with increasing hydrogen content α_P.

Figure A.9 shows the variation of the displacement speed, S_D, normalized by the laminar burning velocity, S_L, versus the dimensionless transverse coordinate, $2y/d$, for all hydrogen-propane-air flames

Finally, Fig. A.10 shows the propagation of the flame front during flashback for C_3H_8/H_2 blends with the iso–T_{ad} hybridization strategy

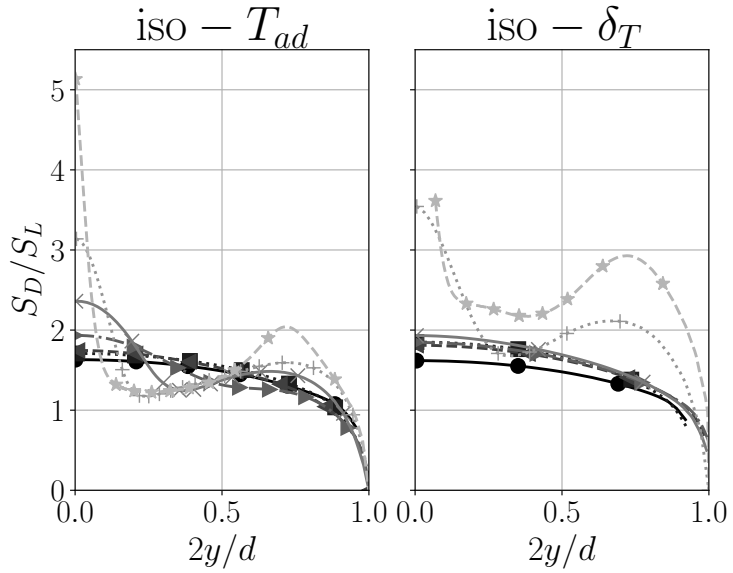

Figure A.12. – Evolution of the normalized displacement velocity S_D/S_L versus the dimensionless transverse coordinate $2y/d$ for H_2-enriched propane-air flames in the iso–T_{ad} (left) and the iso–δ_T (right) hybridization strategies. —●— : $\alpha_P = 0\%$; ···■·· : $\alpha_P = 20\%$; --◀-- : $\alpha_P = 40\%$; -·▶-· : $\alpha_P = 50\%$; —×— : $\alpha_P = 60\%$; ···+·· : $\alpha_P = 80\%$; --★-- : $\alpha_P = 100\%$.

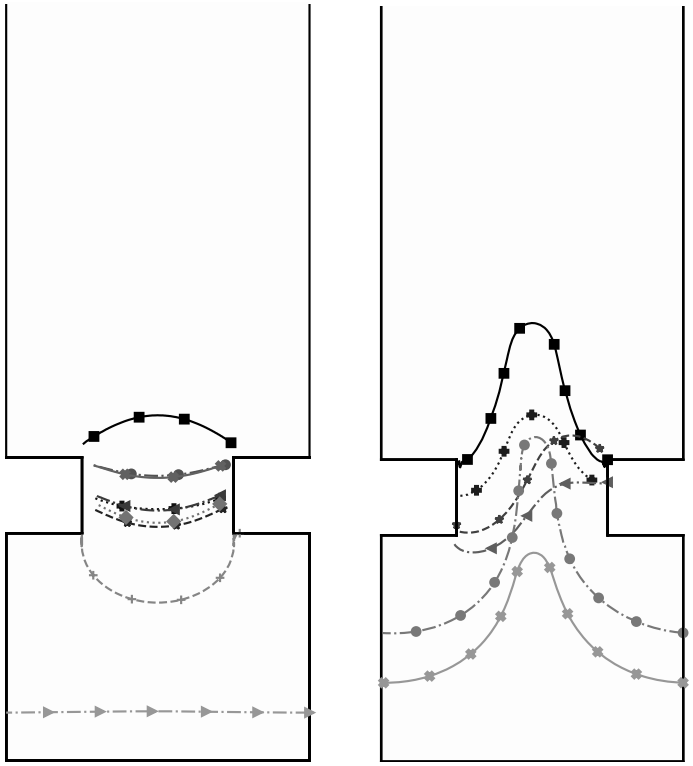

(a) $\alpha_P = 20$ % (b) $\alpha_P = 60$ %

Figure A.13. – Flame front evolution during flashback for the C_3H_8/H_2 blends with the iso–T_{ad} hybridization strategy. Time step between snapshots is 1.45 ms in a) and 0.42 ms in b).

List of Figures

1.1. Headlines announcing negative electricity prices in the European pool. 2
1.2. Evolution of the global total energy supply in EJ by source. Reproduced from IEA [7]. 3
1.3. Multiperforated premixed laminar burner used in condensing boilers. Credits to Hugo Pers. 4
1.4. Porous Media Burner in laboratory conditions. Credits to François Muller. . . . 5
1.5. Unidirectional and counterflow heat recirculating reactors. 8
1.6. Free flame versus Porous Media Combustion (PMC). 9
1.7. Stabilization curve – Speed-up versus flame position – in a finite length porous medium. (a-c) Gas and solid phase temperature profiles at different flame locations. 10
1.8. Schematic of a flame inside a porous medium 12
1.9. From [99]: (a) alumina and (b) silicon carbide ceramic foams with different pore size used in experimental studies. 12
1.10. Different burner designs 13
1.11. Commercial examples of porous burners. Credits to GoGas and Promeos Intelligent Heat. 16
1.12. Picture, blueprints and schematic (from left to right) of the 10 kW Porous Media Burner prototype with integrated heat exchangers developed by Durst et al. in [46]. 16
1.13. Experimental setup used in [152, 153] to apply CARS (left) and axial profile of gas temperature and H_2 concentration obtained inside the burner (right). Reproduced from [152]. 19
1.14. Experimental setup used in [151] to achieve optical access to the interior of the porous burner (left) and OH distribution for various thermal loads at an equivalence ratio of $\phi = 0.71$ (right). Reproduced from [151]. 20
1.15. Transversely averaged profiles of attenuation, $\Delta\overline{\mu}^g(x)$ (a) and temperature (b). (c) X-ray scan of the solid structure. (d) Vertical cross section of the reconstructed 3D temperature field. Reproduced from [101] 20
1.16. Direct flame visualization in a single-layer packed bed structure from Fursenko et al. [158]: transition from surface to submerged combustion (left). $CH^\star$ chemiluminescence imaging in a 2D cylinder array in staggered configuration with controlled wall temperature from Khodsiani et al. [154]: influence of the operating conditions on the flame liftoff distance (right). 21

2.1. Schematic of the burner base. Reproduced from Muller [165]. 26
2.2. Schematic of the POROSITO test rig. 27
2.3. Schematic of the mixing system. 28
2.4. PDF of the uncertainties in ϕ, α_P and P. 28
2.5. Local pore size field, $d_p(\mathbf{x})$ and pore size PDF for a Diamond-based porous matrix with $\epsilon = 0.8$ and $d_p = 2.5$ mm. 30
2.6. Remapping curves for the Diamond topology. 30
2.7. Steps in the geometry-generation process. 31
2.8. Detail of the burner geometry before (left) and after (right) the remeshing operation. 32
2.9. PMBs featuring a topological gradation of porosity (left) and pore size (right). . 32

2.10. Swirled Diamond porous medium with a radial distribution of porosity, a pore size of $d_p = 3.5$ mm and a swirl number of $s = 0.05$. 33
2.11. a) Arrangement of the STDs in a Diamond-TPMS-based porous media. In this topology, the x, y and z-STD are too small for practical purposes. For direct flame visualization, the zy and the yz-STD can be used to access the interior of the porous matrix. b) 3D view of the different volume-partitions in an elementary volume. Green-colored volumes are accessible by imaging the porous medium from one of the major STDs and represent roughly 42% of the total volume. The hidden volume is depicted in red and accounts for approximately 38% of the total volume. The remaining 20% of the volume is occupied by the solid phase. 34
2.12. a) Arrangement of the STDs in a Gyroid-based topology. In this geometry, the y-STD and z-STD are used for direct flame visualization. However, the optical pathways of these two STDs do not intersect inside the burner and thus cannot be combined to apply laser diagnostics. In contrast, the optical pathways of the yz-STD and x-STD are coincident and can be used for laser diagnostics. In this topology there are also four major STDs in the xyz direction but they were not used the present study. b) 3D rendering of the different volume-partitions in an elementary volume. For $\epsilon = 0.8$, the fraction of optically accessible volume using the y-STD is approximately 33% and the hidden volume is roughly 47%. 35
2.13. a) Arrangement of the STDs in the Primitive topology. In this geometry, there are three STDs each aligned with one direction of space. These three STDs intersect inside the cavities of the burner and therefore can be combined to apply laser diagnostics. b) 3D view of the different volume-partitions in an elementary volume. The optically accessible volume in a $\epsilon = 0.7$ burner is approximately 35% of the total volume and the hidden fraction is roughly 35%. 36
2.14. Evolution of the 3D printed material porosity and thermal conductivity as a function of the laser scanning speed and energy density. Reproduced from Simmons *et al.* [172]. 37
2.15. Porous matrices on the printing plate after the additive manufacturing process. . 38
2.16. Schematic of the camera alignment and effect of perspective removal on the STD visualization. 39
2.17. Comparison between flame visualization using $CH^\star$ chemiluminescence and a TC lens (A) and using a conventional imaging setup. 40
2.18. Time-evolution of the temperature readings inside the burner when the operating point is changed by reducing the mixture equivalence ratio ϕ. $\xi_i = x_i/L$ denotes the normalized position of the i thermocouple. Measured temperatures are generally in the range $1000 < T < 1500$ K. 41
2.19. (A) Backlight image. (B) $CH^\star$ chemiluminescence signal. (C) Masked and cropped image. 42
2.20. Matrix form of the $CH^\star$ chemiluminescence image that is used to compute the axial and radial profiles of $CH^\star$ luminosity. 42
2.21. Procedure to compute the axial profile of $CH^\star$ and the flame position $\xi_f = x_f/L$. 43
2.22. PDF of the temperature correction $T_{b_1} - T_{in}$ (left). PDF of the inlet temperature error δT_{in} (right). 48

3.1. Numerical setup 56
3.2. Inline (left) and staggered (right) configurations in tube banks from [176]. 58
3.3. Comparison between the different Nusselt number correlations. Evolution of the Nusselt number, Nu, with the Reynolds number, Re, in different interphase heat exchange models. 60

3.4. Inlet temperature error induced by the use of Dirichlet boundary conditions. . . 61
3.5. XZ-cut of the A species concentration field in Fickian diffusion simulations for the gas (left) and the solid (right) phases in a Diamond topology with $\epsilon = 0.8$. These simulations are used to extract the phase tortuosity. 63
3.6. Correlation between the radiative emission of a black body for $T_s = 1180$ K and the quartz transmissivity as a function of the wavelength. Total quartz transmissivity as a function of the temperature of the radiation source, T, computed as the integral of the curve. 64

4.1. Operating domain of the PMBs for different pore sizes, d_p, spanned by power, P, and equivalence ratio, ϕ. 69
4.2. Flame structure for cases at the blowoff limit with $P = 1$ kW. A) LoS integrated $CH^\star$ chemiluminescence images. B) Profiles of $CH^\star$ from the experiments and normalized heat release rate $\hat{\dot{\omega}}_T$ from simulations. C) Experimental and computed normalized temperature profiles. Results in (B) and (C) are presented as a function of $\xi = x/L$. Temperatures are normalized as $(T - T_{in})/(T_{ad} - T_{in})$. . . 70
4.3. Flame speed-up, u_B/S_{L_0}, versus flame position, $\xi_f = x_f/L$, for different powers, P, and pore sizes, d_p. The h_V correlation presented in Kuwahara et al. [186] is used as interphase heat exchange submodel. 71
4.4. Influence of the interphase heat exchange term on the VAM results for 1 kW flames stabilized in the $d_p = 2.5$ mm burner: —●— experimental results; —■— Wakao and Kagei [195]; —⬟— Kuwahara et al. [186]; —◀— Saito and De Lemos [187]; —▶— Zukauskas [176]. The experimental and numerical axial profiles are compared for points A and B. 72
4.5. Flame speed-up, u_B/S_{L_0}, versus flame position, $\xi_f = x_f/L$, for different powers, P, and pore sizes, d_p. The h_V correlation presented in Saito and De Lemos [187] is used as interphase heat exchange submodel. 72
4.6. Influence of solid conductivity, λ_s, on the VAM results for 1 kW flames stabilized in the $d_p = 2.5$ mm burner. A comparison between the experimental and the numerical profiles at different values of λ_s is offered for the points labeled with white markers. 75
4.7. Influence of solid emissivity, Ξ, on the VAM results for 1 kW flames stabilized in the $d_p = 2.5$ mm burner. A comparison between the experimental and the numerical profiles at different values of Ξ is offered for the points labeled with white markers. 76

5.1. $CH^\star$ chemiluminescence imaging of a *Controlled flashback* transient. (A) Ignition with CH_4-Air at $\phi = 0.6$. (B) Hydrogen addition to trigger transition to submerged combustion. (C) Removal of hydrogen. (D) Steady state in thermal equilibrium is reached. 81
5.2. A) Line-of-sight integrated $CH^\star$ signal for three 1 kW CH_4-Air flames at different equivalence ratios. B) Profiles of $CH^\star$ and normalized temperature, $\theta = (T - T_{in})/(T_{ad} - T_{in})$, as a function of the axial position, $\xi = x/L$. 83
5.3. Operating domain spanned by power, P, and equivalence ratio, ϕ, for CH_4-Air flames in PMBs with different porosities $\epsilon = 0.5$ and $\epsilon = 0.8$. 84
5.4. Flame speed-up, u_B/S_{L_0}, versus flame position, $\xi_f = x_f/L$, at various powers for two porosities, ϵ. 84
5.5. A) Operating domain of the $\epsilon = 0.8$ burner for different hydrogen power fractions, α_P, in the $P - \phi$ space. B) Flame speed-up, u_B/S_{L_0}, versus normalized flame position, $\xi_f = x_f/L$, for different powers and hydrogen contents. 85

5.6. Evolution of the ratio between the experimental and the theoretical speed-up, u_B/S_{L_P}, with the H_2 content. 86
5.7. Theoretical speed-up, S_{L_P}/S_{L_0}, versus flame position, ξ_f, for 1 kW CH_4-Air flames in the two burners with different porosity, ϵ. 86

6.1. Experimental setup of the POROSITO test rig. 93
6.2. Raw Mie-scattering (a) and $CH^\star$ chemiluminescence (b) images. The red dotted line indicates the limits of the porous matrix. The focus of the analysis is on the window outlined with white dotted lines in the middle of the burner. 94
6.3. Arrangement of the see-through directions in the Primitive (a1) and Gyroid (b1) topologies. The x-direction is used for laser illumination, and the y and z-directions are used to collect the $CH^\star$ emission of the flame and the Mie-scattering of particles, respectively. a2 and b2 show the intersection between the laser plane and the see-through direction volume for the Primitive and the Gyroid topology, respectively. 95
6.4. Pictures of the experimental setup during operation (a and b). The characteristic scattering trails are clearly visible in (b). 96
6.5. Influence of the seeding on flame stabilization. The stabilization curve represents the speed-up, u_B/S_{L_0}, as a function of the dimensionless position of the flame $\xi_f = x_f/L$. 97
6.6. Evaporation, x_v, versus reaction front, x_f, in an adiabatic free flame (a) and in a PMB (b). 97
6.7. Comparison between Line of Sight integrated $CH^\star$ chemiluminescence and binarized Mie-Scattering images for 1 kW CH_4/Air flames with different equivalence ratios ϕ: (a) $\phi = 0.66$, (b) $\phi = 0.62$ and (c) $\phi = 0.60$. 98
6.8. Transition from a symmetrical to an asymmetrical stabilization in a 1 kW inlet-anchored flame when the H_2 content is increased from $\alpha_P = 20\%$ to $\alpha_P = 60\%$. Equivalence ratios are (a) $\phi = 0.55$ and (b) $\phi = 0.35$. 98
6.9. Overview of the experimental setup for the μPIV experiments. a) Global positioning of the cameras with respect to the experiment. b) Detail of the optics cooling system. c) Positioning of the macroscope with respect to the burner. . . 100
6.10. Schematic of the μPIV experiments. a) Top view of the burner, the laser sheet and the backlight. b) Front view of the burner. The target pore is at the burner inlet in the center of the porous matrix. c) Detailed view of the pore: Mie-scattering image, streamlines and computer-generated mask. Note that local axes, (x^*, y^*) are used in μPIV images. 102
6.11. B1: Primtive-based burner with $d_p = 3.5$ mm and $\epsilon = 0.7$. 102
6.12. B2: Primtive-based burner with $d_p = 2.5$ mm and $\epsilon = 0.7$. 102
6.13. B3: Gyroid-based burner with $d_p = 3.5$ mm and $\epsilon = 0.8$. 103
6.14. a) Flow streamlines and Mie-scattering image from μPIV measurements in non-reactive conditions. b) Longitudinal profile of axial velocity, $u(x^*)$. c) Transverse profile of axial velocity $u(y^*)$. 104
6.15. a) Flow streamlines and Mie-scattering image from μPIV measurements in reactive flow conditions. b) Longitudinal profile of axial velocity, $u(x^*)$. c) Transverse profile of axial velocity $u(y^*)$. 105
6.16. Influence of power, P, on the flame structure in burner B1. The hydrogen content is $\alpha_P = 20\%$ and the equivalence ratio is $\phi = 0.55$. For these flames the speed-ups are: (a) $u_B/S_{L_0} = 1.86$, (b) $u_B/S_{L_0} = 2.42$ and (c) $u_B/S_{L_0} = 2.97$. The axial velocity profiles, $u(x^*)$, along the white dotted lines are represented in (d) for cases (a)—○—, (b)···◁··· and (c)-□-. 106

6.17. Influence of power, P, on the flame structure in burner B2. The hydrogen content is $\alpha_P = 20\%$ and the equivalence ratio is $\phi = 0.60$. For these flames the speed-ups are: (a) $u_B/S_{L_0} = 1.21$, (b) $u_B/S_{L_0} = 1.42$ and (c) $u_B/S_{L_0} = 1.66$. The axial velocity profiles, $u(x^*)$, along the white dotted lines are represented in (d) for cases (a)—○— , (b)··◁··· and (c)-□- 106

6.18. Mie-scattering images for three H_2-enriched CH_4-Air with $\phi = 0.55$, $\alpha_P = 20\%$ and different powers: (a) $P = 0.8$ kW, (b) $P = 1.0$ kW and (c) $P = 1.2$ kW. The evaporation front is indicated with a yellow line and the red arrows represent the magnitude and direction of the local consumption speed, S_C. 106

6.19. Evolution of the consumption speed S_C along the flame front for different powers in CH_4-Air flames with $\phi = 0.66$ (a) and in H_2-enriched CH_4-Air flames with $\alpha_P = 20\%$ and $\phi = 0.55$ (b). 107

6.20. Stability domain of burner B1 spanned by power, P, and equivalence ratio, ϕ for CH_4/Air flames. Blowoff limits of burners B4 and B5 in the $P - \phi$ map. 108

6.21. Evolution of the speed-up, u_B/S_{L_0}, with the flame location $\xi_f = x_f/L$, in Primitive and Diamond-based burners with the same pore size $d_p = 3.5$ mm and different porosities. 108

6.22. Streamlines and Mie-scattering image in non-reactive flow conditions for burners B2 (a) and B3 (b). The axial velocity profiles, $u(x^*)$, along the white dotted lines are represented in (c) for cases (a)—○— and (b)··◁··· 109

6.23. Evolution of the linear porosity in the streamwise direction for the three TPMS structures. These three topologies feature the same volumetric porosity $\epsilon = 0.7$, indicated with a black dotted line. 110

6.24. Influence of power, P, on the flame structure in burner B3. The hydrogen content is $\alpha_P = 20\%$ and the equivalence ratio is $\phi = 0.50$. For these flames the speed-ups are: (a) $u_B/S_{L_0} = 2.04$, (b) $u_B/S_{L_0} = 2.52$ and (c) $u_B/S_{L_0} = 4.66$. The axial velocity profiles, $u(x^*)$, along the white dotted lines are represented in (d) for cases (a)—○— , (b)··◁··· and (c)-□- 112

6.25. Influence of equivalence ratio, ϕ, on the flame structure in burner B1. The hydrogen content is $\alpha_P = 20\%$ and the power is $P = 1$ kW. For these flames the speed-ups are: (a) $u_B/S_{L_0} = 2.99$, (b) $u_B/S_{L_0} = 2.41$ and (c) $u_B/S_{L_0} = 2.03$. The axial velocity profiles, $u(x^*)$, along the white dotted lines are represented in (d) for cases (a)—○— , (b)··◁··· and (c)-□- 113

6.26. Influence of hydrogen content on the flame structure in burner B1. In these flames, the power is $P = 1$ kW and equivalence ratio is adjusted to obtain an inlet-anchored flame. For these flames, the speed-ups are: (a) $u_B/S_{L_0} = 1.57$, (b) $u_B/S_{L_0} = 2.03$ and (c) $u_B/S_{L_0} = 8.21$. The axial velocity profiles, $u(x^*)$, along the white dotted lines are represented in (d) for cases (a)—○— , (b)··◁··· and (c)-□- 113

6.27. Mie-scattering images for three CH_4-Air with $\phi = 0.66$ and different powers: (a) $P = 0.8$ kW, (b) $P = 1.0$ kW and (c) $P = 1.2$ kW. The evaporation front is represented with a yellow line and the red arrows indicate the magnitude and direction of the consumption speed S_C. 113

A.1. Adiabatic flame temperature T_{ad} and flame thermal thickness δ_T maps for a one-dimensional premixed laminar flame of methane-hydrogen-air as a function of the mixture global equivalence ratio, ϕ, and the hydrogen content expressed as a power fraction, α_P. 125

A.2. Evolution of equivalence ratio ϕ, laminar burning velocity S_L, thermal thickness δ_T and adiabatic flame temperature T_{ad} versus hydrogen content α_P for the two fuel blends under investigation CH_4/H_2 and C_3H_8/H_2 and the iso–T_{ad} and the iso–δ_T hybridization strategies. : iso–T_{ad} – CH_4; : iso–δ_T – CH_4; : iso–T_{ad} – C_3H_8; : iso–δ_T – C_3H_8. 125
A.3. Sketch of the fluid domain, its geometrical parameters, and the applied boundary conditions. 127
A.4. Normalized heat-release rate for propane-hydrogen-air flames with increasing hydrogen content α_P. 128
A.5. Local equivalence ratio, Φ, normalized by its inlet value for flames with increasing hydrogen content, α_P, for the iso–T_{ad} hybridization strategy. 129
A.6. Evolution of the flashback limit for the different fuel blends and hybridization strategies. : CH_4/H_2 iso–T_{ad}; : CH_4/H_2 iso–δ_T; : C_3H_8/H_2 iso–T_{ad}; : C_3H_8/H_2 iso–δ_T. 130
A.7. Normalized bulk velocity versus effective Lewis number, at the flashback limit for different fuel blends and hybridization strategies. : CH_4/H_2 iso–T_{ad}; : CH_4/H_2 iso–δ_T; : C_3H_8/H_2 iso–T_{ad}; : C_3H_8/H_2 iso–δ_T. 130
A.8. Evolution of the normalized lateral position of the maximum heat release rate versus diffusion-based Lewis number, Le_D, for all cases. : CH_4/H_2 iso–T_{ad}; : CH_4/H_2 iso–δ_T; : C_3H_8/H_2 iso–T_{ad}; : C_3H_8/H_2 iso–δ_T. . . . 132
A.9. Evolution of the normalized displacement velocity S_D/S_L versus the dimensionless transverse coordinate $2y/d$ for H_2-enriched methane-air flames in the iso–T_{ad} (left) and the iso–δ_T (right) hybridization strategies. : $\alpha_P = 0\%$; : $\alpha_P = 20\%$; : $\alpha_P = 40\%$; : $\alpha_P = 50\%$; : $\alpha_P = 60\%$; : $\alpha_P = 80\%$; : $\alpha_P = 100\%$. 132
A.10. Flame front evolution during flashback for the CH_4/H_2 blends with the iso–T_{ad} hybridization strategy. Time step between snapshots is 1.01 ms in a) and 0.45 ms in b). 134
A.11. Normalized heat-release rate for methane-hydrogen-air flames with increasing hydrogen content α_P. 137
A.12. Evolution of the normalized displacement velocity S_D/S_L versus the dimensionless transverse coordinate $2y/d$ for H_2-enriched propane-air flames in the iso–T_{ad} (left) and the iso–δ_T (right) hybridization strategies. : $\alpha_P = 0\%$; : $\alpha_P = 20\%$; : $\alpha_P = 40\%$; : $\alpha_P = 50\%$; : $\alpha_P = 60\%$; : $\alpha_P = 80\%$; : $\alpha_P = 100\%$. 138
A.13. Flame front evolution during flashback for the C_3H_8/H_2 blends with the iso–T_{ad} hybridization strategy. Time step between snapshots is 1.45 ms in a) and 0.42 ms in b). 138

List of Tables

2.1. List of printed PMBs and their topological properties. Prefix -S in the topology nomenclature indicates a swirled topology and NA stands for Non-Available data. 38
2.2. Numerical constants 45
2.3. MFC specifications 45
2.4. Numerical parameters for the calculation of δT_{in}. Constants c and m are taken from [176]. 48

3.1. Heat exchange correlations and domain of validity under a uniform notation . . . 60

4.1. Topology-dependent parameters. 68

5.1. Topological parameters of the PMBs. 82

6.1. Topological parameters of the different PMBs. 94
6.2. Equivalence ratio ϕ resulting in an inlet-anchored flame for each burner and H_2 content. The operating point defined by $P = 1$ kW, and the combinations of α_P and ϕ from this table determine the reference operating condition for each burner in the μPIV experiments. 104

A.1. Properties of one-dimensional unstretched adiabatic C_3H_8 and CH_4 flames at the reference operating point $\alpha_P = 0$. 124

Bibliography

[1] M. R. Allen, P. Friedlingstein, C. A. Girardin, S. Jenkins, Y. Malhi, E. Mitchell-Larson, G. P. Peters, and L. Rajamani, "Net zero: science, origins, and implications," Annu. Rev. Environ. Resour., vol. 47, pp. 849–887, 2022.

[2] M. Wiatros-Motyka, N. Fulghum, and D. Jones, "Global electricity review 2024," 2024.

[3] H. Zsiborács, G. Pintér, A. Vincze, Z. Birkner, and N. H. Baranyai, "Grid balancing challenges illustrated by two european examples: Interactions of electric grids, photovoltaic power generation, energy storage and power generation forecasting," Energy Reports, vol. 7, pp. 3805–3818, 2021.

[4] A. B. Gurung, A. Borsdorf, L. Füreder, F. Kienast, P. Matt, C. Scheidegger, L. Schmocker, M. Zappa, and K. Volkart, "Rethinking pumped storage hydropower in the european alps," Mountain Research and Development, vol. 36, no. 2, pp. 222–232, 2016.

[5] M. Gyalai-Korpos, L. Zentkó, C. Hegyfalvi, G. Detzky, P. Tildy, N. Hegedűsné Baranyai, G. Pintér, and H. Zsiborács, "The role of electricity balancing and storage: developing input parameters for the european calculator for concept modeling," Sustainability, vol. 12, no. 3, p. 811, 2020.

[6] H. Blanco and A. Faaij, "A review at the role of storage in energy systems with a focus on power to gas and long-term storage," Renew Sustain Energy Rev, vol. 81, pp. 1049–1086, 2018.

[7] F. Birol et al., "World energy outlook 2022," International Energy Agency: Paris, France, vol. 522, 2022.

[8] Y. Ju and K. Maruta, "Microscale combustion: Technology development and fundamental research," Progress in energy and combustion science, vol. 37, no. 6, pp. 669–715, 2011.

[9] M. P. Boyce, Gas turbine engineering handbook. Elsevier, 2011.

[10] S. van Renssen, "The hydrogen solution?," Nat Clim Chang, vol. 10, no. 9, pp. 799–801, 2020.

[11] C. Wulf, J. Linßen, and P. Zapp, "Review of power-to-gas projects in europe," Energy Procedia, vol. 155, pp. 367–378, 2018.

[12] G. Gahleitner, "Hydrogen from renewable electricity: An international review of power-to-gas pilot plants for stationary applications," international Journal of hydrogen energy, vol. 38, no. 5, pp. 2039–2061, 2013.

[13] M. Deymi-Dashtebayaz, A. Ebrahimi-Moghadam, S. I. Pishbin, and M. Pourramezan, "Investigating the effect of hydrogen injection on natural gas thermo-physical properties with various compositions," Energy, vol. 167, pp. 235–245, 2019.

[14] D. Haeseldonckx and W. D'haeseleer, "The use of the natural-gas pipeline infrastructure for hydrogen transport in a changing market structure," International Journal of Hydrogen Energy, vol. 32, no. 10-11, pp. 1381–1386, 2007.

[15] N. Yang, J. Deng, C. Wang, Z. Bai, and J. Qu, "High pressure hydrogen leakage diffusion: Research progress," International Journal of Hydrogen Energy, 2023.

[16] R. Oriani, "Hydrogen embrittlement of steels," Annual review of materials science, vol. 8, no. 1, pp. 327–357, 1978.

[17] A. L. Sánchez and F. A. Williams, "Recent advances in understanding of flammability characteristics of hydrogen," Prog Energy Combust Sci, vol. 41, pp. 1–55, 2014.

[18] R. W. Schefer, W. D. Kulatilaka, B. D. Patterson, and T. B. Settersten, "Visible emission of hydrogen flames," Combustion and flame, vol. 156, no. 6, pp. 1234–1241, 2009.

[19] L. Berger, A. Attili, and H. Pitsch, "Intrinsic instabilities in premixed hydrogen flames: Parametric variation of pressure, equivalence ratio, and temperature. part 1-dispersion relations in the linear regime," Combust Flame, vol. 240, p. 111935, 2022.

[20] L. Berger, A. Attili, and H. Pitsch, "Intrinsic instabilities in premixed hydrogen flames: parametric variation of pressure, equivalence ratio, and temperature. part 2–non-linear regime and flame speed enhancement," Combustion and Flame, p. 111936, 2022.

[21] M. W. Melaina, O. Antonia, and M. Penev, "Blending hydrogen into natural gas pipeline networks: a review of key issues," 2013.

[22] Y. Zhao, V. McDonell, and S. Samuelsen, "Experimental assessment of the combustion performance of an oven burner operated on pipeline natural gas mixed with hydrogen," Int J Hydrogen Energy, vol. 44, no. 47, pp. 26049–26062, 2019.

[23] Y. Zhao, V. McDonell, and S. Samuelsen, "Influence of hydrogen addition to pipeline natural gas on the combustion performance of a cooktop burner," Int J Hydrogen Energy, vol. 44, no. 23, pp. 12239–12253, 2019.

[24] Y. Zhao, V. McDonell, and S. Samuelsen, "Assessment of the combustion performance of a room furnace operating on pipeline natural gas mixed with simulated biogas or hydrogen," Int J Hydrogen Energy, vol. 45, no. 19, pp. 11368–11379, 2020.

[25] S. Choudhury, V. G. McDonell, and S. Samuelsen, "Combustion performance of low-nox and conventional storage water heaters operated on hydrogen enriched natural gas," Int J Hydrogen Energy, vol. 45, no. 3, pp. 2405–2417, 2020.

[26] G. Richards, M. McMillian, R. Gemmen, W. A. Rogers, and S. Cully, "Issues for low-emission, fuel-flexible power systems," Prog Energy Combust Sci, vol. 27, no. 2, pp. 141–169, 2001.

[27] T. Lieuwen, V. McDonell, E. Petersen, and D. Santavicca, "Fuel flexibility influences on premixed combustor blowout, flashback, autoignition, and stability," J Eng Gas Turbine Power, vol. 130, no. 1, 2008.

[28] "Hestia project: Hydrogen combustion in aero engines."

[29] "Thyga project: Testing hydrogen admixture for gas applications."

[30] F. H. Vance, L. de Goey, and J. A. van Oijen, "Development of a flashback correlation for burner-stabilized hydrogen-air premixed flames," Combust. Flame, p. 112045, 2022.

[31] H. Pers, A. Aniello, F. Morisseau, and T. Schuller, "Autoignition-induced flashback in hydrogen-enriched laminar premixed burners," Int J Hydrogen Energy, vol. 48, no. 27, pp. 10235–10249, 2023.

[32] H. Pers, P. Masset, E. Flores-Montoya, L. Selle, and T. Schuller, "Influence of slit asymmetry on blow-off and flashback in methane/hydrogen laminar premixed burners," Combustion and Flame, vol. 263, p. 113413, 2024.

[33] E. Flores-Montoya, A. Aniello, T. Schuller, and L. Selle, "Predicting flashback limits in h2 enriched ch4/air and c3h8/air laminar flames," Combustion and Flame, vol. 258, p. 113055, 2023.

[34] H. Pers, A. Aniello, and T. Schuller, "Transition from hydrodynamic flashback to wall-ignition in hydrogen-enriched laminar premixed burners," Combustion and Flame, vol. 266, p. 113514, 2024.

[35] A. Aniello, T. Poinsot, L. Selle, and T. Schuller, "Hydrogen substitution of natural-gas in premixed burners and implications for blow-off and flashback limits," Int J Hydrogen Energy, vol. 47, pp. 33067–33081, 2022.

[36] S. Marragou, H. Magnes, T. Poinsot, L. Selle, and T. Schuller, "Stabilization regimes and pollutant emissions from a dual fuel ch4/h2 and dual swirl low nox burner," International Journal of Hydrogen Energy, vol. 47, no. 44, pp. 19275–19288, 2022.

[37] S. Marragou, H. Magnes, A. Aniello, L. Selle, T. Poinsot, and T. Schuller, "Experimental analysis and theoretical lift-off criterion for h2/air flames stabilized on a dual swirl injector," Proceedings of the Combustion Institute, vol. 39, no. 4, pp. 4345–4354, 2023.

[38] S. Richard, C. Viguier, S. Marragou, and T. Schuller, "Dispositif d'injection de dihydrogene et d'air (fr patent no fr2111267)," Institut National de la Propriété Industrielle, 2021.

[39] Y. Kotani and T. Takeno, "An experimental study on stability and combustion characteristics of an excess enthalpy flame," in Symposium (International) on Combustion, vol. 19, pp. 1503–1509, Elsevier, 1982.

[40] Y. Kotani, H. Behbahani, and T. Takeno, "An excess enthalpy flame combustor for extended flow ranges," in Symposium (International) on Combustion, vol. 20, pp. 2025–2033, Elsevier, 1985.

[41] F. Weinberg, "Combustion temperatures: the future?," Nature, vol. 233, no. 5317, pp. 239–241, 1971.

[42] S. Lloyd and F. Weinberg, "Limits to energy release and utilisation from chemical fuels," Nature, vol. 257, no. 5525, pp. 367–370, 1975.

[43] J. Ellzey, E. Belmont, and C. Smith, "Heat recirculating reactors: Fundamental research and applications," Prog. Energ. Combust., vol. 72, pp. 32–58, 2019.

[44] S. Wood and A. T. Harris, "Porous burners for lean-burn applications," Prog. Energy Combust. Sci., vol. 34, no. 5, pp. 667–684, 2008.

[45] J. Howell, M. Hall, and J. Ellzey, "Combustion of hydrocarbon fuels within porous inert media," Progress in Energy and Combustion Science, vol. 22, no. 2, pp. 121–145, 1996.

[46] F. Durst, D. Trimis, and K. Pickenacker, "Compact porous medium burner and heat exchanger for household applications," European Union commission project report, pp. 1–85, 1996.

[47] M. Toledo, V. Bubnovich, A. Saveliev, and L. Kennedy, "Hydrogen production in ultra-rich combustion of hydrocarbon fuels in porous media," international journal of hydrogen energy, vol. 34, no. 4, pp. 1818–1827, 2009.

[48] M. T. Smucker and J. L. ELLZEY, "Computational and experimental study of a two-section porous burner," Combustion science and Technology, vol. 176, no. 8, pp. 1171–1189, 2004.

[49] V. Khanna, R. Goel, and J. Ellzey, "Measurements of emissions and radiation for methane combustion within a porous medium burner," Combustion science and technology, vol. 99, no. 1-3, pp. 133–142, 1994.

[50] R. Mital, J. Gore, and R. Viskanta, "A study of the structure of submerged reaction zone in porous ceramic radiant burners," Combustion and flame, vol. 111, no. 3, pp. 175–184, 1997.

[51] M. A. Mujeebu, M. Z. Abdullah, M. Z. Bakar, A. A. Mohamad, and M. K. Abdullah, "Applications of porous media combustion technology - A review," Appl. Energy, vol. 86, no. 9, pp. 1365–1375, 2009.

[52] C. Keramiotis, B. Stelzner, D. Trimis, and M. Founti, "Porous burners for low emission combustion: An experimental investigation," Energy, vol. 45, no. 1, pp. 213–219, 2012.

[53] S. Alavandi and A. Agrawal, "Experimental study of combustion of hydrogen–syngas/methane fuel mixtures in a porous burner," International journal of hydrogen energy, vol. 33, no. 4, pp. 1407–1415, 2008.

[54] C. Keramiotis and M. A. Founti, "An experimental investigation of stability and operation of a biogas fueled porous burner," Fuel, vol. 103, pp. 278–284, 2013.

[55] C. E. Arrieta, A. M. García, and A. A. Amell, "Experimental study of the combustion of natural gas and high-hydrogen content syngases in a radiant porous media burner," International Journal of Hydrogen Energy, vol. 42, no. 17, pp. 12669–12680, 2017.

[56] S. Gauthier, E. Lebas, and D. Baillis, "Sfgp 2007-natural gas/hydrogen mixture combustion in a porous radiant burner," Int. J. Chem. Reactor Eng., vol. 5, no. 1, 2007.

[57] R. Habib, B. Yadollahi, A. Saeed, M. H. Doranehgard, and N. Karimi, "On the response of ultralean combustion of ch4/h2 blends in a porous burner to fluctuations in fuel flow—an experimental investigation," Energy & Fuels, vol. 35, no. 10, pp. 8909–8921, 2021.

[58] G. Vignat, T. Zirwes, E. R. Toro, K. Younes, E. Boigné, P. Muhunthan, L. Simitz, D. Trimis, and M. Ihme, "Experimental and numerical investigation of flame stabilization and pollutant formation in matrix stabilized ammonia-hydrogen combustion," Combust. Flame, vol. 250, p. 112642, 2023.

[59] T. Zirwes, G. Vignat, E. R. Toro, E. Boigné, K. Younes, D. Trimis, and M. Ihme, "Improving volume-averaged simulations of matrix-stabilized combustion through direct x-ray μct characterization: Application to nh3/h2-air combustion," Combust. Flame, vol. 257, p. 113020, 2023.

[60] F. M. Pereira, A. A. Oliveira, and F. F. Fachini, "Asymptotic analysis of stationary adiabatic premixed flames in porous inert media," Combust. Flame, vol. 156, no. 1, pp. 152–165, 2009.

[61] F. Pereira, A. Oliveira, and F. Fachini, "Theoretical analysis of ultra-lean premixed flames in porous inert media," Journal of fluid mechanics, vol. 657, pp. 285–307, 2010.

[62] F. M. Pereira, A. A. Oliveira, and F. F. Fachini, "Maximum superadiabatic temperature for stabilized flames within porous inert media," Combustion and flame, vol. 158, no. 11, pp. 2283–2288, 2011.

[63] P.-A. Masset, O. Dounia, and L. Selle, "Fully explicit formulae for flame speed in infinite and finite porous media," Combust. Theory Model., vol. 25, no. 5, pp. 1–28, 2021.

[64] P.-A. Masset, O. Dounia, and L. Selle, "Combustion regimes in inert porous media: From decoupled to hyperdiffusive flames," Combust. Flame, vol. 241, p. 112052, 2022.

[65] D. K. Min and H. D. Shin, "Laminar premixed flame stabilized inside a honeycomb ceramic," International journal of heat and mass transfer, vol. 34, no. 2, pp. 341–356, 1991.

[66] G. Vignat, B. Akoush, E. R. Toro, E. Boigné, and M. Ihme, "Combustion of lean ammonia-hydrogen fuel blends in a porous media burner," Proc. Combust. Inst., vol. 39, no. 4, pp. 4195–4204, 2023.

[67] P.-A. Masset, F. Duchaine, A. Pestre, and L. Selle, "Modelling challenges of volume-averaged combustion in inert porous media," Combust. Flame, vol. 251, p. 112678, 2023.

[68] C. Bedoya, I. Dinkov, P. Habisreuther, N. Zarzalis, H. Bockhorn, and P. Parthasarathy, "Experimental study, 1d volume-averaged calculations and 3d direct pore level simulations of the flame stabilization in porous inert media at elevated pressure," Combustion and Flame, vol. 162, no. 10, pp. 3740–3754, 2015.

[69] E. Boigné, T. Zirwes, D. Y. Parkinson, G. Vignat, P. Muhunthan, H. S. Barnard, A. A. MacDowell, and M. Ihme, "Integrated experimental and computational analysis of porous media combustion by combining gas-phase synchrotron μct, ir-imaging, and pore-resolved simulations," Combustion and Flame, vol. 259, p. 113132, 2024.

[70] M. Sahraoui and M. Kaviany, "Direct simulation vs volume-averaged treatment of adiabatic, premixed flame in a porous medium," Int. J. Heat Mass Tran., vol. 37, no. 18, pp. 2817–2834, 1994.

[71] C. Jainski, M. Rißmann, B. Böhm, J. Janicka, and A. Dreizler, "Sidewall quenching of atmospheric laminar premixed flames studied by laser-based diagnostics," Combustion and Flame, vol. 183, pp. 271–282, 2017.

[72] A. Dreizler and B. Böhm, "Advanced laser diagnostics for an improved understanding of premixed flame-wall interactions," Proceedings of the Combustion Institute, vol. 35, no. 1, pp. 37–64, 2015.

[73] A. Oliveira and M. Kaviany, "Nonequilibrium in the transport of heat and reactants in combustion in porous media," Progress in Energy and Combustion Science, vol. 27, no. 5, pp. 523–545, 2001.

[74] M. A. Mujeebu, M. Z. Abdullah, M. A. Bakar, A. Mohamad, and M. Abdullah, "Applications of porous media combustion technology–a review," Appl. Energy, vol. 86, no. 9, pp. 1365–1375, 2009.

[75] D. Trimis and F. Durst, "Combustion in a porous medium-advances and applications," Combustion science and technology, vol. 121, no. 1-6, pp. 153–168, 1996.

[76] P.-A. Masset, "Modelling challenges of stationary combustion in inert porous media, Ph.D. thesis," 2022.

[77] S. Zhdanok, L. A. Kennedy, and G. Koester, "Superadiabatic combustion of methane air mixtures under filtration in a packed bed," Combustion and Flame, vol. 100, no. 1-2, pp. 221–231, 1995.

[78] K. Hanamura, R. Echigo, and S. A. Zhdanok, "Superadiabatic combustion in a porous medium," International Journal of Heat and Mass Transfer, vol. 36, no. 13, pp. 3201–3209, 1993.

[79] R. V. Fursenko, I. A. Yakovlev, E. S. Odintsov, S. D. Zambalov, and S. S. Minaev, "Pore-scale flame dynamics in a one-layer porous burner," Combust. Flame, vol. 235, p. 111711, 2022.

[80] K. Everaert and J. Baeyens, "Catalytic combustion of volatile organic compounds," Journal of hazardous materials, vol. 109, no. 1-3, pp. 113–139, 2004.

[81] D. Hardesty and F. Weinberg, "Burners producing large excess enthalpies," Combustion Science and Technology, vol. 8, no. 5-6, pp. 201–214, 1973.

[82] A. Jones, S. Lloyd, and F. J. Weinberg, "Combustion in heat exchangers," Proceedings of the Royal Society of London. A. Mathematical and Physical Sciences, vol. 360, no. 1700, pp. 97–115, 1978.

[83] T. Takeno and K. Sato, "An excess enthalpy flame theory," Combust. Sci. Technol., vol. 20, no. 1-2, pp. 73–84, 1979.

[84] W. Jones and B. E. Launder, "The prediction of laminarization with a two-equation model of turbulence," International journal of heat and mass transfer, vol. 15, no. 2, pp. 301–314, 1972.

[85] S. A. Lloyd, "Combustion in double spiral burners," Industrial & engineering chemistry research, vol. 33, no. 7, pp. 1809–1816, 1994.

[86] R. Fursenko, S. Minaev, and V. Babkin, "Thermal interaction of two flame fronts propagating in channels with opposing gas flows," Combustion, Explosion and Shock Waves, vol. 37, no. 5, pp. 493–500, 2001.

[87] Y. Ju and C. Choi, "An analysis of sub-limit flame dynamics using opposite propagating flames in mesoscale channels," Combustion and Flame, vol. 133, no. 4, pp. 483–493, 2003.

[88] V. N. Kurdyumov and M. Matalon, "Analysis of an idealized heat-recirculating microcombustor," Proceedings of the Combustion Institute, vol. 33, no. 2, pp. 3275–3284, 2011.

[89] V. N. Kurdyumov, D. Fernández-Galisteo, and C. Jiménez, "Superadiabatic small-scale combustor with counter-flow heat exchange: Flame structure and limits to narrow-channel approximation," Combustion and Flame, vol. 222, pp. 233–241, 2020.

[90] J. Bosch, D. Fernández-Galisteo, C. Jiménez, and V. N. Kurdyumov, "Superadiabatic small-scale combustors: asymptotic analysis of a two-step chain-branching combustion model," Proceedings of the Combustion Institute, vol. 39, no. 2, pp. 1927–1935, 2023.

[91] I. M. Schoegl and J. L. Ellzey, "Numerical investigation of ultra-rich combustion in counter flow heat exchangers," Combustion science and technology, vol. 182, no. 10, pp. 1413–1428, 2010.

[92] I. Schoegl and J. L. Ellzey, "Superadiabatic combustion in conducting tubes and heat exchangers of finite length," Combustion and flame, vol. 151, no. 1-2, pp. 142–159, 2007.

[93] I. Schoegl and J. L. Ellzey, "A mesoscale fuel reformer to produce syngas in portable power systems," Proceedings of the Combustion Institute, vol. 32, no. 2, pp. 3223–3230, 2009.

[94] I. Schoegl, S. Newcomb, and J. Ellzey, "Ultra-rich combustion in parallel channels to produce hydrogen-rich syngas from propane," International journal of hydrogen energy, vol. 34, no. 12, pp. 5152–5163, 2009.

[95] E. L. Belmont, I. Schoegl, and J. L. Ellzey, "Experimental and analytical investigation of lean premixed methane/air combustion in a mesoscale counter-flow reactor," Proceedings of the Combustion Institute, vol. 34, no. 2, pp. 3361–3367, 2013.

[96] T. Poinsot and D. Veynante, Theoretical and numerical combustion. RT Edwards, Inc., 2005.

[97] F. A. Williams, Combustion theory. CRC Press, 2018.

[98] S. Whitaker, "Advances in theory of fluid motion in porous media," Industrial & engineering chemistry, vol. 61, no. 12, pp. 14–28, 1969.

[99] S. A. Ghorashi, S. A. Hashemi, S. M. Hashemi, and M. Mollamahdi, "Experimental study on pollutant emissions in the novel combined porous-free flame burner," Energy, vol. 162, pp. 517–525, 2018.

[100] C. Hackert, J. Ellzey, and O. Ezekoye, "Combustion and heat transfer in model two-dimensional porous burners," Combust. Flame, vol. 116, no. 1-2, pp. 177–191, 1999.

[101] J. Dunnmon, S. Sobhani, M. Wu, R. Fahrig, and M. Ihme, "An investigation of internal flame structure in porous media combustion via X-ray Computed Tomography," Proc. Combust. Inst., vol. 36, no. 3, pp. 4399–4408, 2017.

[102] S. Sobhani, S. Allan, P. Muhunthan, E. Boigne, and M. Ihme, "Additive manufacturing of tailored macroporous ceramic structures for high-temperature applications," Adv. Eng. Mater., vol. 22, no. 8, p. 2000158, 2020.

[103] S. Gauthier, E. Lebas, and D. Baillis, "One layer porous radiant burners: experimental and numerical study," in Eurotherm Seminar, no. 81, 2007.

[104] M. Samoilenko, P. Seers, P. Terriault, and V. Brailovski, "Design, manufacture and testing of porous materials with ordered and random porosity: Application to porous medium burners," Applied Thermal Engineering, vol. 158, p. 113724, 2019.

[105] K. Dobrego, S. Zhdanok, A. Krauklis, E. Khanevich, A. Zaruba, D. Sakhnovich, and A. Ovcharenko, "Stability of filtration combustion in a cylindrical radiation heater with a porous working medium," Journal of engineering physics and thermophysics, vol. 72, no. 4, pp. 599–605, 1999.

[106] S. Sathe, M. Kulkarni, R. Peck, and T. Tong, "An experimental study of combustion and heat transfer in porous radiant burners," tech. rep., Arizona State Univ., Tempe, AZ (USA). Dept. of Mechanical and Aerospace ..., 1989.

[107] M. Kamal and A. Mohamad, "Combustion in porous media," Proceedings of the Institution of Mechanical Engineers, Part A: Journal of Power and Energy, vol. 220, no. 5, pp. 487–508, 2006.

[108] M. Kamal, "Development of a cylindrical porous-medium burner," Journal of Porous Media, vol. 9, no. 5, 2006.

[109] K. Dobrego, N. Gnezdilov, S. Lee, and H. Choi, "Methane partial oxidation reverse flow reactor scale up and optimization," International journal of hydrogen energy, vol. 33, no. 20, pp. 5501–5509, 2008.

[110] S. Sobhani, D. Mohaddes, E. Boigne, P. Muhunthan, and M. Ihme, "Modulation of heat transfer for extended flame stabilization in porous media burners via topology gradation," Proceedings of the Combustion Institute, vol. 37, no. 4, pp. 5697–5704, 2019.

[111] J. Buckmaster and T. Takeno, "Blow-off and flashback of an excess enthalpy flame," Combustion Science and Technology, 1981.

[112] A. J. Barra and J. L. Ellzey, "Heat recirculation and heat transfer in porous burners," Combust. Flame, vol. 137, no. 1-2, pp. 230–241, 2004.

[113] A. J. Barra, G. Diepvens, J. L. Ellzey, and M. R. Henneke, "Numerical study of the effects of material properties on flame stabilization in a porous burner," Combust. Flame, vol. 134, no. 4, pp. 369–379, 2003.

[114] V. Babkin, A. Korzhavin, and V. Bunev, "Propagation of premixed gaseous explosion flames in porous media," Combustion and Flame, vol. 87, no. 2, pp. 182–190, 1991.

[115] S. Voss, M. Mendes, J. Pereira, S. Ray, J. Pereira, and D. Trimis, "Investigation on the thermal flame thickness for lean premixed combustion of low calorific h2/co mixtures within porous inert media," Proceedings of the Combustion Institute, vol. 34, no. 2, pp. 3335–3342, 2013.

[116] A. Bakry, A. Al-Salaymeh, H. Ala'a, A. Abu-Jrai, and D. Trimis, "Adiabatic premixed combustion in a gaseous fuel porous inert media under high pressure and temperature: Novel flame stabilization technique," Fuel, vol. 90, no. 2, pp. 647–658, 2011.

[117] A. C. Contini and F. M. Pereira, "Numerical study of flame stability within inert porous media with variable void area," Combust. Flame, vol. 246, p. 112475, 2022.

[118] I. Gibson, D. W. Rosen, B. Stucker, M. Khorasani, D. Rosen, B. Stucker, and M. Khorasani, Additive manufacturing technologies, vol. 17. Springer, 2021.

[119] C. Y. Yap, C. K. Chua, Z. L. Dong, Z. H. Liu, D. Q. Zhang, L. E. Loh, and S. L. Sing, "Review of selective laser melting: Materials and applications," Applied physics reviews, vol. 2, no. 4, p. 041101, 2015.

[120] N. Travitzky, A. Bonet, B. Dermeik, T. Fey, I. Filbert-Demut, L. Schlier, T. Schlordt, and P. Greil, "Additive manufacturing of ceramic-based materials," Advanced engineering materials, vol. 16, no. 6, pp. 729–754, 2014.

[121] S. Sobhani, P. Muhunthan, E. Boigné, D. Mohaddes, and M. Ihme, "Experimental feasibility of tailored porous media burners enabled via additive manufacturing," Proceedings of the Combustion Institute, vol. 38, no. 4, pp. 6713–6722, 2021.

[122] I. Malico and J. C. Pereira, "Numerical predictions of porous burners with integrated heat exchanger for household applications," Journal of Porous Media, vol. 2, no. 2, 1999.

[123] I. Malico, X. Zhou, and J. Pereira, "Two-dimensional numerical study of combustion and pollutants formation in porous burners," Combustion science and technology, vol. 152, no. 1, pp. 57–79, 2000.

[124] N. Delalic, D. Mulahasanovic, and E. Ganic, "Porous media compact heat exchanger unit—-experiment and analysis," Experimental Thermal and Fluid Science, vol. 28, no. 2-3, pp. 185–192, 2004.

[125] M. Farzaneh, R. Ebrahimi, M. Shams, and M. Shafiey, "Two-dimensional numerical simulation of combustion and heat transfer in porous burners.," Engineering letters, vol. 15, no. 2, 2007.

[126] R. Schreiber, W. Krill, J. Kesselring, R. Vogt, and M. Lukasiewicz, "Industrial applications of the radiant ceramic fibre burner," in Proceedings of the International Gas Research Conference, pp. 13–16, 1983.

[127] R. Echigo, K. Hanamura, Y. Yoshizawa, and T. Tomimura, "Radiative heat transfer enhancement to a water tube by combustion gases in porous media," Heat transfer science and technology, vol. 6, pp. 703–710, 1987.

[128] P. Nikolaidis and A. Poullikkas, "A comparative overview of hydrogen production processes," Renewable and sustainable energy reviews, vol. 67, pp. 597–611, 2017.

[129] A. Banerjee and D. Paul, "Developments and applications of porous medium combustion: A recent review," Energy, vol. 221, p. 119868, 2021.

[130] M. K. Drayton, A. V. Saveliev, L. A. Kennedy, A. A. Fridman, and Y.-E. D. Li, "Syngas production using superadiabatic combustion of ultra-rich methane-air mixtures," in Symposium (International) on Combustion, vol. 27, pp. 1361–1367, Elsevier, 1998.

[131] E. Belmont, P. Radyjowski, and J. Ellzey, "Effect of geometric scale on heat recirculation and syngas production in a noncatalytic counter-flow reformer," Combustion Science and Technology, vol. 187, no. 6, pp. 874–893, 2015.

[132] M. Toledo, F. Gracia, S. Caro, J. Gómez, and V. Jovicic, "Hydrocarbons conversion to syngas in inert porous media combustion," International journal of hydrogen energy, vol. 41, no. 14, pp. 5857–5864, 2016.

[133] F. Guerrero, L. Espinoza, N. Ripoll, P. Lisbona, I. Arauzo, and M. Toledo, "Syngas production from the reforming of typical biogas compositions in an inert porous media reactor," Frontiers in Chemistry, vol. 8, p. 145, 2020.

[134] Z. Al-Hamamre, S. Diezinger, P. Talukdar, F. Von Issendorff, and D. Trimis, "Combustion of low calorific gases from landfills and waste pyrolysis using porous medium burner technology," Process Safety and Environmental Protection, vol. 84, no. 4, pp. 297–308, 2006.

[135] K. Al-Attab, J. C. Ho, and Z. Zainal, "Experimental investigation of submerged flame in packed bed porous media burner fueled by low heating value producer gas," Experimental Thermal and Fluid Science, vol. 62, pp. 1–8, 2015.

[136] F. Song, Z. Wen, Z. Dong, E. Wang, and X. Liu, "Ultra-low calorific gas combustion in a gradually-varied porous burner with annular heat recirculation," Energy, vol. 119, pp. 497–503, 2017.

[137] H. Dai, Q. Zhao, B. Lin, S. He, X. Chen, Y. Zhang, Y. Niu, and S. Yin, "Premixed combustion of low-concentration coal mine methane with water vapor addition in a two-section porous media burner," Fuel, vol. 213, pp. 72–82, 2018.

[138] S. Wood and A. T. Harris, "Porous burners for lean-burn applications," Progress in Energy and Combustion Science, vol. 34, no. 5, pp. 667–684, 2008.

[139] A. Valera-Medina, H. Xiao, M. Owen-Jones, W. I. David, and P. Bowen, "Ammonia for power," Progress in Energy and combustion science, vol. 69, pp. 63–102, 2018.

[140] V. Pantangi, S. C. Mishra, P. Muthukumar, and R. Reddy, "Studies on porous radiant burners for lpg (liquefied petroleum gas) cooking applications," Energy, vol. 36, no. 10, pp. 6074–6080, 2011.

[141] N. K. Mishra, S. C. Mishra, and P. Muthukumar, "Performance characterization of a medium-scale liquefied petroleum gas cooking stove with a two-layer porous radiant burner," Applied Thermal Engineering, vol. 89, pp. 44–50, 2015.

[142] S. Panigrahy, N. K. Mishra, S. C. Mishra, and P. Muthukumar, "Numerical and experimental analyses of lpg (liquefied petroleum gas) combustion in a domestic cooking stove with a porous radiant burner," Energy, vol. 95, pp. 404–414, 2016.

[143] M. Sharma, S. C. Mishra, and P. Mahanta, "Effect of burner configuration and operating parameters on the performance of kerosene pressure stove with submerged porous medium combustion," Applied Thermal Engineering, vol. 107, pp. 516–523, 2016.

[144] M. Sharma, P. Mahanta, and S. C. Mishra, "Usability of porous burner in kerosene pressure stove: An experimental investigation aided by energy and exergy analyses," Energy, vol. 103, pp. 251–260, 2016.

[145] S. Panigrahy and S. C. Mishra, "Analysis of combustion of liquefied petroleum gas in a porous radiant burner," International Journal of Heat and Mass Transfer, vol. 95, pp. 488–498, 2016.

[146] S. Jugjai and S. Sanitjai, "Parametric studies of thermal efficiency in a proposed porous radiant recirculated burner (prrb): a design concept for the future burner," International Energy Journal, vol. 18, no. 2, 1996.

[147] S. Jugjai, S. Tia, and W. Trewetasksorn, "Thermal efficiency improvement of an lpg gas cooker by a swirling central flame," International Journal of Energy Research, vol. 25, no. 8, pp. 657–674, 2001.

[148] S. Jugjai and N. Rungsimuntuchart, "High efficiency heat-recirculating domestic gas burners," Experimental thermal and fluid science, vol. 26, no. 5, pp. 581–592, 2002.

[149] K. Dobrego, N. Gnesdilov, I. Kozlov, V. Bubnovich, and H. Gonzalez, "Numerical investigation of the new regenerator–recuperator scheme of voc oxidizer," International journal of heat and mass transfer, vol. 48, no. 23-24, pp. 4695–4703, 2005.

[150] N. Gnesdilov, K. Dobrego, and I. Kozlov, "Parametric study of recuperative voc oxidation reactor with porous media," International journal of heat and mass transfer, vol. 50, no. 13-14, pp. 2787–2794, 2007.

[151] B. Stelzner, C. Keramiotis, S. Voss, M. Founti, and D. Trimis, "Analysis of the flame structure for lean methane–air combustion in porous inert media by resolving the hydroxyl radical," Proc. Combust. Inst., vol. 35, no. 3, pp. 3381–3388, 2015.

[152] J. Kiefer, M. Weikl, T. Seeger, F. Von Issendorff, F. Beyrau, and A. Leipertz, "Non-intrusive gas-phase temperature measurements inside a porous burner using dual-pump CARS," Proc. Combust. Inst., vol. 32, no. 2, pp. 3123–3129, 2009.

[153] M. Weikl, S. Tedder, T. Seeger, and A. Leipertz, "Investigation of porous media combustion by coherent anti-stokes raman spectroscopy," Experiments in fluids, vol. 49, no. 4, pp. 775–781, 2010.

[154] M. Khodsiani, R. Namdar, F. Varnik, F. Beyrau, and B. Fond, "Spatially resolved investigation of flame particle interaction in a two dimensional model packed bed," Particuology, vol. 85, pp. 167–185, 2024.

[155] K. Kohse-Hoinghaus and J. B. Jefferies, Applied combustion diagnostics. CRC Press, 2002.

[156] A. C. Eckbreth, Laser diagnostics for combustion temperature and species. CRC press, 2022.

[157] K. Kohse-Höinghaus, "Laser techniques for the quantitative detection of reactive intermediates in combustion systems," Progress in Energy and Combustion Science, vol. 20, no. 3, pp. 203–279, 1994.

[158] R. V. Fursenko, I. A. Yakovlev, E. S. Odintsov, S. D. Zambalov, and S. S. Minaev, "Pore-scale flame dynamics in a one-layer porous burner," Combust. Flame, p. 111711, 2021.

[159] D. Ebi and N. T. Clemens, "Experimental investigation of upstream flame propagation during boundary layer flashback of swirl flames," Combust Flame, vol. 168, pp. 39–52, 2016.

[160] B. A. Rankin, D. R. Richardson, A. W. Caswell, A. G. Naples, J. L. Hoke, and F. R. Schauer, "Chemiluminescence imaging of an optically accessible non-premixed rotating detonation engine," Combustion and Flame, vol. 176, pp. 12–22, 2017.

[161] A. Aniello, D. Laera, S. Marragou, H. Magnes, L. Selle, T. Schuller, and T. Poinsot, "Experimental and numerical investigation of two flame stabilization regimes observed in a dual swirl h2-air coaxial injector," Combustion and flame, vol. 249, p. 112595, 2023.

[162] Y. Zheng, L. Weller, and S. Hochgreb, "Instantaneous flame front identification by mie scattering vs. oh plif in low turbulence bunsen flame," Experiments in Fluids, vol. 63, no. 5, p. 79, 2022.

[163] E. Flores-Montoya, P.-A. Masset, T. Schuller, and L. Selle, "Flame-front tracking in porous media burners," Combust. Flame, 2024.

[164] E. Flores-Montoya, P.-A. Masset, T. Schuller, and L. Selle, "Speed-up drivers for h2-enriched flames in porous media burners," Proceedings of the Combustion Institute, vol. 40, no. 1-4, p. 105666, 2024.

[165] F. Muller, "Multi-physics coupling for hydrogen combustion within porous media, Ph.D. thesis," 2023.

[166] H. Karcher and K. Polthier, "Construction of triply periodic minimal surfaces," Philosophical Transactions of the Royal Society of London. Series A: Mathematical, Physical and Engineering Sciences, vol. 354, no. 1715, pp. 2077–2104, 1996.

[167] I. Maskery, L. Sturm, A. O. Aremu, A. Panesar, C. B. Williams, C. J. Tuck, R. D. Wildman, I. A. Ashcroft, and R. J. Hague, "Insights into the mechanical properties of several triply periodic minimal surface lattice structures made by polymer additive manufacturing," Polymer, vol. 152, pp. 62–71, 2018.

[168] W. H. Meeks III, "The theory of triply periodic minimal surfaces," Indiana Univ. Math. J., pp. 877–936, 1990.

[169] Q. Zhou, "Pymesh—geometry processing library for python," Software available for download at https://github. com/PyMesh/PyMesh, vol. 7, 2019.

[170] A. Fabri and S. Pion, "Cgal: The computational geometry algorithms library," in Proceedings of the 17th ACM SIGSPATIAL international conference on advances in geographic information systems, pp. 538–539, 2009.

[171] A. Handbook, "Properties and selection: irons, steels, and high-performance alloys," ASM International, vol. Vol. 1, 1990.

[172] J. C. Simmons, X. Chen, A. Azizi, M. A. Daeumer, P. Y. Zavalij, G. Zhou, and S. N. Schiffres, "Influence of processing and microstructure on the local and bulk thermal conductivity of selective laser melted 316l stainless steel," Addit. Manuf., vol. 32, p. 100996, 2020.

[173] A. B. Spierings and G. Levy, "Comparison of density of stainless steel 316l parts produced with selective laser melting using different powder grades," in 2009 International Solid Freeform Fabrication Symposium, University of Texas at Austin, 2009.

[174] S. Brohez, C. Delvosalle, and G. Marlair, "A two-thermocouples probe for radiation corrections of measured temperatures in compartment fires," Fire safety journal, vol. 39, no. 5, pp. 399–411, 2004.

[175] N. L. Johnson, S. Kotz, and N. Balakrishnan, Continuous univariate distributions, volume 2, vol. 289. John wiley & sons, 1995.

[176] A. Zukauskas, "Heat transfer from tubes in crossflow," in Advances in heat transfer, vol. 8, pp. 93–160, Elsevier, 1972.

[177] G. De Soete, "Stability and propagation of combustion waves in inert porous media," Symp. (Int.) Combust., vol. 11, no. 1, pp. 959–966, 1967.

[178] T. Takeno, K. Sato, and K. Hase, "A theoretical study on an excess enthalpy flame," in Symposium (International) on Combustion, vol. 18, pp. 465–472, Elsevier, 1981.

[179] B. Deshaies and G. Joulin, "Asymptotic study of an excess-enthalpy flame," Combustion Science and Technology, vol. 22, no. 5-6, pp. 281–285, 1980.

[180] V. N. Kurdyumov, D. Fernández-Galisteo, and C. Jiménez, "Asymptotic study of premixed flames in inert porous media layers of finite width: Parametric analysis of heat recirculation phenomena," Combust. Flame, vol. 241, p. 112109, 2022.

[181] J. C. Ferguson, S. Sobhani, and M. Ihme, "Pore-resolved simulations of porous media combustion with conjugate heat transfer," Proceedings of the Combustion Institute, vol. 38, no. 2, pp. 2127–2134, 2021.

[182] F. Muller, O. Dounia, and L. Selle, "Direct pore-level simulation of hydrogen flame anchoring mechanisms in an inert porous media," Physics of Fluids, vol. 36, no. 1, 2024.

[183] N. Djordjevic, P. Habisreuther, and N. Zarzalis, "Numerical simulation of the combustion in porous media: relative importance of the different transport mechanisms for the flame stabilization," in Proc. 6th Mediterranean Combustion Symposium, 2009.

[184] D. Diamantis, E. Mastorakos, and D. Goussis, "Simulations of premixed combustion in porous media," Combustion Theory and Modelling, vol. 6, no. 3, pp. 383–411, 2002.

[185] N. Djordjevic, P. Habisreuther, and N. Zarzalis, "A numerical investigation of the flame stability in porous burners employing various ceramic sponge-like structures," Chemical engineering science, vol. 66, no. 4, pp. 682–688, 2011.

[186] F. Kuwahara, M. Shirota, and A. Nakayama, "A numerical study of interfacial convective heat transfer coefficient in two-energy equation model for convection in porous media," International journal of heat and mass transfer, vol. 44, no. 6, pp. 1153–1159, 2001.

[187] M. B. Saito and M. J. De Lemos, "A correlation for interfacial heat transfer coefficient for turbulent flow over an array of square rods," J. Heat Transfer, vol. 128, no. 5, pp. 444–452, 2006.

[188] D. G. Goodwin, R. L. Speth, H. K. Moffat, and B. W. Weber, "Cantera: An object-oriented software toolkit for chemical kinetics, thermodynamics, and transport processes," 2018. Version 2.4.0.

[189] G. P. Smith, "Gri-mech 3.0," http://www. me. berkley. edu/gri_mech/, 1999.

[190] J. Delgado, "Longitudinal and transverse dispersion in porous media," Chemical Engineering Research and Design, vol. 85, no. 9, pp. 1245–1252, 2007.

[191] F. E. Teruel, "Entrance effect on the interfacial heat transfer and the thermal dispersion in laminar flows through porous media," Int. J. Therm. Sci., vol. 104, pp. 172–185, 2016.

[192] P.-f. Hsu and J. R. Howell, "Measurements of thermal conductivity and optical properties of porous partially stabilized zirconia," EXPERIMENTAL HEAT TRANSFER An International Journal, vol. 5, no. 4, pp. 293–313, 1992.

[193] N. Wakao and S. Kaguei, "Heat and mass transfer in packed beds, gorden and breach sci," Publishers, New York, vol. 1, pp. 243–295, 1982.

[194] L. Younis and R. Viskanta, "Experimental determination of the volumetric heat transfer coefficient between stream of air and ceramic foam," Int. J. Heat Mass Transfer, vol. 36, no. 6, pp. 1425–1434, 1993.

[195] N. Wakao and T. Funazkri, "Effect of fluid dispersion coefficients on particle-to-fluid mass transfer coefficients in packed beds: correlation of sherwood numbers," Chemical Engineering Science, vol. 33, no. 10, pp. 1375–1384, 1978.

[196] M. B. Saito and M. J. de Lemos, "Interfacial heat transfer coefficient for non-equilibrium convective transport in porous media," International Communications in Heat and Mass Transfer, vol. 32, no. 5, pp. 666–676, 2005.

[197] R. Viskanta, Yimin Xuan, "Numerical investigation of a porous matrix combustor-heater," Numerical Heat Transfer: Part A: Applications, vol. 36, no. 4, pp. 359–374, 1999.

[198] J. Gostick, M. Aghighi, J. Hinebaugh, T. Tranter, M. A. Hoeh, H. Day, B. Spellacy, M. H. Sharqawy, A. Bazylak, A. Burns, et al., "Openpnm: a pore network modeling package," Computing in Science & Engineering, vol. 18, no. 4, pp. 60–74, 2016.

[199] E. Keilegavlen, R. Berge, A. Fumagalli, M. Starnoni, I. Stefansson, J. Varela, and I. Berre, "Porepy: An open-source software for simulation of multiphysics processes in fractured porous media," Computational Geosciences, vol. 25, pp. 243–265, 2021.

[200] J. T. Gostick, Z. A. Khan, T. G. Tranter, M. D. Kok, M. Agnaou, M. Sadeghi, and R. Jervis, "Porespy: A python toolkit for quantitative analysis of porous media images," Journal of Open Source Software, vol. 4, no. 37, p. 1296, 2019.

[201] J. Gostick, M. Aghighi, J. Hinebaugh, T. Tranter, M. A. Hoeh, H. Day, B. Spellacy, M. H. Sharqawy, A. Bazylak, A. Burns, W. Lehnert, and A. Putz, "Openpnm: A pore network modeling package," Comput. Sci. Eng., vol. 18, no. 4, pp. 60–74, 2016.

[202] M. Balat-Pichelin, J. Sans, and E. Bêche, "Spectral directional and total hemispherical emissivity of virgin and oxidized 316l stainless steel from 1000 to 1650 k," Infrared Phys Technol, vol. 123, p. 104156, 2022.

[203] D. Shi, F. Zou, Z. Zhu, and J. Sun, "Modeling the effect of surface oxidation on the normal spectral emissivity of steel 316l at 1.5 μm over the temperatures ranging from 800 to 1100 k in air," Infrared Physics & Technology, vol. 71, pp. 370–377, 2015.

[204] Z. Al-Hamamre, S. Voß, and D. Trimis, "Hydrogen production by thermal partial oxidation of hydrocarbon fuels in porous media based reformer," International Journal of Hydrogen Energy, vol. 34, no. 2, pp. 827–832, 2009.

[205] T. S. Hunnewell, K. L. Walton, S. Sharma, T. K. Ghosh, R. V. Tompson, D. S. Viswanath, and S. K. Loyalka, "Total hemispherical emissivity of ss 316l with simulated very high temperature reactor surface conditions," Nuclear Technology, vol. 198, no. 3, pp. 293–305, 2017.

[206] A. B. Caldeira and Ç. Susantez, "A simplified numerical approach to hydrogen and hydrocarbon combustion in single and double-layer porous burners," International Journal of Hydrogen Energy, vol. 45, no. 60, pp. 35235–35245, 2020.

[207] S.-S. Su, S.-J. Hwang, and W.-H. Lai, "On a porous medium combustor for hydrogen flame stabilization and operation," International journal of hydrogen energy, vol. 39, no. 36, pp. 21307–21316, 2014.

[208] F. Vance, Y. Shoshin, J. Van Oijen, and L. De Goey, "Effect of lewis number on premixed laminar lean-limit flames stabilized on a bluff body," Proc Combust Inst, vol. 37, no. 2, pp. 1663–1672, 2019.

[209] R. K. Hanson, "Combustion diagnostics: planar imaging techniques," in Symposium (International) on Combustion, vol. 21, pp. 1677–1691, Elsevier, 1988.

[210] G. Smallwood, Ö. Gülder, D. Snelling, B. Deschamps, and I. Gökalp, "Characterization of flame front surfaces in turbulent premixed methane/air combustion," Combustion and Flame, vol. 101, no. 4, pp. 461–470, 1995.

[211] Ö. Gülder, G. J. Smallwood, R. Wong, D. Snelling, R. Smith, B. Deschamps, and J.-C. Sautet, "Flame front surface characteristics in turbulent premixed propane/air combustion," Combustion and Flame, vol. 120, no. 4, pp. 407–416, 2000.

[212] W. Xu, A. Wickersham, Y. Wu, F. He, and L. Ma, "3d flame topography obtained by tomographic chemiluminescence with direct comparison to planar mie scattering measurements," Applied optics, vol. 54, no. 9, pp. 2174–2182, 2015.

[213] R. J. Adrian and J. Westerweel, Particle image velocimetry. No. 30, Cambridge university press, 2011.

[214] S. T. Wereley and C. D. Meinhart, "Recent advances in micro-particle image velocimetry," Annual review of fluid mechanics, vol. 42, pp. 557–576, 2010.

[215] M. Raffel, C. E. Willert, F. Scarano, C. J. Kähler, S. T. Wereley, and J. Kompenhans, Particle image velocimetry: a practical guide. springer, 2018.

[216] I. Grant, "Particle image velocimetry: a review," Proceedings of the Institution of Mechanical Engineers, Part C: Journal of Mechanical Engineering Science, vol. 211, no. 1, pp. 55–76, 1997.

[217] R. J. Adrian, "Twenty years of particle image velocimetry," Experiments in fluids, vol. 39, pp. 159–169, 2005.

[218] M. A. Northrup, T. J. Kulp, S. M. Angel, and G. F. Pinder, "Direct measurement of interstitial velocity field variations in a porous medium using fluorescent-particle image velocimetry," Chemical engineering science, vol. 48, no. 1, pp. 13–21, 1993.

[219] M. Shams, I. Currie, and D. James, "The flow field near the edge of a model porous medium," Experiments in fluids, vol. 35, pp. 193–198, 2003.

[220] M. F. Tachie, D. F. James, and I. G. Currie, "Velocity measurements of a shear flow penetrating a porous medium," Journal of Fluid Mechanics, vol. 493, pp. 319–343, 2003.

[221] M. Ahkami, T. Roesgen, M. O. Saar, and X.-Z. Kong, "High-resolution temporo-ensemble piv to resolve pore-scale flow in 3d-printed fractured porous media," Transport in Porous Media, vol. 129, pp. 467–483, 2019.

[222] I. S. Larsson, T. S. Lundström, and H. Lycksam, "Tomographic piv of flow through ordered thin porous media," Experiments in Fluids, vol. 59, pp. 1–7, 2018.

[223] H. Harshani, S. Galindo-Torres, A. Scheuermann, and H. Muhlhaus, "Experimental study of porous media flow using hydro-gel beads and led based piv," Measurement Science and Technology, vol. 28, no. 1, p. 015902, 2016.

[224] J. K. Arthur, D. W. Ruth, and M. F. Tachie, "Piv measurements of flow through a model porous medium with varying boundary conditions," Journal of Fluid Mechanics, vol. 629, pp. 343–374, 2009.

[225] J. Arthur, "Piv study of flow through and over porous media at the onset of inertia," Advances in Water Resources, vol. 146, p. 103793, 2020.

[226] J. G. Santiago, S. T. Wereley, C. D. Meinhart, D. Beebe, and R. J. Adrian, "A particle image velocimetry system for microfluidics," Experiments in fluids, vol. 25, no. 4, pp. 316–319, 1998.

[227] C. D. Meinhart, S. T. Wereley, and J. G. Santiago, "A piv algorithm for estimating time-averaged velocity fields," J. Fluids Eng., vol. 122, no. 2, pp. 285–289, 2000.

[228] D. Durox, S. Ducruix, and F. Lacas, "Flow seeding with an air nebulizer," Experiments in Fluids, vol. 27, pp. 408–413, 1999.

[229] D. Martínez-Ruiz, "On the structure of steady one-dimensional liquid-fueled detonations," Physics of Fluids, vol. 35, no. 8, 2023.

[230] F. H. Vance, Y. Shoshin, L. de Goey, and J. A. van Oijen, "Quantifying the impact of heat loss, stretch and preferential diffusion effects to the anchoring of bluff body stabilized premixed flames," Combust Flame, vol. 237, p. 111729, 2022.

[231] M. Mizomoto, Y. Asaka, S. Ikai, and C. Law, "Effects of preferential diffusion on the burning intensity of curved flames," Symp. (Int.) Combust., vol. 20, no. 1, pp. 1933–1939, 1985.

[232] A. Midilli, M. Ay, I. Dincer, and M. A. Rosen, "On hydrogen and hydrogen energy strategies: I: current status and needs," Renew Sustain Energy Rev, vol. 9, no. 3, pp. 255–271, 2005.

[233] J. Leicher, J. Schaffert, H. Cigarida, E. Tali, F. Burmeister, A. Giese, R. Albus, K. Görner, S. Carpentier, P. Milin, et al., "The impact of hydrogen admixture into natural gas on residential and commercial gas appliances," Energies, vol. 15, p. 777, 2022.

[234] F. Schiro, A. Stoppato, and A. Benato, "Modelling and analyzing the impact of hydrogen enriched natural gas on domestic gas boilers in a decarbonization perspective," Carbon Resources Conversion, vol. 3, pp. 122–129, 2020.

[235] G. L. Basso, B. Nastasi, D. A. Garcia, and F. Cumo, "How to handle the hydrogen enriched natural gas blends in combustion efficiency measurement procedure of conventional and condensing boilers," Energy, vol. 123, pp. 615–636, 2017.

[236] L. Boeck, J. Melguizo-Gavilanes, and J. Shepherd, "Hot surface ignition dynamics in premixed hydrogen–air near the lean flammability limit," Combust Flame, vol. 210, pp. 467–478, 2019.

[237] B. Lewis and G. Von Elbe, Combustion, flames and explosions of gases. Elsevier, 2012.

[238] A. A. Putnam and R. A. Jensen, "Application of dimensionless numbers to flash-back and other combustion phenomena," in Symposium on Combust Flame, and Explosion Phenomena, vol. 3, pp. 89–98, Elsevier, 1948.

[239] F. H. Vance, Y. Shoshin, L. de Goey, and J. A. van Oijen, "Flame stabilization regimes for premixed flames anchored behind cylindrical flame holders," Proc Combust Inst, vol. 38, no. 2, pp. 1983–1992, 2021.

[240] T. B. Kıymaz, E. Böncü, D. Güleryüz, M. Karaca, B. Yılmaz, C. Allouis, and İ. Gökalp, "Numerical investigations on flashback dynamics of premixed methane-hydrogen-air laminar flames," Int J Hydrogen Energy, vol. 47, no. 59, pp. 25022–25033, 2022.

[241] A. Gruber, J. H. Chen, D. Valiev, and C. K. Law, "Direct numerical simulation of premixed flame boundary layer flashback in turbulent channel flow," J Fluid Mech, vol. 709, pp. 516–542, 2012.

[242] C. Eichler and T. Sattelmayer, "Premixed flame flashback in wall boundary layers studied by long-distance micro-piv," Exp Fluids, vol. 52, no. 2, pp. 347–360, 2012.

[243] C. Heeger, R. Gordon, M. Tummers, T. Sattelmayer, and A. Dreizler, "Experimental analysis of flashback in lean premixed swirling flames: upstream flame propagation," Exp Fluids, vol. 49, pp. 853–863, 2010.

[244] M. B. Giles, "Stability analysis of numerical interface conditions in fluid–structure thermal analysis," Int J Numer Methods Fluids, vol. 25, no. 4, pp. 421–436, 1997.

[245] F. Duchaine, N. Maheu, V. Moureau, G. Balarac, and S. Moreau, "Large-eddy simulation and conjugate heat transfer around a low-mach turbine blade," J. Turbomach., vol. 136, no. 5, p. 051015, 2014.

[246] T. J. Poinsot and S. Lelef, "Boundary conditions for direct simulations of compressible viscous flows," J Comput Phys, vol. 101, no. 1, pp. 104–129, 1992.

[247] B. Rochette, F. Collin-Bastiani, L. Gicquel, O. Vermorel, D. Veynante, and T. Poinsot, "Influence of chemical schemes, numerical method and dynamic turbulent combustion modeling on les of premixed turbulent flames," Combust Flame, vol. 191, pp. 417–430, 2018.

[248] C. K. Law, G. Jomaas, and J. K. Bechtold, "Cellular instabilities of expanding hydrogen/propane spherical flames at elevated pressures: theory and experiment," Proceedings of the combustion institute, vol. 30, no. 1, pp. 159–167, 2005.

[249] S. Muppala, M. Nakahara, N. Aluri, H. Kido, J. Wen, and M. Papalexandris, "Experimental and analytical investigation of the turbulent burning velocity of two-component fuel mixtures of hydrogen, methane and propane," Int J Hydrogen Energy, vol. 34, no. 22, pp. 9258–9265, 2009.

[250] F. Dinkelacker, B. Manickam, and S. Muppala, "Modelling and simulation of lean premixed turbulent methane/hydrogen/air flames with an effective lewis number approach," Combust Flame, vol. 158, no. 9, pp. 1742–1749, 2011.

[251] E. Hu, Z. Huang, J. He, and H. Miao, "Experimental and numerical study on laminar burning velocities and flame instabilities of hydrogen–air mixtures at elevated pressures and temperatures," international journal of hydrogen energy, vol. 34, no. 20, pp. 8741–8755, 2009.

[252] C. Tang, Z. Huang, C. Jin, J. He, J. Wang, X. Wang, and H. Miao, "Laminar burning velocities and combustion characteristics of propane–hydrogen–air premixed flames," Int J Hydrogen Energy, vol. 33, no. 18, pp. 4906–4914, 2008.

[253] C. Tang, Z. Huang, J. Wang, and J. Zheng, "Effects of hydrogen addition on cellular instabilities of the spherically expanding propane flames," Int J Hydrogen Energy, vol. 34, no. 5, pp. 2483–2487, 2009.

[254] N. Bouvet, F. Halter, C. Chauveau, and Y. Yoon, "On the effective lewis number formulations for lean hydrogen/hydrocarbon/air mixtures," Int J Hydrogen Energy, vol. 38, no. 14, pp. 5949–5960, 2013.

[255] S. Zitouni, D. Pugh, A. Crayford, P. Bowen, and J. Runyon, "Lewis number effects on lean premixed combustion characteristics of multi-component fuel blends," Combust Flame, vol. 238, p. 111932, 2022.

[256] C. Koren, R. Vicquelin, and O. Gicquel, "Self-adaptive coupling frequency for unsteady coupled conjugate heat transfer simulations," Int J Therm Sci, vol. 118, pp. 340–354, 2017.

[257] G. Pizza, C. E. Frouzakis, J. Mantzaras, A. G. Tomboulides, and K. Boulouchos, "Dynamics of premixed hydrogen/air flames in microchannels," Combust Flame, vol. 152, no. 3, pp. 433–450, 2008.

[258] G. Pizza, C. E. Frouzakis, J. Mantzaras, A. G. Tomboulides, and K. Boulouchos, "Dynamics of premixed hydrogen/air flames in mesoscale channels," Combust Flame, vol. 155, no. 1-2, pp. 2–20, 2008.

[259] C. Jiménez, D. Fernández-Galisteo, and V. N. Kurdyumov, "Flame-acoustics interaction for symmetric and non-symmetric flames propagating in a narrow duct from an open to a closed end," Combust Flame, vol. 225, pp. 499–512, 2021.

[260] A. Dejoan, C. Jiménez, and V. N. Kurdyumov, "Critical conditions for non-symmetric flame propagation in narrow channels: Influence of the flow rate, the thermal expansion, the lewis number and heat-losses," Combust Flame, vol. 209, pp. 430–440, 2019.

[261] A. Dejoan, C. Jiménez, D. Martínez-Ruiz, V. Muntean, M. Sánchez-Sanz, and V. N. Kurdyumov, "Flame propagation in narrow horizontal channels: Impact of the gravity field on the flame shape," Proc Combust Inst, vol. 39, no. 2, pp. 1535–1543, 2023.

[262] N. Burali, S. Lapointe, B. Bobbitt, G. Blanquart, and Y. Xuan, "Assessment of the constant non-unity lewis number assumption in chemically-reacting flows," Combust. Theory Model., vol. 20, no. 4, pp. 632–657, 2016.

[263] J. Van Oijen, A. Donini, R. Bastiaans, J. ten Thije Boonkkamp, and L. De Goey, "State-of-the-art in premixed combustion modeling using flamelet generated manifolds," Prog Energy Combust Sci, vol. 57, pp. 30–74, 2016.

[264] F. Duchaine, S. Jauré, D. Poitou, E. Quémerais, G. Staffelbach, T. Morel, and L. Gicquel, "Analysis of high performance conjugate heat transfer with the OpenPalm coupler," Comput. Sci. Discov., vol. 8, no. 1, p. 015003, 2015.

[265] V. Frayssé, L. Giraud, and S. Gratton, "A set of GMRES routines for real and complex arithmetic on high performance computers, CERFACS," 2003.

RÉPUBLIQUE FRANÇAISE
Liberté
Égalité
Fraternité

Université de Toulouse

Titre : Étude expérimentale de la stabilisation des flammes dans des brûleurs poreux : application des diagnostics optiques dans des géométries imprimées en 3D

Mots clés : Combustion en milieu poreux, Hydrogène, Fabrication additive, Brûleurs optiquement accessibles, Adaptation de la topologie, Diagnostics optiques

Résumé : La transition vers une économie neutre en carbone est confrontée à deux défis majeurs : le stockage de l'excès d'énergie provenant des énergies renouvelables et la décarbonation des processus de combustion dans les secteurs difficiles à électrifier. La stratégie Power to Gas (P2G) propose de résoudre ces problèmes en substituant partiellement l'hydrogène dans le réseau actuel de gaz naturel. Cependant, cela nécessite le développement de brûleurs flexibles capables de s'adapter à des niveaux variables d'hydrogène dans le réseau. Cela est compliqué à cause des différences entre les propriétés de la flamme d'hydrogène et celles des combustibles hydrocarbonés. Les brûleurs poreux (PMBs) sont considérés comme une technologie prometteuse en raison de leurs propriétés uniques. Les PMBs utilisent la recirculation de chaleur pour stabiliser les flammes à l'intérieur de matrices poreuses inertes, incrémentant le taux de consommation de la flamme et atteignant des températures locales superadiabatiques. Cela permet des densités de puissance plus élevées et l'extension des limites d'inflammabilité, ce qui se traduit par des dispositifs compacts et une faible émission de NOx avec des efficacités radiatives élevées.
Le mécanisme fondamental de fonctionnement des brûleurs poreux à l'échelle macroscopique, la recirculation de la chaleur, est bien compris. Cependant, il existe encore une connaissance limitée sur certains phénomènes à l'échelle des pores et de leur influence sur le comportement du système global. En raison de la non-linéarité de la combustion et du transfert de chaleur, la stabilisation de la flamme et les performances du brûleur dépendent fortement des détails à l'échelle des pores. Les modèles de bas ordre actuels n'incluent pas la modélisation des interactions flamme-paroi et des effets de diffusion préférentielle, ce qui entraîne une faible précision. Les diagnostics non intrusifs avancés pourraient être utilisés pour étudier la structure locale de la flamme et guider l'amélioration des modèles de bas ordre. Cependant, les mesures expérimentales dans les PMBs sont entravées par le manque d'accès optique à l'intérieur de la matrice poreuse. Malgré les efforts récents, l'application de diagnostics optiques et non intrusifs dans les PMBs est encore très rare. Cette thèse présente une étude expérimentale sur la combustion en milieu poreux et est consacrée au développement de diagnostics optiques. Des PMBs optiquement accessibles sont produits en combinant des topologies définies par ordinateur avec des techniques de fabrication additive. La méthodologie actuelle offre un accès optique étendu dans une configuration de brûleur 3D sans perturber la structure de la matrice. L'accès optique est utilisé pour appliquer une série de diagnostics optiques, y compris la chimiluminescence CH*, l'imagerie de diffusion de Mie et la micro-PIV. Nos résultats montrent les limites des VAMs actuels et de leurs méthodes de validation. La mise en œuvre de diagnostics novateurs a également révélé différentes tendances de stabilisation dans les flammes enrichies en H2, soulignant l'effet des mécanismes d'ancrage local sur les limites de fonctionnement du brûleur. Enfin, l'accès optique est exploité pour effectuer des diagnostics laser et étudier la structure de la flamme à l'échelle des pores. Nos résultats révèlent différents modes de stabilisation et mettent en évidence l'impact de l'écoulement interstitiel sur les performances du brûleur. Cette thèse ouvre de nouvelles voies pour l'application de diagnostics non intrusifs et plaide pour un développement supplémentaire des techniques expérimentales avancées dans les brûleurs poreux.

Title: Experimental study of flame stabilization in porous burners: development of optical diagnostics in 3D printed geometries

Key words: Porous Media Combustion, Hydrogen, Additive Manufacturing, Optically Accessible Burners, Topology Tailoring, Optical diagnostics

Abstract: Porous Media Burners (PMBs) are a combustion technology based on heat recirculation where a flame is stabilized within the cavities of an inert porous matrix. In PMBs, heat is transferred upstream from the burned to the unburned gas through the solid matrix yielding a preheating of the reactants.
This increases their burning rate allowing for more compact combustion devices and the operation beyond conventional flammability limits. As a result, the stabilization of flames at ultra-lean equivalence ratios is possible, with the subsequent reduction of the flame temperature and NOx emissions. In these burners, a substantial fraction of the power is radiated by the hot solid phase, with radiated power fractions ranging between 20-30 %. This, together with their elevated efficiency and low pollutant emissions, has motivated their commercial use in various infrared heating applications.
In the past years, PMBs have received renewed interest owing to their potential as fuel flexible burners. Their ability to stabilize flames over a wide range of burning rates makes them promising candidates to handle the uneven flame properties of hydrogen and hydrocarbon fuels.
The mechanism of heat recirculation in PMBs is well understood. However, there is still limited knowledge about many pore-scale phenomena that have a critical impact on the macroscopic behavior of the system and its performance.
Advanced nonintrusive diagnostics could be used to study local flame stabilization mechanisms and improve current models. However, experimental measurements in PMBs are hindered by the lack of optical access to the interior of the porous matrix.
This dissertation presents an experimental study on porous media combustion and is devoted to the application of optical diagnostics. Optically accessible PMBs are produced by combining computer-defined topologies with additive manufacturing techniques. This methodology provides an extensive optical access in a 3D burner configuration without altering the matrix structure. Optical access is leveraged to apply CH* chemiluminescence, Mie-scattering imaging and micro PIV. Topology tailoring is exploited to analyze the influence of the geometrical parameters of the porous matrix. Direct flame visualization enables the tracking of the reaction region as a function of the operating conditions, which can be used for model validation. The present results bring to light several limitations of current low order models and highlight the influence of the pore size on flame stabilization. Flame-front tracking is also used to investigate the effect of H2-enrichment on the behavior of the flame. This technique reveals different stabilization trends in H2-enriched flames that are not well retrieved by current models. Mie-scattering permits the quantification of the re-equilibration distance and the analysis of the flame shape. Micro PIV measurements show the influence of the topology on the interstitial flow and on the contribution of hydrodynamic effects to flame stabilization.
This PhD seeks to open new paths for the application of non-intrusive diagnostics in PMBs and to improve the current understanding of flame stabilization mechanisms.